Electronic Thesis and Dissertation Repository

4-20-2016 12:00 AM

Kinetics of Length Scale Dependent Deformation of Gold Microspheres and Micropillars

A Z M Ariful Islam
The University of Western Ontario

Supervisor
Dr. Robert J. Klassen
The University of Western Ontario

Follow this and additional works at: https://ir.lib.uwo.ca/etd

Part of the Engineering Science and Materials Commons, Materials Science and Engineering Commons, and the Nanoscience and Nanotechnology Commons

Recommended Citation

Abstract

In this thesis length and time scale dependence of the operative plastic deformation mechanisms in Au is studied. Uniaxial compression tests were performed at various loading rates on FIB-milled Au micropillars and single-crystalline Au microspheres of diameter ranging from 0.8 to 6.0 µm to investigate the *incipient* and *bulk* plasticity events. Constant-load ambient-temperature creep tests were performed on the micropillars to study the time-dependent plasticity at very slow strain rates. Uniaxial compression tests were also performed on coated Au microspheres to study the effect of extrinsic constraint on the deformation mechanisms.

During uniaxial compression, both the Au micropillars and microspheres displayed strain jumps, the frequency of which decreased with increasing sample diameter and increasing resolved shear stress τ_R. The *bulk* flow stress, corresponding to 5% – 20% average compressive strain, was dependent upon both the strain rate and the specimen diameter. Analysis of the apparent activation volume, V^*, and energy, Q^*, of the deformation process indicated that the operative deformation mechanism for the small 0.8 µm diameter pillars and spheres was characteristic of a mechanism limited by surface nucleation of dislocations while larger diameter samples displayed values indicative of the more common dislocation-obstacle interaction limited deformation mechanism.

The deformation-rate dependence of *incipient* plastic deformation of the Au micropillars and microspheres was also dependent upon the strain rate and sample diameter. For the smallest, sub-micrometer size, samples the *incipient* plasticity was controlled by heterogeneous dislocation nucleation events, while a dislocation-obstacle interaction limited glide process was found to be operative in the larger specimens.

In the extrinsic constraint study, Au microspheres that were coated with a 40 – 80 nm thick Ni layer displayed a slightly increased flow stress compared to similar size uncoated microspheres. The estimated V^* and Q^* values for the coated microspheres suggest that the mechanism responsible for the initiation of first dislocation motion is essentially the same regardless of the presence of a constraining coating.

Keywords

Co-Authorship Statement

The research presented in this thesis is composed of five manuscripts, one published and four will be submitted for publication, which are co-authored by AZM Ariful Islam and Dr. Robert J. Klassen.

The experiments, data analysis, interpretation and manuscript drafting were prepared by AZM Ariful Islam. The data further interpretation and editing of the manuscript were performed by Dr. Robert J. Klassen.

Acknowledgments

I wish to express my sincere gratitude to Professor Robert J. Klassen for his time, support, guidance and ideas provided throughout this project. Without his help, the successful competition of this thesis and the quality of work achieved would not have been possible. His contributions and help are greatly appreciated.

I also wish to thank my past and present colleagues whom I worked with at our Micro Mechanical testing laboratory, Western Nanofabrication Facility, Canadian Centre for Electron Microscopy (McMaster University) and Western Zircon and Accessory Phase Laboratory (ZAPLab), specially Dr. Vineet Bhakhri, Dr. Todd Simpson, Mr. Chris Butcher, Mr. Ivan Barker and all those who have been involved with this project one way or the other for their time and support.

Last but not least, I would like to express my thanks to National Sciences and Engineering Research Council of Canada (NSERC) Discovery Grant program and Ontario Graduate Scholarship (OGS) program for financially supporting this project.

Dedications

I dedicate this thesis to:

My father and mother,
Mohammad Aminul Islam and *Khairun Nahar*

My wife,
Rubaiat Ameena Mithila

My son and daughter,
Taheem Mutakabbir Islam and *Rukayat Subaha Islam.*

Table of Contents

List of Tables

List of Figures

List of Appendices

Nomenclature

Symbols	Definition
b	Burgers vector
n	Strain hardening exponent
m	Strain rate sensitivity
F	Compression force
h	Compression depth
σ	Stress
ε	Strain
$\dot{\varepsilon}$	Strain rate
τ	Shear stress
τ_{0K}	Athermal stress
τ_R	Resolved shear stress
V	Activation Volume
V^*	Apparent activation volume
Q	Activation energy
Q^*	Apparent activation energy
T	Temperature
k	Boltzmann constant
E	Elastic modulus
E_r	Reduced elastic modulus
ν	Poisson's ratio
G	Shear modulus
ΔG_0	Gibbs free energy

Symbols	Definition
R	Universal gas constant
ρ_m	Mobile dislocation density
ν_0	Atomic vibration/jump frequency
M	Taylor Factor

Abbreviations	Definition
NEMS	Nano Electro-Mechanical Systems
MEMS	Micro Electro-Mechanical Systems
FCC	Face Centered Cubic
BCC	Body Centered Cubic
FIB	Focused Ion Beam
TEM	Transmission Electron Microscope
SEM	Scanning Electron Microscope
EBSD	Electron Backscattered Diffraction
AFM	Atomic Force Microscope
FE	Finite Element
SED	Strain Energy Density
SA/V	Surface Area to Volume Ratio
PMMA	Polymethyl Methacrylate

Chapter 1

1   Overview

1.1   Introduction

Nano-/micro electro-mechanical systems (NEMS/MEMS) are being used in many sophisticated applications such as in bio-medical and microelectronics devices. For the development of these advanced systems, constituting materials are used in small volumes. Therefore, understanding mechanical behavior of samples with very small volumes is absolutely necessary in order to realize the full potential of these emerging nano-/micro-technologies [1−5]. Classical laws of mechanics hold that mechanical properties are independent of sample size; however, results of experiments and molecular dynamics simulations indicate that crystals exhibit strong size effects at the sub-micron scale [6]. Plastic deformation in small volumes requires higher stresses than are needed for plastic flow of bulk materials. In bulk form, the yield stress and strength of the material remain essentially independent of the sample size because the sample dimensions are large compared to the length scale characterizing the material's microstructure. However, when the critical dimensions of a device approach the size of material's microstructure a size effect prevails and the bulk properties can no longer be used to predict mechanical behavior [7]. Nix et al. [8] suggested that the length scale dependence of the higher flow stress can arise from either the intrinsic properties of the deforming material or from extrinsic geometrical constraint imposed upon the deformation.

1.2   Objective

The objective of this study is to use micro-mechanical test techniques to understand the effect of microstructure on the underlying mechanisms of plastic deformation of micron and sub-micron size *FCC* metal samples. Understanding the fundamental time-dependent

mechanisms of dislocation nucleation and glide is very important because of recent technological advancement of devices such as MEMS, sensors, actuators etc.

High purity (≥99.99%) polycrystalline and single crystalline Gold (Au) is chosen as a model *FCC* material in this study. Au is chosen because it is the most often used for sub-micron size commercial components and for studies of the length-scale dependence of plastic deformation. Additionally, Au has no native surface oxide layer. Consequently, free surfaces can serve as effective sinks and sources for dislocation, and can inhibit dislocation storage within the deforming volume. As sample dimensions become smaller the role of surfaces becomes more important, and can lead to interesting and unusual mechanical behavior.

1.3   Structure of Thesis

This thesis has been written following the guidelines of the School of Graduate and Postdoctoral Studies at Western University adopting an integrated-article format. It contains 8 chapters, 5 of which are experimental research designed to study the length-scale dependent deformation parameters of small size Au samples.

Chapter 2 of this thesis presents a review of relevant published literature related to the evidence and unique features related to length-scale dependent plastic deformation of small size samples. It also describes various numerical and experimental test techniques used by several researchers to assess the mechanical properties and plastic deformation parameters in various geometries of small size samples. Theories related to the length scale effect on the rate-dependent plasticity and the way to accessing fundamental deformation parameters are also described. This research involves several unique testing and analyzing techniques, a concise description of the primary techniques are also included in this chapter.

Chapter 3 discusses the size dependence of the time dependent plastic deformation behavior of Au micropillars and microspheres. The length scale dependence of the operative mechanisms of time-dependent plastic deformation was studied using room temperature compression, creep, tests performed on Au micropillars and microspheres of

1.0 to 5.0 µm diameter. A part of this chapter was presented in Materials Research Society (MRS) Spring Meeting 2013, San Francisco, California, USA; the 24th Canadian Material Science Conference (CMSC) 2012, Western University, London, Ontario, Canada, and the 25th CMSC 2013, McGill University, Montreal, Canada. A version of this chapter was published in the Materials Research Society Proceedings, May 2013 [9].

Chapter 4 presents the investigation of the size and strain rate dependence of plastic deformation of Au microspheres at room-temperature. Au microspheres of four sizes (0.8 to 6.0 µm diameters) were fabricated and micro-compression tests were performed at different loading rates. Finite Element (FE) analysis was performed to estimate the stress-strain distribution within the compressed microspheres. Finally, the strain rate dependence of the estimated flow stress of the different size microspheres was investigated to determine the operative deformation mechanism. A part of this chapter was presented to the MRS Spring Meeting 2014, San Francisco, California, USA and the 25th Canadian Congress of Applied Mechanics (CANCAM) conference 2015, London, Ontario, Canada. A shorter version of this chapter was published in the 25th CANCAM 2015 proceedings. A version of this chapter is being prepared for journal submission.

Chapter 5 presents the investigation of the deformation-rate dependence of the incipient plastic deformation of Au microspheres of diameter ranging from 0.8 to 6.0 µm. The initial portion of force-displacement data from micro-compression tests performed on the Au microspheres were analyzed further to extract the apparent activation volume and energy controlling the dislocation nucleation/glide process. A version of this chapter is being prepared for journal submission.

Chapter 6 presents the study of the size and strain rate dependence of incipient and bulk plastic deformation of Au micropillars of diameter ranging from 0.8 to 4.0 µm at room temperature using flat-punch micro-compression testing. The dependence of yield stress on the surface area to volume ratio (SA/V) of the micropillars was determined and the results were compared to the trends reported for Au microspheres in Chapter 4. A thermal activation based model was used to interpret the loading rate dependence of the incipient

yield stress, and the associated deformation rate controlling parameters V^* and Q were estimated. A version of this chapter will be submitted for publication to a journal.

Chapter 7 presents the study of the effect of a surface constraining layer, suppression of dislocation nucleation and trapping of mobile dislocations, on the mechanical yield strength and deformation mechanisms of micrometer-size ductile metal samples. For this study single crystal Au microspheres of 3 μm diameter were coated with a sputter-deposited nano-crystalline Ni layer of 40 or 80 nm thickness and room temperature compression tests were performed at three loading rates. Force-displacement (F-h) curves of the coated Au microspheres were obtained and compared with F-h curves from similar diameter uncoated Au spheres. The initial portion of the F-h curves was fitted with a Hertzian contact model and the corresponding incipient force was measured. The apparent activation volume corresponding to the initiation of incipient plasticity was estimated for these coated spheres. Finite element analysis was used to estimate the stress and strain distribution within the compressed coated Au spheres. These data were used to estimate the apparent activation volume and energy corresponding to the plastic deformation at 5% of strain of these coated spheres and results are compared with the uncoated spheres. A part of this chapter was presented to the MRS Spring Meeting 2014, San Francisco, California, USA. A version of this chapter will be submitted for publication to a journal.

This thesis ends in Chapter 8 with a summary of the main findings and scope of future research.

1.4   Contributions

The main contributions of this thesis are given below:

Length-scale dependence of time-dependent plastic deformation mechanism of Au micropillars and microspheres was studied. Long-duration (1800 and 3600s) creep tests were performed and the creep behavior was analyzed. The long-duration creep tests of both the micropillars and microspheres have not been studied before. Nor has the time-dependent plastic deformation mechanism of Au pillars and spheres been studied.

Most of current researcher has investigated the size-dependence of the plasticity of small-volume samples by considering plasticity as essentially being a rate-independent process. This is in fact quite an oversimplification. The research in this thesis investigates, for the first time, the length-scale and strain rate-dependent plasticity and the deformation kinetics of sub-micron size Au pillars and spheres.

The kinetics of the incipient plastic deformation of small size samples was studied. The incipient plastic behavior of Au micropillar and microsphere was not observed before.

The effect of a surface passivation layer on the plastic deformation mechanism of small size samples was also studied. There are only few studies available on this topic for micropillars but none for microsphere therefore the research presented here on this topic represents a significant new contribution to the field.

References

1. J. Greer and W. Nix, Jun. 2006, "Nanoscale gold pillars strengthened through dislocation starvation," *Phys. Rev. B*, Vol. 73, pp. 245410–6.

2. J. R. Greer, C. R. Weinberger, and W. Cai, Oct. 2008, "Comparing the strength of f.c.c. and b.c.c. sub-micrometer pillars: Compression experiments and dislocation dynamics simulations," *Mater. Sci. Eng. A*, Vol. 493, pp. 21–25.

3. J.-Y. Kim and J. R. Greer, 2008, "Size-dependent mechanical properties of molybdenum nanopillars," *Appl. Phys. Lett.*, Vol. 93, p. 101916.

4. C. P. Frick, B. G. Clark, S. Orso, a. S. Schneider, and E. Arzt, Aug. 2008, "Size effect on strength and strain hardening of small-scale [111] nickel compression pillars," *Mater. Sci. Eng. A*, Vol. 489, pp. 319–329.

5. J. R. Greer and J. T. M. De Hosson, Aug. 2011, "Plasticity in small-sized metallic systems: Intrinsic versus extrinsic size effect," *Prog. Mater. Sci.*, Vol. 56, pp. 654–724.

6. J. R. Greer, W. C. Oliver, and W. D. Nix, Apr. 2005, "Size dependence of mechanical properties of gold at the micron scale in the absence of strain gradients," *Acta Mater.*, Vol. 53, pp. 1821–1830.

7. J. Greer, 2006, "Bridging the gap between computational and experimental length scales: a review on nano-scale plasticity," *Rev. Adv. Mater. Sci*, Vol. 13, pp. 59–70.

8. W. D. Nix, J. R. Greer, G. Feng, and E. T. Lilleodden, Feb. 2007, "Deformation at the nanometer and micrometer length scales: Effects of strain gradients and dislocation starvation," *Thin Solid Films*, Vol. 515, pp. 3152–3157.

9. Azm Islam and R. J. Klassen, May 2013, "Study of the Size Dependence of Time-dependent Plastic Deformation of Gold Micro-pillars and Micro-spheres," *MRS Proc.*, Vol. 1580, pp. mrss13–1580–bbb08–03.

Chapter 2

2   Review of Evidence and Theories Related to Length-scale Plasticity

The purpose of this research is to use micromechanical test techniques to study the effect of microstructure on the operative mechanisms of plastic deformation of *FCC* crystalline metal samples of micrometer and sub-micrometer size scale. Understanding the mechanisms of dislocation nucleation and motion in these small samples is now increasingly important because of the development of many technological devices that have size at this scale. Many researchers have studied the size-dependence of the plasticity of small-volume samples by considering plasticity as essentially a rate-independent process. This is in fact quite an oversimplification since plasticity is in general a strain rate-dependent process; however, investigation of the length-scale dependence of the kinetics of the plastic deformation process in ductile crystalline metals is still lacking. Literature relevant to these topics will be discussed in this chapter.

The equivalent stress – strain response of bulk materials is essentially independent of sample size since the sample dimensions are very large in comparison to the characteristic length scale of the material's microstructure. When, however, dimensions of the sample approach that of its microstructural features, such as its grain size or its inter-phase spacing, a size effect prevails and the equivalent stress – strain flow curve of the bulk material no longer accurately predicts the flow behavior of the small sample [1]. This phenomena was first studied in detail by the performance of uniaxial tensile tests on very small diameter metallic and non-metallic whiskers [2]. More recently new, more informative, testing techniques have been used to reveal considerable important information on the differences in the operative deformation mechanisms in small volume samples compared to their bulk counterparts. These developments are discussed below.

2.1 Length-scale Dependence of the Uniaxial Flow Stress

Mechanical tests performed under uniaxial stress conditions on micron- and sub-micron size tensile specimens have been performed as early as 1947, where Fisher and Holloman [2] studied the size dependence of the yield stress of Copper whiskers having micrometer-scale diameters. These whiskers were thought to be initially free of defects (i.e. dislocations) prior to deformation. During deformation in tension, they exhibited initial elastic deformation followed by plastic yielding and failure at very high stress levels which are near to the theoretical strength of the crystal. They proposed that the high initial yield stress is associated with the nucleation of the first dislocation/defect within the otherwise perfect crystalline whisker while the low stress observed subsequent to yielding was attributed to the easy glide of these new dislocations through the essentially dislocation free whisker.

In recent years, uniaxial compression of nanopillars has become the most popular experimental method to investigate the length-scale dependence of plastic deformation in ductile metals. Uchic et al. [3] were the first to use this test methodology to study small-scale mechanical behavior of Focused Ion Beam (FIB) milled Ni micropillars and reported that there was a gradual progression between bulk and size-limited behavior as the micropillar diameter decreased from 40 to 5 µm; significantly higher compressive strength was observed in micropillars of smaller diameter.

Greer and Nix [4,5] continued on from these studies to investigate the uniaxial stress – strain response of Au micropillars of diameter between 0.30 to 7.45 µm. Their results demonstrate that sub-micrometer diameter Au pillars were up to 50 times stronger than bulk Au. They proposed that these high strengths were the result of the operation of a dislocation nucleation controlled plastic deformation process. In this mechanism, once the sample is small enough, the mobile dislocations have a higher probability of travelling, unhindered, across the small distance through the sample to the free surface rather than being pinned by other dislocations within the sample. This mechanism is in contrast to that which commonly occurs in large volume samples where there is a surplus of pre-existing dislocations, or sites within the sample where dislocations can be nucleated at a very low applied stress, and the yield stress of the sample is determined

primarily by the stress required to move these dislocations through the sample (i.e. plasticity is governed by a dislocation-obstacle interaction process). This theory is supported by the observation, reported by Greer and Nix, that stress-strain curves displayed by the Au nanopillars were composed of elastic loading segments separated by discrete displacement bursts (Figure 2.1).
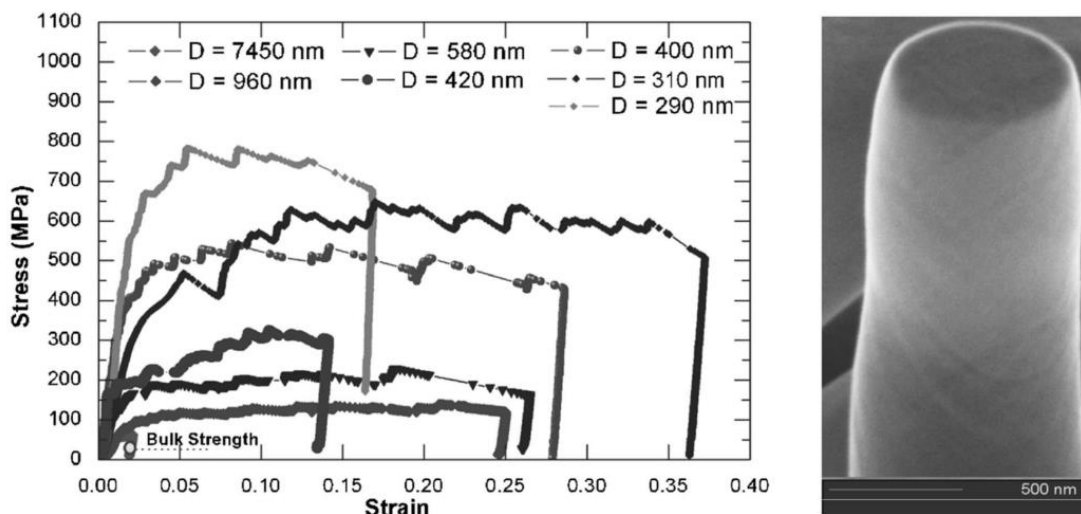
Figure 2.1: (a) Stress-strain behavior of Au micropillars shows that the flow stresses increase significantly as the pillar diameter is decreased and (b) SEM image of a compressed Au pillar after plastic deformation [5].

Volkert et al. [6] performed uniaxial compression tests on single crystal Au pillars ranging in diameter from 0.2 to 8.0 μm and found the compressive yield stress scales roughly as the inverse square root of the pillar diameter (Figure 2.2a). Images of their compressed pillars indicated that deformation occurred by localized shear on the close-packed slip systems that were subjected to the largest resolved shear stress. After an elastic loading regime, the pillars exhibit yielding associated with large discrete strain bursts (Figure 2.2b). Both of these features are attributed to the operation of a dislocation nucleation-limited mechanism in these small micropillars. They tested pillars of different crystal orientation and no obvious differences between the yield stresses and strain hardening rates were observed, suggesting that the stress-strain behavior does not depend strongly on whether single or multiple slip occurs.
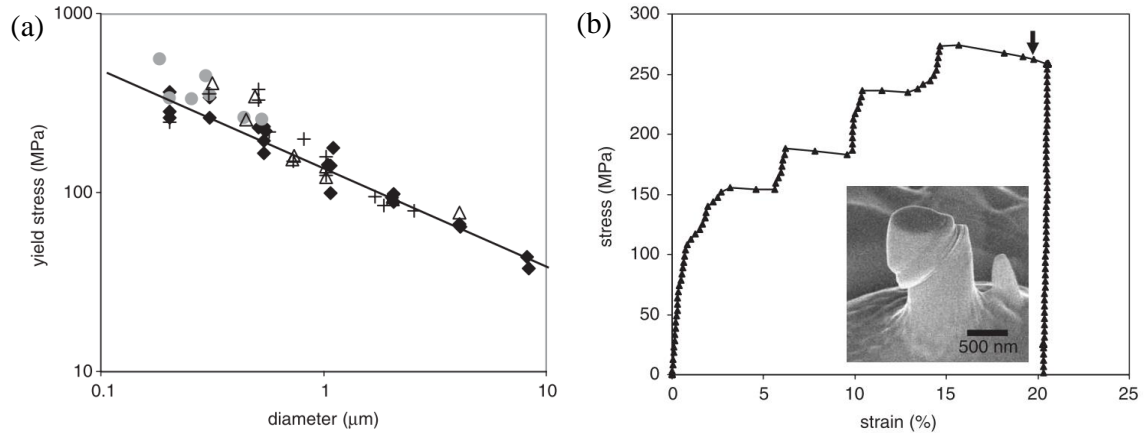
Figure 2.2: (a) Yield stress at 5% plastic strain of different diameter Au micropillars showing strong size dependence, and (b) Engineering stress–strain curve for a 710 nm diameter pillar, displaying discrete strain jumps in the loading curve and the arrow indicates the point at which the 15 second hold begins. In the inset the image shows the pillar deformed by single slip [6].

Frick et al. [7] investigated uniaxial compression behavior of FIB manufactured [111] nickel (Ni) micropillars, ranging from 0.2 to 25.0 µm diameter. The [111] Ni pillars showed a strong increase in yield stress and strain hardening rate with decreasing diameter (Figure 2.3). The strain hardening rate was found to be a function of both pillar diameter and crystal orientation. The observed strain hardening mechanism was believed to be a combination of dislocation–obstacle interaction and dislocation-nucleation limited deformation mechanisms.
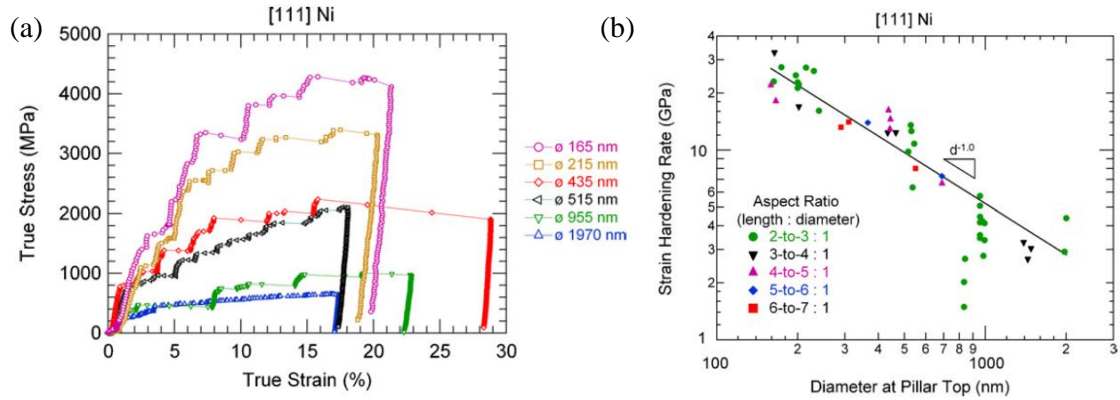
Figure 2.3: (a) Representative compressive true stress–strain behavior for [1 1 1] Ni pillars of various diameters ranging from 2.0 µm to below 200 nm. (b) Logarithmic plot of the slope between the stress at 3% and 10% strain for all [1 1 1] Ni pillars tested to estimate the strain hardening rate [7].

Dimiduk et al. [8] made a direct assessment of the crystal-size dependence of the critical resolved shear stress of single-slip oriented Ni micropillars of diameter ranging from 1 to 40 µm. Their results showed strength increases of up to 15 times over pure Ni and size-affected hardening rates (Figure 2.4). They concluded that, at the micron-size scale, both external geometry and internal structure affects the operative mechanism of plastic deformation.
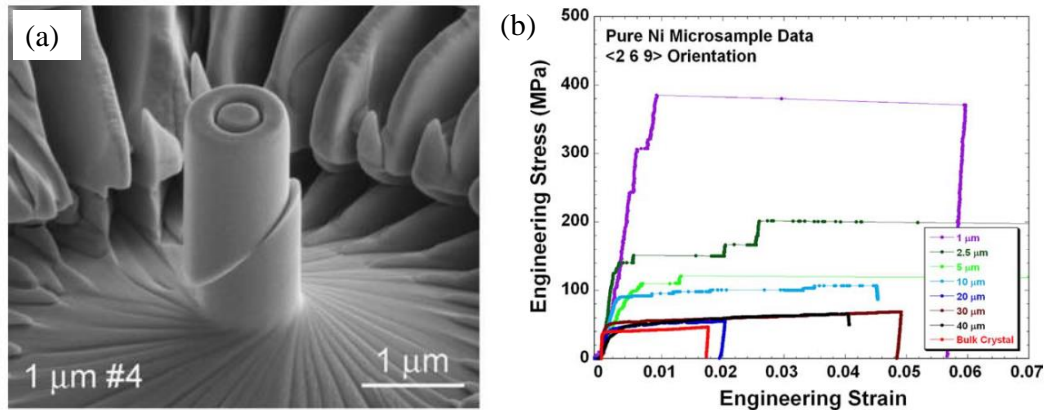
Figure 2.4: SEM images of microcrystals: (a) 1 µm diameter sample after test showing intense localized shear. (b) Engineering stress-strain curves for different diameter Ni pillars [8].

Greer [1] explained the experimental and numerical-simulation results of Au nanopillars. For larger diameter pillars (greater than 100 µm diameter), the shape of the strain-stress curve generated by the numerical dislocation starvation model is consistent with conventional strain-hardening behavior for large *FCC* samples: dislocation elastically interact with each other and form sessile dislocations, for example, Lomer-Cottrell locks, which act as obstacles to the motion of other dislocations. As dislocations become pinned by these locks they form Frank-Read type dislocation sources which cause the total number of dislocations within the sample to increase. Thus, for larger diameter pillars, as shown in Figure 2.5, the dislocation density clearly increases with increasing plastic deformation.
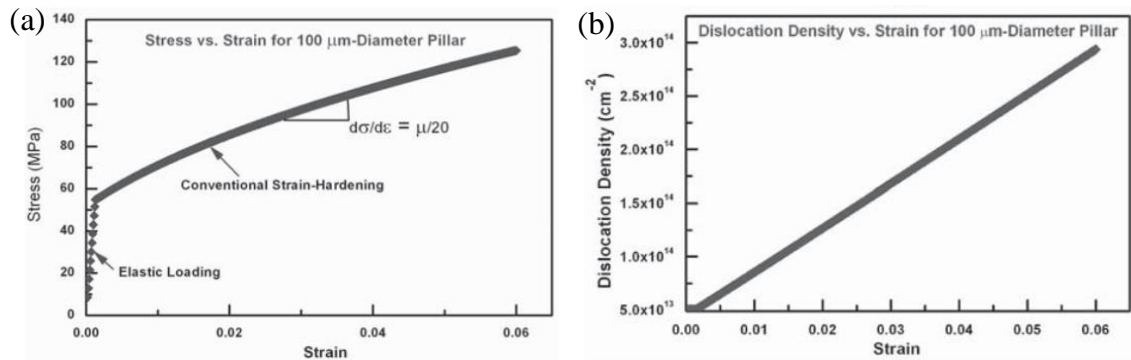
Figure 2.5: Predictions of (a) Stress vs. strain and (b) Dislocation density vs. strain, model for a larger pillar with a 100 µm diameter [1].

On the other hand, the stress and strain model prediction for a smaller, 0.5 µm, diameter pillar is shown in Figure 2.6. After elastic loading the mobile dislocations escape at the nearby free surfaces, thereby reducing the dislocation density, and the crystal becomes dislocation-starved. It is very clear from the comparison of the stress-strain graphs that by the time the pillars are deformed by 7%, the stress level supported by the smaller pillar is at least 3 times higher than that for the larger pillar. It is notable that this model focuses only on the dislocation starvation process and does not incorporate any other physical phenomena such as dislocation reactions with point defects, nucleation of new dislocations within the deforming sample, or time-dependent obstacle-limited dislocation glide processes.
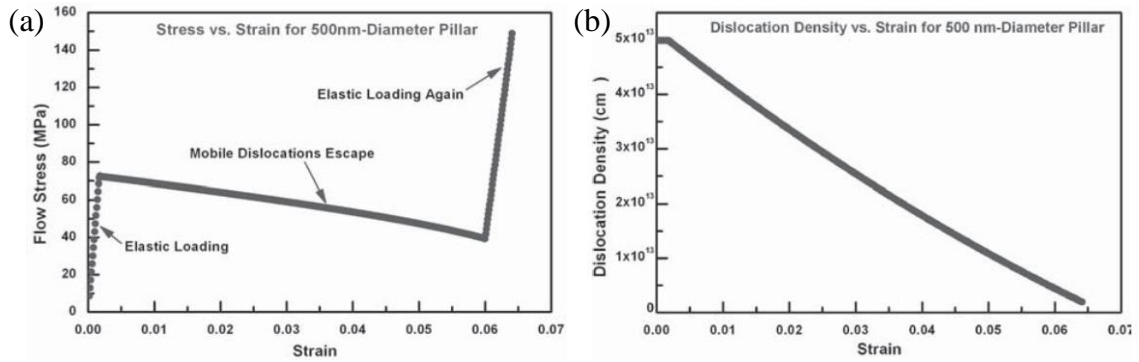
Figure 2.6: Predictions of (a) Stress vs. strain and (b) Dislocation density vs. strain, model for a smaller pillar with a 0.5 µm diameter [1].
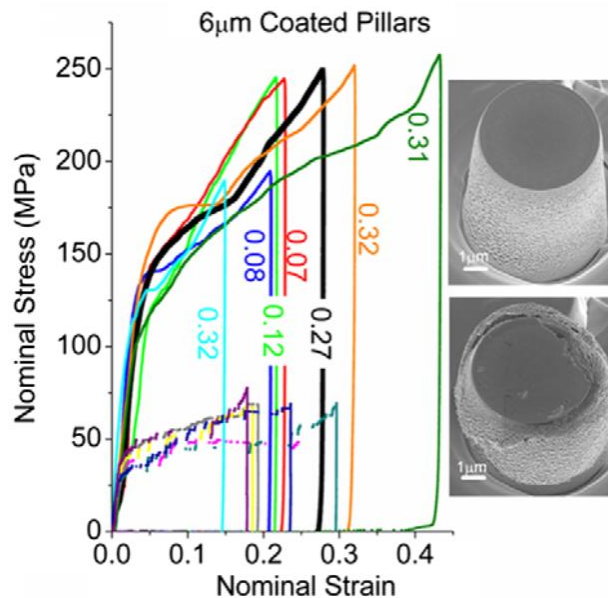
Figure 2.7: Nominal stress–strain response of uncoated (curves without numeric labeling) and tungsten coated Al micropillars displaying much more pronounced and smooth strain hardening compared with uncoated pillars [9].

The studies described above provide strong experimental evidence for the hypothesis that the length-scale dependence of the mechanical strength of ductile metals results from the transition in operative deformation mechanisms from one that is governed by obstacle limited dislocation glide, when specimen dimensions are greater than several micrometers, to one governed by dislocation nucleation from the free surface when the

sample size is less than several micrometers. If this is the case, it is of interest to observe the effect of surface barriers on this length-scale dependence. Ng and Ngan [9] studied the effects of trapping the mobile dislocations by compressing coated and uncoated Al micropillars of diameters ranging from 1.2 to 6.0 µm. As shown in Figure 2.7, the coated samples showed a considerably higher strain-hardening rate and much smoother stress–strain response, suggesting the suppression of dislocation avalanches and a lack of nucleation-controlled plasticity. Post-test TEM examination revealed much higher dislocation density in the coated pillars at the height level of the pillar where the coating had cracked in the final stages of the compression test. Likewise a significant rise in dislocation density and formation of dislocation cells was observed, confirming the trapping of the dislocations inside the deforming micropillars instead of annihilating at the free surface, as was the case in the uncoated micropillars.

One of the major concerns with the use of uniaxial compression tests performed on FIB milled micropillars is that the FIB fabrication technique, which involves metal removal by Ga+ ion beam sputtering, has the possibility of imparting considerable amounts of crystal damage to the fabricated micropillar and these crystal defects could be responsible for the observed increase in flow stress of small-diameter pillars. Several approaches were used to address this issue. Greer et al. [4,5] prepared Au micropillars by four different techniques: FIB milling, FIB milling followed by annealing, FIB milling followed by low-energy Ar+ milling, and samples prepared without FIB milling using a lithography/electroplating followed by annealing process. The amount of Ga+ ion implantation damage was different for the four processing methods. The flow-stress obtained from the experiments for the three different FIB based fabrication methods showed similar trends, however the electrodeposited pillars yielded not only at higher flow stress than bulk but also exhibited a similar rise in strength as the diameter is reduced. Additionally to their experimental results on Ga+ implantation, several literature sources report that the implantation depths for 30KeV Ga+ beam are no more than 60 nm. The surface damage from 30KeV Ga+ beam on FIB-prepared TEM specimens of Pt, W, and Au penetrated not more than 20 − 25 nm into the surface of Au when the Ga+ beam was directed normal to the Au surface [10,11].

2.1.1 Microspherical Particles, Nanodots, Nanoposts, and Nanorods

The previous section describes the extensive research conducted with the use of FIB-milled micropillars loaded in uniaxial compression. While this geometry is still the most commonly used method to study length-scale dependence of plastic deformation it is associated with several difficulties such as the presence of crystal defects resulting from the FIB fabrication process (as described previously) and practical dimensional limitations, such as the fabrication of high degrees of surface flatness and parallelism in sub-micrometer nanopillars, that result from this fabrication process. To overcome these difficulties other test geometries have been developed. Of these, micro-spherical test geometries are particularly attractive since they are relatively easy to construct without the use of FIB milling. Data obtained from studies that use these geometries are presented here.

D Mordehai et al. [12] successfully produced *FCC* single-crystal Au microparticles on a sapphire substrate via a solid-state diffusion dewetting technique (Figure 2.8). They found all microparticles have a {111} facet on the top surface. The size of these microparticles was in the range from 0.2 to 1.0 µm (top diameter).

Although the authors expected the microparticles would be dislocation-fee, since they were formed by long-time annealing just below the melting temperature, TEM observation indicated that a small number of dislocations were present. All visible dislocations were of edge character not residing on close packed {111} planes. Thus, they concluded that the observed dislocations would be sessile during compression tests. In summary, the Au microparticles were free of mobile dislocations prior to compression testing.
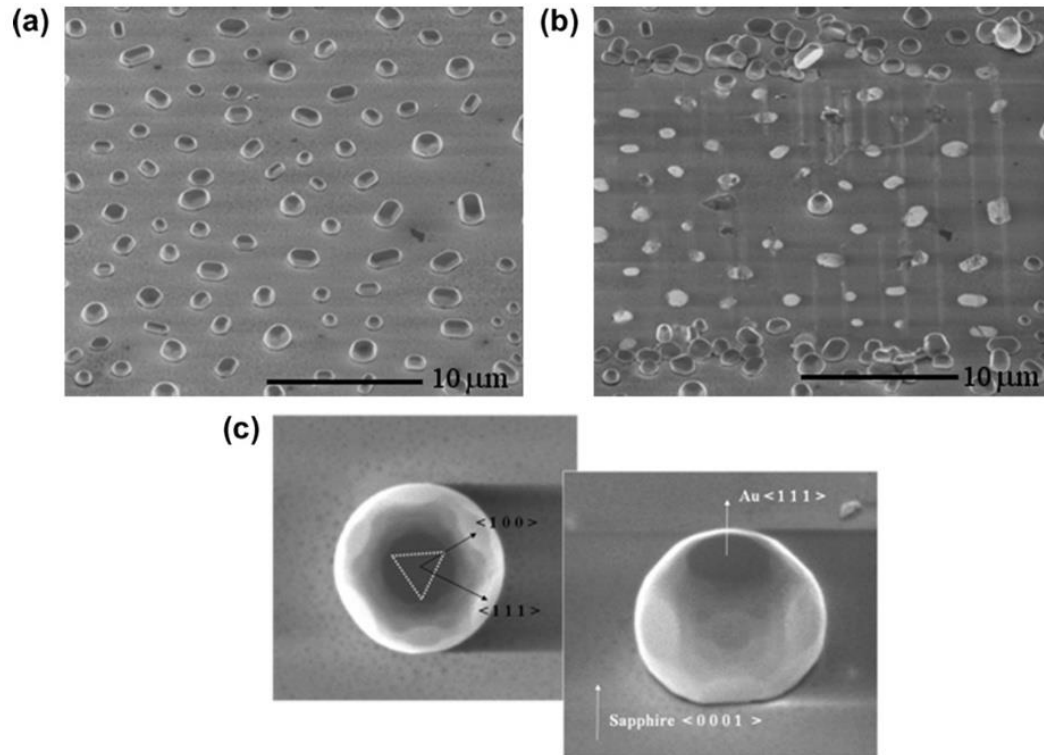
Figure 2.8: The distribution of Au microparticles on a (0001) oriented sapphire substrate. The SEM images before (a) and after (b) the mechanical cleaning. (c) A view from the [111] direction and a 52° tilted view of a single Au microparticle [12].

Several typical experimental load–displacement curves for the Au microparticles of various sizes are shown in Figure 2.9a. Initially, all microparticles exhibit (nearly) continuous load–displacement behavior in what was taken to be elastic deformation. The elastic loading was followed by very large strain bursts such that, in the smaller microparticles, the loading punch came to rest very close to the sapphire substrate. In the large microparticles, the strain burst stopped with the loading punch still well above the substrate. For most of microparticles tested there was a strong dependence of the yield strength on the microparticle size (Figure 2.9b).
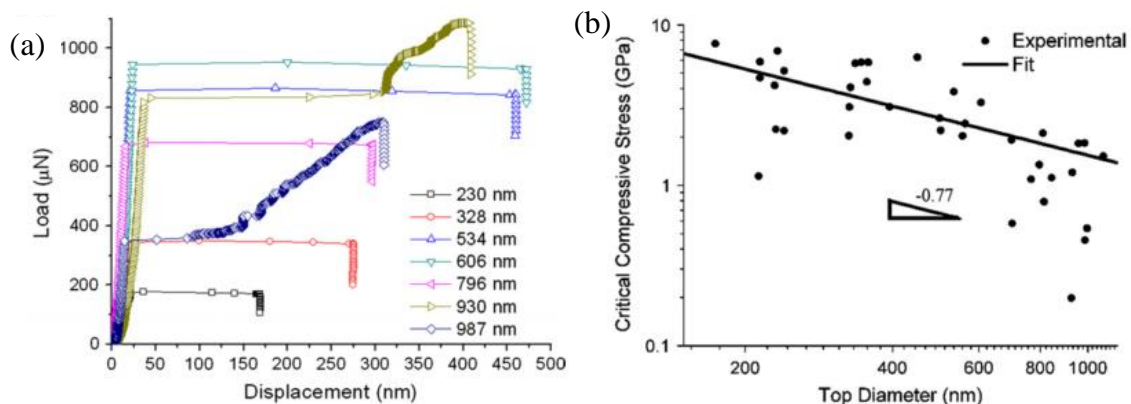
Figure 2.9: (a) Typical load–displacement curves of several representative microparticles and (b) The dependence of the compressive stress on the top facet of the microparticles [12].
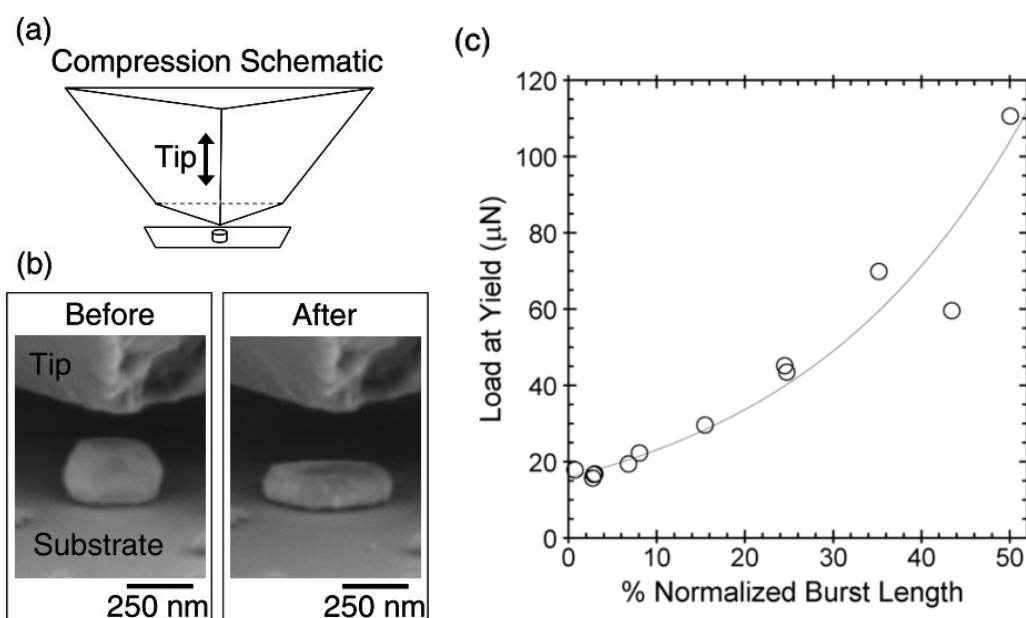
Figure 2.10: (a) Compression schematic of a single crystal Au nanodots with a flat punch nanoindenter. (b) SEM images before and after the compression of a nanodot, the burst associated with this compression at the yield point was equivalent to 50% of the initial height of the structure. (c) Load at yield as a function of the burst length normalized by the initial height of each structure [13].

Mook et al. [13] compressed single crystal nanodots inside a high resolution scanning electron microscope (SEM) using a nanoindenter equipped with a flat punch tip. The nanodots were loaded elastically and then yielded in a stochastic manner at loads ranging from 16 to 110 µN (Figure 2.10). Yielding was instantly followed by displacement bursts. SEM movies and still-images taken during the largest displacement bursts indicated that elastic strain energy within the sample was released by the formation of new surface area in the form of localized slip bands. The apparent energy release rate at yielding was calculated between 10 and 100 Jm^{-2} for burst sizes between 5 and 50% of the structure's initial height.

Maharaj and Bhushan [14] performed load – unload compression tests on spherical Au nanoparticles and Au nanorods (Figure 2.11a-b), using a flat punch nanoindenter and reported findings that were quite in contradiction to the generally held notion that the dislocation nucleation, and not the dislocation-obstacle interaction, mechanism controls plasticity in nano-sized metal samples. Figure 2.11c-d shows load–displacement curves obtained from their tests. The resulting displacement at each new load was either the same or lower than the previous loading. The authors claimed that this was due to increased resistance to deformation as a result of a greater density of dislocations restricting the creation and movement of dislocations (i.e. the operation of dislocation-obstacle limited dislocation glide). Several pop-in events were observed during repeat compression tests at increasing loads indicating multiple slip events to occur during loading.
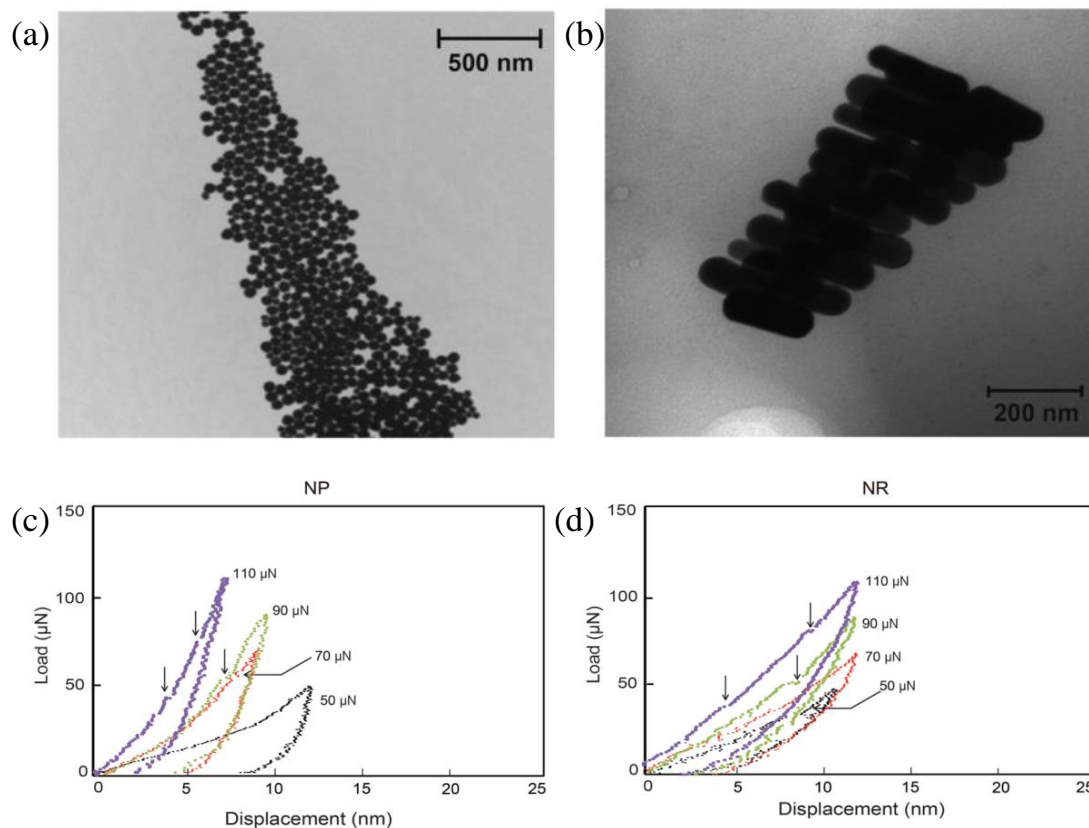
Figure 2.11: TEM images of (a) spherical Au nanoparticles ~50 nm in diameter, (b) Au nanorods 50 nm in diameter and 200 nm in length, (c) and (d) Repeat load–displacement curves for Au nanoparticles and nanorods with the corresponding maximum loads for each compression event. Vertical arrows point to pop-in events [14].

Based on compression experiments and molecular dynamics simulations, Chrobak et al. [15] showed that the mechanical properties of bulk silicon and silicon nanoparticles are significantly different. They found that bulk silicon exists in a state of relative constraint, with its plasticity dominated by phase transformations, whereas silicon nanoparticles are less constrained and display dislocation-driven plasticity. In their experimental studies, compression tests were performed on silicon nanoparticles of radius ranging from 19 to 169 nm using an indentation system with a blunt diamond tip located in a transmission electron microscope (TEM). Their MD simulations of the deformation of silicon nanoparticles (Figure 2.12a), found that the maximum contact pressure attained in the nanoparticles (21.3–23.5 GPa) is nearly twice that of bulk silicon (~12 GPa).

Furthermore, the sudden pressure drop revealed in their simulations (Figure 2.12b), is equivalent to the pop-in observed during the nano-compression experiments and is attributable to the nucleation of mobile dislocations in the otherwise defect-free silicon particle.
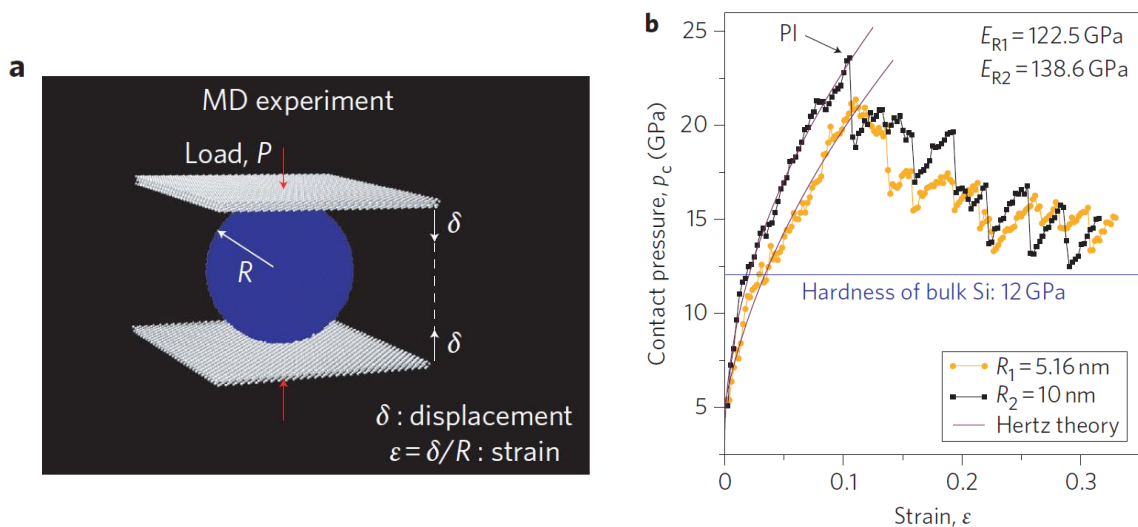
Figure 2.12: Mechanical response of a compressed silicon nanoparticle. (a) MD simulations of silicon nanospheres compressed between two rigid plates. (b) Contact pressure as a function of strain showing that the maximum contact pressure in the nanoparticles is almost twice the hardness of the bulk material [15].

Salehinia et al. [16] used both atomistic simulations and experimental nanoindentation tests to examine the effect of vacancies on the onset of plasticity in a Ni single crystal under contact loading. Molecular dynamics had shown the effect of vacancy position on the yield load, a single vacancy can lower the yield load even when positioned at depths of approximately one-third of the indenter contact radius. In cases where the vacancy position is close to regions of high shear stresses the nucleation of dislocations is related to the location of a vacancy. Complementary experiments have been used to demonstrate the effect of indenter size on the onset of yielding in the presence of vacancies. Both the simulations and experiments show that larger indenter tips increase the chance of weakening the material in the presence of vacancies.

Liu et al. [17] carried out molecular dynamics analyses of defect free Al single crystals subject to bending to investigate dislocation nucleation from free surfaces. Their calculation showed that the slip systems with the largest resolved shear stress were not activated and the values of shear stress at which dislocation nucleation occurs are almost one order in magnitude smaller than those for nucleation in the bulk material. This is consistent with weaker bonding at a free surface than in the interior. It was obtained that dislocation nucleation is not well-represented by a critical value of the resolved shear stress but is reasonably well-represented by the critical stress-gradient criterion.
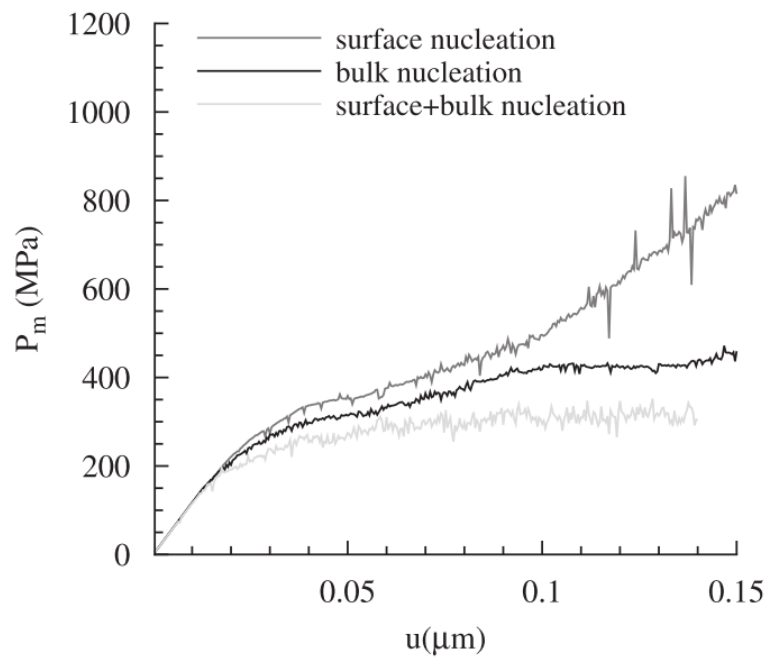
Figure 2.13: Mean contact pressure, P_m, versus indentation depth, u, for crystals containing surface and/or bulk dislocation sources during frictionless contact [18].

Nicola et al. [18] analyzed the indentation of ductile single crystals by a periodic array of flat rigid contacts using a continuum mechanics based "discrete dislocation" plasticity model. They mainly focused on contrasting the response of crystals having dislocation sources on the surface with that of crystals having dislocation sources in the bulk. When there are only bulk sources, the mean contact pressure for sufficiently large contacts is independent of the friction condition, whereas for sufficiently small contact sizes, there is a significant dependence on the friction condition. When there are only surface

dislocation sources the mean contact pressure increases much more rapidly with indentation depth than when bulk sources are present (Figure 2.13) and the mean contact pressure is very sensitive to the strength of the obstacles to dislocation glide. Also, on unloading a layer of tensile residual stress develops when surface dislocation sources dominate. When both surface and bulk dislocation sources are available, the response is generally dominated by the bulk sources.

Therefore, the incipient plasticity (pop-in) phenomenon observed whenever small volume ductile metal samples are tested in compression offers a unique opportunity to quantitatively study dislocation nucleation; a stress-assisted, thermally activated process. Nucleation of dislocation can be homogenous (in defect free volumes) or heterogeneous (i.e. assisted by the presence of defects such as surfaces, inclusions or precipitates, vacancies or grain boundaries). In addition pop-ins can also occur at stresses much below theoretical stress when sufficiently large volumes are probed, presumably, due to the activation of pre-existing dislocations [19].

However of the many studies in literature addressing the issue of the dependence of metal crystals flow stress on the sample size (i.e. length-scale) at room temperature, there are far fewer studies of the rate-dependence of the flow stress and the kinetics of plastic deformation over a similar length-scale.

2.2 Rate-dependent Plastic Deformation

It is well established that plastic deformation of crystalline metals is a kinetic phenomenon where the dislocation motion due to an applied stress is assisted by the intrinsic vibrational "thermal" energy of the atoms [20]. The extent to which the thermal energy of the atoms contributes to the deformation process depends upon the magnitude of the applied stress and the temperature. By studying the dependence of a material's flow stress upon strain rate and temperature allows one to gain important information about the microstructural mechanism by which plastic deformation is occurring.

During plastic deformation of large crystalline metal samples the flow stress is controlled by interactions between gliding dislocations and obstacles present in the material. These interactions can be categorized as either long-range or short range. The long-range interactions are insensitive to the position of a gliding dislocation and are associated with large obstacles such as second-phase precipitates and large arrays of dislocations resulting from work-hardening. It is difficult to activate dislocations past these obstacles, and the component of the flow stress arising from these interactions is essentially insensitive to the strain rate and temperature. These types of obstacles are known as "Athermal" obstacles. Short-range obstacles such as individual dislocations, or dislocation jogs, cause interactions forces on the gliding dislocations that act over only a few atomic distances. These forces can be overcome at finite temperatures with the help of thermal fluctuations of adjoining atoms to the dislocation/obstacle interface. Hence, the stress required to move the dislocation past this type of obstacles is temperature and strain rate dependent. These types of obstacles are known as "Thermal" obstacles.

The plastic shear strain rate $\dot{\gamma}$ in a crystalline solid is expressed in terms of the mobile dislocation density ρ_m, the Burgers vector b of the dislocations, and the average dislocation velocity $\bar{v}$ as

$$\dot{\gamma} = \rho_m b \bar{v} \tag{2.1}$$

If we consider the deforming material as consisting of a crystalline matrix containing a distribution of weak obstacles, $\dot{\gamma}$ becomes limited by the energy required for a dislocation to move past the obstacles.

Figure 2.14 illustrates an idealized force-distance relationship for a dislocation to overcome and move past a discrete obstacle. The total area under this force-distance curve represents the characteristic Gibbs free energy ΔG_0 of the obstacle. For a dislocation to successfully move past this obstacle, part of ΔG_0 will be supplied by the applied mechanical work, $\tau_{app} V^*$, where V^* is the apparent activation volume, and the remainder, which is denoted as $\Delta G(\tau)$, is supplied by thermal vibrations of the atoms at the dislocation/obstacle interface.
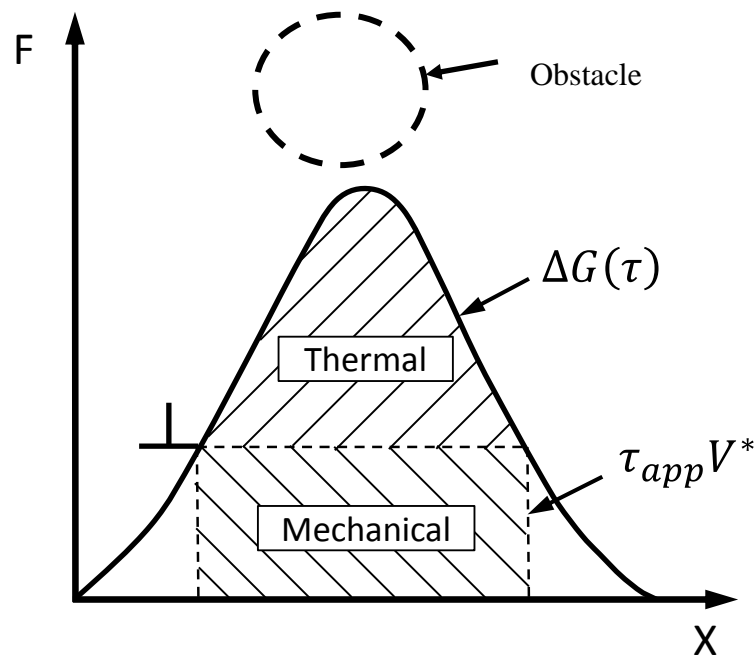
Figure 2.14: Idealized resistance force (F) versus distance (x) profile for obstacles opposing the dislocation motion in a crystalline material containing an obstacle.

The probability that the thermal vibration of the atoms will contribute a kinetic atomic energy of at least $\Delta G(\tau)$ at a particular temperature T is given by the Boltzmann factor, $exp(-\Delta G(\tau)/kT)$, where k is the Boltzmann constant. The velocity of the mobile dislocations is then given in terms of the probability of atoms, which make up the dislocation in the area of the obstacle, having the thermal energy $\Delta G(\tau)$ as

$$\bar{v} = \beta b v_0 exp\left(\frac{-\Delta G(\tau)}{kT}\right) \tag{2.2}$$

In this equation β is a dimensionless constant, and v_0 is a characteristic atomic vibration frequency (usually taken as the Debye frequency). Substituting this expression into Eq. (2.1) gives an expression for shear strain rate $\dot{\gamma}$ in terms of the thermal activation energy $\Delta G(\tau)$. The term ΔG_0 expressed as

$$\Delta G_0 = \tau V + \Delta G(\tau) \tag{2.3}$$

The term ΔG_0 characterizes the strength of the particular obstacle resisting dislocation glide. Table 2.1 lists, approximate values of ΔG_0, proposed by Frost and Ashby, for different classes of obstacles.

Table 2.1: Classification of obstacles according to their strength in terms of ΔG₀ [21]

Obstacle	ΔG_0	Example
Strong	$2\ \mu b^3$	Large or strong precipitates
Medium	$0.2 - 1.0\ \mu b^3$	Forest dislocations, small or weak precipitates
Weak	$< 0.2\ \mu b^3$	Lattice resistance, solid solution hardening

The highest stress a perfect crystal can sustain without undergoing immediate structural transformation at temperature 0 K, referred to as the ideal strength, is approximately $E/10$ where E is the elastic modulus of the material. The measured strength of bulk crystals is typically far below the ideal strength because of the large number of grown-in defects, such as dislocations, that are present. The yield strength of these bulk crystals is limited by the resistance to dislocation motion; therefore, the typical flow stress is about a factor of 100 below the ideal strength.

The equations presented above suggest that increasing the temperature will increase the probability that atoms locate at a dislocation/obstacle interface will have kinetic energy greater than $\Delta G(\tau)$ and hence the flow stress will decrease with increasing temperature.

This is of course exactly what is usually observed in metals. Since this thermally-assisted mode of dislocation motion requires a waiting period while the dislocation remains pinned by the obstacle until the atoms at the dislocation/obstacle interface attain $\Delta G(\tau)$, the strength of a material is also inherently dependent upon the loading-, or the strain-, rate. We use the parameter referred to as the "activation volume, V" to characterize the rate dependence of the operative dislocation-obstacle limited deformation mechanism. This is done by rearranging terms in Equation (2.3) as [22]

$$V(\tau, \text{T})=-\left.\frac{\partial\left(Q_0 - Q(\tau)\right)}{\partial\tau}\right|_T \tag{2.4}$$

Deformation operation by different dislocation-obstacle interactions display different activation volumes, such as, $V = 0.1b^3$ for creep deformation by lattice diffusion and $V = 1000b^3$ for deformation by dislocation glide past obstacles via an Orowan bowing type mechanism [22].

The activation volume V can be determined by both experimentation and by atomistic modeling. It thus provides a unique link in coupling two approaches for revealing the rate-controlling deformation mechanisms. In experiments, the activation volume can be determined by measuring the strain rate sensitivity of the flow stress of a material. During a uniaxial tension experiment, the empirical power-law relation between flow stress σ and strain rate $\dot{\varepsilon}$ which most bulk ductile metal samples display is

$$\frac{\sigma}{\sigma_0} = \left(\frac{\dot{\varepsilon}}{\dot{\varepsilon}_0}\right)^m \tag{2.5}$$

where σ_0 and, $\dot{\varepsilon}_0$ are the stress and corresponding strain rates at a known reference condition, m is the non-dimensional rate sensitivity index and is typically between 0 and 1; $m = 0$ gives the rate-independent limit and $m = 1$ corresponds to the linear Newtonian flow. The "apparent" activation volume V^* is conventionally defined as

$$V^* = \sqrt{3}kT\frac{\partial ln\dot{\varepsilon}}{\partial\sigma} \tag{2.6}$$

The strain rate sensitivity, m can be related to the activation volume, V^* by combining the Eqs. 2.5 and 2.6 as

$$m = \sqrt{3}\frac{kT}{\sigma V^*}$$ (2.7)

In these equations the factor $\sqrt{3}$ arises because the von Mises yield criterion is invoked to convert the normal stress σ to an effective shear stress τ^*, i.e., $\tau = \sigma^*/\sqrt{3}$. Since τ^* is related to the resolved shear stress on a single slip plane τ by $\tau^* = M/\sqrt{3}\tau$, where M = 3.1 is the typical Taylor factor for an *FCC* metal deforming by dislocation glide along the {111}<110> crystal system [23], it follows that the true activation volume V associated with a unit process and the apparent activation volume V^* measured from a polycrystalline sample are related by

$$V^* = \frac{\sqrt{3}}{M}V$$ (2.8)

In Chapter 5, 6 and 7 of this thesis, the activation volume during incipient plasticity of Au microspheres was estimated using a physics based model describe by several researchers [24–26]. The following is a detailed description of this model.

The average strain rate, $\dot{\varepsilon}$, of the microspheres can be described in terms of the motion of a population of ρ_m dislocations as

$$\dot{\varepsilon} = \rho_m b\bar{v}$$ (2.9)

In the absence of any applied shear stress

$$\bar{v} = v_0 b.\,exp\left(-\frac{Q}{kT}\right) - v_0 b.\,exp\left(-\frac{Q}{kT}\right)$$ (2.10)

In the right side of this equation, the first term represents for the forward jumps and the second term represents the backward jumps. i.e. both the forward and backward jumps are equal. Now when the shear stress (τ) is applied,

The $\bar{v}$ can be determined by a standard approach for a stress activation process:

$$\bar{v} = v_0 b\left[exp\left(-\frac{(\tau_p - \tau)V}{kT}\right) - exp\left(-\frac{(\tau_p + \tau)V}{kT}\right)\right]$$ (2.11)

where v_0 is the attempt frequency and τ_p is the lattice resistance or the Peierls stress, which is the stress needed to make the dislocations move in the absence of any thermal energy. τ is the applied shear stress, V is the activation volume, T is the absolute temperature, and k is the Boltzmann's constant.

$$\bar{v} = v_0 b \left[exp\left(\frac{\tau V}{kT}\right) - exp\left(-\frac{\tau V}{kT}\right) \right] . exp\left(-\frac{\tau_p V}{kT}\right) \tag{2.12}$$

Since, $\sinh(x) = \frac{e^x - e^{-x}}{2}$, the above equation can be written as,

$$\bar{v} = v_0 b . 2 \sinh\left(\frac{\tau V}{kT}\right) . exp\left(-\frac{\tau_p V}{kT}\right) \tag{2.13}$$

Putting this, $\bar{v}$ into Eq. 2.9 obtain,

$$\frac{d\varepsilon}{dt} = 2\rho_m b^2 v_0 . \sinh\left(\frac{\tau V}{kT}\right) . exp\left(-\frac{\tau_p V}{kT}\right) \tag{2.14}$$

$$\sinh\left(\frac{\tau V}{kT}\right) = \frac{\frac{d\varepsilon}{dt}}{2\rho_m b^2 v_0} . exp\left(\frac{\tau_p V}{kT}\right) \tag{2.15}$$

Combining these equations and solving for the applied shear stress yields the following relationship:

$$\tau = \frac{kT}{V} sinh^{-1} \left[\frac{\frac{d\varepsilon}{dt}}{2\rho_m v_0 b^2} exp\left(\frac{\tau_p V}{kT}\right) \right] \tag{2.16}$$

In another case, when shear stress, τ is applied and the applied mechanical work (τV) is large,

$$\bar{v} = v_0 b \left[exp\left(-\frac{(\tau_p - \tau)V}{kT}\right) - exp\left(-\frac{(\tau_p + \tau)V}{kT}\right) \right] \tag{2.17}$$

For large mechanical work (τV), the probability to backward jumps is negligible, therefore,

$$v_0 b . exp\left(-\frac{(\tau_p + \tau)V}{kT}\right) \approx 0 \tag{2.18}$$

The Eq. 2.17 becomes,

$$\bar{v} = v_0 b \cdot exp\left(-\frac{(\tau_p - \tau)V}{kT}\right)$$

(2.19)

Substituting the value of $\bar{v}$ into Eq. 2.9

$$\frac{d\varepsilon}{dt} = \rho_m b^2 v_0 \cdot exp\left(-\frac{(\tau_p - \tau)V}{kT}\right)$$

(2.20)

Rearranging the above equation, we can get the following simplified expression:

$$\tau = \tau_p + \frac{kT}{V}\ln\left[\frac{d\varepsilon}{dt}\right] - \frac{kT}{V}\ln[\rho_m b^2 v_0]$$

(2.21)

This relationship forms the basis of typical analyses of compression tests at elevated temperatures [24–26], a plot of the shear flow stress against the natural logarithm of strain rate, at a particular temperature, should result in a linear relationship of slope kT/V. Therefore, V can be determined through the obtained slope. The total activation energy, Q, of deformation rate controlling obstacles can then be estimated as $Q = \tau_{0K}V$, where τ_{0K} is the athermal stress of Au [27].

2.2.1 Length-scale Effects on Rate-dependent Plasticity

The activation volume V and strain rate sensitivity m of the flow stress provide a direct link between experimentally measurable plastic flow characteristics and underlying operative deformation mechanisms. However, this link can be complicated by such important factors as mobile dislocation density and strain hardening. In the cases of nanopillars or nanospheres the density of mobile dislocations is negligibly small. Under these conditions, the ultra-strength deformation will be rate-limited by the rate at which dislocations are activated from the surface of the sample. In this case the experimentally measured apparent activation parameters are directly related to surface dislocation nucleation [22].

Schuh et al. [28] also measured the probability of occurrence of the first measurable strain jump during nanoindentation tests performed on Pt at temperature up to 200°C. The measured rate of strain jumps ($\dot{\eta}$), was expressed in terms of an Arrhenius function of the temperature T, applied stress σ, activation energy ΔG and activation volume V of the deformation process as,

$$\dot{\eta} = \dot{\eta}_0 . exp\left(\frac{\Delta G - \sigma V}{kT}\right)$$ (2.22)

The measured ΔG was considerably lower than would be expected for the energy to nucleate a dislocation from a perfect Pt crystal. This suggests that the intrinsic dislocation nucleation was occurring at crystal imperfections within the test sample. Similar conclusions regarding dislocation nucleation stress during nano-indentation have been reached by others [29, 30]. A detailed characterization of the effect of specific types of dislocation nucleation sources on the temperature- and stress-dependence of the rate of intrinsic dislocation nucleation during nano-indentation and micro-pillar compression has yet to be done.

Mook et al. [31] studied freestanding *FCC* nanoposts of aluminum and permalloy undergoing large strain uniaxial compression tests. The nanoposts were produced, without FIB milling, by e-beam lithography technique with radii ranging from 0.05 to 0.15 μm (Figure 2.15) and were nanocrystalline with a (111) texture and surface roughness below 1 nm. They observed a large amount of scatter in the flow stress obtained during compression of these nanoposts and the flow stress tended to increase with decreasing contact radius (Figure 2.15c). The apparent activation volumes V^* required for plastic deformation of these structures were found to be quite small when compared to the V^* for the deformation of bulk materials, and V^* dropped by an order of magnitude as the yield strength increased by a factor of three (Figure 2.15d). They concluded that this is consistent with near-surface dislocation nucleation as the controlling plasticity mechanism.
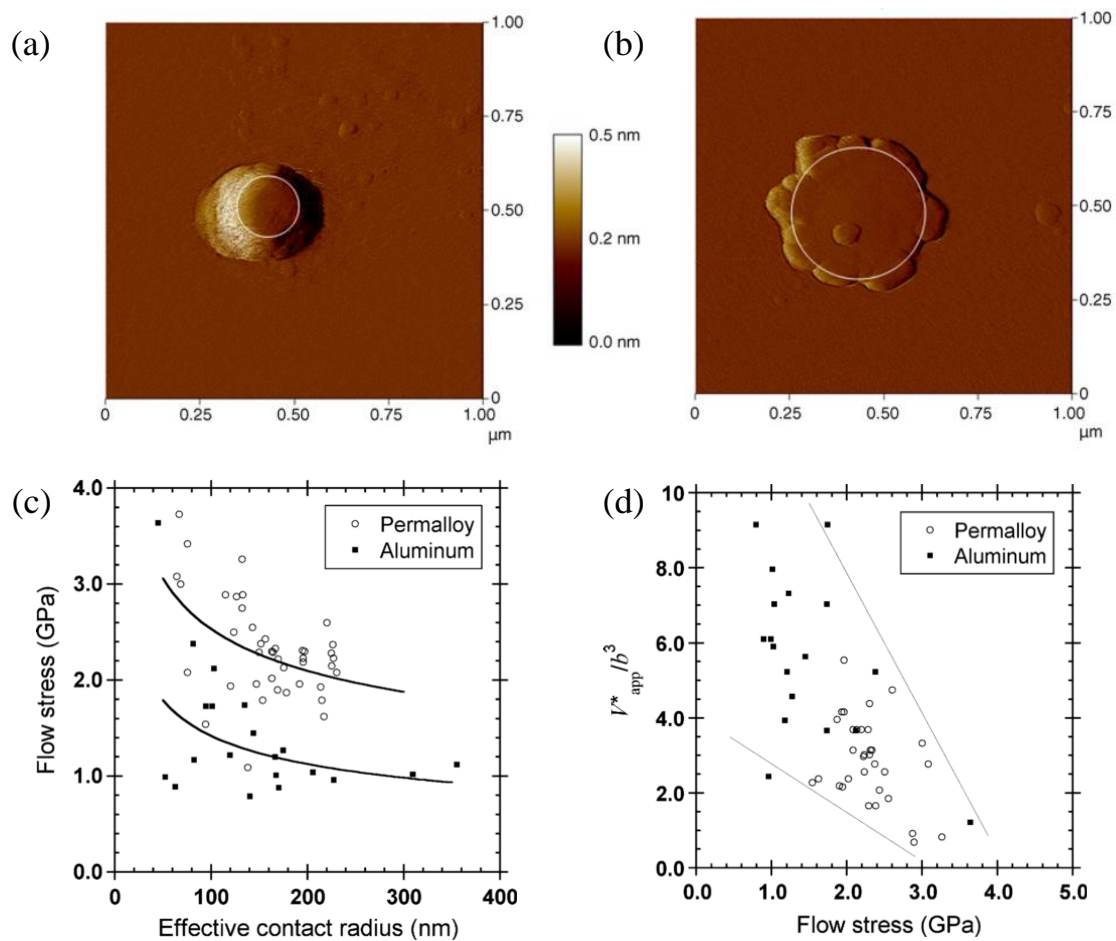
Figure 2.15: The AFM deflection image of an aluminum nanoposts (a) before compression (initial radius of 82 nm) and (b) after compression (final radius of 175 nm). (c) Flow stress as a function of the effective contact radius and (d) the apparent activation volume versus flow stress, for the aluminum and permalloy nanoposts [31].
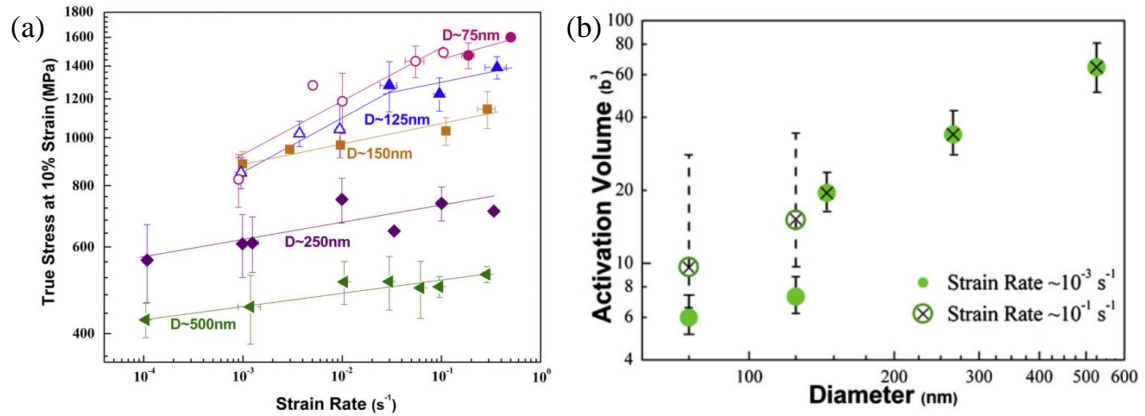
Figure 2.16: (a) Flow stress at 10% strain as a function of strain rate for Cu nanopillars (75 to 500 nm) [32]. (b) Activation volume versus diameter at two different strain rates denoting the change in activation volume for the smallest diameters [33].

Jennings [32,33] demonstrated a significant effect of both strain rate and sample size on the compressive strength of single-crystal Cu nanopillars with diameters ranging from 0.075 up to 0.500 µm. The flow stress, at 10% strain, as a function of strain rate for all diameters pillars is shown on Figure 2.16a. The slopes of the curves correspond to the strain rate sensitivity, *m* ranging between 0.027 and 0.057 displayed an increasing trend with decreasing pillar diameter. The apparent activation volume V^* estimated for the two smallest diameter pillars (0.075 and 0.125 µm) was about ~6 and ~$7.3b^3$, but was between 9.6 and $62b^3$ when the pillar diameter was above 0.150 µm (Figure 2.16b). They proposed a plasticity mechanism transition from dislocation multiplication via the operation of truncated dislocation sources, also referred to as single-arm sources, in pillars with diameters greater than 0.150 µm to dislocation nucleation from the surface in the smaller diameter samples.

Chen et al. [34] found the V^* is about $0.13b^3$ for tensile tests performed on "dislocation scarce" single-crystal Pd nanowhiskers. In these samples it was concluded that surface dislocation nucleation was the predominant mechanism controlling plastic yielding.

Schneider et al. [35] performed compression test on *BCC* [001] and [235] oriented Mo single crystal pillars ranging from 0.2 to 5.0 µm diameter. The smaller pillars showed a

strong dependence of flow stress upon loading rate and the calculated V^* was between 1.3 to 5.3b^3 from the smallest to the largest pillars.

Atomistic modeling of the uniaxial compression on Cu (111) nanowire was studied by Zhu et al. [36]. They created surface steps on the (111) surface and found the calculated V^*s are about 2b^3. The small magnitude of V^* was associated with surface dislocation nucleation. They also found that surface sources have a unique kinetic signature: a small activation volume leading to increase strain rate and temperature sensitivities of flow stress. They concluded that the activation volume associated with surface dislocation nucleation is characteristically in the range of $1 - 10b^3$.
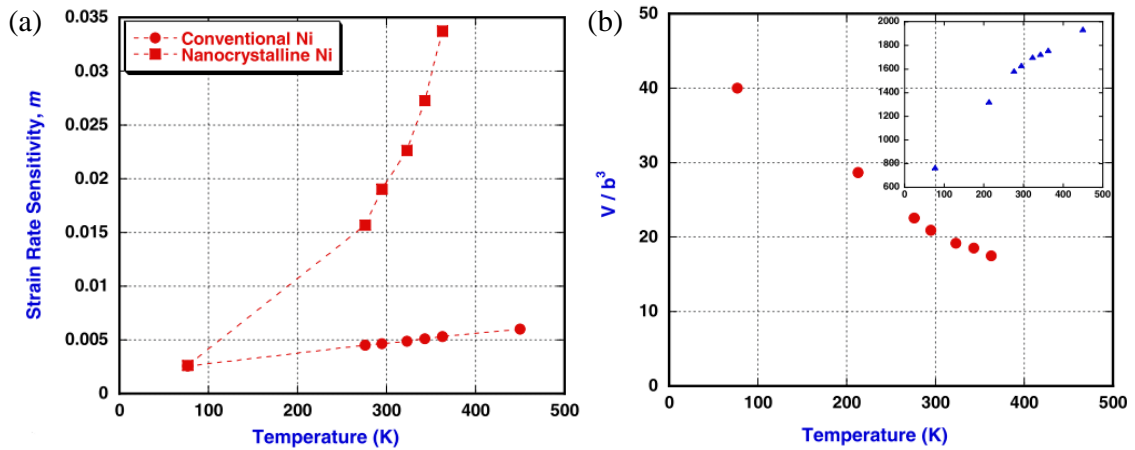
Figure 2.17: (a) Strain rate sensitivity, m at different temperature for conventional coarse-grained Ni (circles) and nanocrystalline Ni (squares). (b) Comparison of apparent activation volume at different temperature of nanocrystalline Ni (circles) and conventional coarse-grained Ni (triangles) shows inset in the same plot [37].

Wang et al. [37] carried out strain rate jump tests and stress relaxation tests over a range of deformation temperatures (77–373 K) on electrodeposited nanocrystalline Ni with an average grain size of ~30 nm. The values of the activation volume obtained at different temperatures are much smaller than those for the normal rate-controlling mechanism in bulk *FCC* metals. This suggests that the thermally activated process in nanocrystalline Ni is different from the conventional forest dislocation cutting mechanism. The strain rate sensitivity, m corresponding to the nanocrystalline Ni was found to be higher than coarse-

grained polycrystalline Ni (Figure 2.17a). A stronger temperature dependence consistent with the higher activation energy and smaller activation volume was observed. There appears to be an additional activated process in action, with a higher activation barrier. The apparent activation volume was found to be about $20b^3$ for nanocrystalline Ni at about room temperature (Figure 2.17b). This value is one to two orders of magnitude lower than the typical value governing normal dislocation-obstacle controlled plastic deformation of bulk Ni (see inset Figure 2.17b).

Afrin and Ngan [38] carried out compression creep tests at room temperature on micron-sized Ni_3Al pillars produced by FIB milling. The nominal creep rates of these micropillars were found to be very high, at $\sim 10^{-5}$ s^{-1}. Their observation, shown in Figure 2.18, suggest that the deformation at the pillar head is likely to be caused by surface diffusion. The absence of any sign of deformation within the main body of the pillar indicates that lattice diffusion did not happen, which is reasonable considering the low test temperature. The stress exponent of the creep deformation of these pillars was also close to unity, implying linear diffusional flow being the dominating creep mechanism. Microscopic evidence suggests deformation is due to surface diffusion at the pillar heads. Their estimated activation energy was $\sim 0.30 \pm 0.02$ eV for the low temperature diffusional creep mechanism.
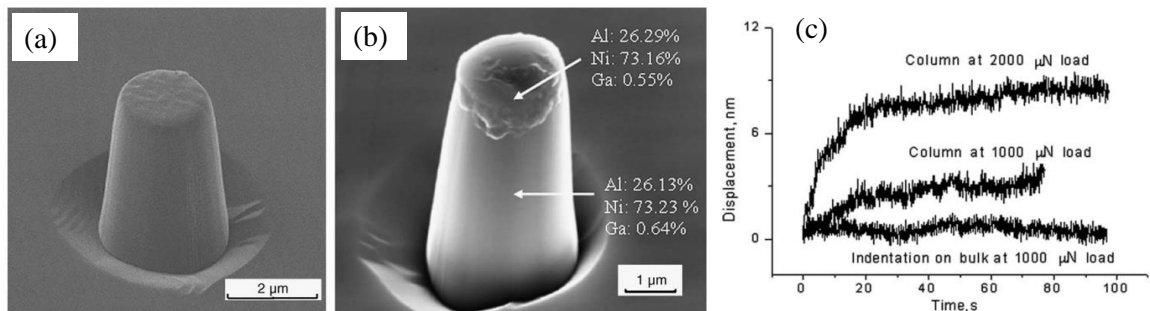
Figure 2.18: SEM images of Ni_3Al micropillar (a) before and (b) after creep testing at 2000 µN load. In Fig. b, EDX measurements of the deformed head of the pillar and the shafts revealed that the same chemical compositions, indicating that the material flowing down the pillar heads was indeed Ni_3Al. (c) Creep displacement during load hold of the micropillar and bulk-material [38].
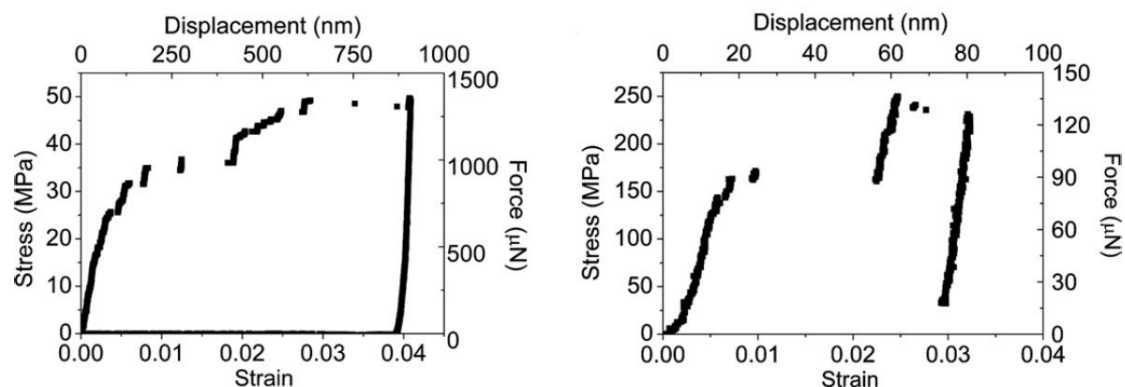
Figure 2.19: The stress-strain response of (a) 6.3 and (b) 0.8 µm, diameter Al pillars [39].

Ng and Ngan [39] studied the overall stress-strain response of micron-sized Al pillars, fabricated by FIB milling, which were subjected to uniaxial compression. They found that the deformation of Al micropillars is a jerky process with a stochastic nature (Figure 2.19). Their TEM investigation revealed that the dislocation density increased only very slightly even after severe plastic deformation. They reported that both the probability of occurrence and the size of the discrete displacement jumps observed during compression of these Al micropillars were exponentially related to the applied stress. When the micropillars were subjected to constant-load creep tests the frequency of the displacement jumps decreased with increasing creep time and a steady strain rate creep component also contributed to the measured creep strain. This suggests that multiple mechanisms of dislocation nucleation controlled and dislocation-obstacle interaction controlled dislocation glide may contribute to the intrinsic creep of sub-micron size metal samples.

Na and Ngan [40] also performed compression testing on FIB milled ~6 µm diameter bi-crystal Al pillars. They reported that introducing a grain boundary inside the micropillar resulted in very different mechanical behavior, specifically, the pillar shows much smoother and homogeneous deformation, in addition to a higher work hardening rate, compared to single-crystal pillars of similar size. These improved deformation characteristics were attributed to the increased storage of dislocations as a result of the presence of the grain boundary.

Choi et al. [41] performed room temperature uniaxial creep experiments on nanocrystalline Ni pillars of diameters ranging from 0.6 to 2.0 μm. At a given stress, much higher total creep strains and strain rates accrue in the smaller pillars (Figure 2.20), which is likely due to the increased contributions of free surfaces. The calculated apparent activation volume $V*$ increases in the range of $0.5 - 2.2b^3$ with decreasing stress and increasing pillar diameter. These measured values of stress exponent and the activation volume suggests that the nanoscale creep event under low stresses may be dominated by diffusion-controlled mechanisms.
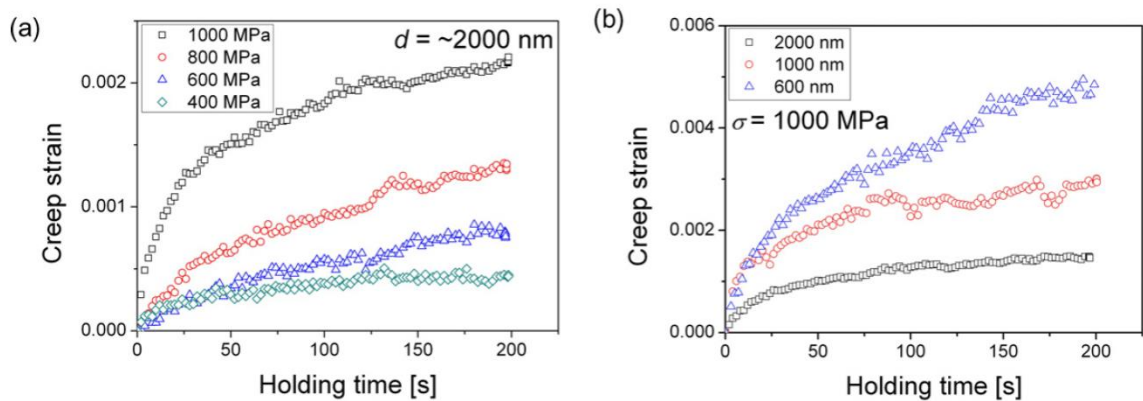
Figure 2.20: Creep strain vs. time curve: (a) effect of the applied stress; (b) effect of the pillar size [41].

Wang et al. [42] conducted both uniaxial creep and nanoindentation creep on nanocrystalline Ni and directly compared the two sets of data. Micropillars, with a nominal diameter of 2 μm, were fabricated by FIB milling and Ni films, with a grain size of 14 nm, were prepared by electrodeposition. The stress exponent under the two test conditions was found to be almost the same, indicating a similar creep mechanism. However, the strain rate measured by nanoindentation creep was about 100 times faster than that by uniaxial creep. The faster creep rate was caused by the facts that the stress state under nanoindentation is more complex and severe than the uniaxial condition. The creep activation energy for the two creeps is also the same and both correspond to the activation energy for grain-boundary diffusion in Ni, suggesting that a similar diffusion-assisted dislocation glide process is operative in both testing situations.

2.2.2 Summary

The data presented in this section indicates that small, sub-micrometer, diameter metal samples deform plastically by a mechanism that is different from that occurring in large bulk samples in several ways: i) they display substantially high initial yield stress, ii) they deform plastically by a stochastic process involving intermittent strain jumps, iii) their operative deformation mechanism is characterized by small activation volumes compared to that of bulk metal deformation modes. Although these observations have now been reported by numerous independent investigators, there remain considerable unanswered questions and some conflicting findings related to the role of certain important features such as surface condition (coated or uncoated, rough or smooth), presence of pre-existing dislocations or internal obstacles to dislocation glide (such as grain boundaries or precipitates), and crystallographic orientation on the operative mechanisms of the time-dependent deformation of these small volume samples. It is against this background of evidence, or lack thereof, which the experimentation presented in the subsequent chapters of this thesis is performed.

This thesis research involves several unique testing and analysis techniques which will now be described in some detail.

2.3 Experimental and Analytical Methods

What follows is a concise description of the primary experimental and analytical techniques that are used in the research described in this thesis.

2.3.1 Instrumented Flat-punch Micro-Indentation

The uniaxial micro-compression and creep testing of Au micropillars and microspheres carried out in this study were performed with a computer-controlled NanoTest indentation machine manufactured by Micro Materials Ltd. (Wrexham, UK) [43]. The instrument consists of a vertically mounted ceramic pendulum that rotates about a frictionless pivot Figure 2.21. The upper end of the pendulum is attached to an electromagnetic coil wrapped around an aluminum core. When electrical current is supplied to the coil that top of the pendulum is attracted to a permanent magnet which, in turn, causes the bottom of the pendulum, containing flat-punch diamond indenter, to move towards the test sample (such as a micropillar or a microsphere). The force applied to the pendulum is directly proportional to the current fed to the coil. A parallel plate capacitor is attached to the bottom end of the pendulum. The change in capacitance across the parallel plates is proportional to the displacement of the indenter. The electromagnetic coil actuator is capable of applying up to 20 N force with a precision of $\pm$ 100 nN. The capacitance displacement gauge has a displacement range of about 50 µm.

The test sample is attached to a stage whose motion is operated by means of three DC motors in an XYZ configuration. These motors are controlled from a motherboard that has three power modules, an electronic interface module and a backlash control unit. Power supply to the system is from the computer while magnetic encoders control the motor positioning. When current is applied to the coil, the probe's maximum movement and pendulum orientation are determined by the limit stop setting.
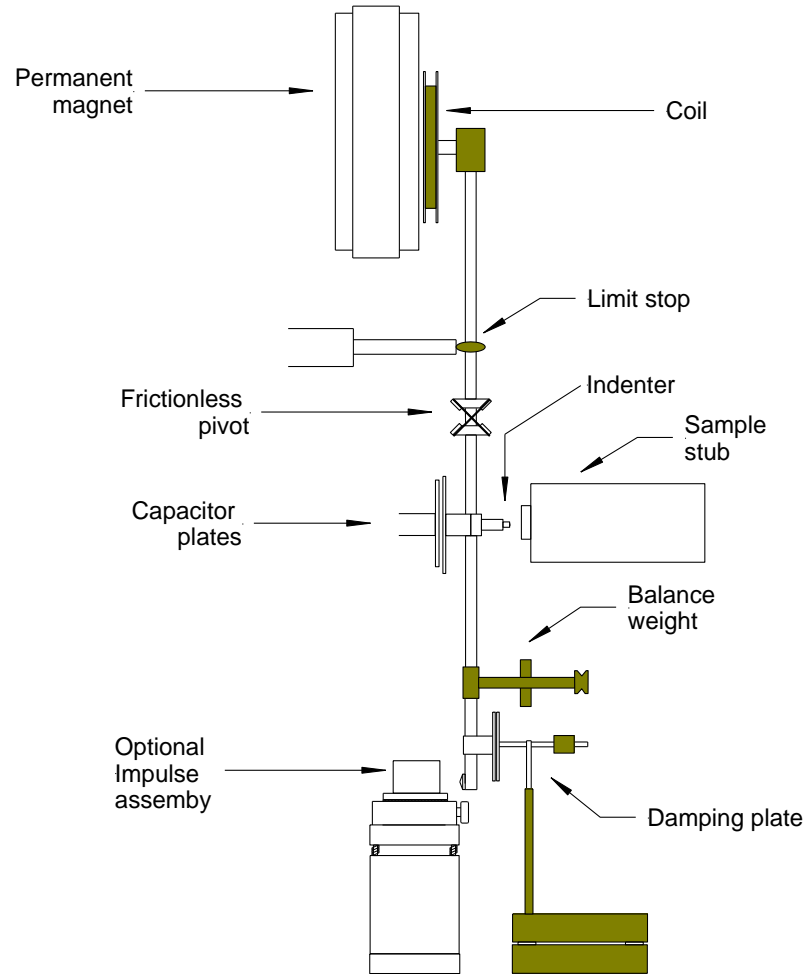
Figure 2.21: Schematic diagram of a micro-indentation tester assembly fitted with a flat-punch indenter used for uniaxial compression and creep test of the Au small scale samples [43].

The diamond flat-punch indenter used in this study to perform uniaxial compression and creep tests was made by FIB milling a flat surface on a diamond Berkovich pyramidal indenter. The projected area of the flat surface is an equilateral triangle with ~15 μm sides. The circular flat area on the center of the triangle is ~8.7 μm as shown in Figure 2.22a. The side view of the flat-punch indenter tip in Figure 2.22b showing the smoothness of the flat tip surface.
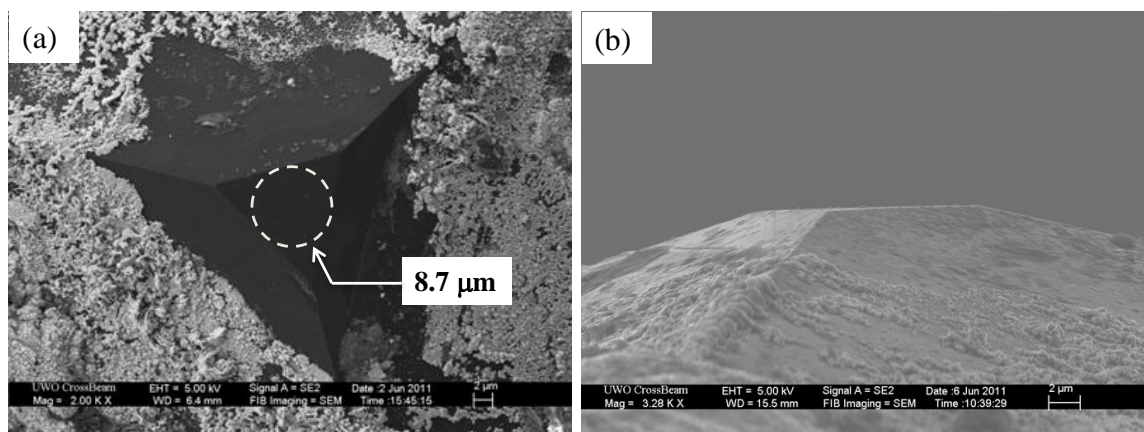
Figure 2.22: Flat-punch indenter used in this study for uniaxial compression and creep tests. (a) Top view of the indenter showing the flat surface circumference area and (b) Side view of the flat-punch indenter tip showing the surface smoothness of the flat surface.

The machine works by measuring the motion of a probe (indenter) when in contact with a material surface. The sequence begins by applying an increasing amount of force on the probe to either indent or compress the surface of a polished sample or feature to a predetermined force/depth at a defined loading rate. The force, depth and time of the test are recorded by the NanoTest software installed on the computer system. The software allows the user to positioning the sample stage, finding the sample surface, specifying different parameters such as the loading and unloading rates, the maximum indentation depth and the maximum indentation force. The software also allows post-processing of the test data to collect and analyze the data and determine the mechanical properties of the material.

To accurately perform compression and creep tests, it is very necessary to perform load, depth and microscope calibrations to ensure that the instrument is recording accurate and repeatable output data. Load calibrations are conducted by hanging weights, of known mass, to the pendulum while the machine records the voltage required to fix the actuator coil to balance the pendulum in a vertical position. Depth calibration is performed using a sample of known material properties (fused silica). No force is applied to the indenter

during this test, rather the DC motor is used to move the stage, with the reference sample attached, to make contact with the indenter. The X-stage translational DC motor then moves the sample a fixed amount further toward the indenter resulting in movement of the capacitor plate and a change in signal amplitude from the capacitor. With proper calibration the capacitance gauge will record indenter displacement of about $0.05 - 0.06$ nm/bit. Finally, the microscope calibration is carried out by performing micro-indentation on a polished Al sample to know the exact vertical and horizontal distance between the flat-punch indenter tip and the reference point of the optical microscope that is attached to the indentation tester. Microscope calibration is vital to properly compress the Au microspheres and micropillars used in this study.

2.3.2 Electron Backscattered Diffraction (EBSD)

Electron Backscattered Diffraction is a widely used technique for obtaining information about the crystallographic orientation of a specimen surface. The technique is usually performed with an SEM. The electron beam strikes the specimen and the electrons are elastically scattered from a region of the crystal directly below the surface. Electrons that strike the surface at an angle that satisfies the Bragg's condition (described below) will reflect very strongly from the surface and cause a bright "Kikuchi" line to appear on a fluorescent phosphor screen located in the SEM near to the specimen. Each lattice plane is represented on the fluorescent screen by a Kikuchi band. By comparing the pattern of the Kikuchi bands that appear on the fluorescent screen to theoretically determined patterns corresponding to specific crystal structures the crystallographic orientation of the surface of the sample can be determined.

The configuration of a typical EBSD instrument is shown in Figure 2.23. In general, an EBSD system consists of a specimen preferably tilted at about 70° from the horizontal, a phosphor screen which is fluoresced by back scattered electrons emitting from the specimen, a sensitive charge coupled device (CCD) video camera for viewing the diffraction pattern on the phosphor screen, a vacuum interface for mounting the phosphor screen and CCD camera in the SEM chamber, electronic hardware to control the SEM,

and a computer to control the EBSD experiments, analyze the diffraction pattern and display the results.
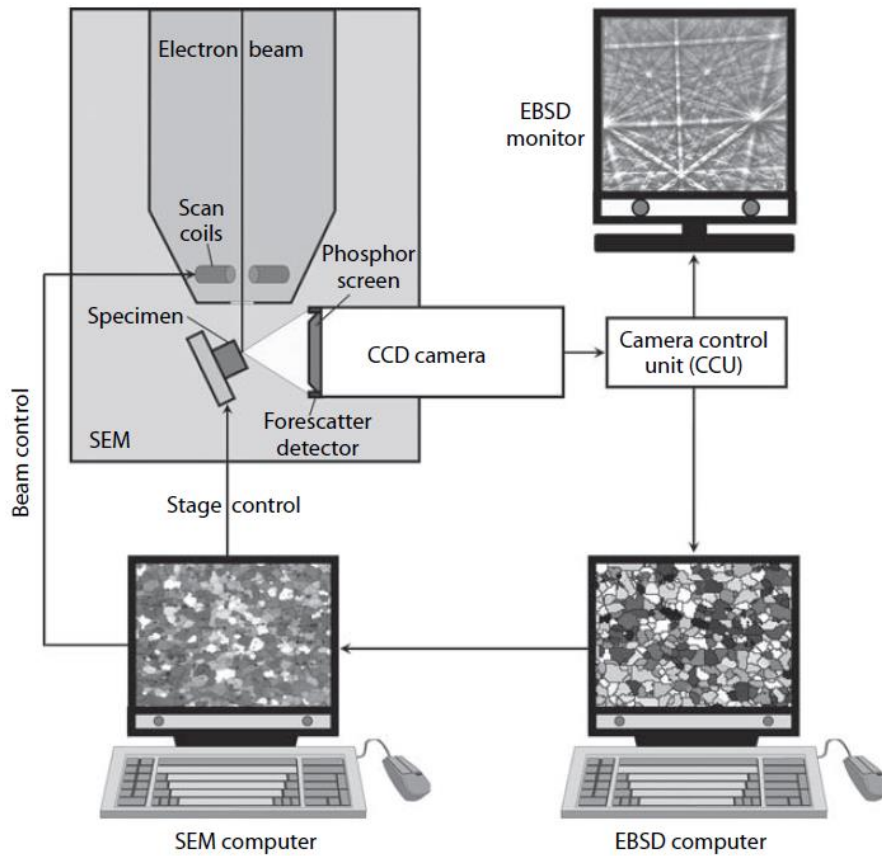
Figure 2.23: Schematic diagram of the components of an EBSD system [44].

During the experimentation, the intensity of the back-scattered electrons depends upon their incident angle θ to the sample surface (Figure 2.24). At certain characteristic angles, θ_B, the backscattered electron intensity reaches a maximum and this angle is related to the inter-planar spacing, d, of a family of crystal planes in the sample by the Bragg's law:

$$n\lambda = 2d \sin \theta_B \tag{2.23}$$

where n is an integer, and λ is the wavelength of the incident electrons. These electrons are diffracted to form a set of paired large angle cones corresponding to each diffracting plane. When used to form an image on the fluorescent screen the regions of enhanced electron intensity between the cones produce the characteristic Kikuchi bands of the

electron backscatter diffraction pattern (Figure 2.25a). The center lines of the Kikuchi bands correspond to the projection of the diffracting planes on the phosphor screen. The Kikuchi bands are indexed in terms of the Miller indices of the diffracting crystal planes which formed them. Each point on the phosphor screen corresponds to the intersection of a crystal direction with the screen. In particular, the intersections of the Kikuchi bands correspond to the intersection of zone axes in the crystal. Therefore, these points are used to index the crystal direction for the zone axis and the positions of the Kikuchi bands are used to calculate the orientation of the diffracting crystal (Figure 2.25b). So, analysis of Kikuchi pattern: Each band = diffraction of a family of planes; Intersections of bands = intersections of planes = zone axes; Angles between bands = angles between planes; Position of bands, directly linked to the crystallographic orientation.

The orientation of the crystal lattice is measured with respect to some reference frame. A graphical representation of the orientation of the crystal coordinate system in terms of the specimen coordinate system is referred to as a pole figure. Conversely, a graphical representation of the orientation of the specimen coordinate system in terms of the crystal coordinate system is referred to as an inverse pole figure.
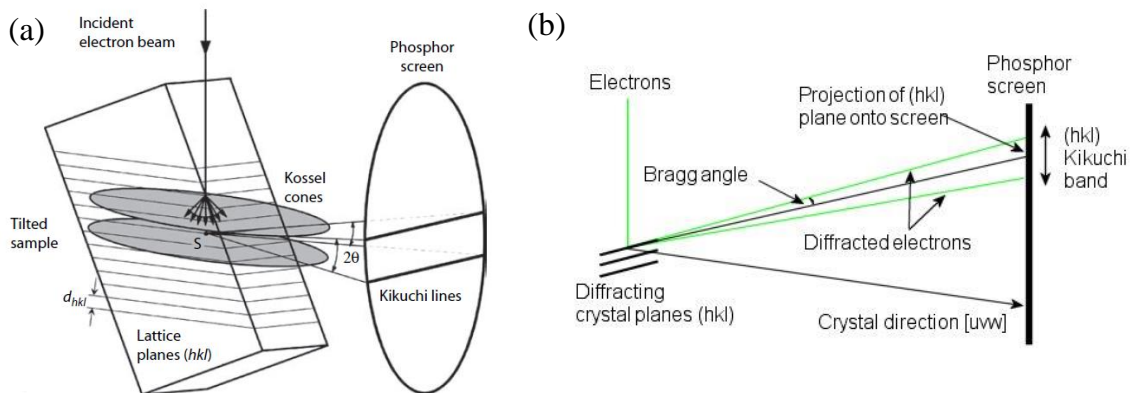
Figure 2.24: Formation of backscattered Kikuchi pattern by EBSD in a SEM. (a) Origin of Kikuchi lines from the tilted specimen [44]. (b) Schematic illustration of how features in the diffraction pattern are related to the crystal structure [45].
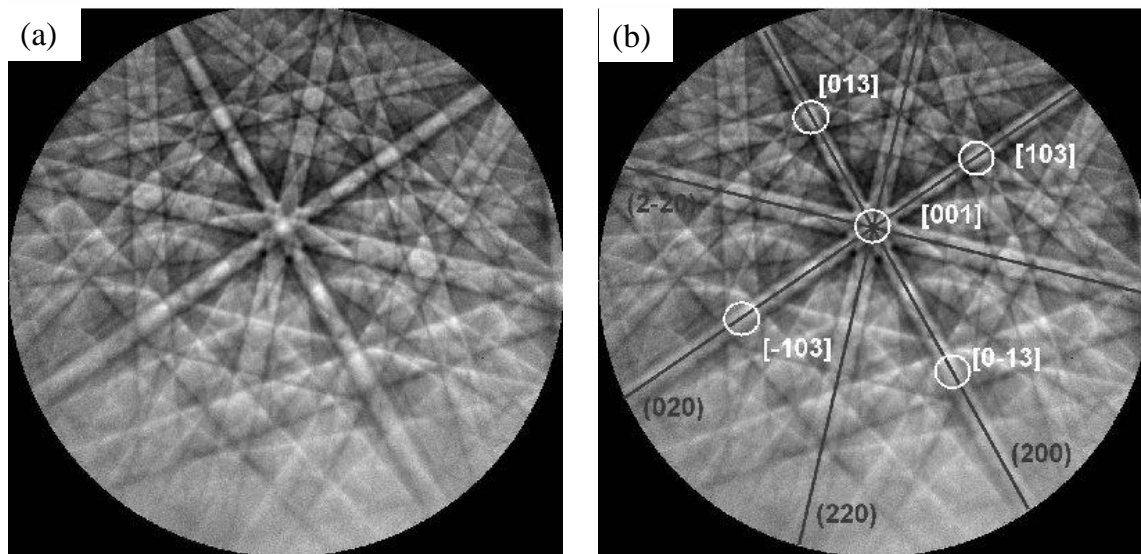
Figure 2.25: (a) A diffraction pattern from nickel collected at 20 kV accelerating voltage. (b) Indexing of the diffraction pattern. Kikuchi bands are labelled in terms of the Miller indices of the crystal planes that generated them (black). The planes project onto the screen at the center of the bands. Kikuchi band intersections are labelled with crystal direction that meets the screen at this point (white). This direction is the zone axis of the planes corresponding to the intersecting Kikuchi bands [45].

2.3.3 The Focused Ion Beam Instrument

A focused ion beam (FIB) instrument is very similar to an SEM. While FIB instruments can be stand-alone equipment, the one used in our studies, LEO (Zeiss) 1540XB FIB/SEM, was incorporated with an SEM to form a dual-beam system with enhanced capabilities. The FIB ion column is mounted at an angle of 54° to the sample stage in a horizontal position. This system is fitted with a sample transfer airlock compartment that allows for rapid sample change without causing significant disruption to the high vacuum of the main chamber. It is also fitted with a six axes sample stage that allows for complex sample manipulation. Other major components include liquid metal ion source, an ion column, an electron column, detectors gas inlets and a computer system used to control and operate the instrument.
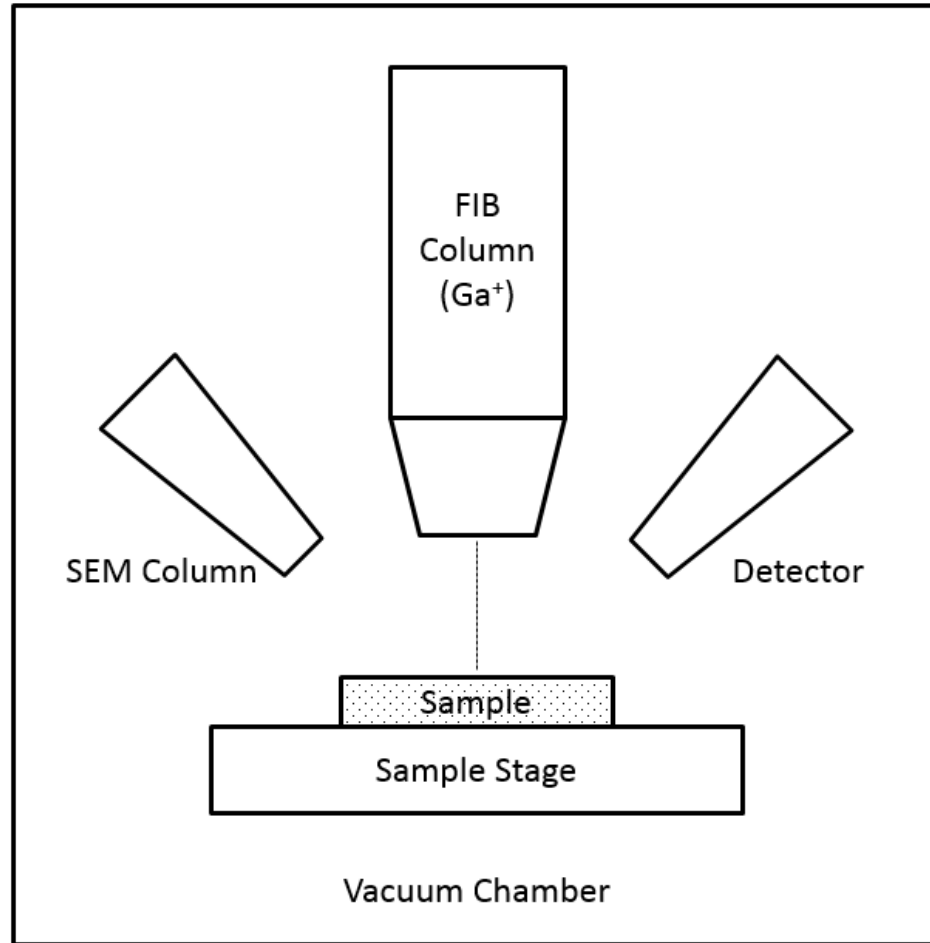
Figure 2.26: A schematic diagram of a basic FIB system showing the major components [46].

Figure 2.26 shows a schematic diagram of a basic FIB instrument without the electron column. Micromachining is carried out by sputter milling that basically involves sputtering of atoms from the surface of the material. For milling purposes, a liquid metal gallium ion source (LMIS) is needed. Ga+ ions are commonly used for this primarily purpose because of its low melting temperature of 29.8 °C.

The FIB milled micropillars studied in this thesis, for each micropillar fabrication process, a 10 nA Ga+ beam was used to mill a larger diameter circular area of 60.0 µm diameter to 6.0 µm diameter to insure the flat punch indenter, used to perform the subsequent mechanical testing did not contact the surrounding material while

compressing the micro-pillar. A 200 pA Ga+ beam was used to fine polish the 6.0 μm diameter surface to the desired micropillar diameter from 5.0 to 0.8 μm diameter.

The Ga+ beam is focused to a very small spot size using electromagnetic lenses located within the ion column. The focused ion beam can then be very accurately moved (rastered) anywhere on the sample surface with the use of electromagnetic scanning coil. When the FIB instrument is equipped with an electron beam column, as was the instrument used in this study, the focused electron beam can be also scanned across the sample surface to monitor the FIB milling process, in real-time and at high resolution [46].

References

1. J. Greer, 2006, "Bridging the gap between computational and experimental length scales: a review on nano-scale plasticity," *Rev. Adv. Mater. Sci*, Vol. 13, pp. 59–70.

2. J. C. Fischer and J. H. Holloman, 1947, "A statistical theory of fracture," *Trans. AIME*, Vol. 171, p. 546.

3. M. D. Uchic, D. M. Dimiduk, J. N. Florando, and W. D. Nix, Aug. 2004, "Sample dimensions influence strength and crystal plasticity.," *Science*, Vol. 305, pp. 986–9.

4. J. R. Greer, W. C. Oliver, and W. D. Nix, Apr. 2005, "Size dependence of mechanical properties of gold at the micron scale in the absence of strain gradients," *Acta Mater.*, Vol. 53, pp. 1821–1830.

5. J. Greer and W. Nix, Jun. 2006, "Nanoscale gold pillars strengthened through dislocation starvation," *Phys. Rev. B*, Vol. 73, pp. 245410–6.

6. C. A. Volkert and E. T. Lilleodden, Nov. 2006, "Size effects in the deformation of sub-micron Au columns," *Philos. Mag.*, Vol. 86, pp. 5567–5579.

7. C. P. Frick, B. G. Clark, S. Orso, a. S. Schneider, and E. Arzt, Aug. 2008, "Size effect on strength and strain hardening of small-scale [111] nickel compression pillars," *Mater. Sci. Eng. A*, Vol. 489, pp. 319–329.

8. D. M. Dimiduk, M. D. Uchic, and T. a. Parthasarathy, Sep. 2005, "Size-affected single-slip behavior of pure nickel microcrystals," *Acta Mater.*, Vol. 53, pp. 4065–4077.

9. K. S. Ng and a. H. W. Ngan, 2009, "Effects of trapping dislocations within small crystals on their deformation behavior," *Acta Mater.*, Vol. 57, pp. 4902–4910.

10. F. Machalett, K. Edinger, J. Melngailis, M. Diegel, K. Steenbeck, and E. Steinbeiss, 2000, "Direct patterning of gold oxide thin films by focused ion-beam irradiation," *Appl. Phys. A Mater. Sci. Process.*, Vol. 71, pp. 331–335.

11. B. Arnold, D. Lohse, H.-D. Bauer, T. Gemming, K. Wetzig, and K. Binder, 2003, "Surface Damages on FIB prepared TEM-Specimens :," *Microsc. Microanal.*, Vol. 9, pp. 140–141.

12. D. Mordehai, S.-W. Lee, B. Backes, D. J. Srolovitz, W. D. Nix, and E. Rabkin, Aug. 2011, "Size effect in compression of single-crystal gold microparticles," *Acta Mater.*, Vol. 59, pp. 5202–5215.

13. W. M. Mook, C. Niederberger, M. Bechelany, L. Philippe, and J. Michler, Feb. 2010, "Compression of freestanding gold nanostructures: from stochastic yield to predictable flow," *Nanotechnology*, Vol. 21, pp. 055701–9.

14. D. Maharaj and B. Bhushan, 2014, "Nanomanipulation, nanotribology and nanomechanics of Au nanorods in dry and liquid environments using an AFM and depth sensing nanoindenter," *Nanoscale*, Vol. 6, p. 5838.

15. D. Chrobak, N. Tymiak, A. Beaber, O. Ugurlu, W. W. Gerberich, and R. Nowak, 2011, "Deconfinement leads to changes in the nanoscale plasticity of silicon," *Nat. Nanotechnol.*, Vol. 6, pp. 480–484.

16. I. Salehinia, V. Perez, and D. F. Bahr, 2012, "Effect of vacancies on incipient plasticity during contact loading," *Philos. Mag.*, Vol. 92, pp. 550–570.

17. Y. Liu, E. Van der Giessen, and A. Needleman, 2007, "An analysis of dislocation nucleation near a free surface," *Int. J. Solids Struct.*, Vol. 44, pp. 1719–1732.

18. L. Nicola, a. F. Bower, K. S. Kim, a. Needleman, and E. Van der Giessen, 2007, "Surface versus bulk nucleation of dislocations during contact," *J. Mech. Phys. Solids*, Vol. 55, pp. 1120–1144.

19. D. Catoor, Y. F. Gao, J. Geng, M. J. N. V Prasad, E. G. Herbert, K. S. Kumar, G. M. Pharr, and E. P. George, 2013, "Incipient plasticity and deformation mechanisms in single-crystal Mg during spherical nanoindentation," *Acta Mater.*, Vol. 61, pp. 2953–2965.

20. U. F. Kocks, a. S. Argon, and M. F. Ashby, Jan. 1975, "Thermodynamics and Kinetics of Slip," *Prog. Mater. Sci.*

21. F. H. J. and M. F. Ashby, *Deformation-Mechanism Maps*. Pergamon Press, 1982.

22. T. Zhu and J. Li, Sep. 2010, "Ultra-strength materials," *Prog. Mater. Sci.*, Vol. 55, pp. 710–757.

23. W. D. Callister, *Materials Science and Engineering: an Introduction*, 7th ed. New York, NY: John Wiley & Sons, Inc, 2007.

24. B. Baufeld and M. B. and D. B. Messerschmidt, U, 1994, "Plasticity of Cubic Zirconia between 700 C and 1150 C Observed by Macroscopic Compression and by in situ Tensile Straining Tests," *Key Eng. Mater.*, Vol. 97–98, pp. 431–436.

25. P. Pirouz, J. L. Demenet, M. H. Hong, 2001, "On transition temperatures in the plasticity and fracture of semiconductors," *Philos. Mag. A*, Vol. 81, pp. 1207–1227.

26. V. Bhakhri, J. Wang, N. Ur-rehman, C. Ciurea, F. Giuliani, and L. J. Vandeperre, Sep. 2011, "Instrumented nanoindentation investigation into the mechanical behavior of ceramics at moderately elevated temperatures," *J. Mater. Res.*, Vol. 27, pp. 65–75.

27. J. M. Wheeler, C. Niederberger, C. Tessarek, S. Christiansen, and J. Michler, Jan. 2013, "Extraction of plasticity parameters of GaN with high temperature, in situ micro-compression," *Int. J. Plast.*, Vol. 40, pp. 140–151.

28. C. A. Schuh, J. K. Mason, and A. C. Lund, 2005, "Quantitative insight into dislocation nucleation from high-temperature nanoindentation experiments.," *Nat. Mater.*, Vol. 4, pp. 617–621.

29. K. Van Vliet, J. Li, T. Zhu, S. Yip, and S. Suresh, 2003, "Quantifying the early stages of plasticity through nanoscale experiments and simulations," *Phys. Rev. B*, Vol. 67, pp. 1–15.

30. R. E. Miller, L. E. Shilkrot, and W. a. Curtin, 2004, "A coupled atomistics and discrete dislocation plasticity simulation of nanoindentation into single crystal thin films," *Acta Mater.*, Vol. 52, pp. 271–284.

31. W. M. Mook, M. S. Lund, C. Leighton, and W. W. Gerberich, Oct. 2008, "Flow stresses and activation volumes for highly deformed nanoposts," *Mater. Sci. Eng. A*, Vol. 493, pp. 12–20.

32. A. T. Jennings, J. Li, and J. R. Greer, Aug. 2011, "Emergence of strain-rate sensitivity in Cu nanopillars: Transition from dislocation multiplication to dislocation nucleation," *Acta Mater.*, Vol. 59, pp. 5627–5637.

33. A. T. Jennings and J. R. Greer, 2011, "Heterogeneous dislocation nucleation from surfaces and interfaces as governing plasticity mechanism in nanoscale metals," *J. Mater. Res.*, Vol. 26, pp. 2803–2814.

34. L. Y. Chen, M. He, J. Shin, G. Richter, and D. S. Gianola, 2015, "Measuring surface dislocation nucleation in defect-scarce nanostructures," *Nat. Mater.*, Vol. 14, pp. 707–714.

35. A. Schneider, 2010, "Mechanical properties of small scale BCC metal structures."

36. T. Zhu, J. Li, A. Samanta, A. Leach, and K. Gall, 2008, "Temperature and strain-rate dependence of surface dislocation nucleation," *Phys. Rev. Lett.*, Vol. 100, p. 25502.

37. Y. Wang, a Hamza, and E. Ma, Jun. 2006, "Temperature-dependent strain rate sensitivity and activation volume of nanocrystalline Ni," *Acta Mater.*, Vol. 54, pp. 2715–2726.

38. N. Afrin and a. H. W. Ngan, Jan. 2006, "Creep of micron-sized Ni3Al columns," *Scr. Mater.*, Vol. 54, pp. 7–12.

39. K. S. Ng and a. H. W. Ngan, May 2008, "Stochastic nature of plasticity of aluminum micro-pillars," *Acta Mater.*, Vol. 56, pp. 1712–1720.

40. K. S. Ng and a. H. W. Ngan, Nov. 2009, "Deformation of micron-sized aluminium bi-crystal pillars," *Philos. Mag.*, Vol. 89, pp. 3013–3026.

41. I.-C. Choi, Y.-J. Kim, M.-Y. Seok, B.-G. Yoo, J.-Y. Kim, Y. Wang, and J. Jang, Feb. 2013, "Nanoscale room temperature creep of nanocrystalline nickel pillars at low stresses," *Int. J. Plast.*, Vol. 41, pp. 53–64.

42. C. L. Wang, Y. H. Lai, J. C. Huang, and T. G. Nieh, Feb. 2010, "Creep of nanocrystalline nickel: A direct comparison between uniaxial and nanoindentation creep," *Scr. Mater.*, Vol. 62, pp. 175–178.

43. B. Beake, S. Goodes, S. Jones, R. Parkinson, N. Pickford, L. Roberts, and J. Smith, "NanoTest User Manual Version 2.0." Micro Materials Ltd., 2002.

44. O. Engler and V. Randle, *Introduction to Texture Analysis*, 2nd ed. CRC Press Taylor and Francis Group, 2010.

45. "EBSD Oxford Instruments." [Online]. Available: http://www.ebsd.com/ebsd-explained/basics-of-ebsd/interpreting-the-diffraction-pattern. [Accessed: 24-Nov-

2015].

46.   L. A. Giannuzzi and F. A. Stevie, *Introduction To Focused Ion Beams*. New York, NY: Springer Science+Business Media, Inc., 2005.

Chapter 3

3 Study of the Size Dependence of Time-dependent Plastic Deformation of Au Micropillars and Microspheres[1]

In this study the length scale dependence of the operative mechanisms of time-dependent plastic deformation was studied using room temperature compression tests performed on Au micropillars and microspheres of 1.0 to 5.0 µm diameter. The samples tested displayed deformation that had a component of random strain jumps. In the case of the Au micropillars, the frequency of the strain jumps showed a bilinear dependence upon pillar diameter with the frequency being larger, and more sensitive to diameter, when the pillar diameter was small (and τ_R was high). We suggest that this indicates a transition from deformation occurring by deformation on multiple slip planes to deformation occurring predominantly by single-plane dislocation slip when the pillar diameter is less than 2 µm.

The strain jump frequency during the constant-load micropillar creep tests showed a linear dependence upon τ_R. Creep tests performed on the microspheres of 5.0 µm diameter displayed displacement jump frequency that was essentially independent of the applied load while the jump frequency increased with increasing load for the smaller 2.5 µm diameter microspheres. We suggest that this difference is related to the volume of the microsphere. When the volume is small, the component of the deformation that occurs by a stochastic dislocation glide process is increased and becomes strongly dependent upon the magnitude of the local shear stress.

---

[1] The manuscript in this chapter is an extended version of the one published in Materials Research Society Proceedings, May 2013 [AZM Islam, R.J. Klassen, MRS Online Proc. Libr., Vol. 1580, pp. 1–6]

3.1 Introduction

Initiation of plastic deformation in very small size samples, about 1 µm in length dimension, requires a much higher stress than in larger "bulk" samples. It is generally accepted that the stress required to initiate plastic deformation in such small volumes is controlled by the process of dislocation nucleation rather than dislocation glide [1–8]. Experimental data upon which we base our understanding of the length-scale dependence of plasticity are obtained primarily from nano-indentation and micropillar compression tests. Recently, micropillar compression tests have provided the most significant data owing primarily to their simple uniaxial stress state. Many researchers have reported that the overall stress-strain response during uniaxial compression of micron-sized pillars displays a "jerky" stochastic nature and the probability of the occurrence and the size of the discrete displacement jumps are related to the applied stress [9–13]. When the micropillars are subjected to constant-load creep tests the frequency of the displacement jumps decreases with increasing creep time and a steady strain rate creep component also contributes to the measured creep strain [11,12]. This suggests that multiple mechanisms of dislocation nucleation and/or obstacle-limited dislocation glide may contribute to the intrinsic creep of sub-micron size metal samples.

Recently single crystal metal microspheres have been tested in place of micropillars. These spheres can be fabricated at a lower cost and in greater quantity than the focused ion beam (FIB) milled micropillars. Although these spheres clearly do not undergo constant-stress deformation when subjected to uniaxial compression, they display stochastic deformation characteristics similar to compressed micropillars. Several researchers have produced *FCC* single-crystalline pure Au microspheres on a sapphire substrate by the solid-state diffusion dewetting technique [14–16]. It is this technique that we use in this study to investigate the length-scale dependence of the operative mechanisms of time-dependent plastic deformation of high purity Au microspheres. In this study we also compare the creep response of these Au microspheres to Au micropillars made, of the same dimension, using conventional FIB milling techniques.

3.2 Experimental

3.2.1 Micropillar Fabrication

A 0.5 mm thick foil of 99.99% pure polycrystalline Au was mechanically prepared by grinding with successively finer grades of SiC papers followed by final polishing in a 0.05 µm colloidal alumina slurry. The sample was then annealed at 500°C for 12 hours to promote grain growth and then chemically etched by emersion, at 25°C for about 2 minutes, in an aqueous solution of 8 wt% Iodine and 21 wt% Potassium Iodide. The Au removal rate in this solution was about 28 angstroms per second. The flow diagram of the sample preparation is shown in Figure 3.1a. The grain size of the Au was measured between 20 to 300 µm (Figure 3.1b).

Four sets of micropillars, designated A to D, were fabricated by FIB milling at the Nanofabrication Laboratory at Western University (London, Ontario, Canada). The diameters of the micropillars were approximately 1, 2, 3, and 5 µm and the diameter/height ratio was between 1: 1 and 1: 3. Five pillars were fabricated for each set of micropillars; two pillars were used for constant loading rate uniaxial compression tests and three were used for constant uniaxial load creep tests. In total, nineteen micropillars were tested in this study.

Electron back scatter diffraction (EBSD) was used to index the crystallographic orientation of the grains comprising the Au surface upon which the micropillars were made. EBSD analysis was performed at The Canadian Centre for Electron Microscopy, Brockhouse Institute for Materials Research, McMaster University, Hamilton, Ontario, Canada, on the sample by dividing the sample into six areas to capture all the micropillars. Figure 3.2 shows SEM images of two areas where most of the micropillars were located. The orientation maps and the corresponding inverse pole figure of these areas are shown in Figure 3.3. Inverse pole figures are a form of graphical representation of the orientation of sample with respect to the conventional (*hkl*) crystal coordinate indices. In the maps the red, green, and blue colors represent the [001], [101], and [111] crystallographic directions. The grains from which micropillars are made are designated

G1 to G5 as shown in Figure 3.2. Specific geometric and crystallographic details of each micropillar are given in Table 3.1.
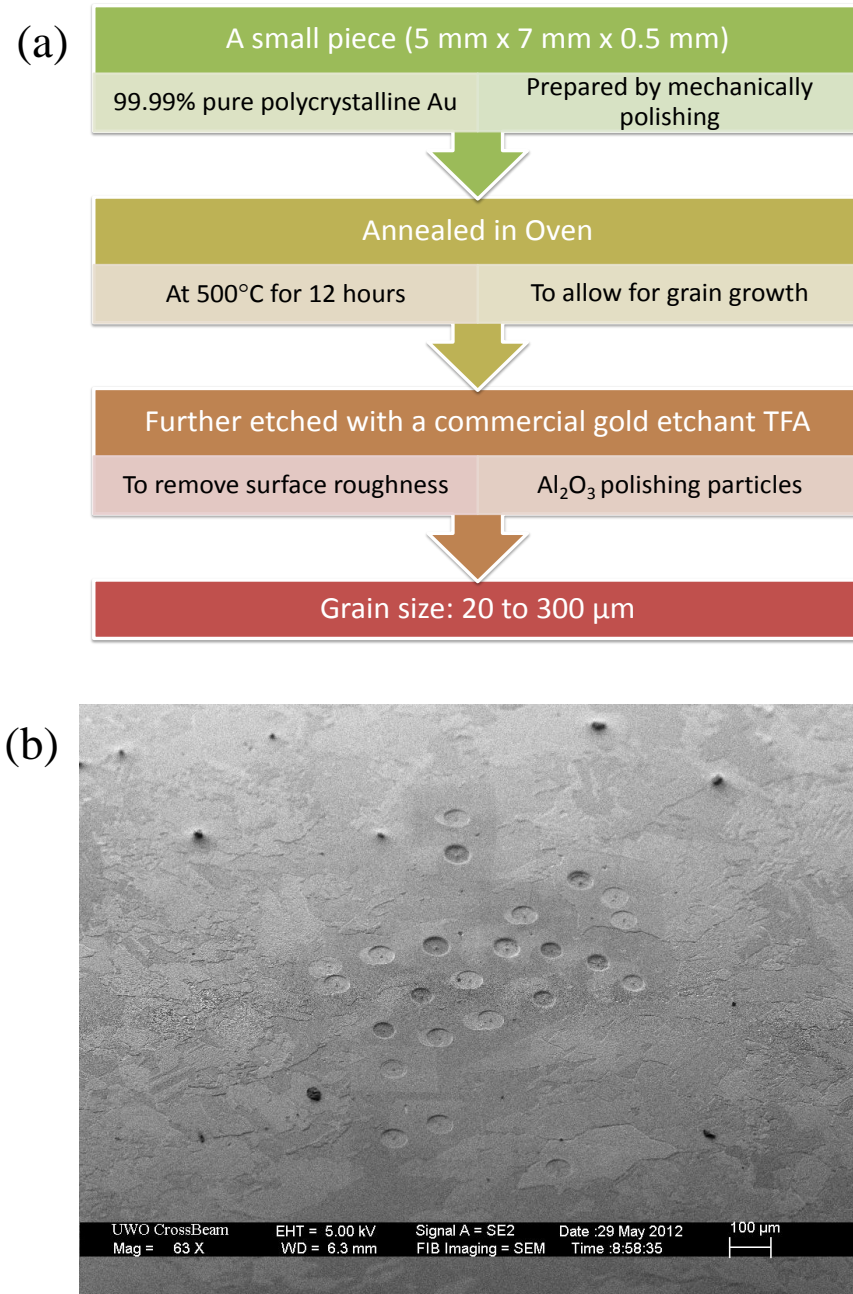
Figure 3.1: (a) Flow diagram shows the steps involved in the preparation of the bulk Au sample for micropillar fabrication. (b) SEM image shows the exposed grains on the Au sample. FIB milling was used to fabricate micropillars, identified as G1 − G5 (Figure 3.2), on some of the exposed grains. Grain size: 20 − 300 µm.
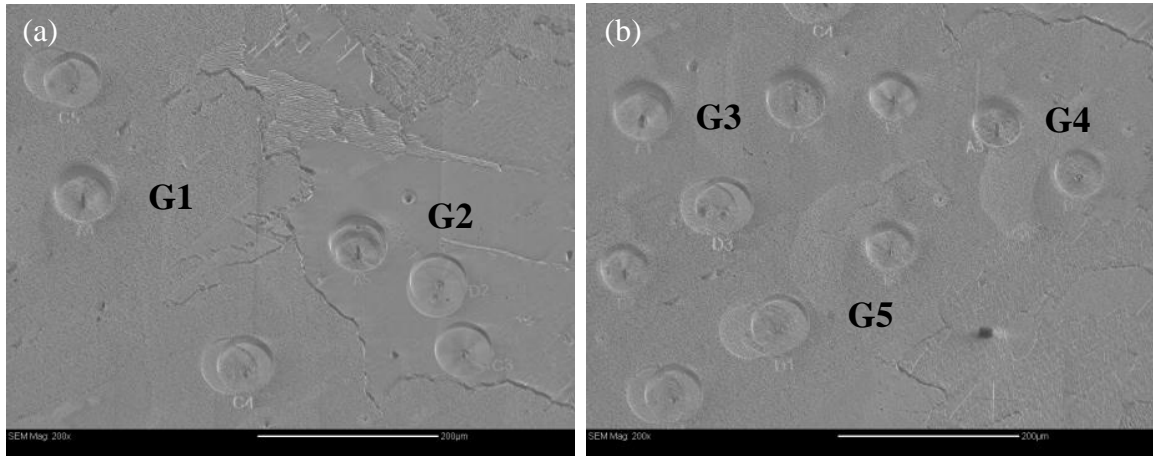
Figure 3.2: SEM images of the Au grains (a) Area 1 and (b) Area 2, labelled G1 to G5, containing the test micropillars.
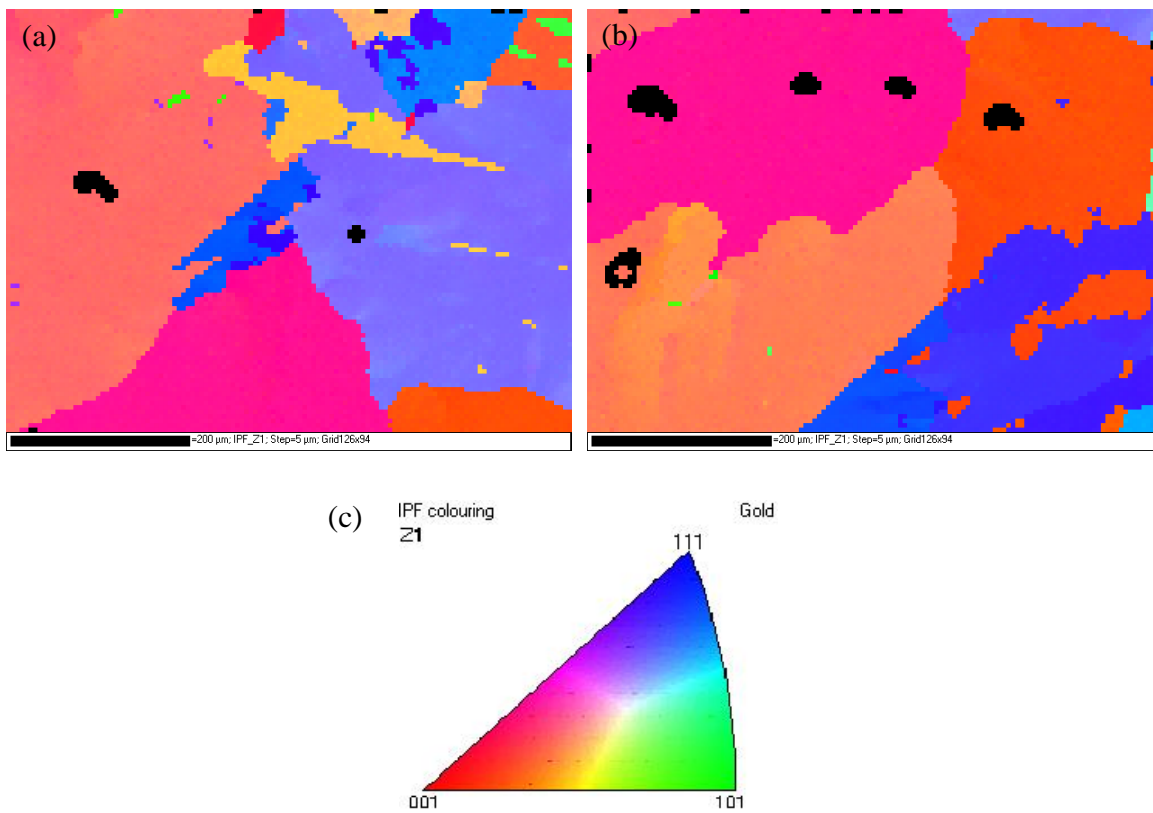
Figure 3.3: Inverse pole figure showing the crystallographic orientation map of (a) the Area 1 (Figure 3.2a) and (b) the Area 2 (Figure 3.2b). The crystal Z direction is normal to the surface of the sample. (c) Color key for the maps.

Table 3.1: Summary of the geometry and crystallographic orientation of the seventeen Au micropillars used in this study.

Sample Name	Pillar Diameter (µm)		Pillar Height (µm)	Axial crystallographic direction of the pillar	Schmid factor for the active {111}<110> slip system (Eq. 3.1)	Loading rate (mN/s)	Test details CL = Creep load (mN) and Time (sec)
	Top	Avg.					
A_1	4.97	5.35	6.5	<0.7, 0.5, 0.5>	0.80	0.05	Compression
A_2	4.81	5.30	5.5	<0.7, 0.5, 0.5>	0.37	0.03	CL= 0.20, 3600s
A_4	4.90	5.29	5.7	<0.7, 0.4, 0.6>	0.78	0.04	CL= 0.40, 3600s
A_5	4.80	5.34	6.2	<0.8, 0.5, 0.3>	0.62	0.02	CL= 0.40, 3600s
B_1	2.74	3.01	4.4	<0.7, 0.4, 0.6>	0.63	0.01	CL= 0.20, 3600s
B_2	2.81	3.28	4.4	<0.7, 0.4, 0.6>	0.70	0.01	CL= 0.20, 1800s
B_3	2.80	3.25	4.2	<0.7, 0.4, 0.6>	0.75	0.03	Compression
B_5	2.62	3.22	4.4	<0, 0.2, 0.9>	0.50	0.04	Compression
C_1	1.99	2.49	3.2	<0.7, 0.4, 0.6>	0.46	0.01	CL= 0.20, 1800s
C_2	1.60	1.81	3.5	<0.7, 0.4, 0.6>	0.78	0.01	CL= 0.20, 1800s
C_3	1.70	2.20	2.9	<0.8, 0.5, 0.3>	0.79	0.02	CL= 0.15, 1800s
C_4	1.74	2.14	3.2	<0.7, 0.5, 0.5>	0.75	0.03	Compression
C_5	1.76	2.10	3.4	<0.7, 0.4, 0.6>	0.46	0.01	CL= 0.15, 1800s
D_1	0.80	1.08	1.7	<0.7, 0.4, 0.6>	0.72	0.05	Compression
D_2	0.84	1.20	2.3	<0.8, 0.5, 0.3>	0.67	0.01	CL= 0.10, 1800s
D_3	0.74	1.16	1.9	<0.7, 0.4, 0.6>	0.57	0.01	CL= 0.10, 1800s
D_4	0.87	0.98	1.8	<0.7, 0.5, 0.5>	0.65	0.01	CL= 0.10, 1800s

3.2.2 Microsphere Fabrication

Gold microspheres were fabricated on a (0001) sapphire surface. An A8 PMMA positive photoresist layer was spin-deposited on the sapphire surface and e-beam lithography was used to project a grid of 2.5 and 5.0 µm diameter circles upon the photoresist. After the exposed photoresist was removed, a polycrystalline Au film of 300 nm thickness was deposited by e-beam evaporation. The remaining photoresist was then removed and the 2.5 and 5.0 µm diameter, 0.3 µm thick, Au cylinders were annealed in-vacuum at 1000°C. During this anneal the Au dewetted from the sapphire substrate and took the form of a single-crystal sphere, of 2.5 to 5.0 µm diameter, oriented with the <111> direction normal to the sapphire surface [14]. This lithographic/deposition procedure ensured that Au spheres of precise diameter and spacing were produced which we could

subsequently be test in compression. Twenty two Au microspheres were made and tested in this study (Figure 3.4).
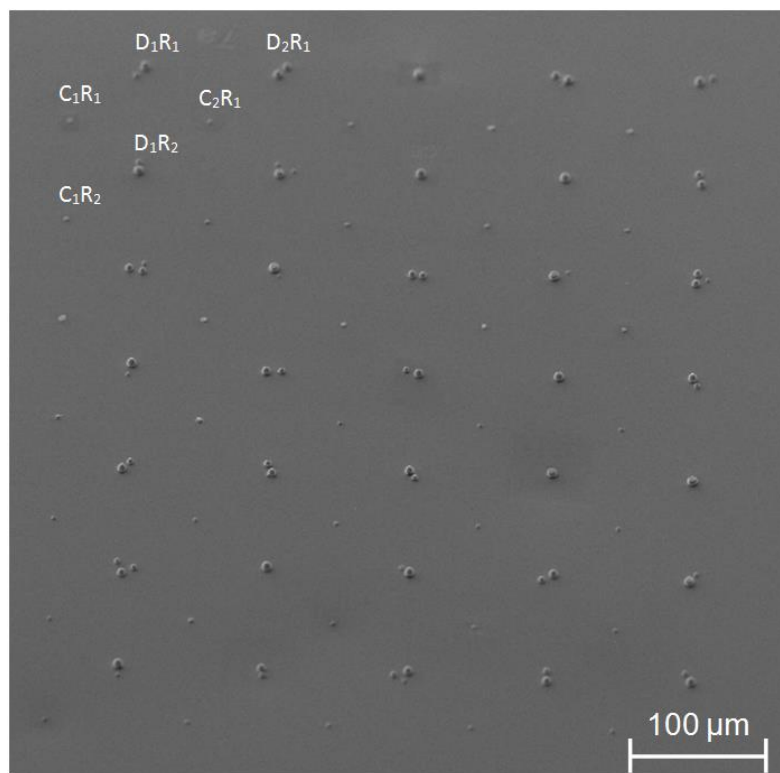
Figure 3.4: Shows the array (5 * 7 matrixes) of 2.5 and 5.0 µm microspheres fabricated using e-beam lithography patterning technique.

Table 3.2: Summary of the geometry of the Au microspheres used in this creep study.

Specimen Designation	Sphere diameter (µm)	Loading rate (mN/sec)	Creep test details	
			Creep load (mN)	Time (s)
C_1R_6	2.4	0.01	0.10	3600
C_3R_6	2.5	0.01	0.10	3600
C_4R_5	2.4	0.01	0.15	3600
C_5R_7	2.4	0.01	0.15	3600
C_5R_5	2.5	0.01	0.20	3600
C_4R_7	2.5	0.01	0.25	3600
C_5R_4	2.5	0.02	0.25	3600
C_1R_5	2.5	0.02	0.30	1800
C_3R_4	2.5	0.02	0.35	1800
C_4R_4	2.5	0.02	0.40	1800
D_4R_7	5.6	0.01	0.30	3600
D_1R_5	5.5	0.02	0.40	3600
D_4R_6	5.5	0.02	0.50	3600
D_5R_4	5.8	0.04	0.60	3600
D_4R_4	5.5	0.04	0.60	1800
D_5R_7	5.9	0.04	0.70	3600
D_5R_6	5.6	0.04	0.70	1800
D_1R_4	6.2	0.04	0.80	3600
D_5R_5	5.5	0.04	0.80	3600
D_1R_7	6.0	0.04	0.90	3600
D_4R_5	5.6	0.05	0.90	3600
D_2R_6	6.3	0.05	1.10	3600

3.2.3 Micro-compression Tests

The Au micropillars and microspheres were compressed with an instrumented micro-indentation tester (Micro Materials Ltd., Wrexham UK) fitted with a diamond flat punch indenter. The contact face of the flat punch was in the shape of an equilateral triangle with 8.7 µm sides. An optical microscope and a computer-controlled translation stage were used to position the test samples in line with the flat punch.

The micropillars and microspheres were tested by compression at loading rates between 0.01 and 0.05 mN/sec. During these tests the applied load and the displacement of the

punch were recorded about every 0.5 sec. Constant-load creep tests were also performed by compressing the samples to a prescribed load and then holding the load constant for 1800 to 3600 seconds while recording the displacement of the punch about every 10 seconds. From these data the average stress and strain in the test samples could be determined. Table 3.1 and Table 3.2 provide specific details for the seventeen micropillar and the twenty two microsphere compression tests performed in this study.

3.3 Results and Discussion

3.3.1 Uniaxial Compression of the Au Micropillars and Microspheres

Figure 3.5 and Figure 3.6, show SEM micrographs taken before and after the compression of several Au micropillars and microspheres. The 5 µm diameter micropillars showed considerable increase in diameter after compression, indicating the occurrence of uniform plastic deformation, while the smaller diameter micropillars deformed by localized shear on specific slip planes.

The true stress – true strain plots for a representative micropillar from each of the four pillar diameters is shown in Figure 3.7a. The true stress – true strain curve for the largest, 5 µm, diameter pillars were smooth and almost identical in shape and magnitude to those reported by Greer et al. [1,2] for similar size Au pillars. The smaller diameter pillars showed irregular "stepped" stress – strain response similar to what was reported by others [2,5,9]. The frequency of the "steps" increased with decreasing pillar diameter. This supports previous theories that plastic flow in the small diameter Au micropillars occurs by the sudden collective motion of dislocations along specific slip systems [2,4,10,13].

The flow stress is clearly larger for the small diameter pillars compared to the large diameter pillars. Figure 3.7b shows a logarithmic true stress – true strain plot of the same data as in Figure 3.7a. The strain-hardening coefficient n, indicated by the slope of the data ranges between $n = 0.24$ and 0.40 which is of similar magnitude to previously reported values of $n = 0.20 - 0.25$ obtained from large-specimen uniaxial testing of Au [17].

The comparison of flow stress at 5 and 10% strain for all diameter micropillars is plotted in Figure 3.8. At 5% strain, the average flow stress of the 1 and 5 µm pillars is about 240 and 45 MPa, which shows an almost 5 times increase in strength for the smaller pillar. Similarly, at 10% strain, the strength increases about 4 times when the pillar diameter decreased from 5 to 1 µm. A significant increase in strength and change of work hardening of the Au micropillars were observed as a function of decreasing diameter.
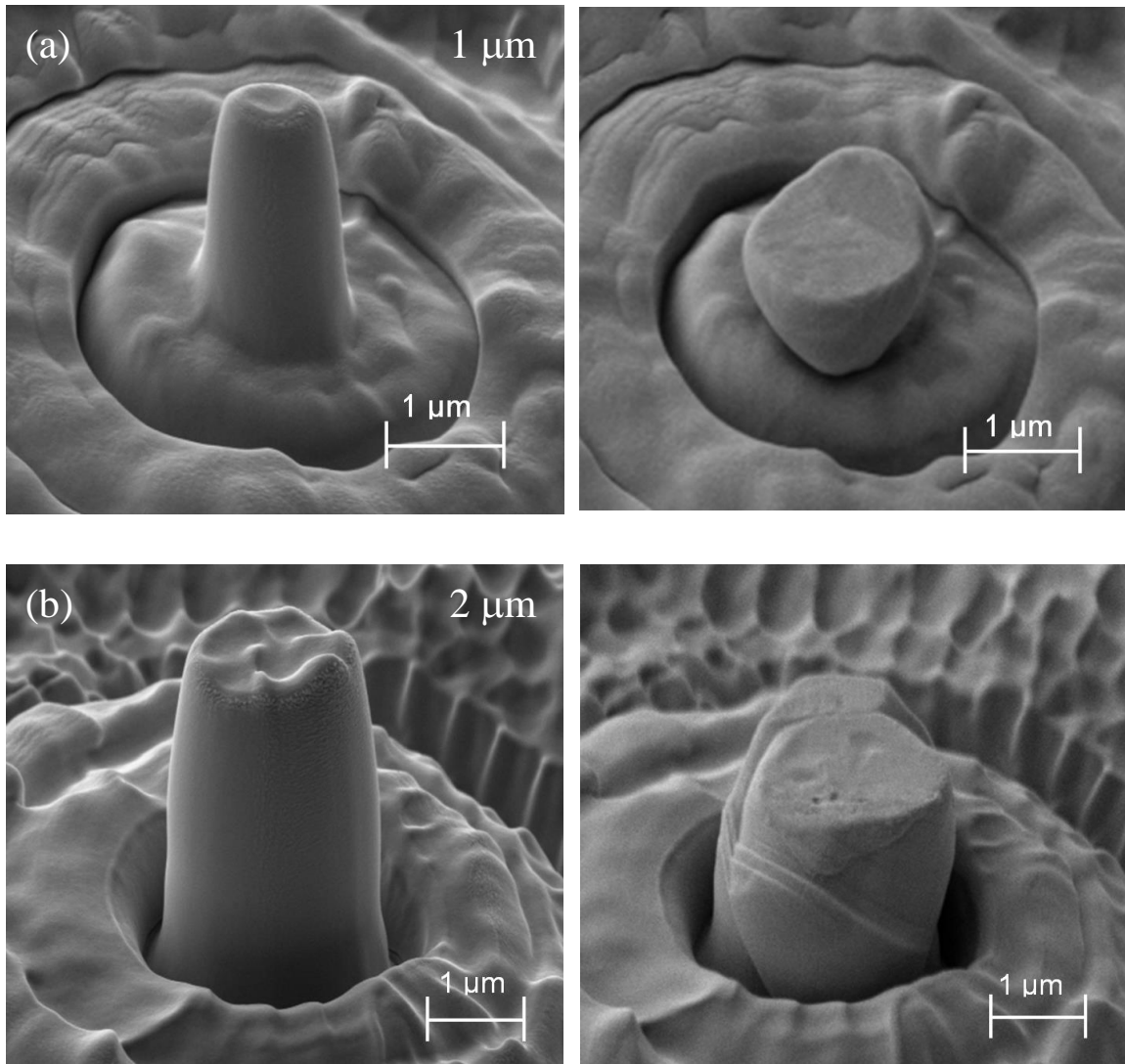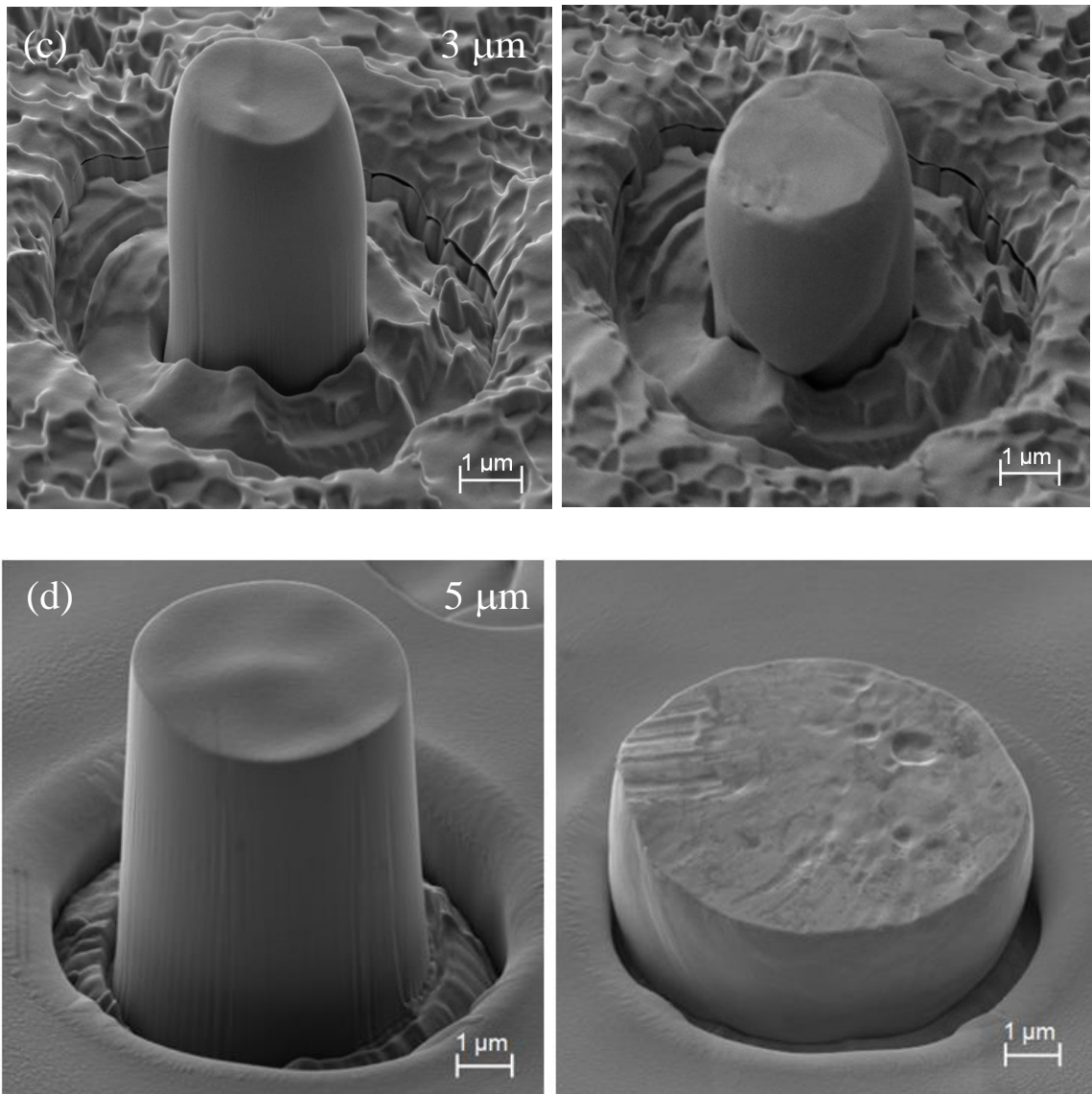
Figure 3.5: SEM images before and after deformation of: (a) 1, (b) 2, (c) 3 and (d) 5 µm diameter Au micropillars.
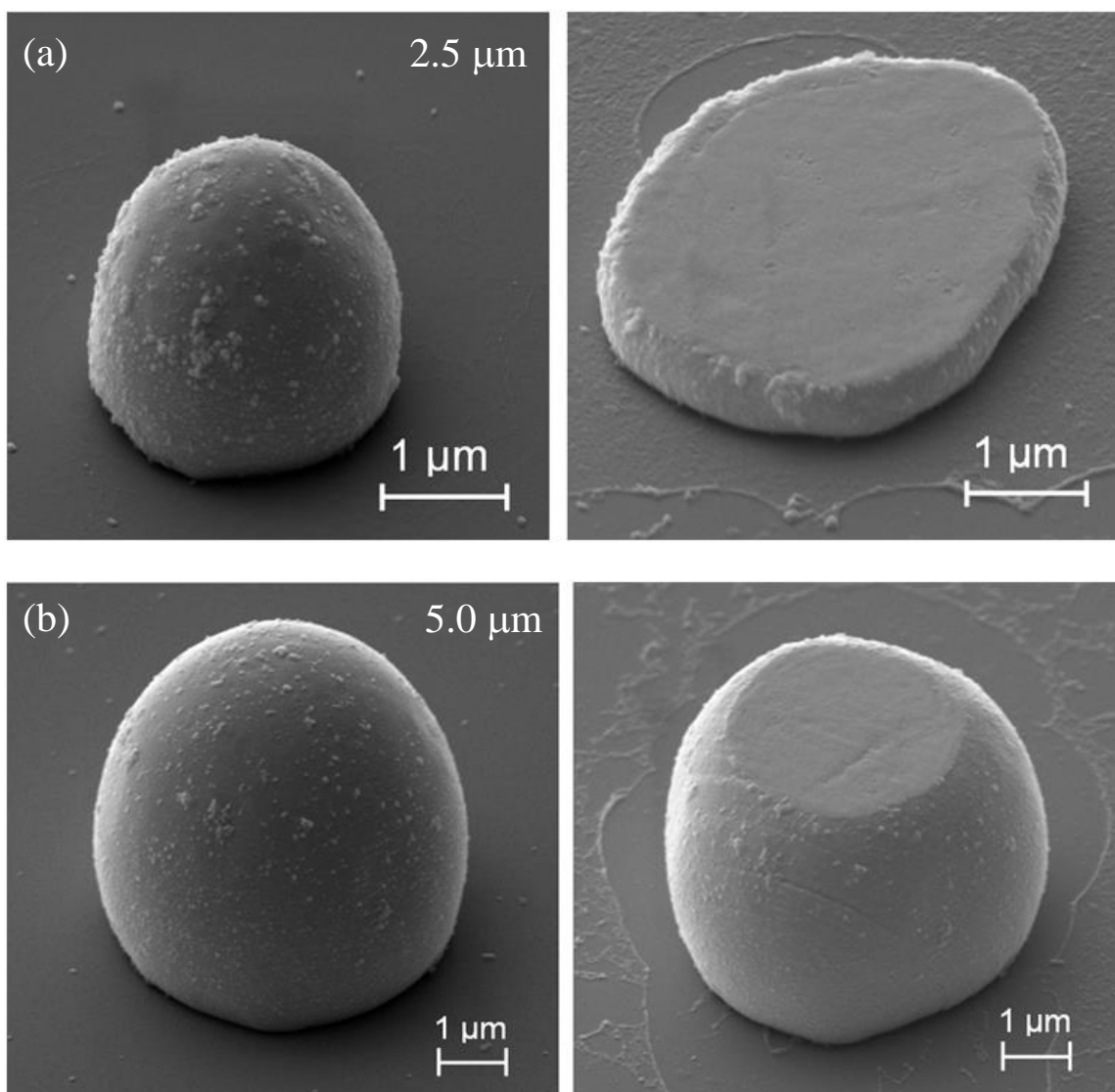
Figure 3.6: SEM images before and after deformation of: (a) 2.5 and (b) 5.0 µm diameter Au microspheres. The sapphire substrate is nonconductive and the fabricated microspheres were not connected to each other, thus a ~15 nm thick layer of Cr was deposited on the samples to promote electrical conduction and reduce charging during SEM imaging. Some deposited Cr particle can be seen on the surface of the microspheres.
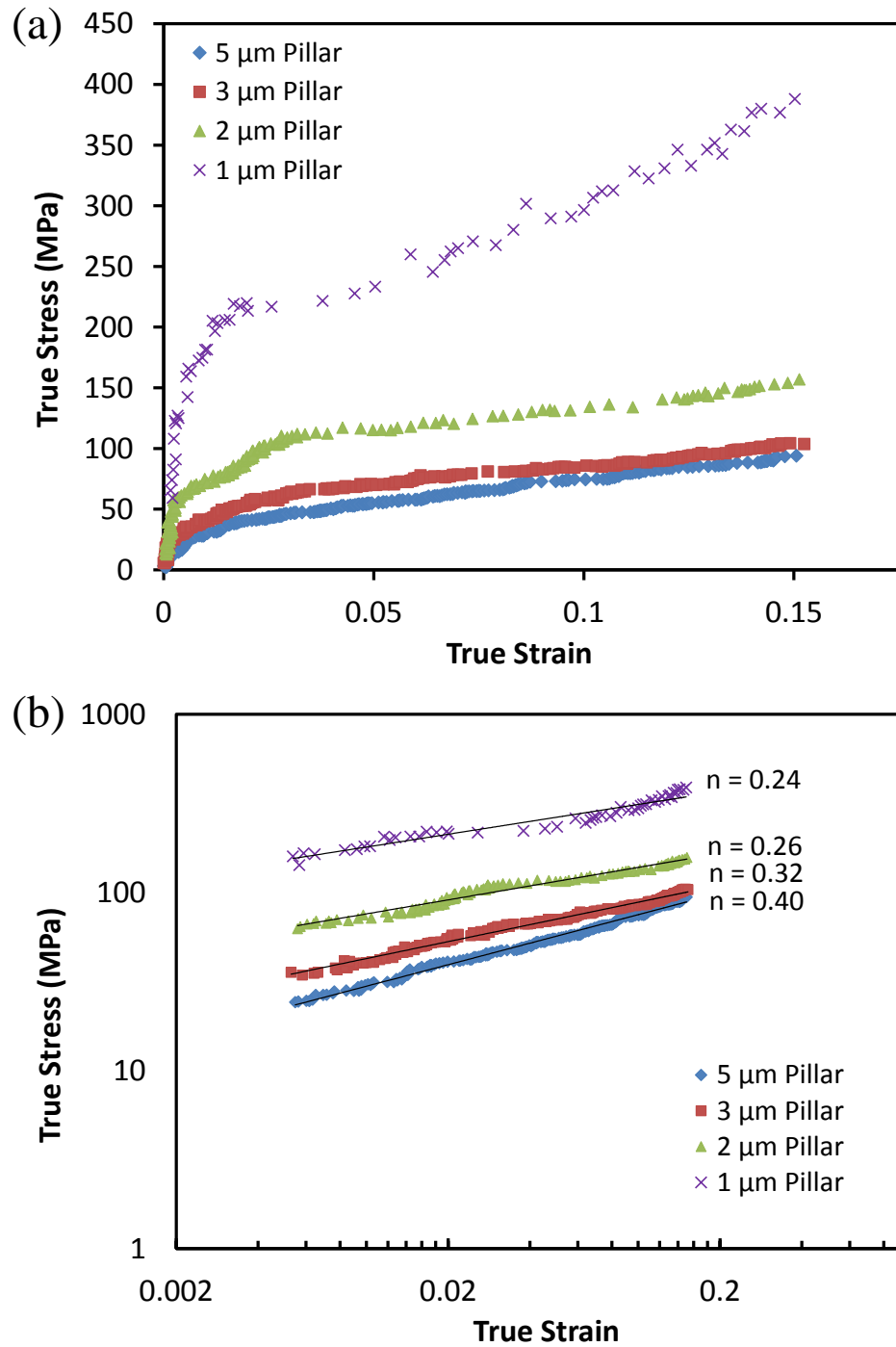
Figure 3.7: (a) Plot of true normal stress versus normal strain for one representative test performed on each Au micropillar diameter and (b) logarithmic true stress – true strain plot of the same data as in Figure 3.7a.
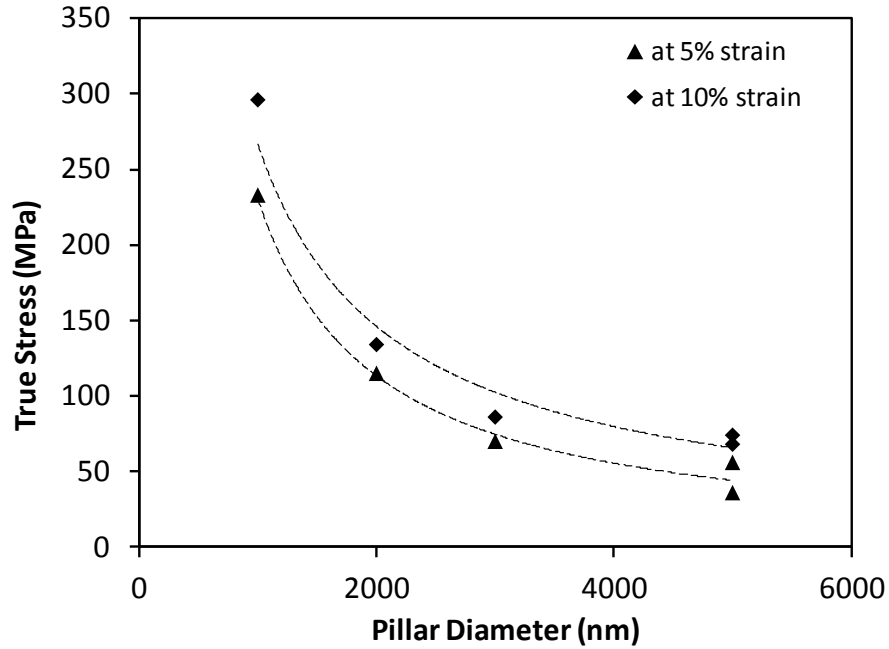
Figure 3.8: Representation of the changes of flow stresses at two different strain (5% and 10%) with decreasing pillar diameter from 5 to 1 µm. The dotted lines represents power law fitting.

In the *FCC* materials slip occurs along $< 110 >$ directions upon the closed-packed $\{111\}$ planes. Therefore, $\{111\} < 110 >$ represents the operative slip system for *FCC* crystals. The *FCC* materials contains four unique closed-packed planes of the form $\{111\}$ and three independent closed-packed directions of the form $< 110 >$ upon each plane. Thus, a total of twelve possible slip systems exist. For each micropillar the applied shear stress τ_R acting upon the active slip plane in the direction of dislocation motion was calculated as

$$\tau_R = \sigma(\cos \phi)(\cos \lambda) \tag{2.1}$$

Where, σ is the applied normal compressive stress, ϕ and λ are the angles between the loading direction and the normals to the slip plane and the slip direction respectively. The system on which slip occurs is the one which possesses the largest Schmid factor, $(\cos \phi)(\cos \lambda)$. The angles ϕ and λ were determined from the EBSD data and measurements taken from the SEM images of the deformed micropillars.

Figure 3.9 shows τ_R, corresponding to 3% plastic strain, versus micropillar diameter. τ_R increased at a low rate with decreasing pillar diameter between 2 and 5 µm but with considerably increased rate when the pillar diameter is smaller, in the range from 1 to 2 µm. Comparing the images of the deformed micropillars (Figure 3.5) with the trends shown in Figure 3.9 suggests that this change in dependence of τ_R upon pillar diameter coincides with the change in deformation from one of dislocation multiple-slip, in the large diameter micropillars, to one of predominantly single-slip in the small diameter micropillars.
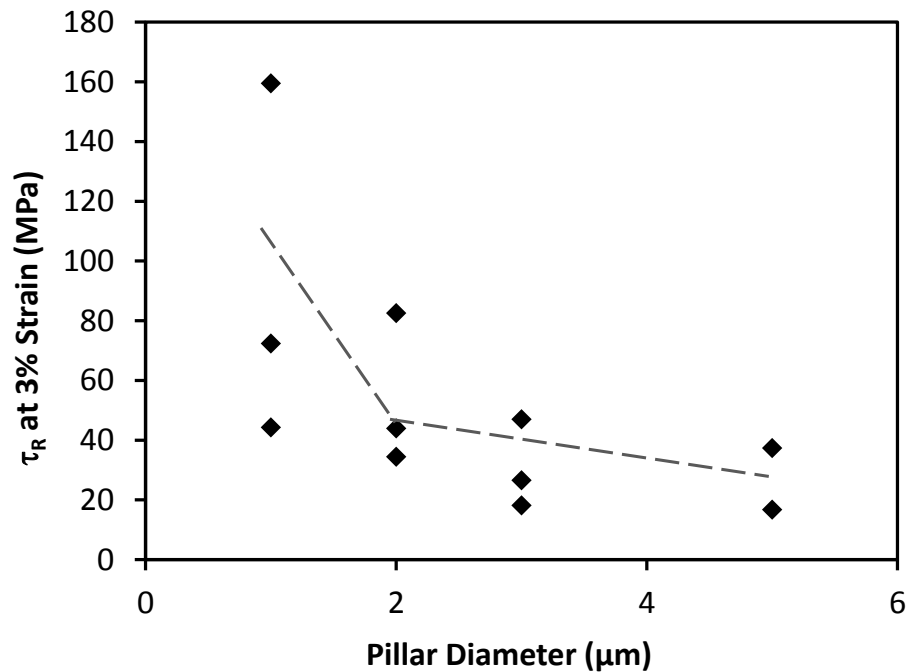
Figure 3.9: Resolved shear flow stress τ_R (Eq. 3.1) necessary for 3% strain versus Au micropillar diameter.

3.3.2 Time-dependent Plastic Deformation

Room temperature time-dependent plastic deformation behavior of Au was studied for all the four (1, 2, 3 and 5 µm) diameter micropillars and the two (2.5 and 5.0 µm) diameter microspheres. For this study, the maximum creep load was selected below the yield load of Au micropillars and spheres, and the flat-punch indenter was held at that selected load for about 3600 seconds for larger diameter pillars and spheres (5.0 µm), and 1800 seconds for smaller diameter pillars (1 and 2 µm) and spheres (2.5 µm). Time-depth response data were recorded during the holding period. The details of the specimen size and creep test of both micropillar and microsphere are tabulated in Table 3.1 and Table 3.2.

Figure 3.10 shows plots of micropillar displacement versus time during the constant-load creep of representative samples of large- and small-diameter Au micropillars. All the samples that we tested displayed deflection-time responses consisting of sudden strain jumps superimposed upon uniform time-dependent deformation. Analysis of our creep data indicated that the applied force varied by less than 6% over the duration of these constant force creep tests and, thus, the observed strain jumps were not directly related to significant changes in the applied load to the test sample. The observed strain jumps are similar to previously reported findings [11–13]. The frequency of deflection jumps and the resulting normal strain ε are shown as a function of τ_R in Figure 3.11. The average strain jumps per hour is plotted against micropillar diameter shown in Figure 3.12. The average frequency of strain jumps linearly decreased with increasing pillar diameter. The magnitude of deformation resulting from stochastic strain jumps increases with the increasing applied shear stress τ_R. Since the magnitude of τ_R is larger for the small diameter micropillars (Figure 3.9) the contribution from stochastic strain jumps to the total creep strain is also considerably larger for these micropillars.
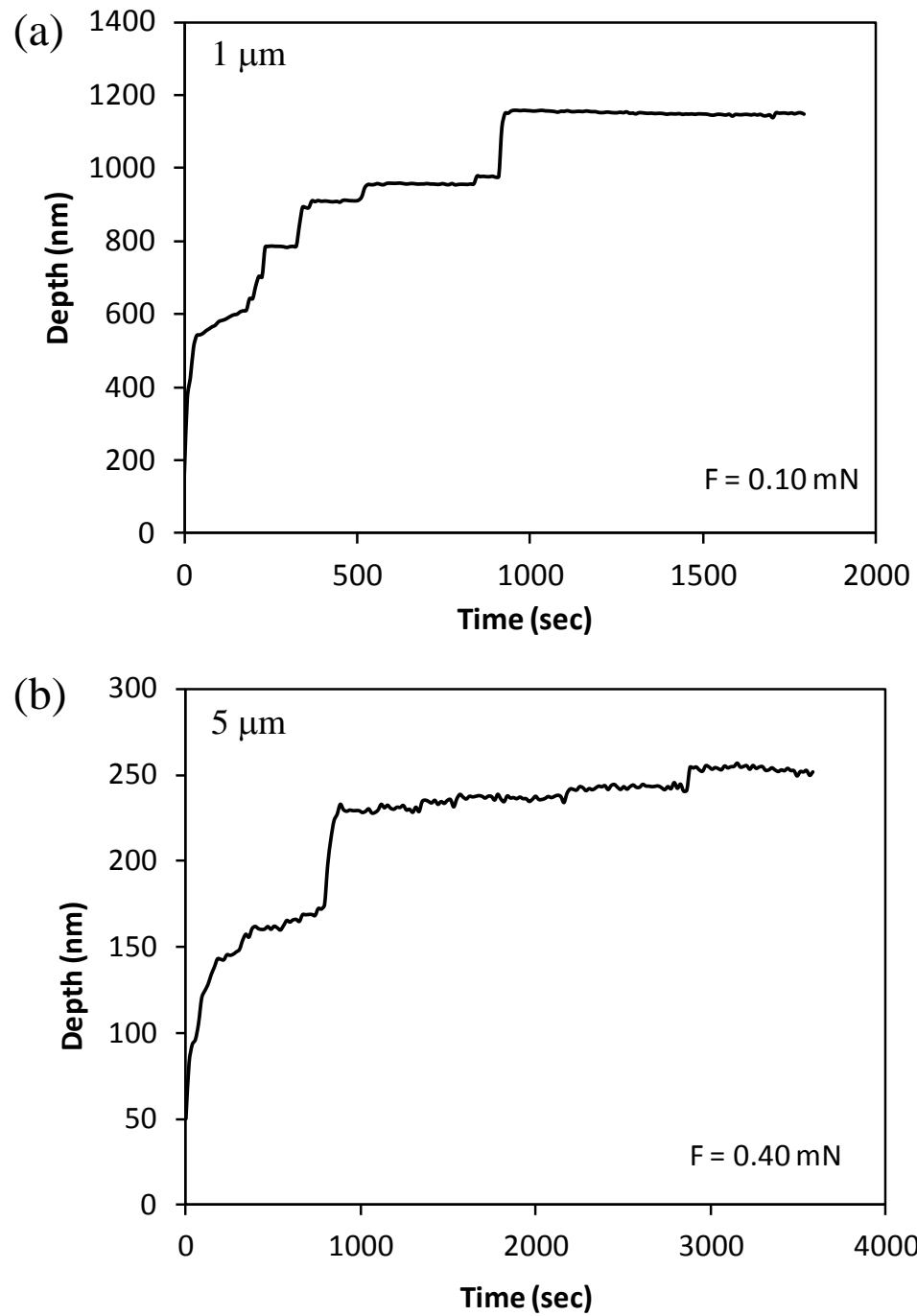
Figure 3.10: Representative displacement-time curves from constant-load creep tests performed on (a) 1 and (b) 5 µm diameter Au micropillars. The applied load, *F* is indicated on each graph.
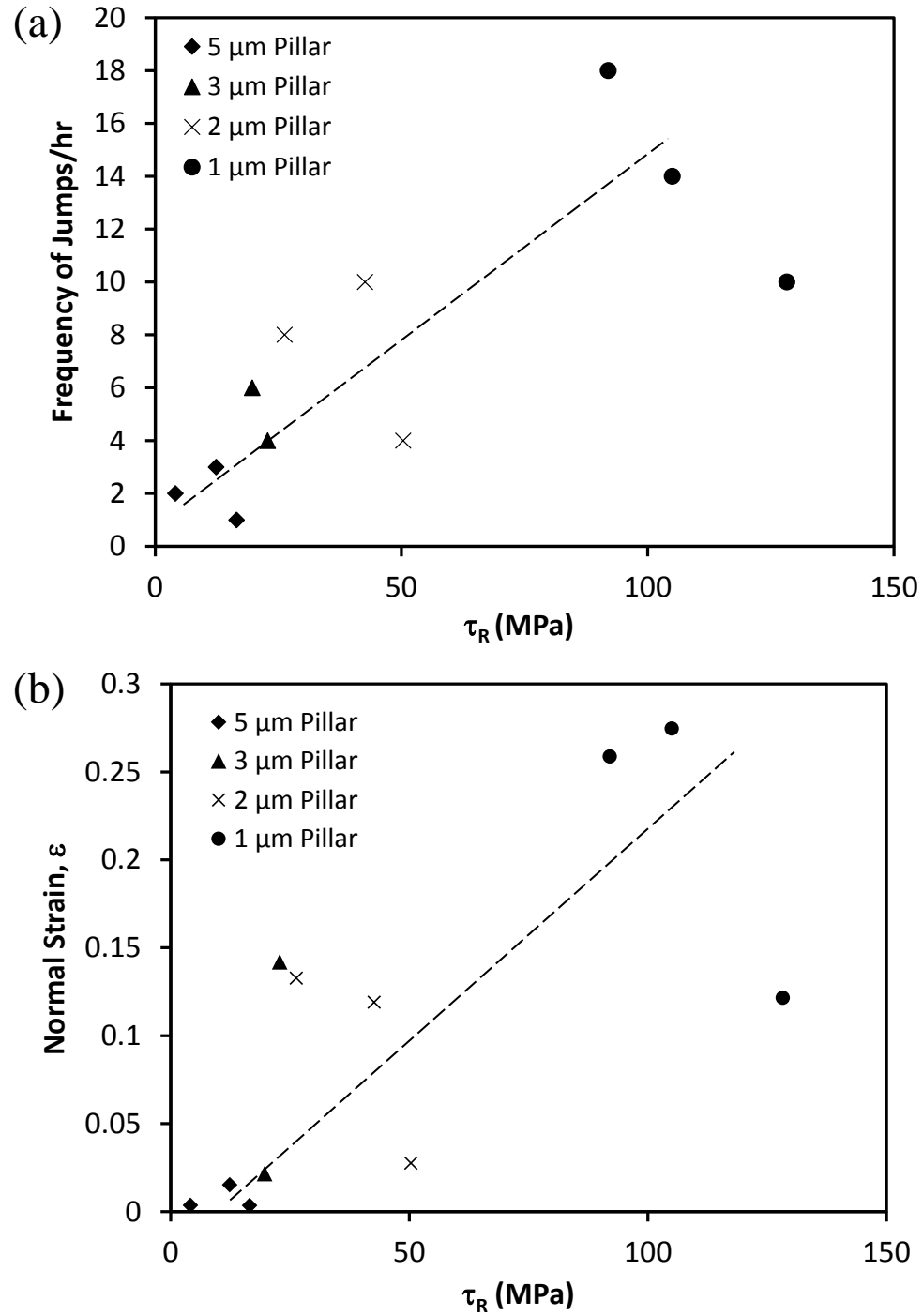
Figure 3.11: Relationship between (a) the frequency of strain jumps and (b) the resulting normal strain ε versus the applied resolved shear stress τ_R for the Au micropillars tested in constant-uniaxial load compression.
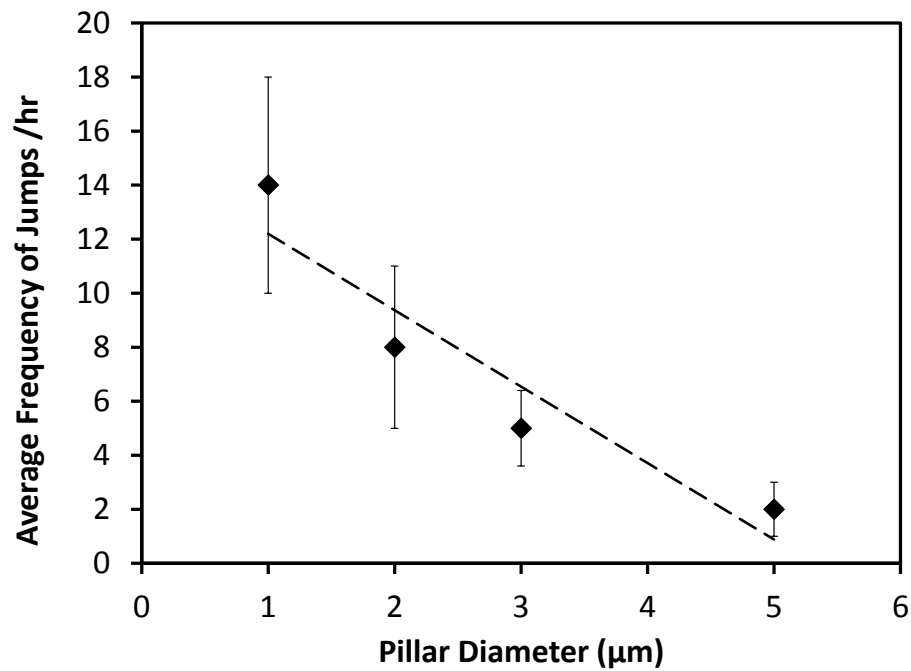
Figure 3.12: Average frequency of strain jumps for four diameters (1, 2, 3 and 5 µm) Au micropillars during constant uniaxial load creep tests.

A total of twenty-two Au microspheres, 2.5 and 5.0 µm diameter, were tested in this study (Table 3.2). Figure 3.13 shows plots of microsphere displacement versus time during the constant-load creep of representative samples of large- and small-diameter Au microspheres. During constant-load creep of the Au microspheres deformation occurs as a result of a complex state of stress within the sample. The frequency of displacement jumps was calculated and plotted them as a function of applied force (Figure 3.14). While it is clear that the stress state within the deforming microspheres is variable, and highly complex, comparison of the dependence of the deformation jump frequency to the applied load for creep tests performed on microspheres of the same initial diameter gives insight to the operative mechanisms of time-dependent deformation. Figure 3.14b indicates that for the large 5.0 µm diameter microspheres, the rate at which deflection jumps occur is essentially independent of applied load while for the smaller 2.5 µm diameter microspheres, the deflection jump rate increases with increasing applied load (Figure 3.13a).
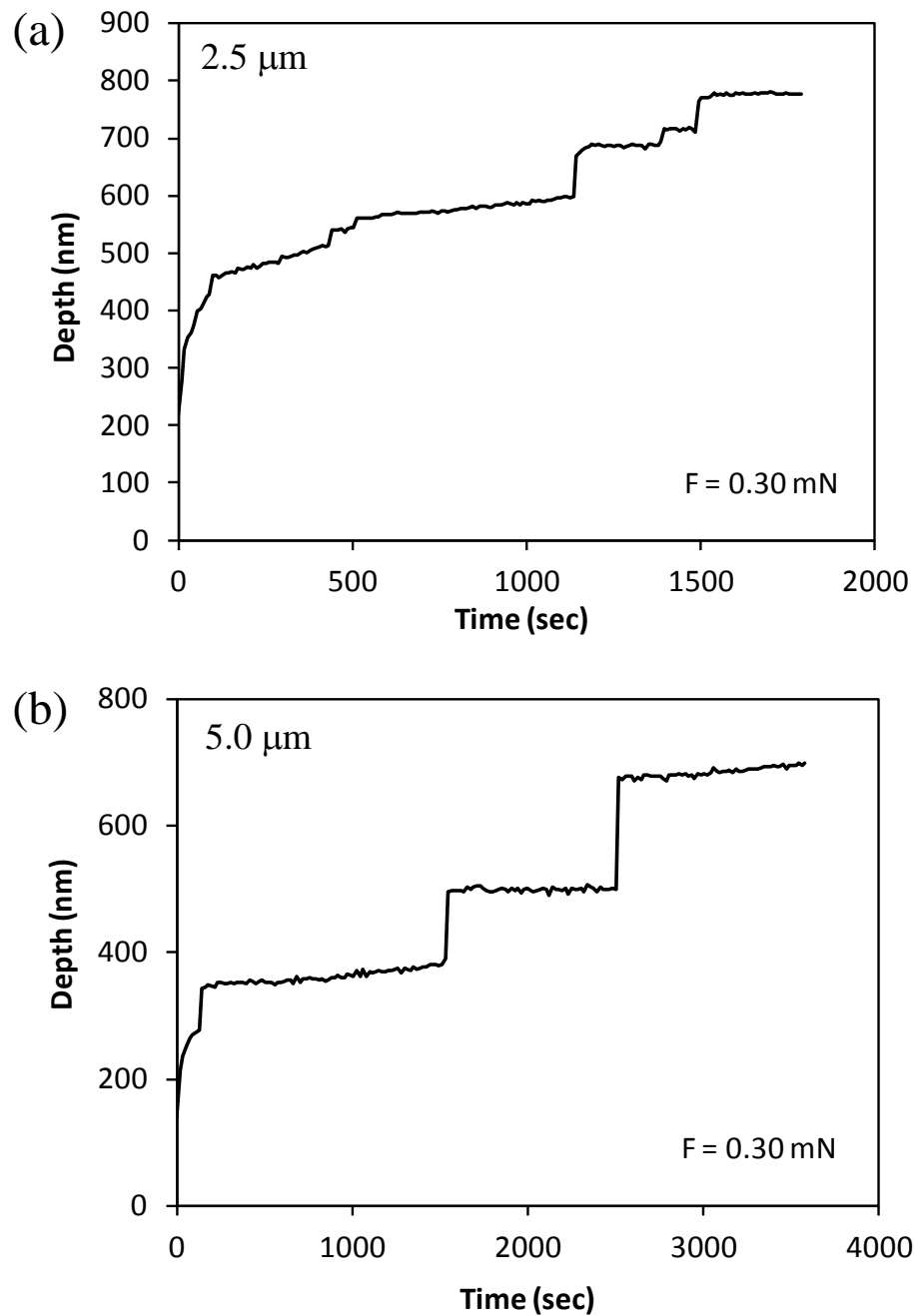
Figure 3.13: Representative displacement-time curves from constant-load creep tests performed on (a) 2.5 and (b) 5.0 µm diameter Au microsphere. The applied creep load, F is indicated on each graph.
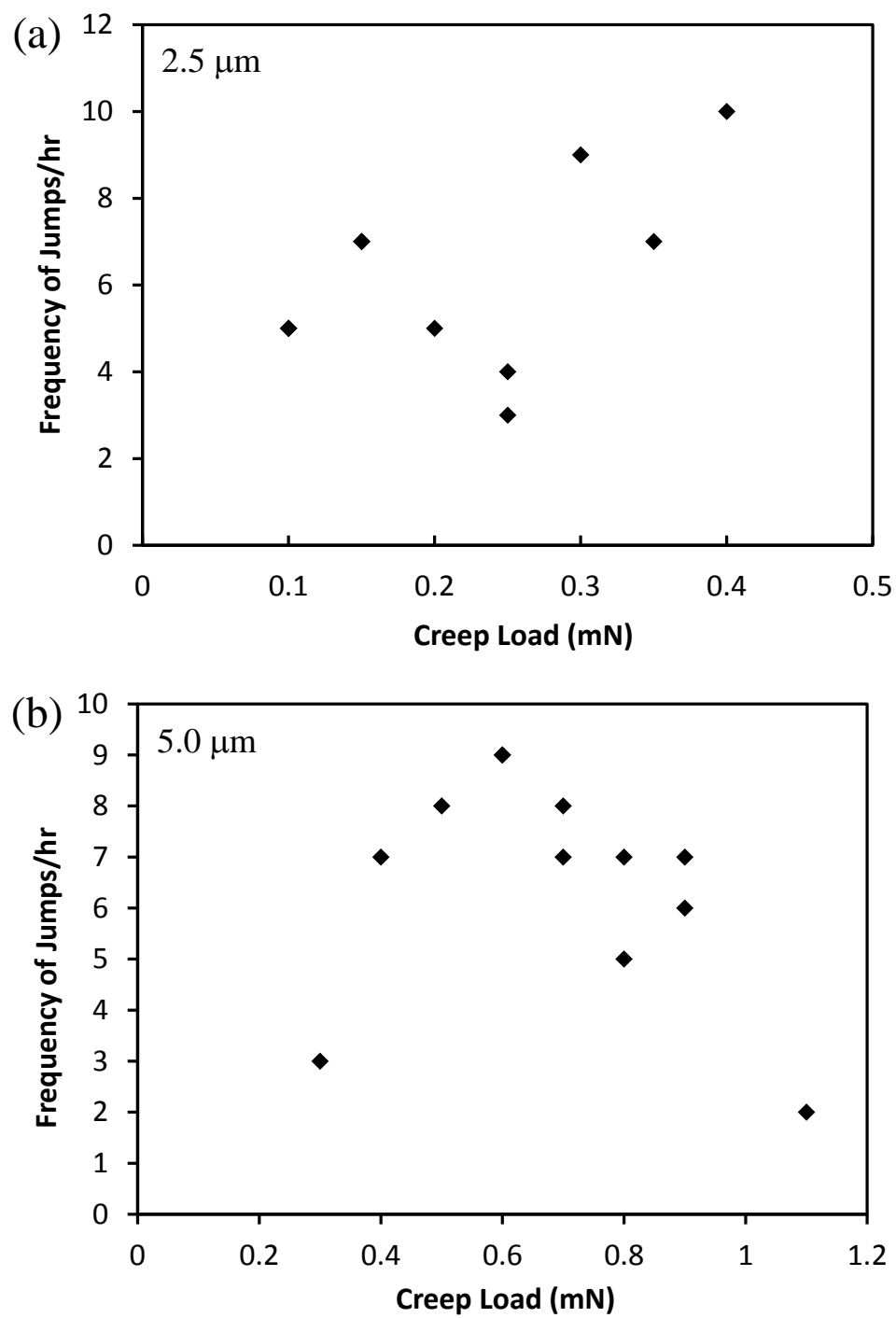
Figure 3.14: Strain jump frequency versus applied compressive load for (a) 2.5 and (b) 5.0 µm diameter Au microspheres.

3.4 Conclusions

In this study the length scale dependence of the operative mechanisms of time-dependent plastic deformation was studied using compression tests performed on Au micropillars and microspheres of 1.0 to 5.0 µm diameter. The samples were tested at room temperature and displayed deformation that had a component of random strain jumps. In the case of the Au micropillars, the frequency of the strain jumps showed a bilinear dependence upon pillar diameter with the frequency being larger, and more sensitive to diameter, when the pillar diameter was small (and τ_R was high). We suggest that this indicates a transition from deformation occurring by multiple-slip to deformation occurring predominantly by single-plane dislocation slip when the pillar diameter is less than 2 µm.

The strain jump frequency during the constant-load micropillar creep tests showed a linear dependence upon τ_R. Constant-load creep tests performed on the microspheres of 5.0 µm diameter displayed displacement jump frequency that was essentially independent of applied load while the jump frequency increased with increasing load for the smaller 2.5 µm diameter microspheres. We suggest that this difference is related to the volume of the microsphere: when the volume is small, the component of the deformation that occurs by a stochastic dislocation glide process is increased and becomes strongly dependent upon the magnitude of the applied local shear stress.

The next chapter of this thesis will present the kinetics of size and strain rate dependence of plastic deformation of Au microspheres of size ranges between 0.8 and 6.0 µm diameter.

References

1. J. R. Greer, W. C. Oliver, and W. D. Nix, Apr. 2005, "Size dependence of mechanical properties of gold at the micron scale in the absence of strain gradients," *Acta Mater.*, Vol. 53, pp. 1821–1830.

2. J. Greer and W. Nix, Jun. 2006, "Nanoscale gold pillars strengthened through dislocation starvation," *Phys. Rev. B*, Vol. 73, pp. 245410–6.

3. W. D. Nix, J. R. Greer, G. Feng, and E. T. Lilleodden, Feb. 2007, "Deformation at the nanometer and micrometer length scales: Effects of strain gradients and dislocation starvation," *Thin Solid Films*, Vol. 515, pp. 3152–3157.

4. J. Greer, 2006, "Bridging the gap between computational and experimental length scales: a review on nano-scale plasticity," *Rev. Adv. Mater. Sci*, Vol. 13, pp. 59–70.

5. C. P. Frick, B. G. Clark, S. Orso, a. S. Schneider, and E. Arzt, Aug. 2008, "Size effect on strength and strain hardening of small-scale [111] nickel compression pillars," *Mater. Sci. Eng. A*, Vol. 489, pp. 319–329.

6. J.-Y. Kim and J. R. Greer, 2008, "Size-dependent mechanical properties of molybdenum nanopillars," *Appl. Phys. Lett.*, Vol. 93, p. 101916.

7. A. Kunz, S. Pathak, and J. R. Greer, Jun. 2011, "Size effects in Al nanopillars: Single crystalline vs. bicrystalline," *Acta Mater.*, Vol. 59, pp. 4416–4424.

8. A. S. Schneider, B. G. Clark, C. P. Frick, P. a. Gruber, and E. Arzt, May 2009, "Effect of orientation and loading rate on compression behavior of small-scale Mo pillars," *Mater. Sci. Eng. A*, Vol. 508, pp. 241–246.

9. M. D. Uchic, D. M. Dimiduk, J. N. Florando, and W. D. Nix, Aug. 2004, "Sample dimensions influence strength and crystal plasticity.," *Science*, Vol. 305, pp. 986–9.

10. D. M. Dimiduk, M. D. Uchic, and T. a. Parthasarathy, Sep. 2005, "Size-affected single-slip behavior of pure nickel microcrystals," *Acta Mater.*, Vol. 53, pp. 4065–4077.

11. K. S. Ng and a. H. W. Ngan, Dec. 2007, "Creep of micron-sized aluminium columns," *Philos. Mag. Lett.*, Vol. 87, pp. 967–977.

12. K. S. Ng and a. H. W. Ngan, May 2008, "Stochastic nature of plasticity of aluminum micro-pillars," *Acta Mater.*, Vol. 56, pp. 1712–1720.

13. C. A. Volkert and E. T. Lilleodden, Nov. 2006, "Size effects in the deformation of sub-micron Au columns," *Philos. Mag.*, Vol. 86, pp. 5567–5579.

14. D. Mordehai, S.-W. Lee, B. Backes, D. J. Srolovitz, W. D. Nix, and E. Rabkin, Aug. 2011, "Size effect in compression of single-crystal gold microparticles," *Acta Mater.*, Vol. 59, pp. 5202–5215.

15. D. Mordehai, M. Kazakevich, D. J. Srolovitz, and E. Rabkin, Apr. 2011, "Nanoindentation size effect in single-crystal nanoparticles and thin films: A comparative experimental and simulation study," *Acta Mater.*, Vol. 59, pp. 2309–2321.

16. S.-W. Lee, D. Mordehai, E. Rabkin, and W. D. Nix, Jul. 2011, "Effects of focused-ion-beam irradiation and prestraining on the mechanical properties of FCC Au microparticles on a sapphire substrate," *J. Mater. Res.*, Vol. 26, pp. 1653–1661.

17. Michael F. Ashby and David R. H. Jones, *Engineering Materials 1 an introduction to their properties and applications*, 2nd ed. Oxford, UK: Butterworth-Heinemann, 2002.

Chapter 4

4   Plastic Deformation of Gold Microspheres

In this chapter size and strain rate dependence of plastic deformation of Au microspheres was investigated at room-temperature using micro-compression testing. The contact yield stress was observed to increase from 210 MPa for 6.0 µm to 865 MPa for 0.8 µm diameter spheres. The apparent activation volume, V^*, associated with the rate dependent plastic deformation remained constant at $4 - 6b^3$ for 0.8 and 1.0 µm spheres over strains up to 20% whereas it displayed an increasing trend from $12 - 42b^3$ for 3.0 and 6.0 µm diameter specimens. These findings suggest that the operative deformation mechanism was dependent upon the diameter of the sphere. Our test data suggest that the larger spheres deformed by a mechanism of dislocation-obstacle limited glide whereas, the smaller spheres deformed by a dislocation-starvation mechanism.

4.1 Introduction

Nano-/micro electro-mechanical systems (NEMS/MEMS) are being used in many sophisticated applications such as in bio-medical and microelectronics devices. For the development of these advanced systems, constituting materials are used in small volumes. Therefore, understanding mechanical behavior of samples with very small volumes is absolutely necessary in order to realize the full potential of these emerging nano-/micro-technologies [1]. In particular, the use of microspherical particles is being explored as drug delivery systems in biomedical applications [2]. Additionally, these structures are of wide interest in nanotechnology because of their potential use in the fabrication of nano-scale electrical devices, such as transistors and resistors [3]. Information about their mechanical properties and deformation mechanisms is essential to understanding their performance during manufacturing, processing and end-user applications.

The topic of mechanical behavior of materials in small volumes has been of tremendous interest to the scientific community for over the past few decades [4]. In bulk form, the yield stress and strength of the material remain essentially independent of the sample size because the sample dimensions are large compared to the length scale characterizing the material's microstructure. However, when the critical dimensions of a device approach the size of the material's microstructure a size effect prevails and the bulk properties can no longer be used to predict mechanical behavior [5].

In initial studies, the measured hardness of common materials displays an inverse dependence upon the indentation depth and this was explained in terms of hardening associated with the formation of geometrical necessary dislocations (GNDs) to accommodate the large strain gradients imposed by the nanoindentation process [6,7].

Recently, micro-compression tests on focused ion beam (FIB) machined nano- and micro-pillars have shown that single crystalline metals containing dislocations also display size dependent yield stress even in the absence of strain gradients [5,6,8–10]. These high strengths were associated with the dislocation starved conditions that prevail in small volumes, causing the operative deformation mechanism to be limited solely by the dislocation nucleation process at the sample surface rather than dislocation-obstacle interactions within the sample. While all of these studies are consistent with the tenet that smaller is stronger, a unified plasticity mechanism encompassing all deformation length scales has yet to be established [1,11].

In this work, we have investigated the size and strain rate dependence of the mechanical behavior of metallic microspheres. For this purpose, Gold (Au) spheres of four sizes (0.8 to 6.0 µm diameters) were fabricated and micro-compression tests were performed at different loading rates. FE analysis was performed to estimate the stress-strain distribution within the compressed microspheres. Finally, the strain rate dependence of the estimated flow stress of the different size microspheres was investigated to determine the operative deformation mechanism.

4.2 Materials and Methods

4.2.1 Sample Preparation

(a)

a. Spin coat electron sensitive polymer resist (A8 PMMA)

b. Expose the polymer with an electron beam

c. Develop exposed polymer

d. Deposit Au thin film (e-beam evaporation)

e. Lift-off remaining resist (PG remover)

f. Annealing at 1000°C

(b)
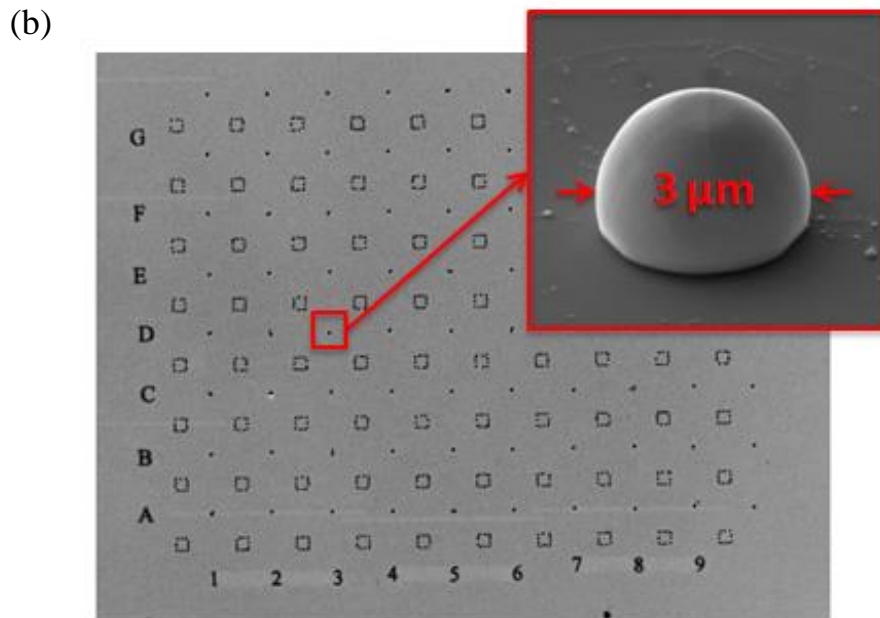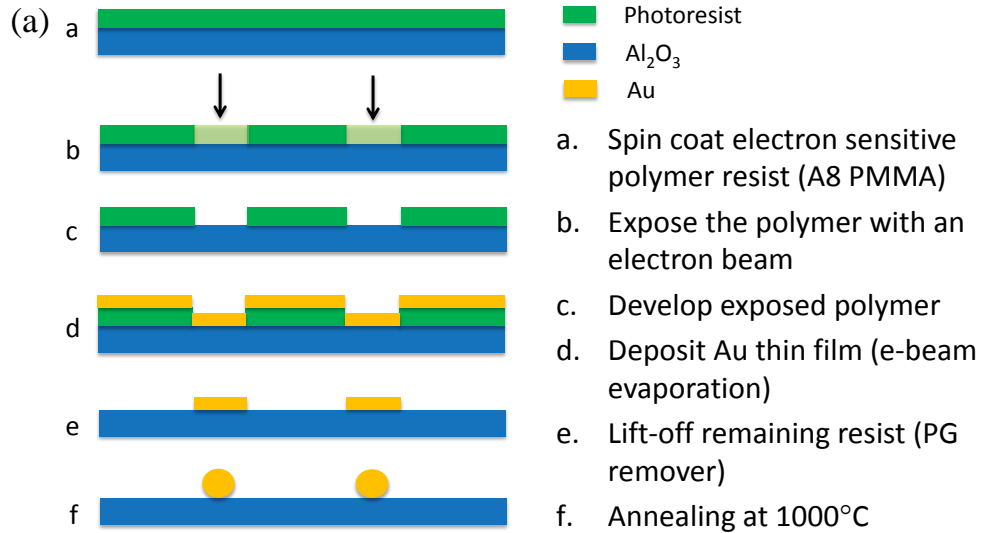
Figure 4.1: (a) Schematic diagram showing the steps used to fabricate Au microspheres and (b) the fabricated Au microspheres are equidistant from each other, therefore no mechanical manipulator is needed to isolate them for compression testing.

Gold microspheres were fabricated on a (0001)-oriented sapphire (α-Al_2O_3) surface. An A8 PMMA positive photoresist layer was spin-coated on the O_2 plasma cleaned sapphire surface and e-beam lithography was used to project a grid of 1.5 to 12.0 µm diameter circles upon the photoresist. After the exposed photoresist was removed, a polycrystalline Au film of 100 to 600 nm thickness was deposited by e-beam evaporation. The remaining photoresist was then removed and the resulting Au cylinders, of 1.5 to 12.0 µm diameter and 0.1 to 0.6 µm height, were annealed in-vacuum at 1000°C (Figure 4.1). During annealing the Au de-wetted from the sapphire substrate and took the form of facetted single-crystal spheres of 0.8 to 6.0 µm diameter (Figure 4.2). The facets were {111} close packed planes [12–14]. About 100 Au microspheres were fabricated for each diameter. As the sapphire substrate is nonconductive, and the fabricated microspheres were not connected to each other, a 10 − 15 nm thick layer of Cr was deposited on the microsphere pattern surface to improve the SEM imaging. Post-imaging, Cr layer was removed with Hydrofluoric (HF) acid to perform compression tests on the microspheres. Similarly, the deformed microspheres were imaged by depositing 10 − 15 nm thick layer of Cr.

4.2.2 Microsphere Compression

The Au microspheres were compressed with an instrumented NanoTest platform by Micro Materials Ltd (Wrexham, UK) fitted with a 9 µm diameter diamond flat punch indenter. About 60 compression tests were performed for four different sized spheres. The compression tests were carried out by loading the indenter at a constant loading rate to a maximum depth of about 20% of the initial sphere diameter. The loading rates, ranged from 0.01 to 1.00 mN/sec, and were used to study the strain rate dependence of plastic deformation of the spheres.
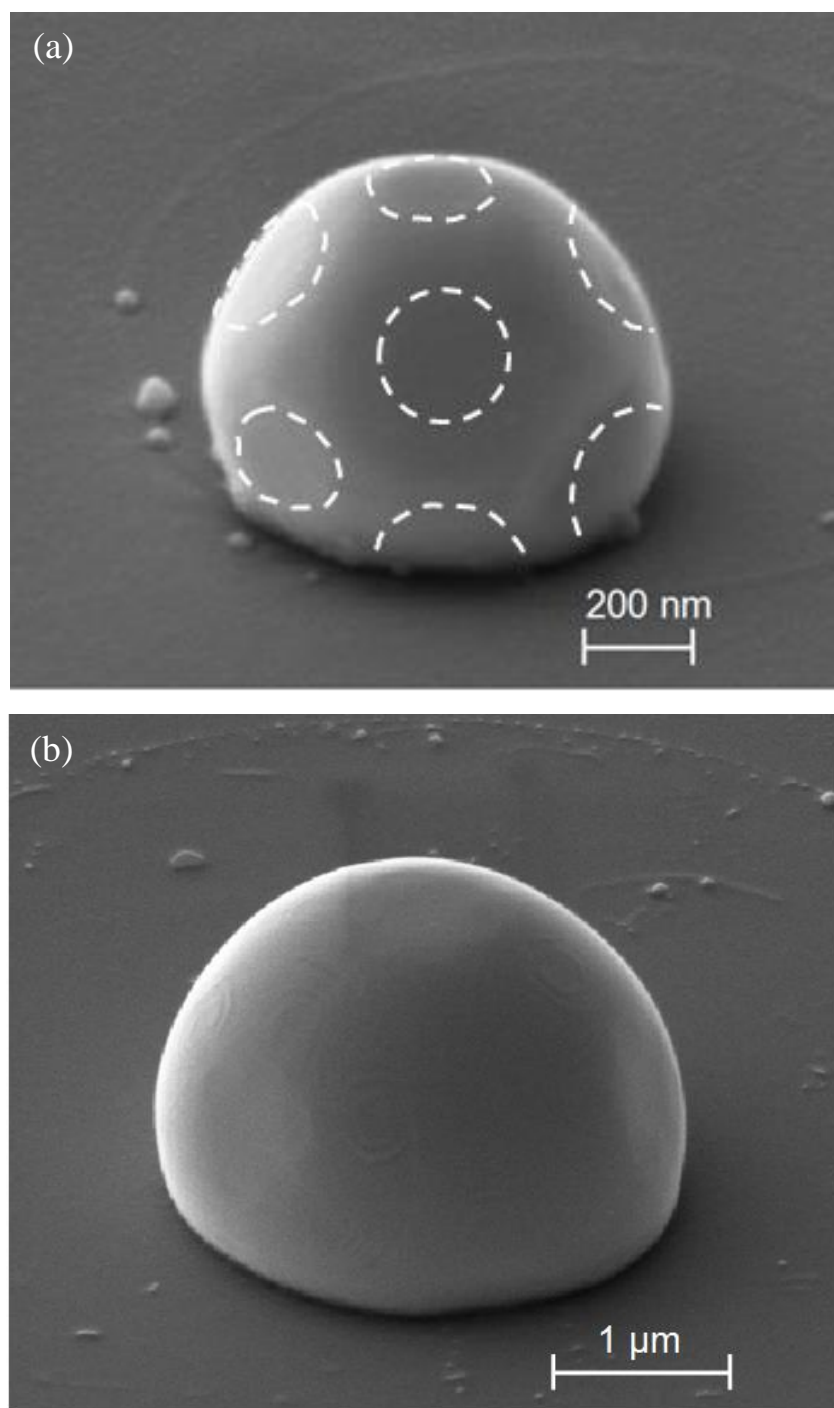
Figure 4.2: SEM images of as fabricated (a) 0.8 and (b) 3.0 µm diameter Au microspheres. Facets are marked by white dotted lines in the image (a).

4.2.3 Finite Element Simulations

FE simulations of the microsphere compression were performed using the mesh shown in Figure 4.3. The shape and dimension of the microsphere were obtained from measurements made from SEM images. In the simulation, the flat-punch indenter and the substrate were assumed to be analytical rigid and frictionless. The microsphere was meshed with 4-node linear axisymmetric quadrilateral elements.

R (μm)	A (μm)	B (μm)	C (μm)
0.38	0.10	0.36	0.33
0.50	0.13	0.48	0.43
1.50	0.45	1.42	1.30
3.00	0.45	2.98	2.60
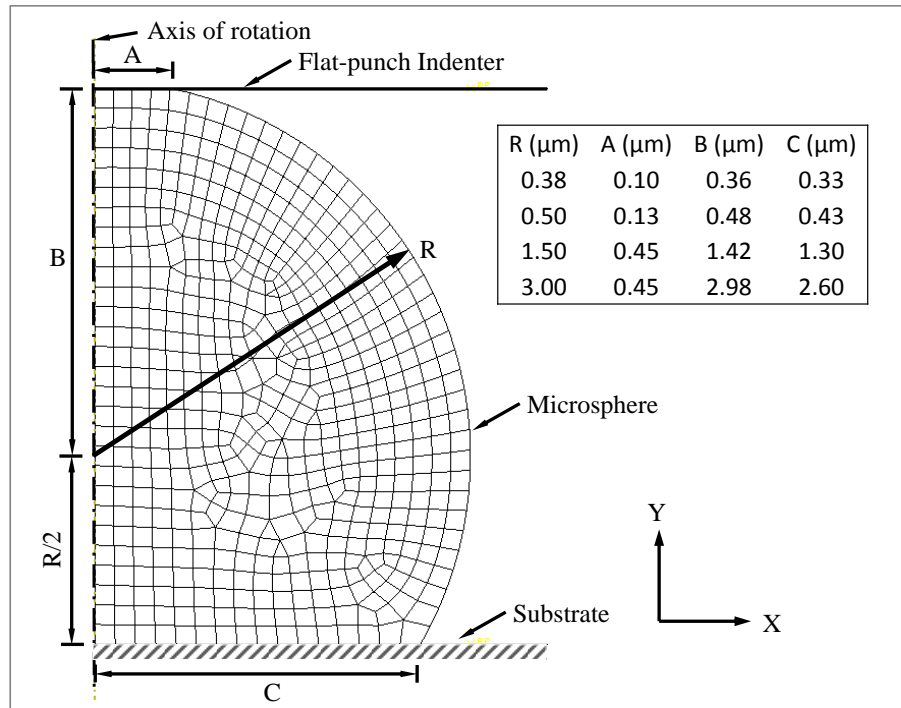
Figure 4.3: Schematic representation of the FE mesh used in this study. The dimension of the different Au microspheres analyzed is shown in the insets.

The compression process was simulated by imposing downward displacement of the nodes at the flat punch/sphere interface (Region A in Figure 4.3). All simulations were performed by defining multiple analysis steps. Isotropic elastic properties of the gold, Young's Modulus, $E = 79$ GPa [15] and Poisson's ratio, $\nu = 0.42$ [16], were used. The force-depth response obtained from the simulation (Figure 4.4) was matched with the experimental force-depth response curve for the tested microspheres, by adjusting the multi-linear rate-dependent isotropic plastic flow properties of Au in the FE model [17].

In total, 12 models were created for four different diameter microspheres (0.8 to 6.0 µm) compressed at three loading-rates.
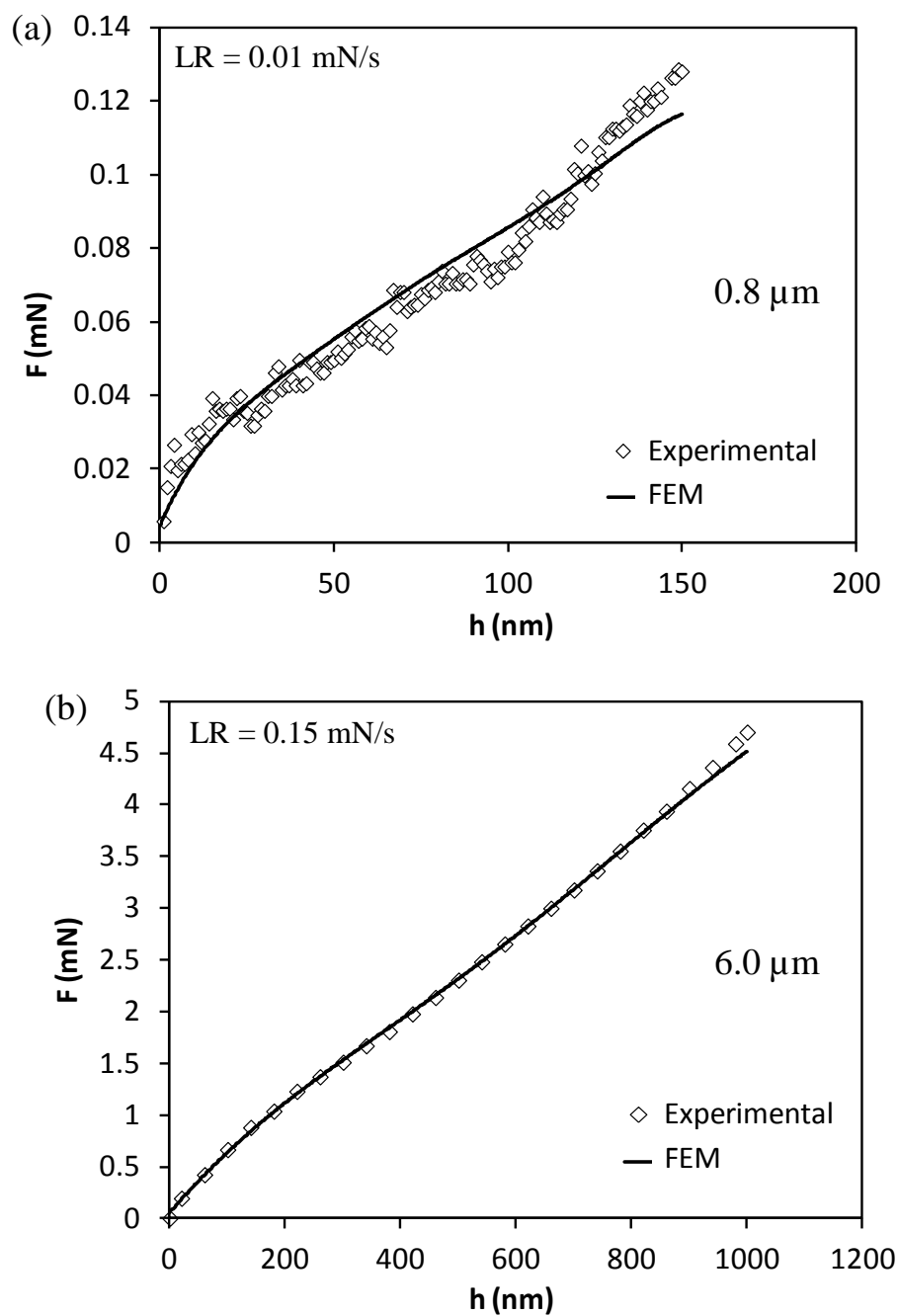
Figure 4.4: FE simulated *F-h* curves matched with experiment *F-h* curves: (a) 0.8 and (b) 6.0 µm Au spheres.

4.3 Results

4.3.1 Experimental Micro-compression Tests

Figure 4.5 shows the experimental force-displacement (F-h) curves for the smaller, 0.8 and 1.0 µm, and larger, 3.0 and 6.0 µm, diameter microspheres compressed at loading rates of 0.01 to 1.0 mN/sec. The deformation force F of the small 0.8 µm diameter spheres shows a strong dependence upon the loading rate.

Besides loading rate dependence, discrete load jumps in the F-h curves were observed for the tested spheres and the frequency of these jumps increased with decreasing sphere diameter.

Similar load-jump features were previously reported in nanoindentation and nano-/micro-pillar compression studies and were associated with the initiation of dislocation nucleation/avalanche events in nano-sized crystalline samples [1,4,5,10–14]. SEM images of the deformed 3.0 and 6.0 µm diameter spheres are shown in Figure 4.6. Multiple slips lines corresponding to {111}<110> slip systems can be seen.

(a) 0.8 μm

(b) 1.0 μm
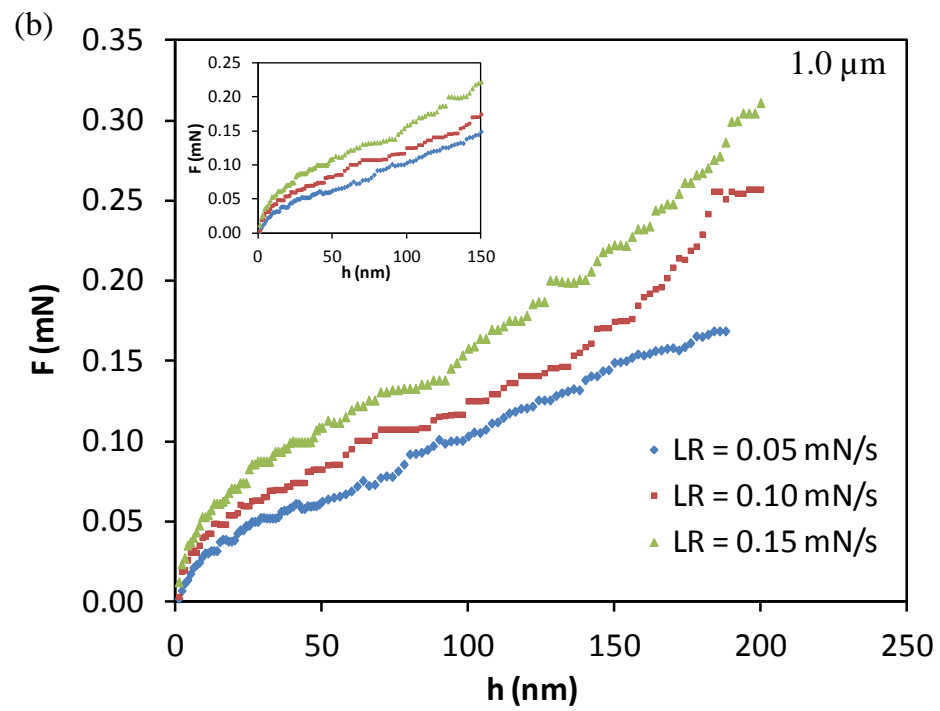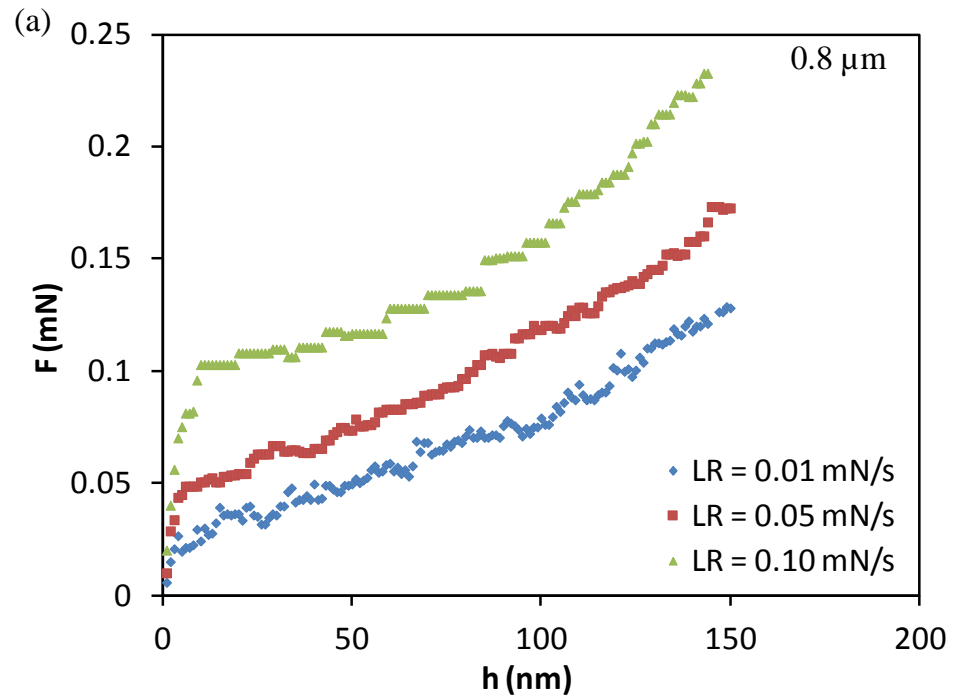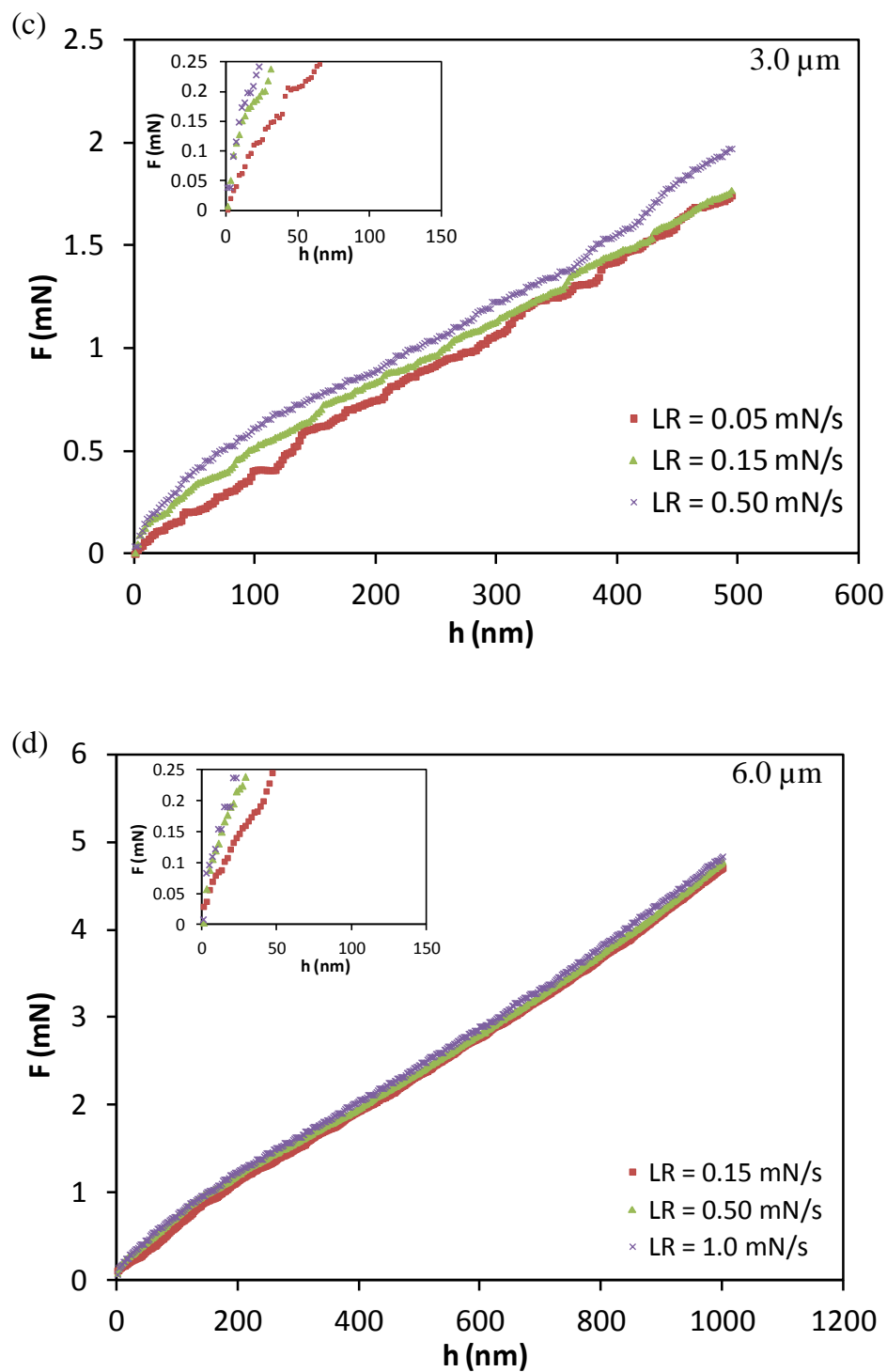
Figure 4.5: Experimentally obtained force, *F* versus displacement, *h* response for (a) 0.8, (b) 1.0, (c) 3.0 and (d) 6.0 µm Au microspheres loaded at three different rates. The insets are the initial part of the *F-h* curve at the same scale as Fig. 4.5a.
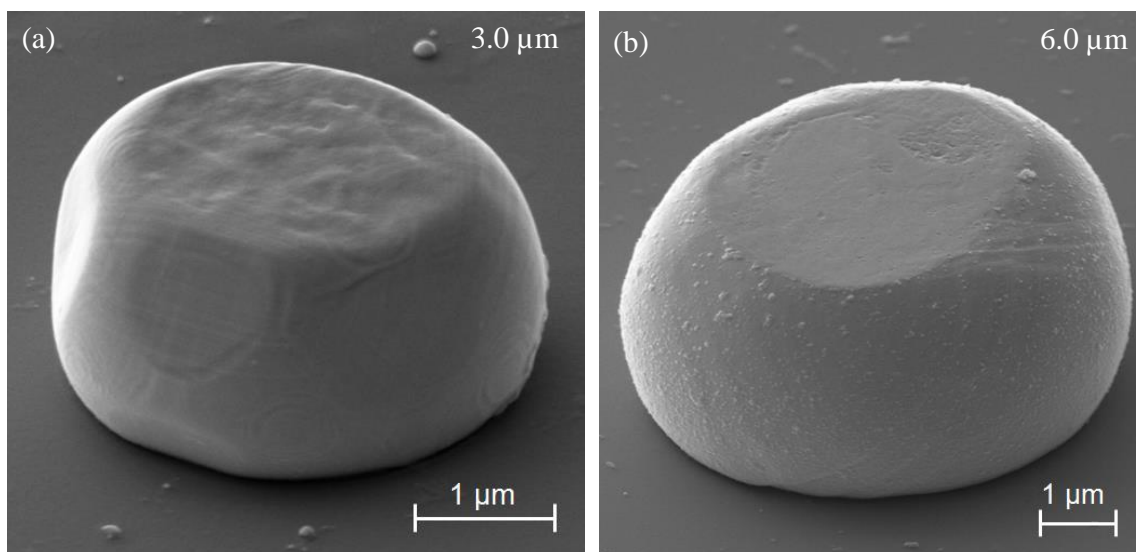
Figure 4.6: Compressed microspheres (a) 3.0 and (b) 6.0 µm. In these images, multiple slips lines corresponding to {111}<110> slip systems are visible.

The apparent contact stress corresponding to the start of plastic yielding of the Au microspheres was expressed as the initial yielding force divided by the area of the {111} facet at the top of the sphere upon which the flat-punch indenter contacted. In this way the maximum contact stress of the smallest, 0.8 µm, diameter sphere was estimated to be between 670 MPa and 2 GPa while the largest, 6.0 µm, diameter sphere was between 210 and 350 MPa over the three loading rates tested.

Bei et al. [18] have shown that surface damage from the FIB milling pillars can affect the response of a compressed structure, and will minimize displacements bursts during its testing. The microspheres tested in this study show the true response of the materials since they are fully annealed monocrystalline samples made without the use of ion milling.

4.3.2 Stress-Strain Curve from FE Simulation

The stress-strain distribution in the compressed spheres was analyzed using FE simulations. The von Mises stress-strain data were collected for each load-depth increment from the nodes along the axis of rotation of the FE model of the microsphere. The distribution of the von Mises equivalent stress and strain along the axis of rotation during plastic deformation at highest loading rates is plotted in Figure 4.7.

The average von Mises stress-strain data, collected from the nodes along the axis of symmetry of the model, were recorded for each load-depth increment. Figure 4.8 shows the average von Mises stress versus von Mises strain curves for the 0.8, 1.0, 3.0 and 6.0 µm diameter microspheres compressed at the three loading rates. The yield stress increases with increasing loading rates for all size microspheres; however, the yield stress of the smallest spheres displayed significantly greater loading rate dependence. The von Mises stress values, corresponding to 20% von Mises strain, for 0.8 µm spheres increased from 275 to 425 MPa with increasing loading rate from 0.01 to 0.10 mN/s whereas for largest 6.0 µm diameter spheres they increased from 215 to 225 MPa. These data indicate that the strain rate dependence of yield stress is increased with decreasing sphere diameter.
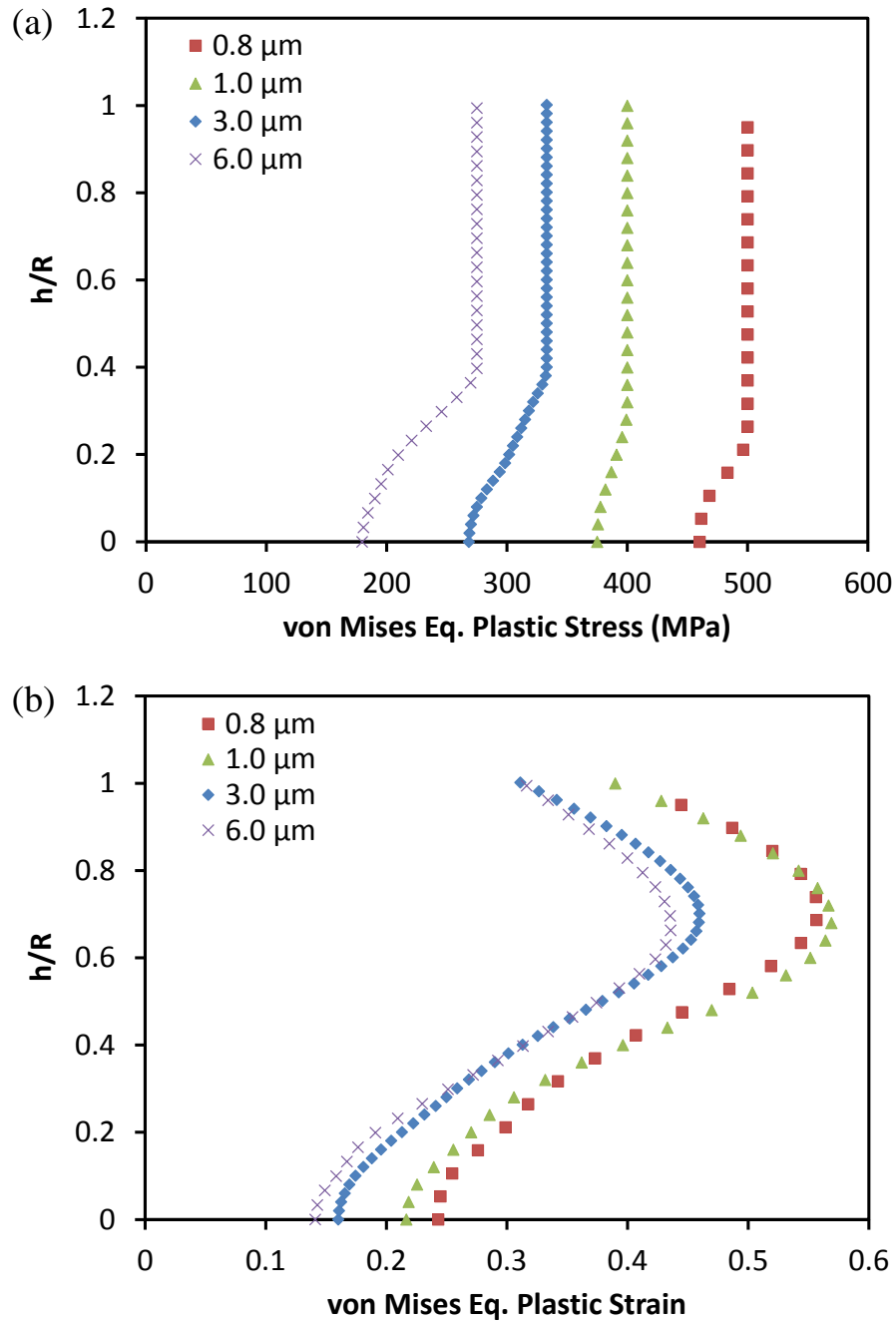
Figure 4.7: von Mises equivalent plastic, (a) stress and (b) strain distribution at the highest loading rates of the Au microspheres during micro-compression. In these plots, *h/R* is the normalized distance along the axis of rotation of the sphere during compression, *h* is the deformed sphere depth and *R* is the sphere radius (Figure 4.3).

(a) 0.8 μm

LR = 0.01 mN/s
LR = 0.05 mN/s
LR = 0.10 mN/s

(b) 1.0 μm

LR = 0.05 mN/s
LR = 0.10 mN/s
LR = 0.15 mN/s
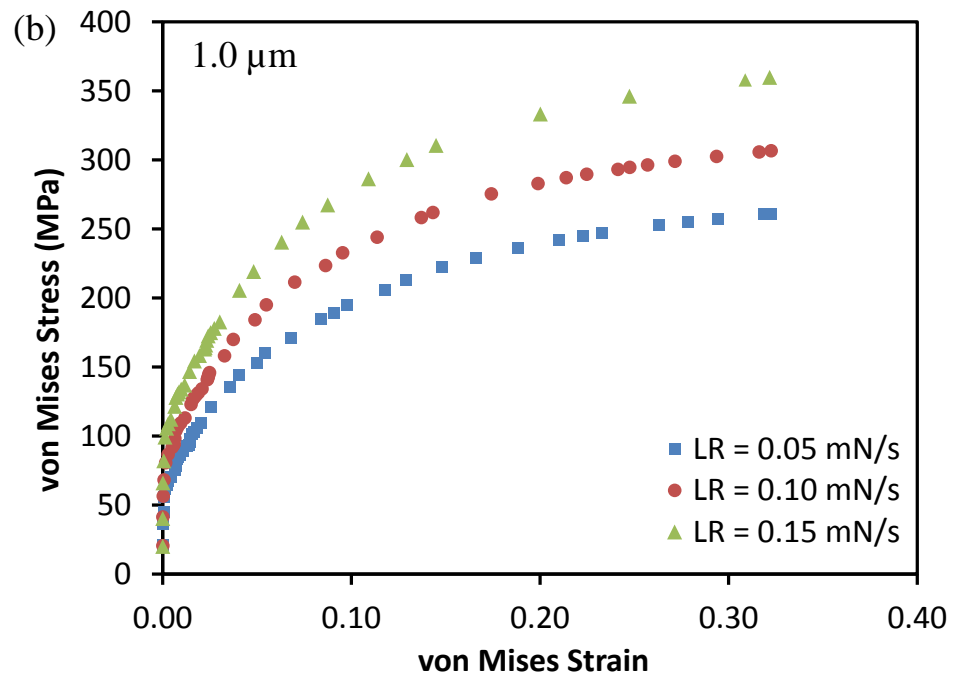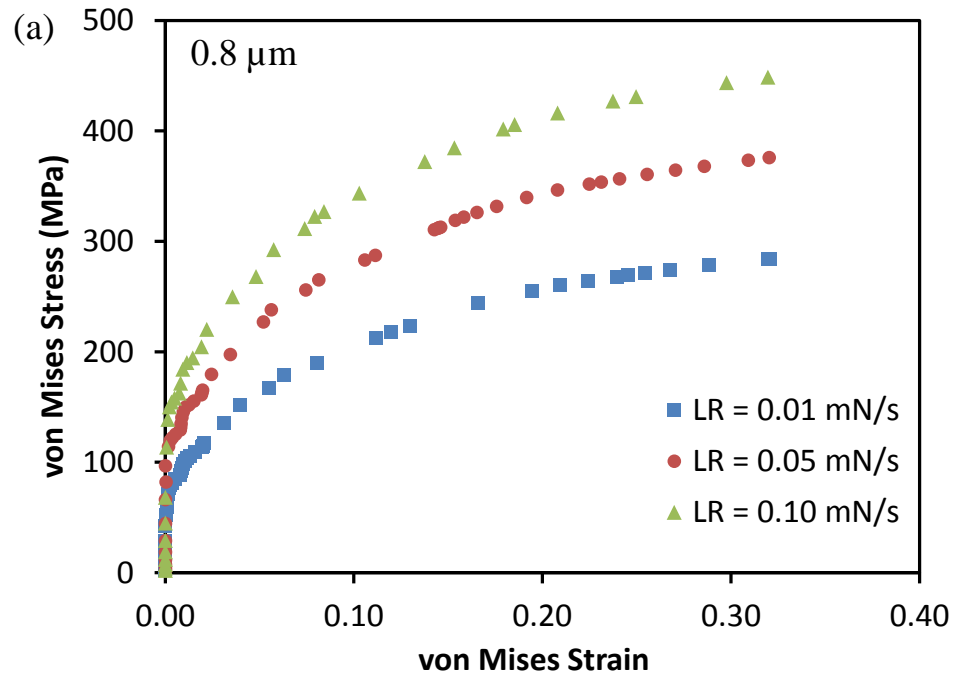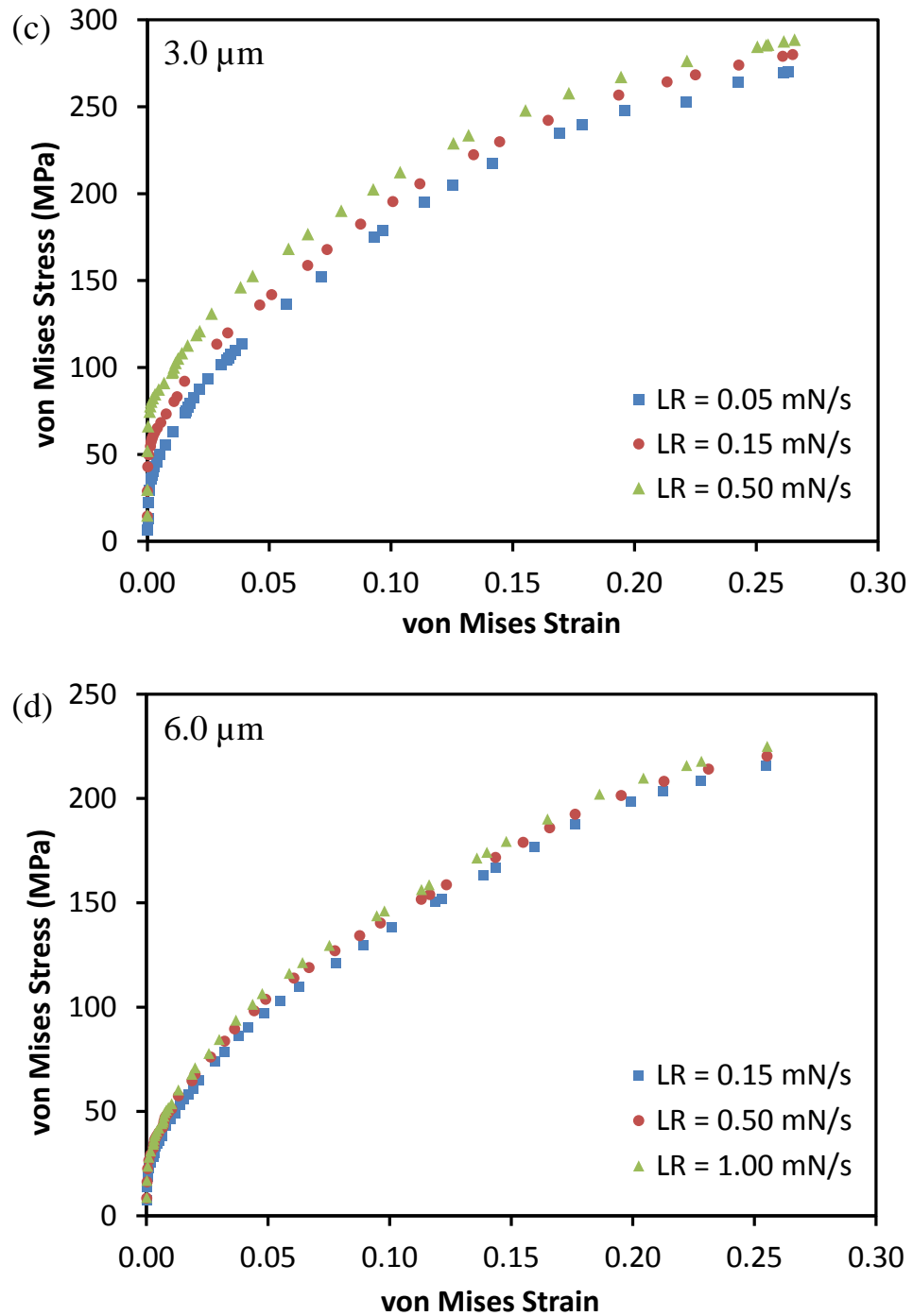
Figure 4.8: von Mises stress verses strain responses for the (a) 0.8, (b) 1.0, (c) 3.0 and (d) 6.0 μm diameter Au microspheres obtained from FE analyses performed at three loading rates.

4.4 Discussion

Besides enhanced strain rate sensitivity with decreasing sphere size it is clear from Figure 4.8 that, for a particular strain and strain rate, small diameter spheres display a higher flow stress than large diameter spheres and this is consistent with previously reported length scale-dependence of plasticity [1,4,5,8,9,11]. The strain, strain rate, and temperature dependence of the flow stress σ of plastically deforming metals is often described in terms of the following Arrhenius relationship [19];

$$\sigma = A\varepsilon^n \dot{\varepsilon}^m exp\left[-\frac{Q}{RT}\right] \tag{4.1}$$

where ε is strain, $\dot{\varepsilon}$ is strain rate, A is a material constant, n is the strain hardening exponent, m is the strain rate sensitivity, Q is the activation energy, T is the absolute temperature and R is the universal gas constant.

Figure 4.9a shows the strain dependence of the flow stress at strain rates of $3.9*10^{-2}$ sec^{-1}, $1.4*10^{-1}$ sec^{-1} and $2.6*10^{-1}$ sec^{-1} at 295k for 0.8 µm diameter spheres. The calculated values of n are 0.30, 0.27, and 0.26 respectively. These values of n are significantly less than those of the larger 6.0 µm diameter spheres (Figure 4.9c)

For 0.8 µm diameter microspheres, the calculated values of the strain rate sensitivity m, corresponding to four constant ε values of 0.05, 0.10, 0.15, 0.20, were 0.30, 0.28, 0.26, and 0.24 (Figure 4.9b). Which was considerably more than the m values for the 6.0 µm diameter microspheres (Figure 4.9d).
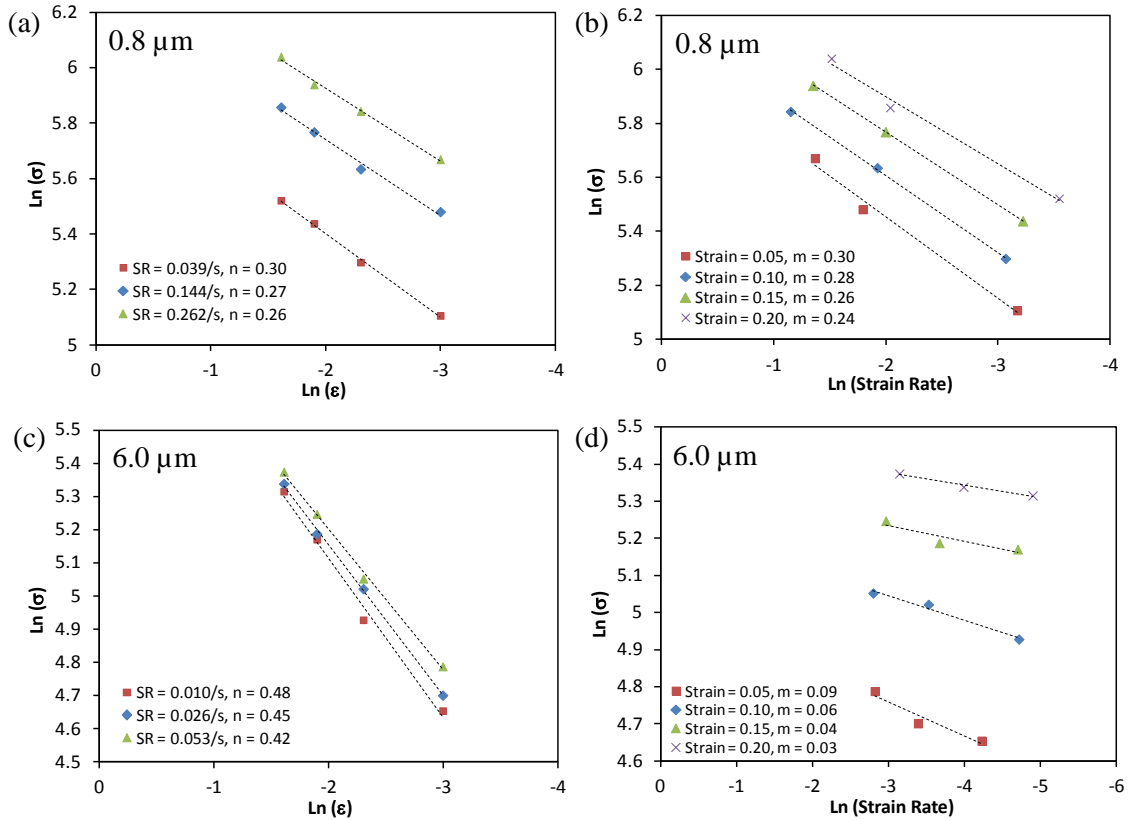
Figure 4.9: (a) and (c) Log (σ) vs. Log (ε) plots showing the effect of strain rate on *n* and (b) and (d) Log (σ) vs. Log (strain rate) plots showing the effect of strain on *m* for 0.8 and 6.0 µm Au spheres.

Figure 4.10 shows *n* (plotted against $\dot{\varepsilon}$) and *m* (plotted against ε) for all the microsphere diameters tested in this study. The strain-hardening exponent *n* for the larger, 6.0 and 3.0 µm diameter spheres ranged between 0.40 – 0.50 and showed clear strain rate dependence. These values are consistent with those reported in the literature for bulk soft *FCC* metals [19]. The calculated *n* values for the smaller (0.8 to 1.0 µm) diameter Au microspheres were, however, lower, approximately 0.3, and were significantly less dependent upon the strain rate. These noticeable differences between the smaller and larger diameter spheres indicate that the smaller spheres deform differently than the larger spheres, which undergo plastic deformation similar to bulk metals.
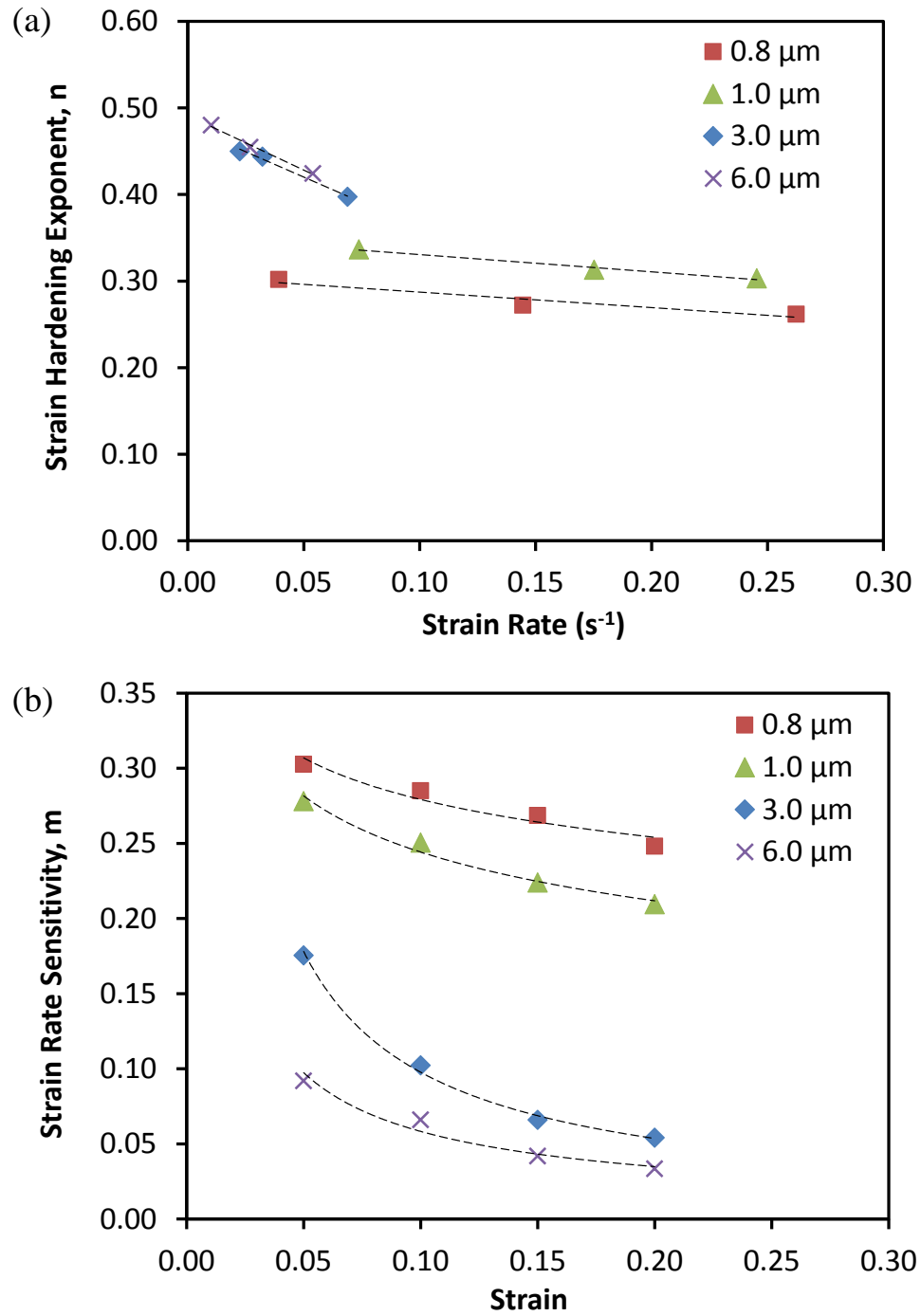
Figure 4.10: (a) Strain hardening exponent, *n* and (b) Strain rate sensitivity, *m* for all diameters Au microspheres tested in this study.

The values of *m*, Figure 4.10b, increased with decreasing sphere diameter indicating that the flow stress becomes more strain rate-sensitive in the smaller diameter sphere. For the 6.0 µm diameter sphere, *m* decreased from 0.08 to 0.03 as the ε increased from 0.05 to 0.20. The *m* value of 0.03 is typical of bulk *FCC* metals [20]. This is another indication that the large diameter Au microspheres deformed in a manner similar to bulk Au. The smaller diameter spheres (0.8 – 1.0 µm) displayed significantly higher *m* value ranging between 0.2 – 0.3.

The strain rate dependence of the deformation behavior sheds light on the operative deformation mechanism. Some recent attempts have been made to characterize the length scale dependence of the strain rate sensitivity of the flow stress of nanocrystalline Ni. In these studies it was observed that nanocrystalline Ni, displayed higher strain rate sensitivity than normal Ni [21]. A notable effect of both strain rate and sample size on the compressive strength of single crystalline Cu nanostructures was also reported by Jennings et al., they observed that smallest diameter (125 nm) Cu nanostructure displayed, a flow stress with a clear strain rate sensitivity arising from the operation of thermally-activated surface dislocation sources [22].

In pure metals, such as Au samples studied here, mobile dislocations are frequently obstructed by various obstacles, such as point defects and other dislocations and these barriers are overcome by thermal activation. The strength for impeding dislocation glide is characterized by their apparent activation volume, V^* [23,24].

In the deformation of small volume samples, such as our 0.8 µm diameter Au spheres, dislocation nucleation from the sample surface is very likely to contribute significantly to the deformation process and thus affect the measured activation volume. Atomistic simulations have predicted dislocation nucleation from free surfaces has an apparent activation volume of $1\sim10b^3$ which would result in a significant thermal contribution to the source's strength [25]. Dislocation cross-slip in conventional crossed grained *FCC* materials has a broad range of activation volumes $\sim10\sim100b^3$ [26]. The operation of Fank-Read dislocation sources, whose activation volume is relatively large, $\sim100\sim1000b^3$, would make an almost negligible thermal contribution to its strength [24].

Because of their different thermal activation characteristics, the variation of activation volumes between the two mechanisms, dislocation of nucleations from surfaces and dislocation nucleation from internal Frank-Read sources, should show considerably different strain rate dependence. Surface dislocation nucleation mechanism is highly strain rate dependent while dislocation nucleation from internal Frank-Read sources will have minimal strain rate dependence [22].

Using the strain rate sensitivity values m, V^* can be calculated using the following equation [27–29];

$$V^* = \sqrt{3}kT/m\sigma \qquad (4.2)$$

Where σ is the applied stress, k is the Boltzmann constant and T is the absolute temperature. Using the above relationship, the strain dependence of estimated activation volumes of all Au microspheres is illustrated in Figure 4.11.
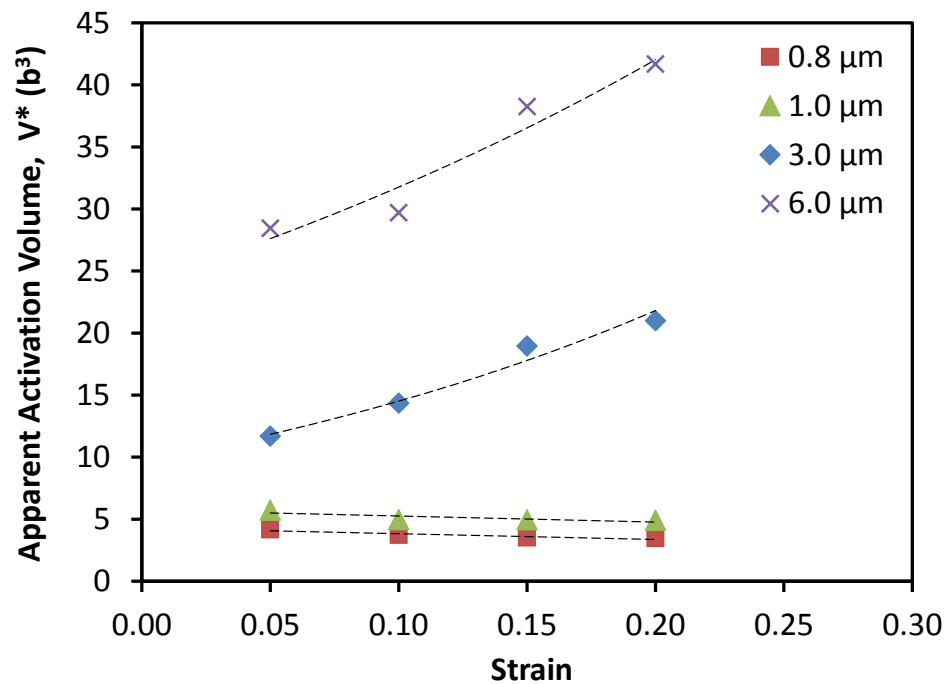
Figure 4.11: Apparent activation volume V^* plotted as a function of strain for the different diameter Au microspheres.

The obtained V^* values were converted to parameters of apparent activation energy Q^*, necessary for a dislocation to overcome the obstacles that impede its movement through the sample using the relation, $Q^* = \tau_{0K}V^*$ [30], (Table 4.1). In order to estimate the total athermal apparent activation energy, Q^* ($\tau_{0K}.V^*$), of deformation rate controlling obstacles, athermal stress, $\tau_{0K} = 256$ MPa was used [31]. When the strain increased from 5 to 20%, the estimated athermal Q^* value ranged between 0.16 to 0.14 eV for 0.8 µm sphere, and 1.10 to 1.61 eV for 6.0 µm sphere. In the case when $Q^* \sim 0.2$ eV, dislocation obstacle strength is weak and dislocation glide is essentially controlled by the lattice resistance [31]. This is observed for our small diameter Au spheres (Table 4.1). For the larger diameter spheres, Q^* is between 1 to 2 eV which suggests that deformation is controlled by a mechanism of obstacle-limited dislocation glide [31]. In the case of the larger diameter Au spheres in this study, the internal obstacles to dislocation glide will be dislocation-dislocation interactions.

Table 4.1: The estimated apparent activation energy during Au sphere deformation.

Sphere Size	Apparent activation energy, Q^* in eV at different level of strain			
(µm)	5%	10%	15%	20%
0.8	0.16	0.14	0.14	0.14
1.0	0.22	0.19	0.19	0.19
3.0	0.45	0.55	0.73	0.81
6.0	1.10	1.15	1.47	1.61

Figure 4.11 shows the calculated V^* versus strain for the Au microspheres in this study. The plotted V^* are normalized with respect to b^3, where the Burgers vector of Au is taken as $b = 0.289$ nm [32,33]. The V^* remained independent of strain during compression, with approximately a constant value of $4 - 6b^3$, for the smaller diameter, 0.8 and 1.0 µm, spheres whereas, for larger diameter, 3.0 and 6.0 µm spheres, the estimated V^* increased from $12 - 42b^3$, with increasing strain. The low V^* values, $4 - 6b^3$, for the smaller diameter spheres in this work are similar to previously reported estimates for *FCC* metals by Mook and Gerberich [34], and are characteristic of dislocation nucleation events during plastic deformation. These findings are also consistent with frequent discrete load

jumps that were observed in the *F-h* curves for 0.8 and 1.0 µm spheres (Figure 4.4a–b) and suggest that plastic deformation for these smaller diameter spheres is controlled by a dislocation nucleation mechanism. This notion is further supported by high contact stress estimations (~ 865MPa) for the smaller spheres. These contact stress values are close in magnitude to the calculated ideal shear strength for Au (~ 800MPa) [35]. On the other hand, the larger, 3.0 and 6.0 µm, diameter spheres displayed smoother *F-h* curves (Figure 4.4c–d) and deformed at much lower contact stresses (340 − 210 MPa). Also, the *V** magnitude (12 − 42b^3) and its tendency to increase with increasing strain are typical of the operation of a dislocation-obstacle interaction limited deformation mechanism which is common in bulk ductile metals [23].

4.5 Conclusions

In this study the dependence of the plastic deformation of Au microspheres upon sphere diameter (0.8 − 6.0 µm) and strain rate at ambient temperature is investigated using micro-compression testing. Our study observed that the dependence of flow stress upon both strain and strain rate was lightly dependent upon the diameter of the Au microspheres. Analysis of the apparent activation volume, *V** and energy *Q** of the deformation process indicated that the operative deformation mechanism, for the small 0.8 − 1.0 µm diameter spheres was typical of a mechanism limited by the surface nucleation of dislocation, and for larger 3.0 − 6.0 µm diameter spheres was controlled by the dislocation-obstacle interaction limited mechanism, which is typical for bulk *FCC* metals. These findings are particularly important in case of emerging nano/micro-technologies, making use of materials at ever decreasing scales.

The next chapter of this thesis will present the kinetics of size and strain rate dependence of incipient plastic deformation of these small size Au microspheres.

References

1. W. D. Nix, J. R. Greer, G. Feng, and E. T. Lilleodden, Feb. 2007, "Deformation at the nanometer and micrometer length scales: Effects of strain gradients and dislocation starvation," *Thin Solid Films*, Vol. 515, pp. 3152–3157.

2. K. Park, Jul. 2007, "Nanotechnology: What it can do for drug delivery.," *J. Control. Release*, Vol. 120, pp. 1–3.

3. M. L. B. Palacio and B. Bhushan, Apr. 2013, "Depth-sensing indentation of nanomaterials and nanostructures," *Mater. Charact.*, Vol. 78, pp. 1–20.

4. W. M. Mook, C. Niederberger, M. Bechelany, L. Philippe, and J. Michler, Feb. 2010, "Compression of freestanding gold nanostructures: from stochastic yield to predictable flow," *Nanotechnology*, Vol. 21, pp. 055701–9.

5. J. Greer, 2006, "Bridging the gap between computational and experimental length scales: a review on nano-scale plasticity," *Rev. Adv. Mater. Sci*, Vol. 13, pp. 59–70.

6. W. Nix and H. Gao, 1998, "Indentation size effects in crystalline materials: a law for strain gradient plasticity," *J. Mech. Phys. Solids*, Vol. 46, pp. 411–425.

7. K. W. McElhaney, J. J. Vlassak, and W. D. Nix, Jan. 1998, "Determination of indenter tip geometry and indentation contact area for depth-sensing indentation experiments," *J. Mater. Res.*, Vol. 13, pp. 1300–1306.

8. J. R. Greer, W. C. Oliver, and W. D. Nix, Apr. 2005, "Size dependence of mechanical properties of gold at the micron scale in the absence of strain gradients," *Acta Mater.*, Vol. 53, pp. 1821–1830.

9. J. R. Greer, C. R. Weinberger, and W. Cai, Oct. 2008, "Comparing the strength of f.c.c. and b.c.c. sub-micrometer pillars: Compression experiments and dislocation dynamics simulations," *Mater. Sci. Eng. A*, Vol. 493, pp. 21–25.

10. A. S. Schneider, B. G. Clark, C. P. Frick, P. a. Gruber, and E. Arzt, May 2009, "Effect of orientation and loading rate on compression behavior of small-scale Mo pillars," *Mater. Sci. Eng. A*, Vol. 508, pp. 241–246.

11. C. P. Frick, B. G. Clark, S. Orso, a. S. Schneider, and E. Arzt, Aug. 2008, "Size effect on strength and strain hardening of small-scale [111] nickel compression pillars," *Mater. Sci. Eng. A*, Vol. 489, pp. 319–329.

12. D. Mordehai, S.-W. Lee, B. Backes, D. J. Srolovitz, W. D. Nix, and E. Rabkin, Aug. 2011, "Size effect in compression of single-crystal gold microparticles," *Acta Mater.*, Vol. 59, pp. 5202–5215.

13. D. Mordehai, M. Kazakevich, D. J. Srolovitz, and E. Rabkin, Apr. 2011, "Nanoindentation size effect in single-crystal nanoparticles and thin films: A comparative experimental and simulation study," *Acta Mater.*, Vol. 59, pp. 2309–2321.

14. S.-W. Lee, D. Mordehai, E. Rabkin, and W. D. Nix, Jul. 2011, "Effects of focused-ion-beam irradiation and prestraining on the mechanical properties of FCC Au microparticles on a sapphire substrate," *J. Mater. Res.*, Vol. 26, pp. 1653–1661.

15. C. A. Volkert and E. T. Lilleodden, Nov. 2006, "Size effects in the deformation of sub-micron Au columns," *Philos. Mag.*, Vol. 86, pp. 5567–5579.

16. D. Maharaj and B. Bhushan, 2014, "Nanomanipulation, nanotribology and nanomechanics of Au nanorods in dry and liquid environments using an AFM and depth sensing nanoindenter," *Nanoscale*, Vol. 6, p. 5838.

17. R. F. Gibson, H.-K. Jang, S. Simkhada, Q. Yu, H.-I. Kim, and J. Suhr, 2014, "Use of Nanoindentation, Finite Element Simulations, and a Combined Experimental/Numerical Approach to Characterize Elastic Moduli of Individual Porous Silica Particles," *Part. Sci. Technol.*, Vol. 6351, pp. 213–218.

18. H. Bei, S. Shim, G. M. Pharr, and E. P. George, Oct. 2008, "Effects of pre-strain on the compressive stress–strain response of Mo-alloy single-crystal micropillars," *Acta Mater.*, Vol. 56, pp. 4762–4770.

19. R. W. Cahn, *Strengthening Methods in Crystals*, Vol. 17. Halstead Press Division, Wiley, 1972.

20. M. Dao, L. Lu, Y. F. Shen, and S. Suresh, Dec. 2006, "Strength, strain-rate sensitivity and ductility of copper with nanoscale twins," *Acta Mater.*, Vol. 54, pp. 5421–5432.

21. Y. M. Wang, A. V. Hamza, and E. Ma, 2005, "Activation volume and density of mobile dislocations in plastically deforming nanocrystalline Ni," *Appl. Phys. Lett.*, Vol. 86, p. 241917.

22. A. T. Jennings, J. Li, and J. R. Greer, Aug. 2011, "Emergence of strain-rate sensitivity in Cu nanopillars: Transition from dislocation multiplication to dislocation nucleation," *Acta Mater.*, Vol. 59, pp. 5627–5637.

23. U. F. Kocks, a. S. Argon, and M. F. Ashby, Jan. 1975, "Thermodynamics and Kinetics of Slip," *Prog. Mater. Sci.*, Vol. 19.

24. T. Zhu and J. Li, Sep. 2010, "Ultra-strength materials," *Prog. Mater. Sci.*, Vol. 55, pp. 710–757.

25. T. Zhu, J. Li, A. Samanta, A. Leach, and K. Gall, 2008, "Temperature and strain-rate dependence of surface dislocation nucleation," *Phys. Rev. Lett.*, Vol. 100, p. 25502.

26. P. Rodriguez, 2004, "Grain size dependence of the activation parameters for plastic deformation: Influence of crystal structure, slip system, and rate-controlling dislocation mechanism," *Metall. Mater. Trans. A*, Vol. 35, pp. 2697–2705.

27. Y. Wang, a Hamza, and E. Ma, Jun. 2006, "Temperature-dependent strain rate sensitivity and activation volume of nanocrystalline Ni," *Acta Mater.*, Vol. 54, pp. 2715–2726.

28. H. Somekawa and C. A. Schuh, Dec. 2011, "Effect of solid solution elements on nanoindentation hardness, rate dependence, and incipient plasticity in fine grained magnesium alloys," *Acta Mater.*, Vol. 59, pp. 7554–7563.

29. T. Zhu, J. Li, S. Ogata, and S. Yip, Mar. 2009, "Mechanics of Ultra-Strength Materials," *MRS Bull.*, Vol. 34, pp. 167–172.

30. J. M. Wheeler, C. Niederberger, C. Tessarek, S. Christiansen, and J. Michler, Jan. 2013, "Extraction of plasticity parameters of GaN with high temperature, in situ micro-compression," *Int. J. Plast.*, Vol. 40, pp. 140–151.

31. F. H. J. and M. F. Ashby, *Deformation-Mechanism Maps*. Pergamon Press, 1982.

32. W. D. Nix and S. Lee, 2011, "Micro-pillar plasticity controlled by dislocation nucleation at surfaces," *Philos. Mag.*, Vol. 91, pp. 1084–1096.

33. V. Bhakhri and R. J. Klassen, Apr. 2009, "The strain-rate dependence of the nanoindentation stress of gold at 300 K: A deformation kinetics-based approach," *J. Mater. Res.*, Vol. 24, pp. 1456–1465.

34. W. M. Mook, M. S. Lund, C. Leighton, and W. W. Gerberich, Oct. 2008, "Flow stresses and activation volumes for highly deformed nanoposts," *Mater. Sci. Eng. A*, Vol. 493, pp. 12–20.

35. S. Ogata, J. Li, N. Hirosaki, Y. Shibutani, and S. Yip, Sep. 2004, "Ideal shear strain of metals and ceramics," *Phys. Rev. B*, Vol. 70, pp. 104104–7.

Chapter 5

5   Kinetics of Incipient Plasticity of Gold Microspheres

Flat-punch micro-compression testing was employed to investigate the strain rate dependence of incipient plastic deformation in Au microspheres of diameter ranging from 0.8 to 6.0 µm. While the load corresponding to the onset of incipient plasticity increased with decreasing sphere diameter, the magnitude of this critical load also increased with increasing loading rate. This size dependence of the critical incipient load was attributed to the presence of vacancies whose density increased with increasing microsphere size. A thermal activation based model was used to interpret the loading-rate dependence of measured incipient loads, apparent activation volume, V^*, and energy, Q^*, values were found to be $0.2b^3$ and 0.01eV for 0.8 µm sphere and increased to $2.1b^3$ and 0.08eV for 6.0 µm spheres. These estimated values indicate that the incipient plasticity is controlled by heterogeneous nucleation events and are consistent with surface self-diffusion mechanism, implying that surface played a prominent role during the onset of plastic deformation in tested microspheres.

5.1   Introduction

Micro-spherical particles are currently being used in applications as diverse as bio-medical drug delivery systems to large surface area electrodes energy-storage devices. Their usefulness in these applications arises from their high surface to volume ratio and ease of fabrication. Furthermore, it is well established that materials when used at small-scales, ranging from nano- to micro-meter size, display considerably enhanced mechanical properties compared to their bulk counterparts [1–10].

Many small-scale uniaxial compression or indentation hardness studies have observed that plastic deformation occurs by stochastic mechanism of discrete "displacement jumps" corresponding to the motion of single or groups of dislocations [11–14]. The nucleation of the first dislocation during small scale experiments is assumed to occur

homogenously within the material when the magnitude of the shear stress within the deformed volume approaches the theoretical shear strength of the material [15–20]. Nanoindentation hardness have shown that strain jumps associated with dislocation nucleation occur at a stress level that corresponds to nearly the ultimate shear strength of the material.

William Paul et al. [21] investigated the initial plastic damage to a 100 nm thick Au (111) single crystal using a well-defined W (111) indenter with the combination of scanning tunneling microscopy (STM) and atomic force microscopy (AFM) and found the stress corresponding to the initial displacement jump events was much lower than the theoretical shear strength, which suggests that dislocations were inhomogenously nucleated within the bulk.

The theoretical strength representing the atomic bonding strength of a material, is very high in comparison to its measured bulk strength. In an ideal perfect metal sample, a very high strength will be required to break the inter-atomic bonds necessary to nucleate a dislocation. This process is generally called homogenous dislocation nucleation. But, when a material contains pre-existing dislocations or internal/external surfaces from which dislocations can be easily nucleated, the material will begin plastic deformation at a stress much below its theoretical strength. This process is referred to a heterogeneous dislocation nucleation. Both experimental and theoretical studies are necessary to completely understand the effect of sample size on the transition from homogenous to heterogeneous dislocation nucleation. Most of the work in this area to date has been of a computational/numerical modelling approach. Experimental investigations in this area are still lacking.

In this work, we present the force-depth responses from compression tests performed at different loading rates on Au microspheres of diameters ranging from 0.8 to 6.0 µm at ambient temperature. The main purpose of this work is to study the incipient plastic behavior of small size *FCC* metal samples. We analyse the force-displacement data from compression tests performed on the Au microspheres to extract the apparent activation volume and energy controlling the dislocation nucleation/glide process.

5.2 Materials and Methods

5.2.1 Sample Preparation

Gold microspheres were fabricated on a (0001)-oriented α-Al_2O_3 (Sapphire) surface. An A8 PMMA positive photoresist layer was spin-deposited on the O_2 plasma cleaned sapphire surface and e-beam lithography was used to project a grid of 1.5 to 12.0 µm diameter circles upon the photoresist. After the exposed photoresist was removed, a polycrystalline Au film of 100 to 600 nm thickness was deposited by e-beam sputter deposition. The remaining photoresist was then removed and the 1.5 to 12.0 µm diameter, 0.1 to 0.6 µm thick, Au cylinders were annealed in-vacuum at 1000°C. During the annealing process the Au de-wetted from the sapphire substrate and took the form of monocrystalline spheres, of 0.8 to 6.0 µm diameter. The spheres displayed a facetted surface. Previous studies have identified similar facets in Au microsphere as being of {111} orientation [22–24]. About 100 Au microspheres were fabricated for each diameter of 0.8, 1.0, 3.0 and 6.0 µm (Figure 5.1). As, the sapphire substrate is nonconductive and the fabricated microspheres were equidistant and also not connected to each other, around 10 − 15nm layer of Cr was deposited on the microsphere pattern surface for SEM imaging. Post- imaging, Cr layer was removed to perform compression tests on the microspheres. Similarly, the deformed microsphere were imaged by depositing 10 − 15nm layer of Cr.

5.2.2 Microsphere Compression

The Au microspheres were compressed with an instrumented NanoTest nano-indentation hardness testing platform constructed by Micro Materials Ltd (Wrexham, UK). A 9 µm diameter diamond flat punch indenter was attached to the indentation tester. In total, around 60 compression tests were performed for the four different sized spheres. The tests were carried out by pressing the flat-punch against the Au microsphere at a constant loading rate to maximum displacement of 20% of the original diameter of the sphere. Loading rates, ranging from 0.01 to 1.00 mN/sec, were used to study the strain rate dependence of the incipient plasticity of the microspheres.
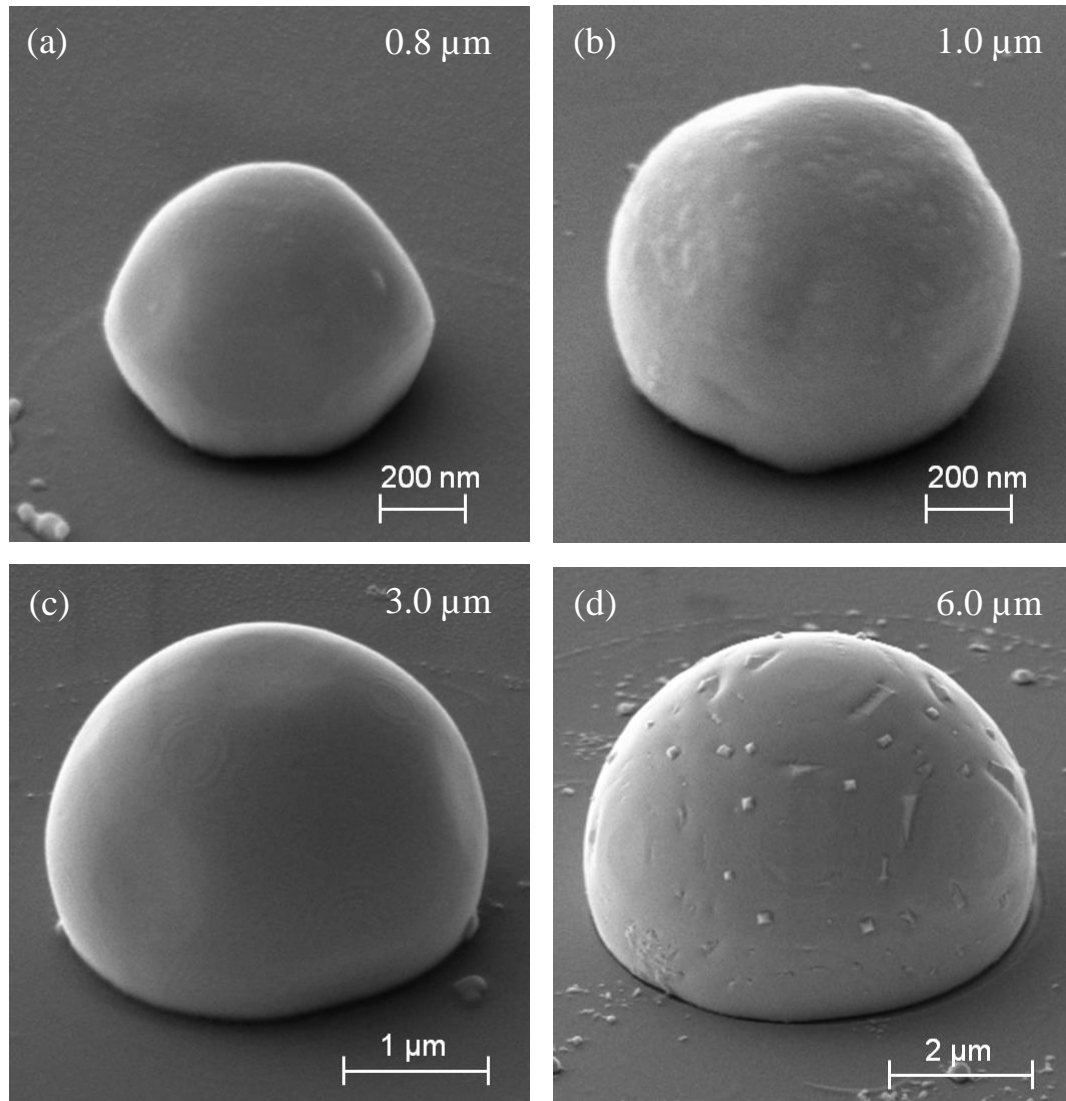
Figure 5.1: SEM images of representative: (a) 0.8, (b) 1.0, (c) 3.0 and (d) 6.0 µm diameter Au microsphere.

5.3 Data Analysis and Results

5.3.1 Prediction of Contact Stress

Stress-strain curves of the deformed microspheres can be prepared from experimentally obtained load-displacement data using an alternative or a simplified method, which was used by the other researcher's [22,23,25]; stress can be obtained by instantaneous force, F divided by the instantaneous contact area, πr^2 by assuming circular contact area, where r

is the top facets radius and similarly strain can be obtained dividing the compression depth to the height of the sphere. To calculate the instantaneous contact area accurately, the change of facet length with compression depth of the Au microspheres was calculated from the FE model as described in Section 4.2.3.
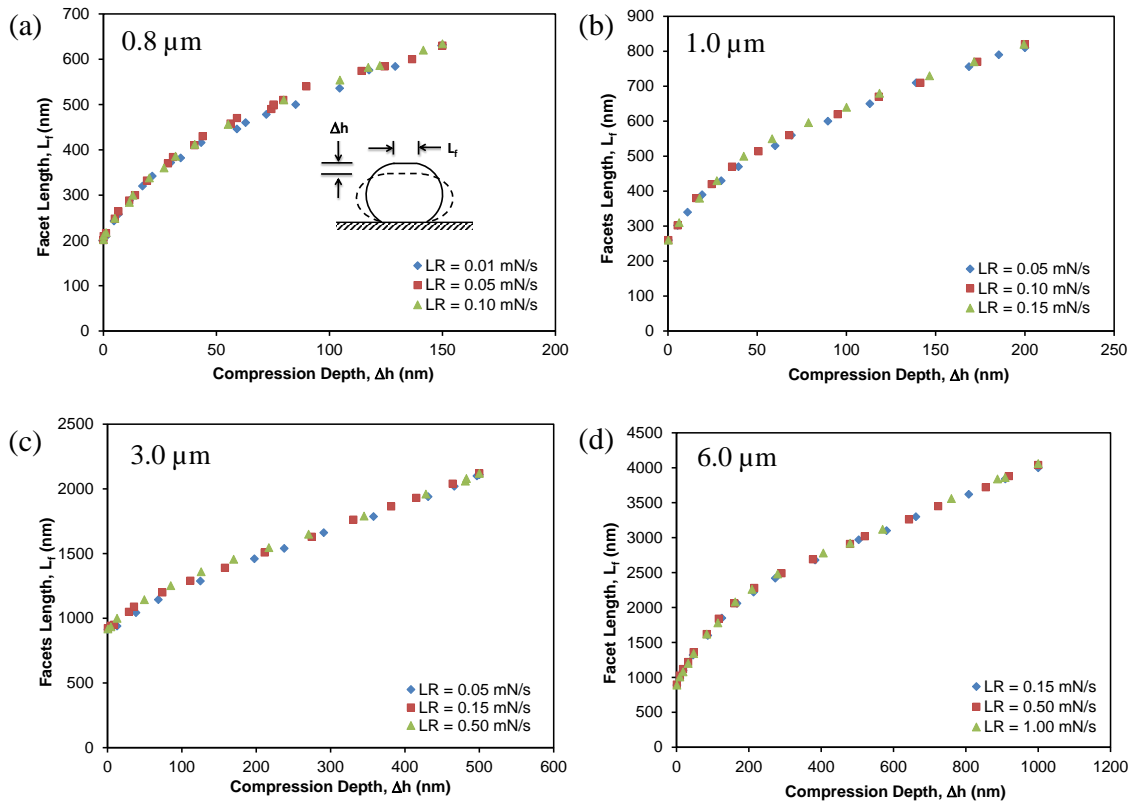
Figure 5.2: Change of top facets diameter during FE simulation of Au microspheres deformation under uniaxial compression at different loading rates for, (a) 0.8, (b) 1.0, (c) 3.0 and (d) 6.0 µm diameter spheres.

The top facets diameter of the deformed microspheres was recorded from FE simulation model (Chapter 4). The predicted facet diameter during compression is shown in Figure 5.2 for a range of Au microsphere diameters loaded at various loading rates. It is clear from the Figure 5.2 that loading rates have little effect on the facet length changes. Using these facet diameters along with force data from the experimental compression tests (Figure 4.5), contact stress versus average axial strain values was calculated (Figure 5.3).
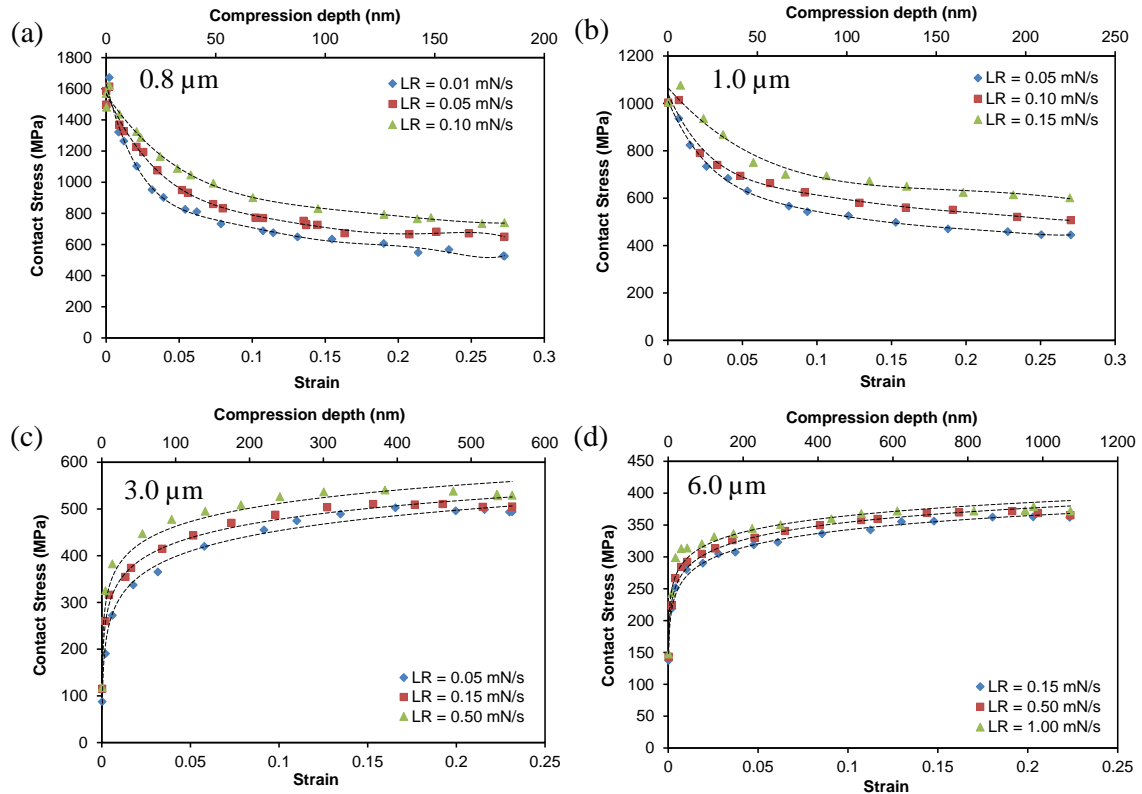
Figure 5.3: Contact stress-strain curves of Au microspheres of (a) 0.8, (b) 1.0, (c) 3.0 and (d) 6.0 µm diameter at different loading rates.

In Figure 5.3, small (0.8 and 1.0 µm) diameter spheres show very high contact stress during the initial stages of deformation around 1.7 and 1.1 GPa. The contact stress decreased gradually until 10% of strain, after that the change of contact stress with strain is almost constant. On the other hand, large (3.0 and 6.0 µm) diameter spheres showed contact stress that increased gradually with strain and loading rates. At the highest loading rate, yield contact stresses are about 400 and 310 MPa for 3.0 and 6.0 µm diameter microspheres. This change in the strain dependent of the contact stress for small and large diameter Au microspheres indicates that different mechanisms are operating during the deformation process.

5.3.2 Hertzian Approximation

Figure 5.4 shows the Force-displacement (F-h) curves of four different diameter Au spheres (0.8, 1.0, 3.0 and 6.0 µm) compressed at loading rates from 0.01 to 1.00 mN/s. The strain rate, expressed as the change of strain with respect to time at the incipient load, was determined from the test data at each loading rate.

Also included in the Figure 5.4 are the elastic loading trends based upon Hertzian contact between an elastic half-space to a depth, h indenting an elastic sphere of radius, R.

In the Hertzian elastic contact model, the contact force, F is related to h as [26]

$$F = \frac{4}{3} E_r R^{1/2} h^{3/2} \tag{5.1}$$

where E_r is the reduced elastic modulus which is given as

$$\frac{1}{E_r} = \frac{1 - v_1^2}{E_1} + \frac{1 - v_2^2}{E_2} \tag{5.2}$$

where, E_1, E_2 are Elastic moduli and v_1, v_2 are Poisson's ratios associate with the sphere and the half-space. For this work, E_r was calculated by considering isotropic elastic properties of E_1 = 1141 GPa, v_1 = 0.07 [27] for the diamond flat-punch indenter and E_2 = 79 GPa [28], v_2 = 0.42 [8] for the Au microspheres. R is the radius of the Au microsphere.
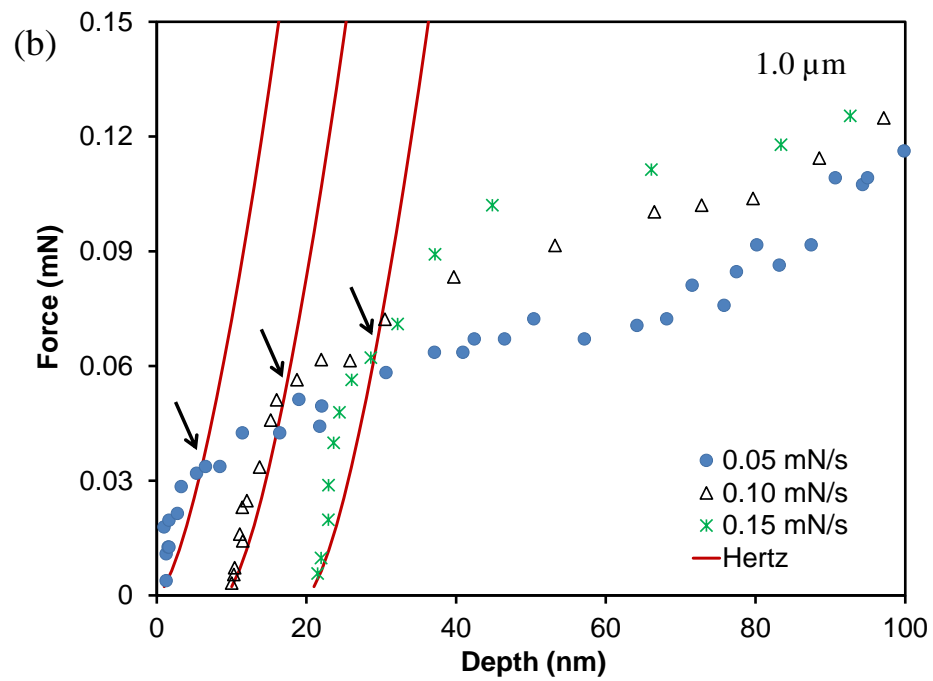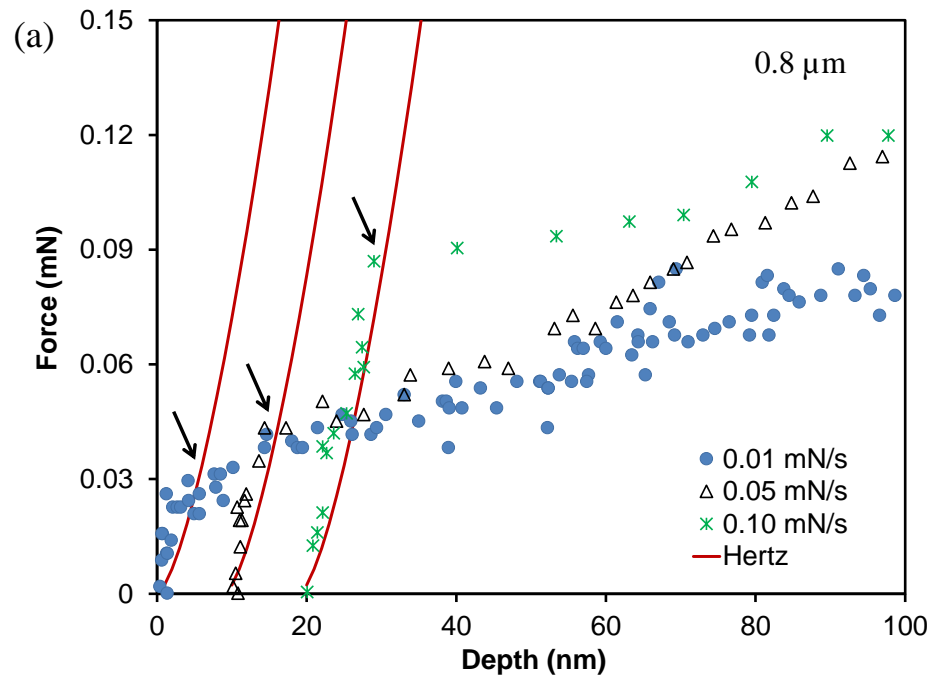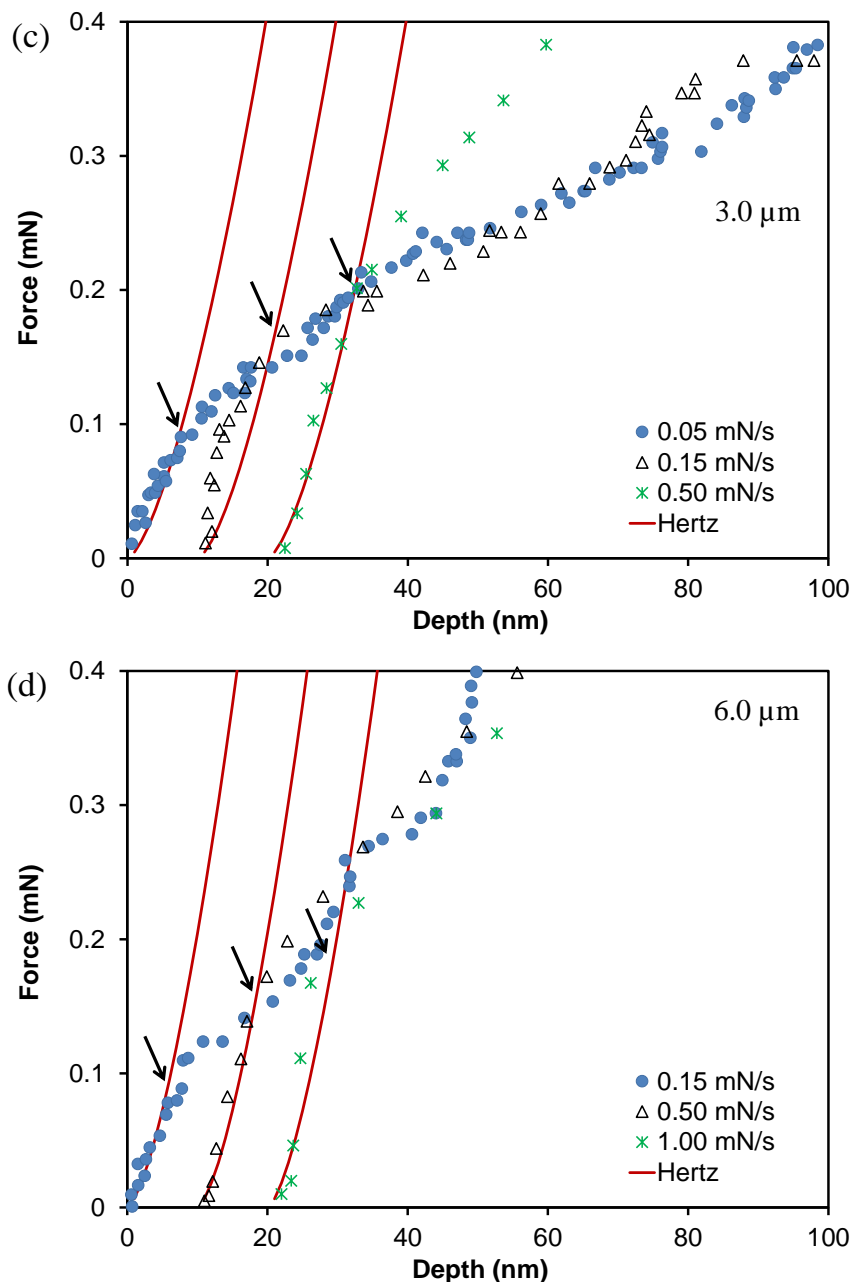
Figure 5.4: Representative *F-h* curves measured during compression of the Au microspheres at three different loading rates, (a) 0.8, (b) 1.0, (c) 3.0 and (d) 6.0 µm diameter Au microspheres. For each test the initial portion of the *F-h* curve is well matched by the *F-h* elastic response predicted by the Hertzian contact model (Eq. 5.1) (solid red lines). The load corresponding to the first incipient plasticity event is marked by the black arrow. For the sake of clarity, the displacement data for three different loading rates is offset by 10 nm in these figures.

The first deviation from these Hertzian elastic loading profiles is considered as the initiation of incipient plasticity. As can be seen in Figure 5.4, the incipient load clearly displayed an increasing trend with increasing loading rates for each microsphere diameter. This indicates that incipient load, and hence the yield strength, of these structures is strain rate sensitive. For the smallest microsphere (0.8 µm) diameter, the incipient load increased from 0.035 ± 0.012 mN to 0.087 ± 0.022 mN as the loading rates increased from 0.01 to 0.10 mN/s (Figure 5.4a). Incipient load increased from 0.092 ± 0.022 mN to 0.185 ± 0.033 mN as the loading rates increased from 0.15 to 1.00 mN/s for the largest microsphere (6.0 µm) diameter (Figure 5.4d). Table 5.1 shows the details of the loading rate and corresponding incipient load for all the diameter Au microspheres.

The increasing incipient load with increasing loading rate indicates that the incipient yield stress σ_y, of the tested microspheres increased with increasing strain rates. The incipient load data was converted to incipient stress by dividing it by the area of the {111} facet upon which the flat-punch indenter contacted the Au sphere. The facets area was measured from SEM images of the microspheres. A corresponding effective shear stress, τ_y was then calculated from σ_y [2]

$$\tau_y = 0.55\sigma_y \qquad (5.3)$$

---

[2] The effective shear stress was obtained by multiplying the yield strength by the Schmid factor for the <111> loading axis, assuming uniaxial loading. Plastic deformation to occur in *FCC* metals there are 12 independent slip systems, {111}<110>. As these Au microspheres have shown <111> direction normal to the sapphire surface, therefore Schmid factor for all possible slip systems were calculated and highest Schmid factor was found to be 0.55 for the (111)[101] and (111)[110] slip systems [48].

Table 5.1 Summary of loading rate and the corresponding incipient load of the tested Au microspheres

Sphere diameter (µm)	Loading rate (mN/sec)	Incipient Load, L_i (mN)
	0.01	0.035 ± 0.012
0.8	0.05	0.046 ± 0.018
	0.10	0.087 ± 0.022
	0.05	0.045 ± 0.021
1.0	0.10	0.056 ± 0.012
	0.15	0.072 ± 0.011
	0.05	0.096 ± 0.019
3.0	0.15	0.173 ± 0.051
	0.50	0.203 ± 0.061
	0.15	0.092 ± 0.022
6.0	0.50	0.157 ± 0.024
	1.00	0.185 ± 0.033

5.3.3 The Elastic Strain Energy Density (SED) Associated with Incipient Plasticity

For the tested microsphere compressions, the elastic energy that is stored within the Au microspheres can be measured directly from the load-displacement curves shown in Figure 5.4. The total stored elastic strain energy density is represented by the area under the *F-h* curve up to the yield point normalized with respect to the volume of the sphere. For the microsphere between 0.8 to 6.0 µm diameters, total elastic strain energy densities values were found between, 5 to 20 J/cm^3 for 0.8 µm diameter sphere, and between 0.031 to 0.098 J/cm^3 for 6.0 µm diameter sphere (Figure 5.5). The strain energy densities for the smallest diameter spheres are consistent with the value found from literature (5 to 20 J/cm^3) for Au microspheres of 340 nm initial nominal diameter [13].
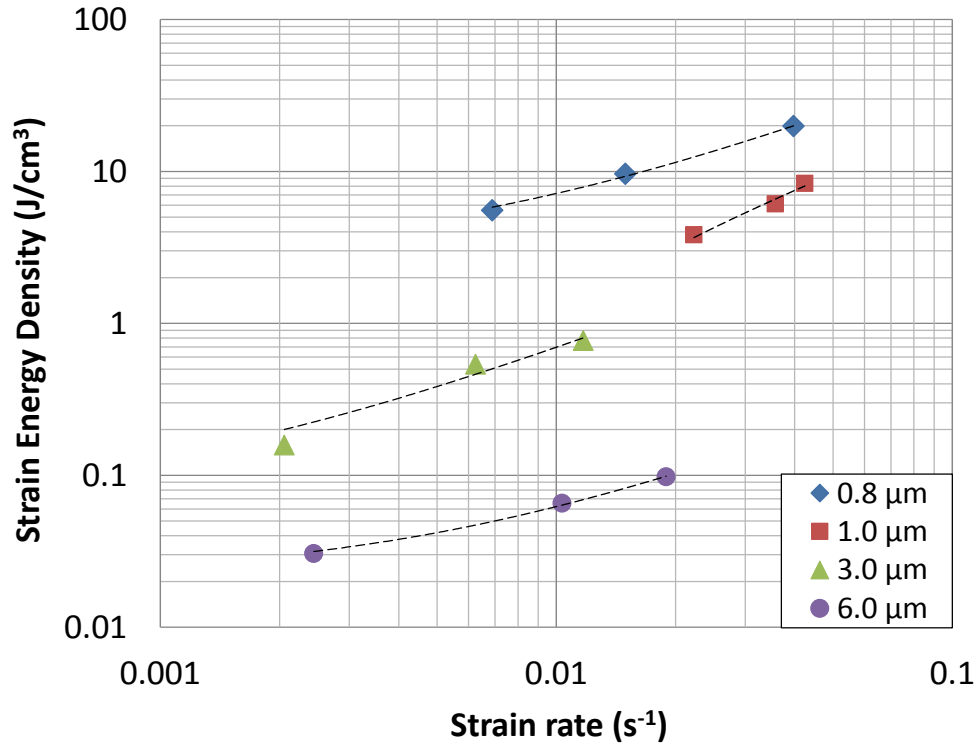
Figure 5.5: The total elastic strain energy density at different the strain rates for 0.8 to 6.0 µm diameter Au spheres during initial yielding.

In Figure 5.5, incipient SEDs are plotted on a log-log plot as a function of strain rates for the Au microspheres. SED has an inverse relationship with sphere diameters i.e. smaller spheres exhibits larger SED during the incipient deformation. However, it is evident that SED increases as stain rate increases for all microspheres.

The SED during the plastic deformation of these microspheres can be calculated using the area under the contact stress-strain curve (Figure 5.3). Contact stress-strain data in Figure 5.3 were fitted with a 5th order polynomial function (as shown in dotted line in the Figure 5.3) and numerical integration was used to calculate the area under the stress-strain curve i.e. SED at different level of strain.
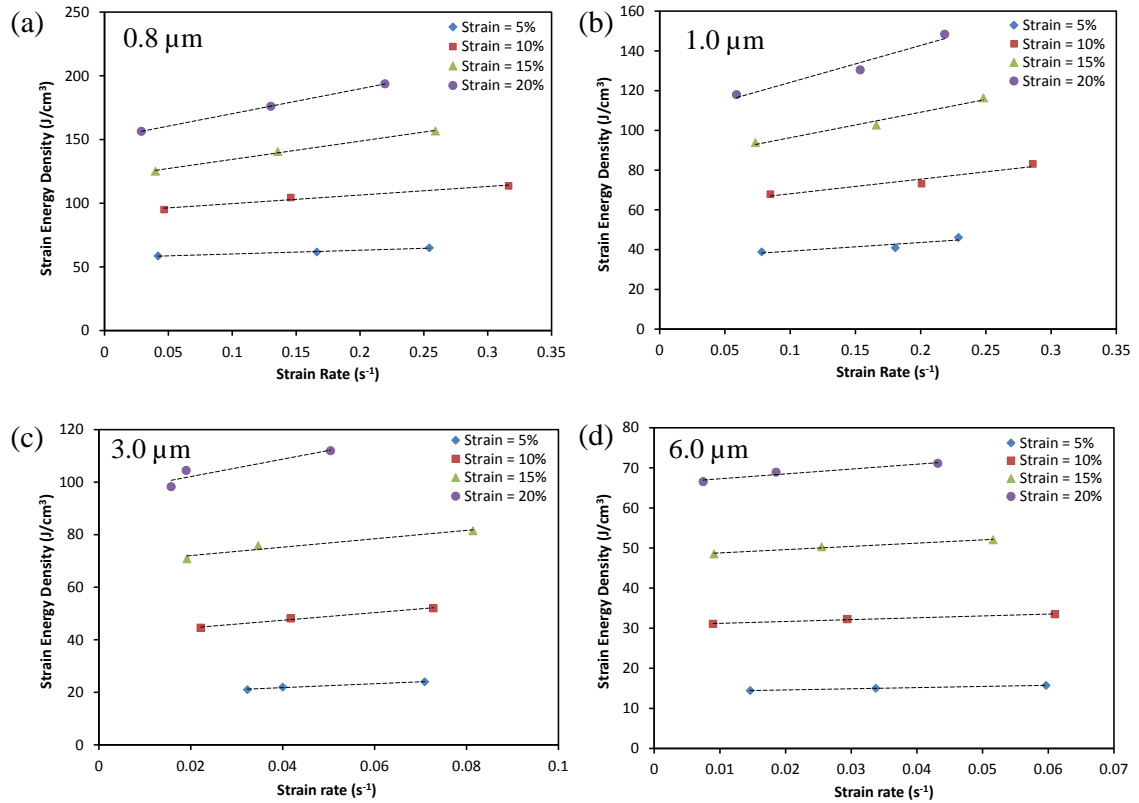
Figure 5.6: Effect of strain rate on the strain energy density (J/m^3) at different level of strain for Au microspheres of different sizes: (a) 0.8, (b) 1.0, (c) 3.0 and (d) 6.0 µm diameter.

Figure 5.6 shows the calculated SED at different level of strain and strain rate for the microspheres. At any given strain level, SED increases with strain rate for smaller (0.8 µm) diameter sphere but SED is almost constant with strain rate for larger (6.0 µm) diameter sphere. Effect of microsphere size and strain rate on SED for all microsphere deformation process is combined in Figure 5.7. At 5 % strain, for example SED changes from 58 to 64 J/m^3 for 0.8 µm sphere and from 14 to 15 J/m^3 for 6.0 µm sphere (Figure 5.8).
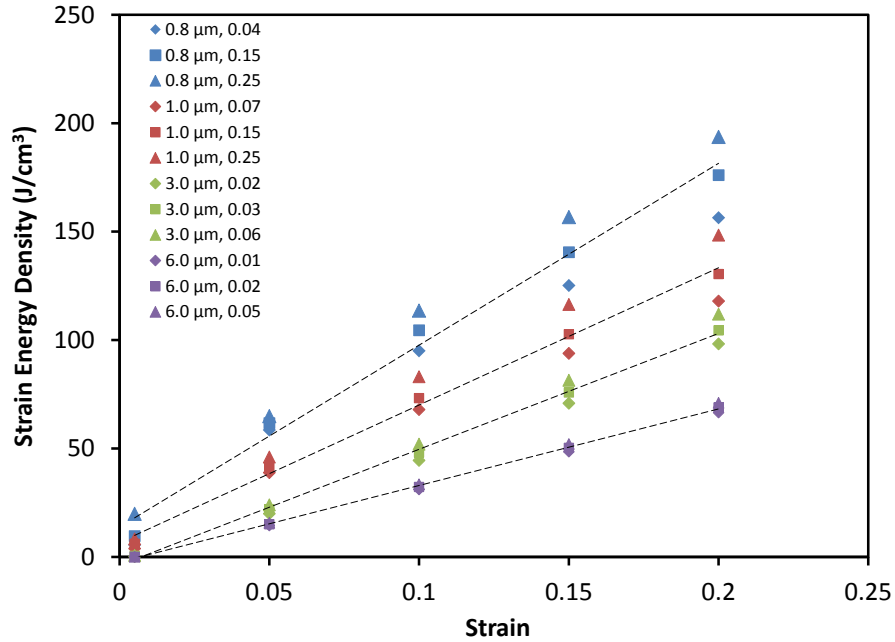
Figure 5.7: Effect of sphere size and strain rate on strain energy density during all microsphere deformation process.
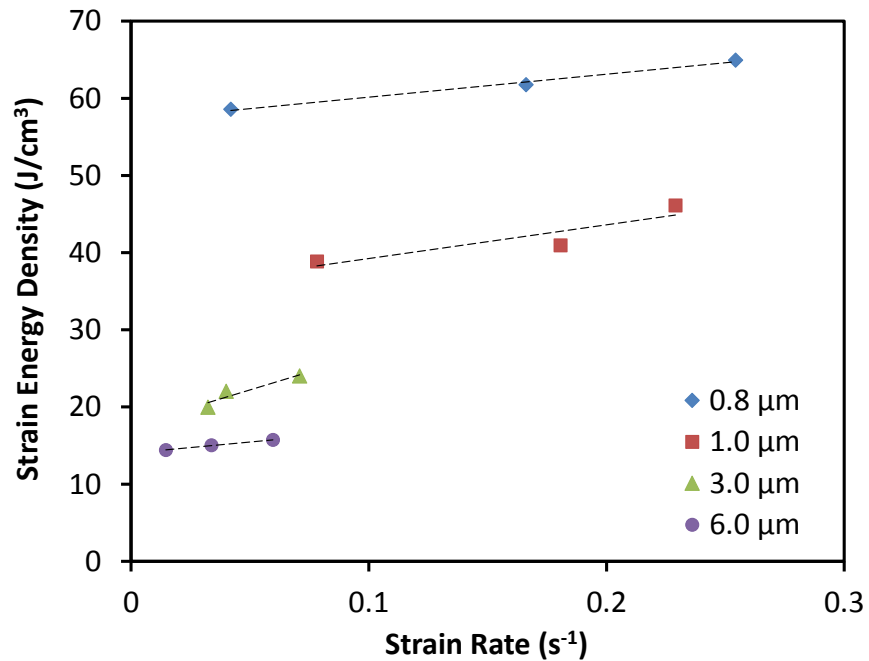
Figure 5.8: Shows the SED as a function of strain rates at 5% strain during all microsphere deformation process.

5.3.4 The Activation Volume and Activation Energy of Incipient Plastic Deformation

The average strain rate, $\dot{\varepsilon}$, of the microspheres can be described in terms of the motion of dislocations by the following Orowan's equation [29];

$$\dot{\varepsilon} = \frac{d\varepsilon}{dt} = \rho_m b \bar{v} \tag{5.4}$$

where ρ_m is the density of mobile dislocations, b and $\bar{v}$ are the magnitude of the Burgers vector and the velocity of dislocation. The dislocation velocity $\bar{v}$ expressed by the following standard approach for a stress activation process [30]:

$$\bar{v} = v_0 b \left[exp\left(-\frac{(\tau_p - \tau)V}{kT} \right) - exp\left(-\frac{(\tau_p + \tau)V}{kT} \right) \right] \tag{5.5}$$

where v_0 is the atomic jump frequency, τ_p is the athermal lattice resistance, (i.e. the Peierls stress) needed to cause a dislocation to move, τ is the applied shear stress, V is the activation volume, T is the absolute temperature, and k is the Boltzmann's constant. Combining Eqs. 5.4 and 5.5 with the assumption that $\tau V \gg kT$, the second term in square brackets of Eq. 5.5 is much less than the first, and assuming also that the activation volume can be treated as constant, the following expression for τ can be arrived at

$$\tau = \tau_p + \frac{kT}{V} \ln \dot{\varepsilon} - \frac{kT}{V} \ln[\rho_m b^2 v_0] \tag{5.6}$$

This relationship forms the basis of typical analyses of compression tests at elevated temperatures [30–32], a plot of the shear flow stress against the natural logarithm of strain rate, at a particular temperature, should result in a linear relationship of slope kT/V. The total activation energy, Q, of deformation rate controlling obstacles can then be estimated as $Q = \tau_{0K}V$, where τ_{0K} is the athermal stress of Au [33]. The estimations of the activation energy Q and the activation volume V provide information on the underlying deformation rate controlling mechanism in the Au microspheres.

The normalized shear stress, corresponding to the first incipient plastic strain event, τ_{incip}/G, obtained from the incipient loads of the microspheres compressed at different strain rates is shown in Figure 5.9. In these plots the elastic shear modulus of $G_{Au} = 23.8$ GPa was used [34]. The figure indicates that the incipient stress increases as the strain rates increased for all the spheres. The incipient shear stress of the 6.0 µm diameter spheres is the lowest and the 0.8 µm diameter spheres is the highest. Also included on the graph is the theoretical shear strength, which is normally estimated between ~G/30 to G/10 for *FCC* metals such as Au [35–37].
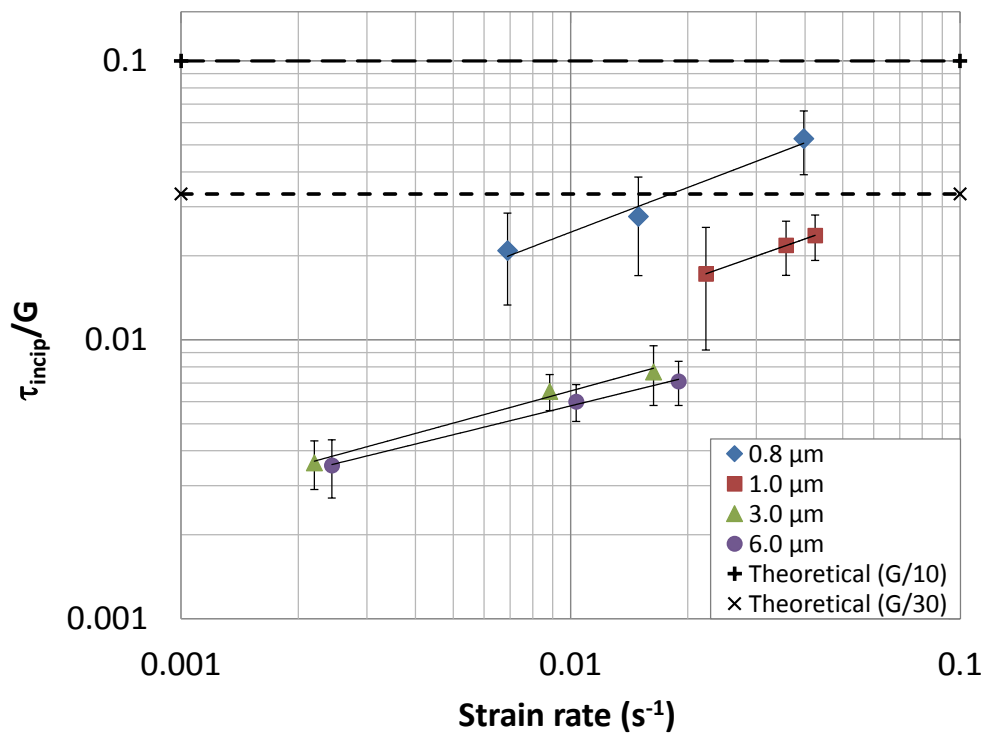
Figure 5.9: Normalized incipient shear stress versus strain rate of Au microspheres. Included in the plot are dashed lines indicating common estimates of the ideal theoretical shear strength ($\tau_{ideal} = G/30$ to $G/10$) of a metal.

It is notable that the normalized incipient shear stress of the smaller, 0.8 and 1.0 µm diameter spheres, approaches the estimated theoretical strength limit for Au, while the larger, 3.0 and 6.0 µm diameter spheres, displayed incipient plastic yielding at considerably lower stress levels.

It is interesting to notice that besides bulk deformation behavior in *Chapter 4*, incipient stress in the tested microspheres also displays both strain rate and size dependence. The strain rate dependence of the incipient stress suggests that the deformation mechanism controlling these events involves a time-dependent diffusion based process. The size dependence of the incipient stress can be explained by increased vacancy sites with increasing facet size[3] i.e. the contact area between the flat-punch indenter and microspheres. Salehinia et al. [38] demonstrated that the presence of vacancies underneath the indenter during a nano-indentation hardness test on single crystal Ni strongly affects the incipient loads. Increased population of vacancies underneath the larger contact area lowered the yield load compared to smaller indentations where higher incipient loads were observed. This study showed that the vacancy concentration beneath a nano-indenter will influence the subsequent dislocation nucleation stress and can thus influence the time-dependence of the deformation process.

Mordehai et al. [22] performed MD simulations on Au micro-particles, and reported that the first dislocation nucleation events, which is related to the large incipient dislocation burst, occurs at the upper facet vertices, where the facetted sphere contacts compressing surface, regardless of the micro-particle size. They suggested that the initial number of potential dislocation nucleation sites is constant, regardless of particle size, and the size effect on the incipient yield load is associated with the probability of dislocation nucleation at these vertices.

The slope of strain rate dependence of τ in Figure 5.9 is kT/V^*, and thus provides information on the apparent activation volume, V^*, (Eq. 5.6). The length-scale dependence of V^* is shown in Figure 5.10 where the estimated value of V^* for the microspheres is plotted versus a length scale parameter (sphere diameter). The plotted V^* are normalized with respect to b^3, where $b_{Au} = 0.289$ nm [39,40]. The estimated V^* during incipient plasticity of 0.8 and 1.0 µm diameter Au spheres are about 0.2 and $0.4b^3$ respectively. It is important to notice here is that the V^* values obtained here is much

---

[3] The facet size of 0.8, 1.0, 3.0 and 6.0 µm diameter Au microspheres was measured around 210 ± 29, 259 ± 27, 842 ± 88 and 835 ± 52 nm respectively.

lower than the *V** obtained during the bulk deformation of these two diameters microspheres (*Ch. 4*) which were of the order of $4 - 6b^3$. Similarly, the estimated average incipient *V** for larger (3.0 and 6.0 µm) diameter Au spheres are about 1.8 and $2.1b^3$ respectively, whereas the estimated *V** obtained from bulk deformation of these spheres were between $12 - 42b^3$ (*Ch. 4*). The much lower activation volumes obtained here during initial yielding of Au microspheres is consistent with previously reported studies that have reported activation volumes of $1.5b^3$ for single crystalline Ni_3Al [41], $0.5b^3$ for single crystalline platinum [18] and about $0.2 - 1.0b^3$ for Magnesium [42]. In these studies the low *V** are attributed to heterogeneous dislocation nucleation events where dislocations are nucleated at pre-existing defects such as vacancy or vacancy cluster, an impurity atom, or free surfaces [42]. Zhu et al. [43] confirmed by the molecular dynamic simulation that an activation volume for dislocation nucleation at a free surface is of the order of $1 - 10b^3$. Included in Figure 5.10 are the apparent activation volumes reported by these studies plotted against an appropriate length scale (i.e. indentation depth or specimen length).
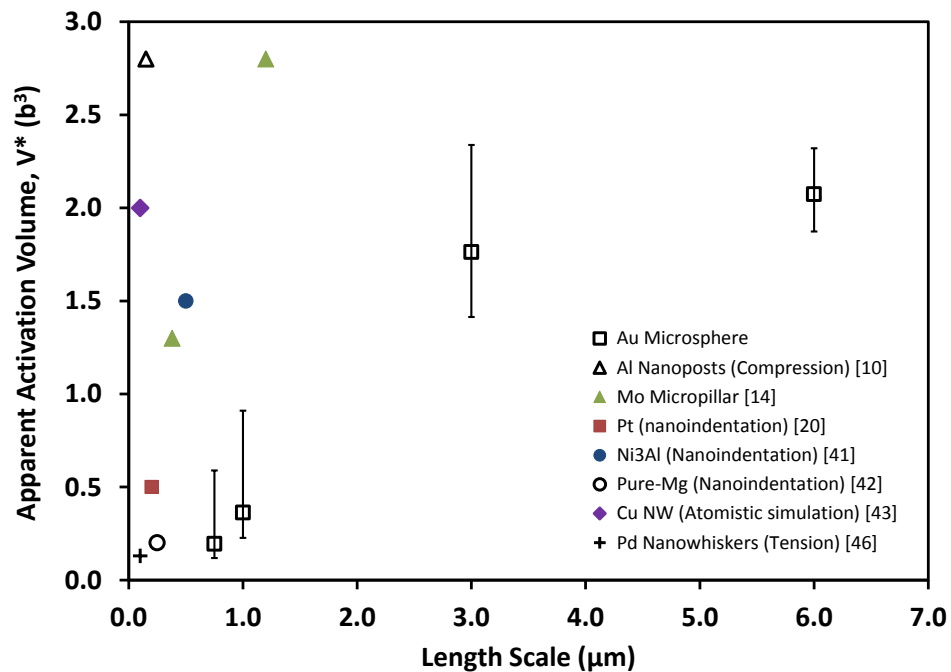
Figure 5.10: The change of apparent activation volume, *V** during incipient plastic deformation of different diameter Au microspheres.

In order to estimate the apparent activation energy, $Q^* = \tau_{0K} V^*$, of the deformation rate controlling obstacles, in the Au microspheres tested in this study, athermal stress, $\tau_{0K} = 256$ MPa was used [44]. The calculated Q^* values ranged between 0.01 to 0.08eV as the microsphere size increased from 0.8 to 6.0 µm. The estimated magnitudes of V^* and Q^* here are of the order of surface self-diffusion based processes as reported by Liu et al. [45]. These results are also consistent with the findings from a recent study by Chen et al. [46,47] in which authors employed nano-tensile experiments to investigate the kinetics of incipient plastic deformation in Pd whiskers. Authors interpreted results using a thermal activation based model, similar to the one used in the present study, and reported similar activation volume and activation energy values and attributed stress-assisted surface diffusion process as rate controlling mechanism.

5.4 Summary

Flat-punch micro-compression testing was employed to investigate the deformation-rate dependence of the incipient plastic deformation of Au microspheres of diameter ranging from 0.8 to 6.0 µm. The incipient yield load increased with increasing loading rate for a particular sized microsphere, whereas, it decreased with increasing microsphere size. The size dependence of incipient loads was attributed to the presence of vacancies whose amount increased, as a result of increased flat-punch/sphere contact area, in the larger diameter microspheres. A thermal activation based model was used to interpret the loading-rate dependence of the measured incipient loads. The apparent activation volume, V^*, and energy, Q^*, values were found to be $0.2b^3$ and 0.01eV for 0.8 µm sphere and increased to $2.1b^3$ and 0.08eV for 6.0 µm spheres. These estimated values indicate that the incipient plasticity is controlled by heterogeneous dislocation nucleation events occurring at, or near, the flat-punch/sphere interface the rate of which is highly dependent upon the rate of surface self-diffusion of the Au atoms. This study illustrates the importance of surfaces on the onset of plastic deformation in crystalline metal nano-structures such as microspheres, micropillars and microbeams.

The next chapter of this thesis will present the kinetics of incipient and bulk plastic deformation of Au micropillars of diameter ranging from 0.8 to 4.0 µm.

References

1. J. R. Greer, W. C. Oliver, and W. D. Nix, Apr. 2005, "Size dependence of mechanical properties of gold at the micron scale in the absence of strain gradients," *Acta Mater.*, Vol. 53, pp. 1821–1830.

2. W. D. Nix, J. R. Greer, G. Feng, and E. T. Lilleodden, Feb. 2007, "Deformation at the nanometer and micrometer length scales: Effects of strain gradients and dislocation starvation," *Thin Solid Films*, Vol. 515, pp. 3152–3157.

3. J.-Y. Kim and J. R. Greer, Oct. 2009, "Tensile and compressive behavior of gold and molybdenum single crystals at the nano-scale," *Acta Mater.*, Vol. 57, pp. 5245–5253.

4. W. Mook, J. Nowak, C. Perrey, C. Carter, R. Mukherjee, S. Girshick, P. McMurry, and W. Gerberich, Jun. 2007, "Compressive stress effects on nanoparticle modulus and fracture," *Phys. Rev. B*, Vol. 75, pp. 214112–10.

5. C. P. Frick, B. G. Clark, S. Orso, a. S. Schneider, and E. Arzt, Aug. 2008, "Size effect on strength and strain hardening of small-scale [111] nickel compression pillars," *Mater. Sci. Eng. A*, Vol. 489, pp. 319–329.

6. M. D. Uchic, D. M. Dimiduk, J. N. Florando, and W. D. Nix, Aug. 2004, "Sample dimensions influence strength and crystal plasticity.," *Science*, Vol. 305, pp. 986–9.

7. D. Maharaj and B. Bhushan, 2012, "Effect of spherical Au nanoparticles on nanofriction and wear reduction in dry and liquid environments," *Beilstein J. Nanotechnol.*, Vol. 3, pp. 759–772.

8. D. Maharaj and B. Bhushan, 2014, "Nanomanipulation, nanotribology and nanomechanics of Au nanorods in dry and liquid environments using an AFM and depth sensing nanoindenter," *Nanoscale*, Vol. 6, p. 5838.

9. R. Purkayastha and R. McMeeking, 2013, "A parameter study of intercalation of lithium into storage particles in a lithium-ion battery," *Comput. Mater. Sci.*, Vol. 80, pp. 2–14.

10. W. M. Mook, M. S. Lund, C. Leighton, and W. W. Gerberich, Oct. 2008, "Flow stresses and activation volumes for highly deformed nanoposts," *Mater. Sci. Eng. A*, Vol. 493, pp. 12–20.

11. J. Greer and W. Nix, Jun. 2006, "Nanoscale gold pillars strengthened through dislocation starvation," *Phys. Rev. B*, Vol. 73, pp. 245410–6.

12. J. R. Greer, C. R. Weinberger, and W. Cai, Oct. 2008, "Comparing the strength of f.c.c. and b.c.c. sub-micrometer pillars: Compression experiments and dislocation dynamics simulations," *Mater. Sci. Eng. A*, Vol. 493, pp. 21–25.

13. W. M. Mook, C. Niederberger, M. Bechelany, L. Philippe, and J. Michler, Feb. 2010, "Compression of freestanding gold nanostructures: from stochastic yield to predictable flow," *Nanotechnology*, Vol. 21, pp. 055701–9.

14. A. S. Schneider, B. G. Clark, C. P. Frick, and E. Arzt, Jan. 2009, "Correlation between Activation Volume and Pillar Diameter for Mo and Nb BCC Pillars," *MRS Proc.*, Vol. 1185, pp. 1185–II07–04.

15. J. Li, K. J. Van Vliet, T. Zhu, S. Yip, and S. Suresh, Jul. 2002, "Atomistic mechanisms governing elastic limit and incipient plasticity in crystals," *Nature*, Vol. 418, pp. 307–310.

16. A. Gouldstone, N. Chollacoop, M. Dao, J. Li, A. Minor, and Y. Shen, Jul. 2007, "Indentation across size scales and disciplines: Recent developments in experimentation and modeling," *Acta Mater.*, Vol. 55, pp. 4015–4039.

17. S. N. Dub, Y. Y. Lim, and M. M. Chaudhri, 2010, "Nanohardness of high purity Cu (111) single crystals: The effect of indenter load and prior plastic sample strain," *J. Appl. Phys.*, Vol. 107, p. 043510.

18. J. K. Mason, A. C. Lund, and C. A. Schuh, 2006, "Determining the activation energy and volume for the onset of plasticity during nanoindentation," *Phys. Rev. B*, Vol. 73, pp. 1–14.

19. D. Lorenz, A. Zeckzer, U. Hilpert, P. Grau, H. Johansen, and H. Leipner, 2003, "Pop-in effect as homogeneous nucleation of dislocations during nanoindentation," *Phys. Rev. B*, Vol. 67, pp. 1–4.

20. C. A. Schuh, J. K. Mason, and A. C. Lund, 2005, "Quantitative insight into dislocation nucleation from high-temperature nanoindentation experiments.," *Nat. Mater.*, Vol. 4, pp. 617–621.

21. W. Paul, D. Oliver, Y. Miyahara, and P. H. Grütter, 2013, "Minimum threshold for incipient plasticity in the atomic-scale nanoindentation of Au(111)," *Phys. Rev. Lett.*, Vol. 110, pp. 1–5.

22. D. Mordehai, S.-W. Lee, B. Backes, D. J. Srolovitz, W. D. Nix, and E. Rabkin, Aug. 2011, "Size effect in compression of single-crystal gold microparticles," *Acta Mater.*, Vol. 59, pp. 5202–5215.

23. S.-W. Lee, D. Mordehai, E. Rabkin, and W. D. Nix, Jul. 2011, "Effects of focused-ion-beam irradiation and prestraining on the mechanical properties of FCC Au microparticles on a sapphire substrate," *J. Mater. Res.*, Vol. 26, pp. 1653–1661.

24. D. Mordehai, M. Kazakevich, D. J. Srolovitz, and E. Rabkin, Apr. 2011, "Nanoindentation size effect in single-crystal nanoparticles and thin films: A comparative experimental and simulation study," *Acta Mater.*, Vol. 59, pp. 2309–2321.

25. Z.-J. Wang, Z.-W. Shan, J. Li, J. Sun, and E. Ma, Feb. 2012, "Pristine-to-pristine regime of plastic deformation in submicron-sized single crystal gold particles," *Acta Mater.*, Vol. 60, pp. 1368–1377.

26. L. Kogut and I. Etsion, 2002, "Elastic-Plastic Contact Analysis of a Sphere and a Rigid Flat," *J. Appl. Mech.*, Vol. 69, p. 657.

27. D. Catoor, Y. F. Gao, J. Geng, M. J. N. V Prasad, E. G. Herbert, K. S. Kumar, G.

M. Pharr, and E. P. George, 2013, "Incipient plasticity and deformation mechanisms in single-crystal Mg during spherical nanoindentation," *Acta Mater.*, Vol. 61, pp. 2953–2965.

28. C. A. Volkert and E. T. Lilleodden, Nov. 2006, "Size effects in the deformation of sub-micron Au columns," *Philos. Mag.*, Vol. 86, pp. 5567–5579.

29. E. Orowan, Jan. 1940, "Problems of plastic gliding," *Proc. Phys. Soc.*, Vol. 52, pp. 8–22.

30. V. Bhakhri, J. Wang, N. Ur-rehman, C. Ciurea, F. Giuliani, and L. J. Vandeperre, Sep. 2011, "Instrumented nanoindentation investigation into the mechanical behavior of ceramics at moderately elevated temperatures," *J. Mater. Res.*, Vol. 27, pp. 65–75.

31. B. Baufeld and M. B. and D. B. Messerschmidt, U, 1994, "Plasticity of Cubic Zirconia between 700 C and 1150 C Observed by Macroscopic Compression and by in situ Tensile Straining Tests," *Key Eng. Mater.*, Vol. 97–98, pp. 431–436.

32. P. Pirouz, J. L. Demenet, M. H. Hong, 2001, "On transition temperatures in the plasticity and fracture of semiconductors," *Philos. Mag. A*, Vol. 81, pp. 1207–1227.

33. J. M. Wheeler, C. Niederberger, C. Tessarek, S. Christiansen, and J. Michler, Jan. 2013, "Extraction of plasticity parameters of GaN with high temperature, in situ micro-compression," *Int. J. Plast.*, Vol. 40, pp. 140–151.

34. Y. Kamimura, K. Edagawa, and S. Takeuchi, 2013, "Experimental evaluation of the Peierls stresses in a variety of crystals and their relation to the crystal structure," *Acta Mater.*, Vol. 61, pp. 294–309.

35. D. Hull and D. Bacon, *Introduction to dislocations*, 4th ed. Jordan Hill, Oxford: Butterworth-Heinemann, 2001.

36. S. S. Brenner, 1956, "Tensile strength of whiskers," *J. Appl. Phys.*, Vol. 27, pp. 1484–1491.

37. H. Bei, S. Shim, G. M. Pharr, and E. P. George, Oct. 2008, "Effects of pre-strain on the compressive stress–strain response of Mo-alloy single-crystal micropillars," *Acta Mater.*, Vol. 56, pp. 4762–4770.

38. I. Salehinia, V. Perez, and D. F. Bahr, 2012, "Effect of vacancies on incipient plasticity during contact loading," *Philos. Mag.*, Vol. 92, pp. 550–570.

39. W. D. Nix and S. Lee, 2011, "Micro-pillar plasticity controlled by dislocation nucleation at surfaces," *Philos. Mag.*, Vol. 91, pp. 1084–1096.

40. V. Bhakhri and R. J. Klassen, 2009, "The strain-rate dependence of the nanoindentation stress of gold at 300 K : A deformation kinetics-based approach."

41. P. C. Wo, L. Zuo, and a. H. W. Ngan, 2005, "Time-dependent incipient plasticity in Ni3Al as observed in nanoindentation," *J. Mater. Res.*, Vol. 20, pp. 489–495.

42. H. Somekawa and C. A. Schuh, Dec. 2011, "Effect of solid solution elements on

nanoindentation hardness, rate dependence, and incipient plasticity in fine grained magnesium alloys," *Acta Mater.*, Vol. 59, pp. 7554–7563.

43. T. Zhu, J. Li, A. Samanta, A. Leach, and K. Gall, 2008, "Temperature and strain-rate dependence of surface dislocation nucleation," *Phys. Rev. Lett.*, Vol. 100, p. 25502.

44. F. H. J. and M. F. Ashby, *Deformation-Mechanism Maps*, 1st ed. New York, USA: Pergamon Press, 1982.

45. C. L. Liu, J. M. Cohen, J. B. Adams, and a F. Voter, 1991, "EAM study of surface self-diffusion," *Surf. Sci.*, Vol. 253, pp. 334–344.

46. L. Y. Chen, M. He, J. Shin, G. Richter, and D. S. Gianola, 2015, "Measuring surface dislocation nucleation in defect-scarce nanostructures," *Nat. Mater.*, Vol. 14, pp. 707–714.

47. J. Li, 2015, "Dislocation nucleation: Diffusive origins," *Nat. Mater.*, Vol. 14, pp. 656–657.

48. W. D. Callister, *Materials Science and Engineering: an Introduction*, 7th ed. New York, USA: John Wiley & Sons, Inc, 2007.

Chapter 6

6   Kinetics of Plastic Deformation of Au Micropillars

The size and strain rate dependence of incipient and bulk plastic deformation of Au micropillars of diameter ranging from 0.8 to 4.0 µm were studied at room temperature using flat-punch micro-compression testing. The yield stress of the micropillars was observed to increase from 102 to 350 MPa when pillar diameter decreased from 4.0 to 0.8 µm. EBSD analysis was performed to determine the crystallographic orientation of the micropillars and the critical resolved shear stress associated with the onset of plastic deformation was calculated. The dependence of yield stress on the surface area to volume ratio (SA/V) of the micropillars was determined and the results were compared to the trends reported for Au microspheres in Chapter 4. The results suggest that smaller size Au samples, 0.8 µm diameter pillars and 0.8 µm diameter spheres, with SA/V ratio >5, deform differently than larger size samples with SA/V ratio <5. The magnitude of the apparent activation volume V^* and energy Q^* displayed by the micropillars corresponding to an average uniaxial plastic strain of 5% indicated that the operative deformation mechanism was dependent upon the diameter of Au micropillar. The size dependence of the early, incipient, stage of plastic deformation was also determined for the Au micropillars. For a specific sized micropillar the incipient yield stress increased with increasing loading rate while, for a specific loading rate, it decreased with increasing micropillar diameter. A thermal activation based model was used to interpret the loading rate dependence of the incipient yield stress, and the associated deformation rate controlling parameters V^* and Q^* were estimated.

6.1   Introduction

Mechanical properties of crystalline metals at small-scale deformation is currently of tremendous scientific interest and various experimental test techniques have been employed to study the microstructural phenomena responsible for the marked increase in yield strength that occurs when the dimension of the test sample is less than about $1 - 5$ µm (see Chapter 3).

In this chapter, we report an investigation of the size and strain rate dependence of the flow stress, both incipient and after 5% plastic strain, of Au micropillars of three diameters (0.8, 2.0, and 4.0 µm) that were tested at three loading rates. The purpose of this work is to determine the operative mechanisms that control the plastic deformation of these small size *FCC* metal samples.

6.2   Methods

6.2.1   Micropillar Fabrication

A 0.5 mm thick foil of 99.95% pure polycrystalline Au was mechanically prepared by grinding with successively finer grades of SiC papers followed by final polishing in 0.05 µm colloidal alumina slurry. The sample was then annealed at 900°C for 12 hours and then chemically etched by emersion, in an aqueous solution of 8 wt% Iodine and 21 wt% Potassium Iodide, for about 2 minutes at 25°C. The Au removal rate in this solution was about 28 angstroms per second. The grain size of the Au was large, as a result of the annealing, and was measured at between 20 to 600 µm.

The Au micropillars were fabricated by FIB milling at the Nanofabrication Laboratory at Western University (London, Ontario, Canada). The diameter of the micropillars was 0.8, 2.0 and 4.0 µm and the diameter/height ratio was between 1:1 and 1:3. At least ten micropillars of each diameter were fabricated.

6.2.2   EBSD Analysis

Electron back scatter diffraction (EBSD) was used to index the crystallographic orientation of the grains comprising the Au surface upon which the micropillars were made. The EBSD was performed at the Zircon and Accessory Phase Laboratory (ZAPLab) at Western University (London, Ontario, Canada). Figure 6.1 shows SEM images of two areas where most of the micropillars were located. The orientation maps and the corresponding inverse pole figures of these areas are shown in Figure 6.2. The grains from which micropillars were made are designated G1 to G6 in Figure 6.2.

For each micropillar the applied shear stress τ_R acting upon the active dislocation slip plane in the direction of dislocation motion was calculated as

$$\tau_R = \sigma \cos\phi \cos\lambda \tag{6.1}$$

where, σ is the applied normal compressive stress, ϕ and λ are the angles between the loading direction and the slip plane normal and the slip direction respectively. The crystal system on which dislocation first slip occurs is the one possessing the largest Schmid factor $\cos\phi \cos\lambda$. *FCC* materials, such as Au, deform plastically by dislocation slip along the $\{111\} < 110 >$ slip system. Twelve possible slip planes/directions exist within this system.

The Miller indices corresponding to the axial direction of micropillars are shown in Table 6.1. The angle ϕ was determined from the dot product of the *<hkl>* pillar normal direction (Table 6.1) and normal vectors $\langle 111 \rangle, \langle \bar{1}11 \rangle, \langle 1\bar{1}1 \rangle, \langle 11\bar{1} \rangle$ of the $\{111\}$ family of close-packed planes. Similarly, the angle λ was determined from the dot product of the *<hkl>* pillar normal direction and the three independent closed packed directions, $[110], [101], [011]$ of the $< 110 >$ family of close-packed crystal directions. The calculated maximum Schmid factor of the different grains containing micropillars is summarized in Table 6.1.
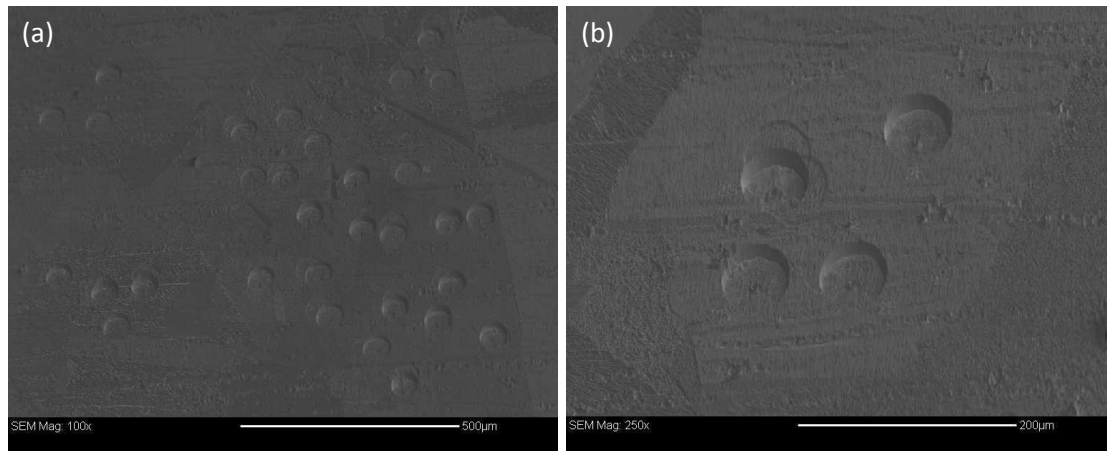
Figure 6.1: SEM images of the Au micropillars fabricated by FIB milling into different grains of the sample
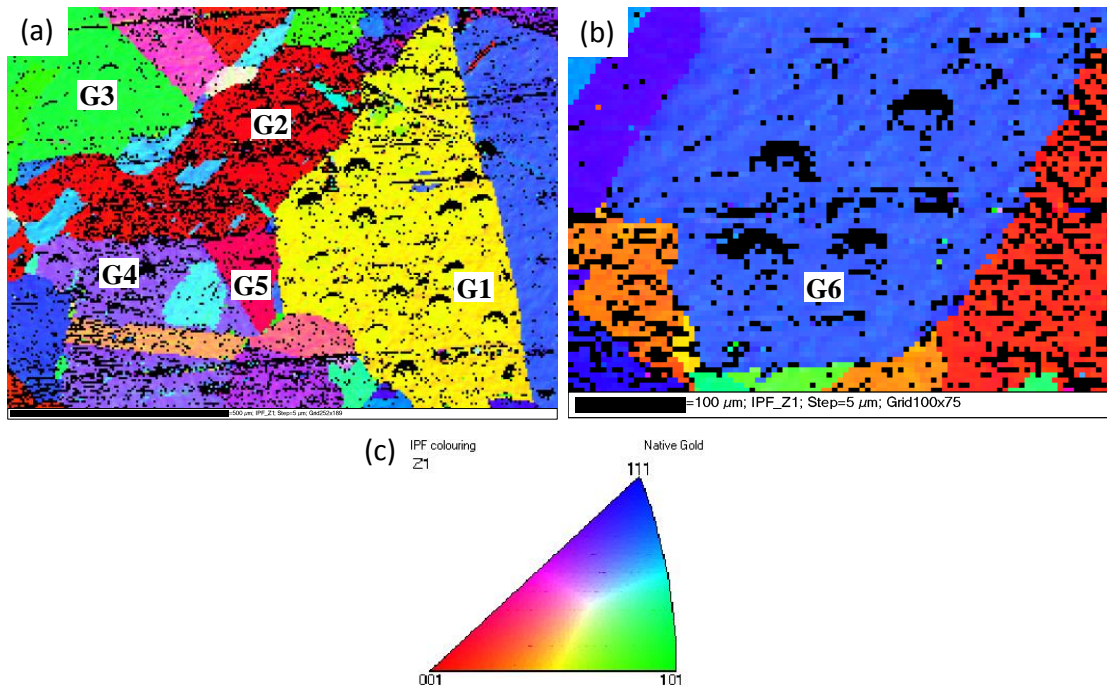
Figure 6.2: Inverse pole figure showing the crystallographic orientation map of the different grains, labelled G1 to G6, containing the test Au micropillars. The crystal Z direction (loading direction) is normal to the surface of the sample. (c) Color key for the maps.

Table 6.1: Summary of the grain containing Au micropillars, their crystallographic orientation and the calculated maximum Schmid factor.

Grain Designation	Axial crystallographic direction of the grain	Fabricated micropillars on the grains (A, B and C represents 0.8, 2.0 and 4.0 µm dia. pillars)	Maximum Schmid factor for the {111}<110> slip system (Eq. 6.1)
G1	<0.4, 0.1, 0.9>	A2, A4, A5, A7 2B, 2C, 2D, 2H, 2I, 2J, 2K 4C, 4D, 4E, 4F, 4G, 4H, 4I, 4J, 4K	0.26
G2	<0.5, 0.1, 0.9>	A3, A8, A9	0.19
G3	<0.1, 0.7, 0.7>	A6, A11	0.32
G4	<0.5, 0.3, 0.8>	A10, 2A, 4A, 4B	0.32
G5	<0.2, 0.2, 0.9>	A1	0.23
G6	<0.6, 0.4, 0.7>	A12, 2E, 2F, 2G	0.33

6.2.3   Micropillar Compression Tests

The Au micropillars were compressed on an instrumented NanoTest platform made by Micro Materials Ltd (Wrexham, UK) and fitted with a ~ 9 µm diameter flat punch diamond indenter. An optical microscope and a computer-controlled translation stage were used to position the micropillars in line with the flat-punch. About 30 micropillars were tested in compression. The compression tests were carried out by loading the micropillars at a constant rate to an average compressive strain of about 20%. The loading rates ranged from 0.01 to 0.30 mN/sec (Table 6.2).

Table 6.2: Summary of the geometry of the twenty-five Au micropillars used in this study.

Overall pillar size	Pillar Designation	Pillar Average Diameter (µm)	Pillar Height (µm)	Loading rate (mN/s)	Surface Area, SA (µm^2)	Volume, V (µm^3)	SA/V ratio
0.8 µm	A1	0.69	1.95	0.10	4.60	0.73	6.31
	A4	0.86	2.05	0.01	6.12	1.19	5.14
	A6	0.78	2.05	0.05	5.50	0.98	5.62
	A7	0.82	2.06	0.05	5.83	1.09	5.36
	A8	0.78	1.80	0.01	4.89	0.86	5.68
	A9	0.82	1.90	0.10	5.42	1.00	5.40
	A10	0.78	1.60	0.05	4.40	0.76	5.75
	A11	0.83	1.95	0.10	5.62	1.05	5.33
	Average	0.80 ± 0.05	1.92 ± 0.16		5.30 ± 0.61	0.96 ± 0.16	5.58 ± 0.36
2.0 µm	2A	2.00	4.30	0.05	30.15	13.51	2.23
	2C	1.90	4.60	0.15	30.29	13.04	2.32
	2D	2.15	4.20	0.01	31.99	15.25	2.10
	2E	2.10	4.32	0.01	31.96	14.96	2.14
	2F	2.00	4.30	0.15	30.15	13.51	2.23
	2G	2.10	4.40	0.05	32.49	15.24	2.13
	2H	1.95	4.50	0.15	30.55	13.44	2.27
	2J	1.90	4.40	0.05	29.09	12.47	2.33
	2K	1.99	4.60	0.01	31.86	14.30	2.23
	Average	2.01 ± 0.09	4.40 ± 0.14		30.95 ± 1.15	13.97 ± 1.01	2.22 ± 0.08
4.0 µm	4A	4.30	6.90	0.15	107.71	100.18	1.08
	4C	4.20	7.04	0.05	106.72	97.52	1.09
	4D	4.10	7.42	0.05	108.76	97.94	1.11
	4E	4.10	6.87	0.15	101.67	90.68	1.12
	4F	4.10	7.98	0.15	115.97	105.34	1.10
	4G	3.95	6.60	0.05	94.14	80.86	1.16
	4H	3.90	6.60	0.30	92.79	78.83	1.18
	4I	4.12	6.60	0.30	98.74	87.97	1.12
	Average	4.10 ± 0.13	7.00 ± 0.48		103.31 ± 7.92	92.42 ± 9.45	1.12 ± 0.03

6.3 Results

6.3.1 Micropillar Force vs Displacement Response

Figure 6.3 shows SEM micrographs taken before and after the compression of representative Au micropillars of 0.8 to 4.0 µm diameter. All the micropillars deformed by localized shear on specific slip planes. Multiple slips lines corresponding to {111}<110> slip can be seen.

Figure 6.4 to Figure 6.6 shows the experimentally obtained force-displacement (*F-h*) curves for the 0.8, 2.0, and 4.0 µm diameter micropillars compressed at three loading rates. For a given displacement *h*, the micropillars all display increased deformation force *F* with increased loading rate.
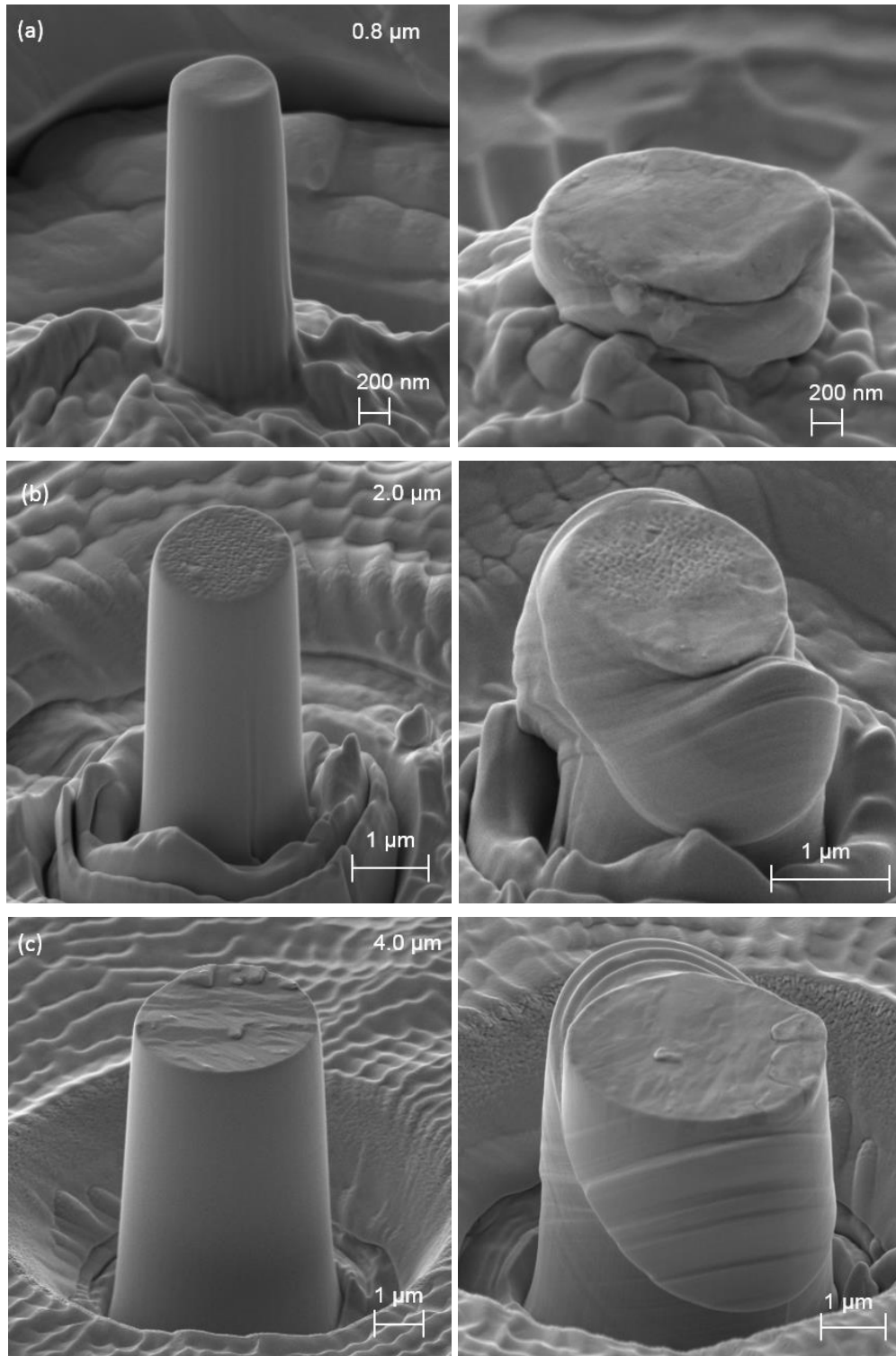
Figure 6.3: Representative SEM images before and after deformation of (a) 0.8, (b) 2.0 and (c) 4.0 µm diameter Au micropillars. In these images, multiple slips lines corresponding to {111}<110> slip systems are clearly visible.
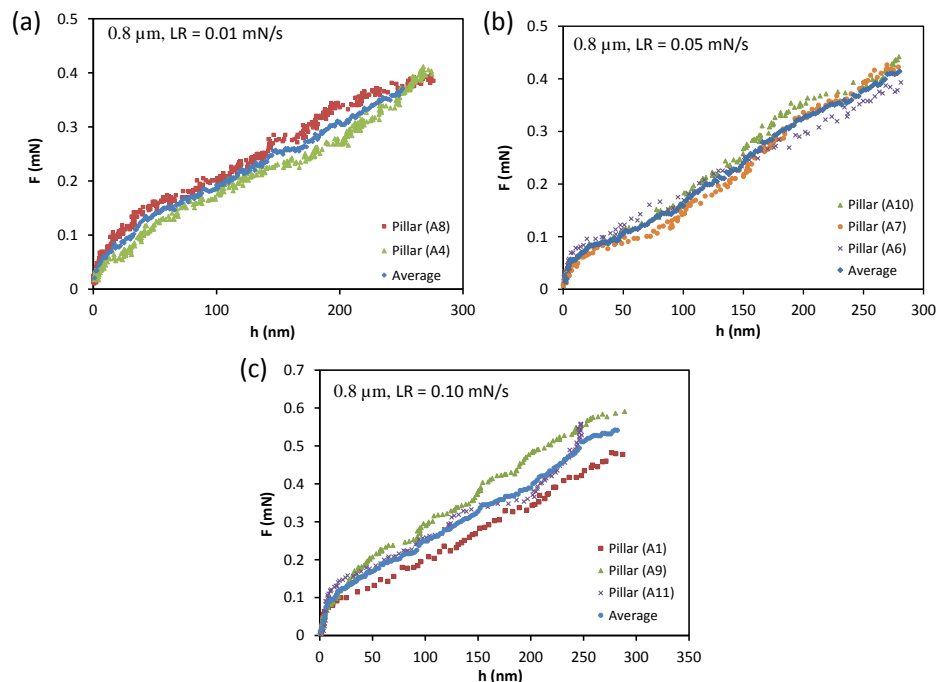
Figure 6.4: Experimentally obtained *F-h* response for 0.8 µm diameter Au micropillars loaded at three different rates, (a) 0.01, (b) 0.05 and (c) 0.10 mN/s.
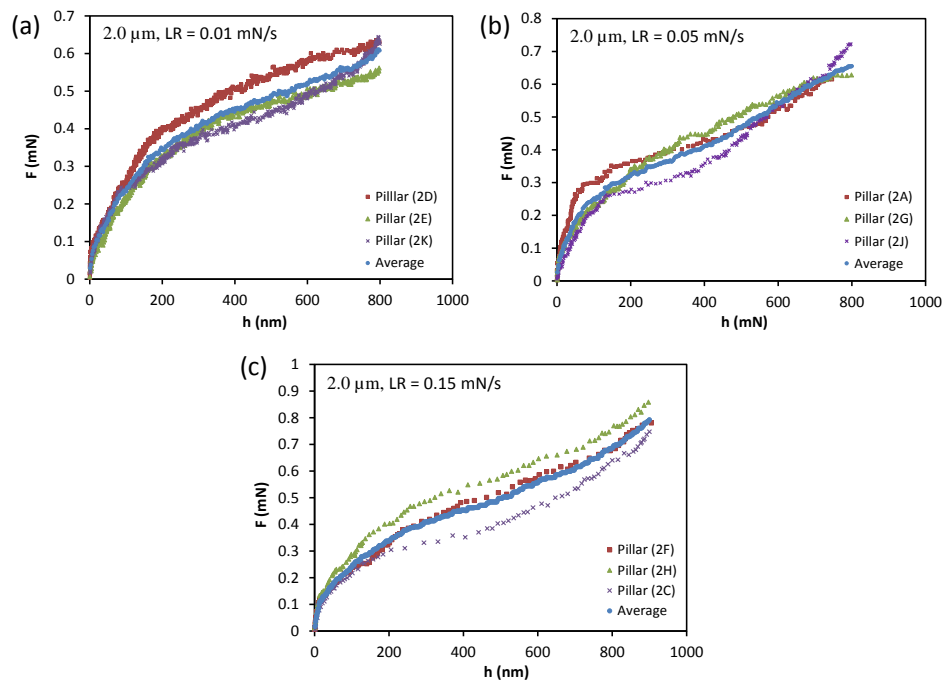
Figure 6.5: Experimentally obtained *F-h* response for 2.0 µm diameter Au micropillars loaded at three different rates, (a) 0.01, (b) 0.05 and (c) 0.15 mN/s.
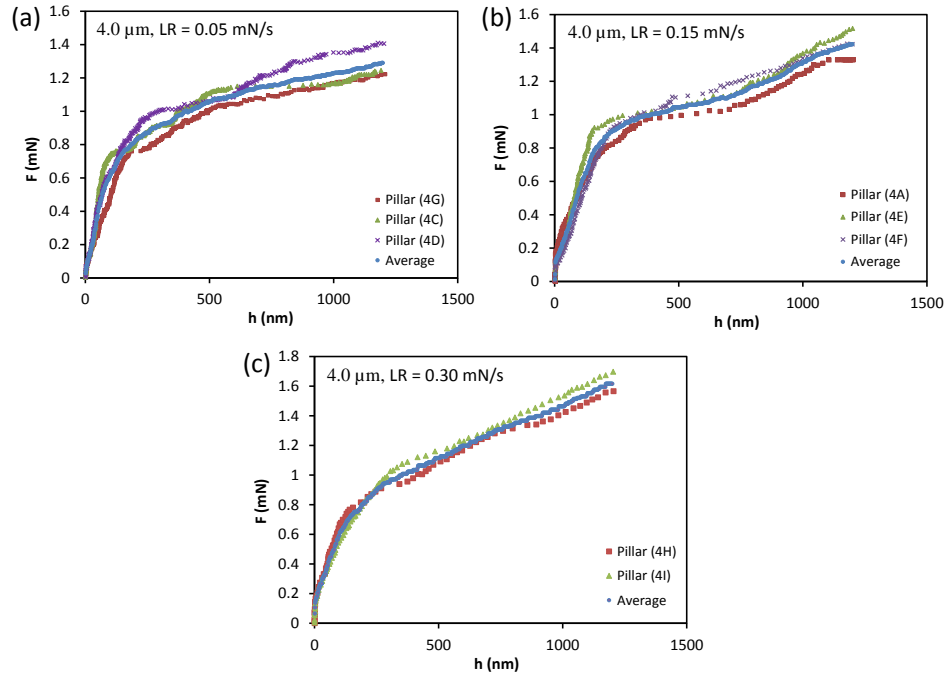
Figure 6.6: Experimentally obtained *F-h* response for 4.0 µm diameter Au micropillars loaded at three different rates, (a) 0.05, (b) 0.15 and (c) 0.30 mN/s.

6.3.2 True Stress-strain Response

Figure 6.7 to Figure 6.9 show plots of the true stress-strain and the corresponding critical resolved shear stress-true strain response of the tested Au micropillars compressed at three loading rates. The true and the engineering stress and strain are related by the following equations [1],

$$\sigma_T = \sigma(1 + \varepsilon) \tag{6.2}$$

$$\varepsilon_T = ln(1 + \varepsilon) \tag{6.3}$$

where, σ_T and ε_T represents true stress and strain while σ and ε represents the engineering stress and strain. The critical resolved shear stress was obtained using the Eq. 6.1 and the maximum Schmid factors as shown in Table 6.1.

The true stress-strain curve for the smallest diameter pillars (0.8 µm) showed irregular "stepped" stress-strain responses similar to what was reported by others and is associated with the onset of deformation via a dislocation nucleation/avalanche mechanism [2–9]. The largest diameter (4.0 µm) pillars showed smooth stress-strain response which is almost identical in shape and magnitude to those reported by Greer et al for similar size Au pillars [10,11].

It was reported by Bei et al. [12] that ion-induced surface damage resulting from the FIB milling process can affect the $\sigma-\varepsilon$ response of micropillars and minimize displacement bursts during testing. In comparison to the *F-h* curves displayed by similar size microspheres in compression (Chapter 4), the micropillars show noticeably lower frequency of the discrete stress jumps.

6.3.3   Comparison of Critical Resolved Shear Stress

Figure 6.10 shows a comparison of the calculated resolved shear stress, τ_R of the Au micropillars compressed at the three loading rates. The yield τ_R increases with increasing loading rates for all size micropillars. The smallest diameter sphere displayed a strong dependence upon the loading rate. It can be observed clearly when considering the data at low strain levels, say less than 5%, the loading rate dependence of τ_R is increased when the micropillar diameter is small.
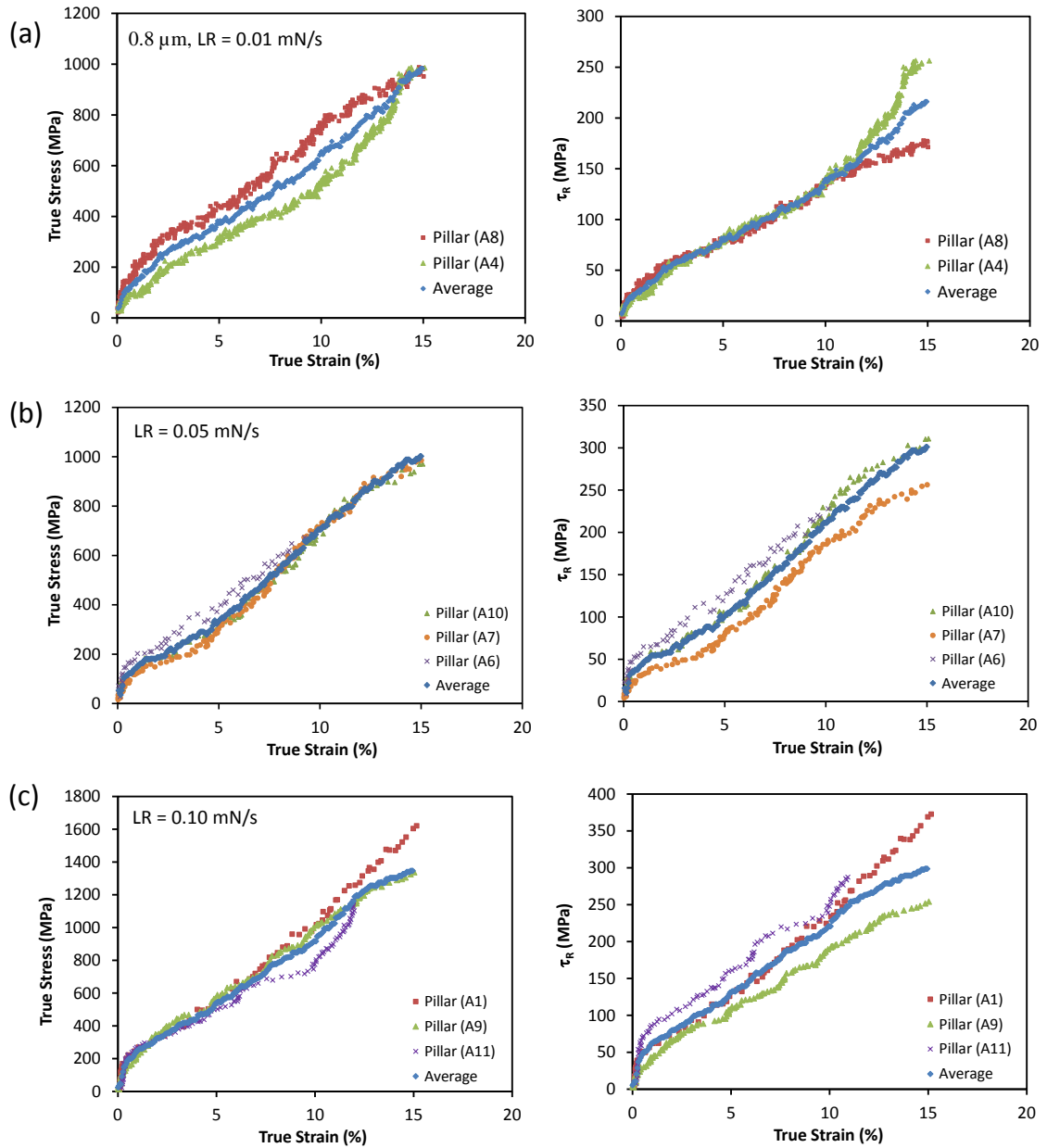
Figure 6.7: The true stress versus true strain responses and the corresponding τ_R versus true strain plots for 0.8 µm diameter Au micropillars compressed at three different loading rates of (a) 0.01, (b) 0.05 and (c) 0.10 mN/s.
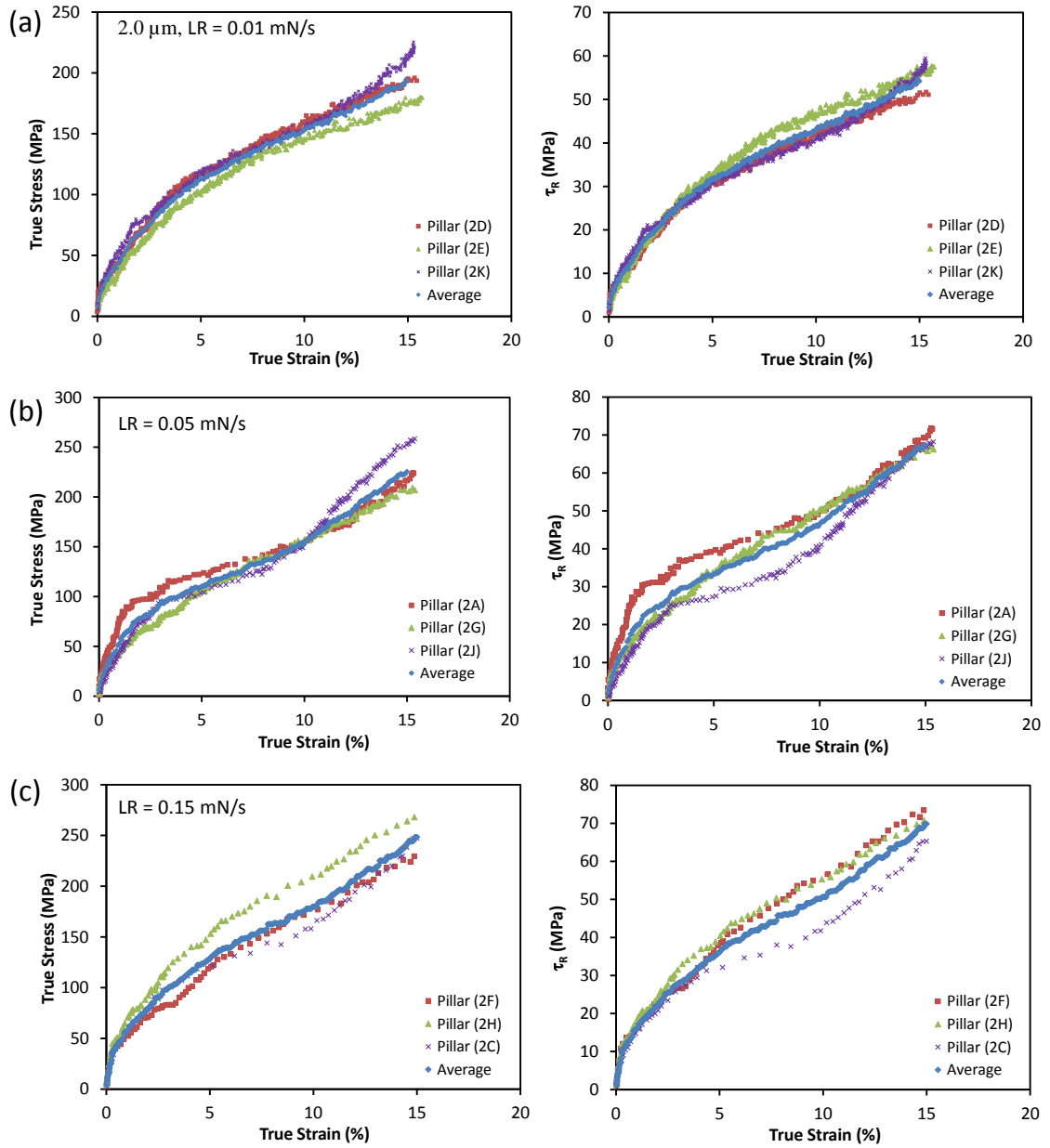
Figure 6.8: The true stress versus true strain responses and the corresponding τ_R versus true strain plots for 2.0 µm diameter Au micropillars compressed at three different loading rates of (a) 0.01, (b) 0.05 and (c) 0.15 mN/s.
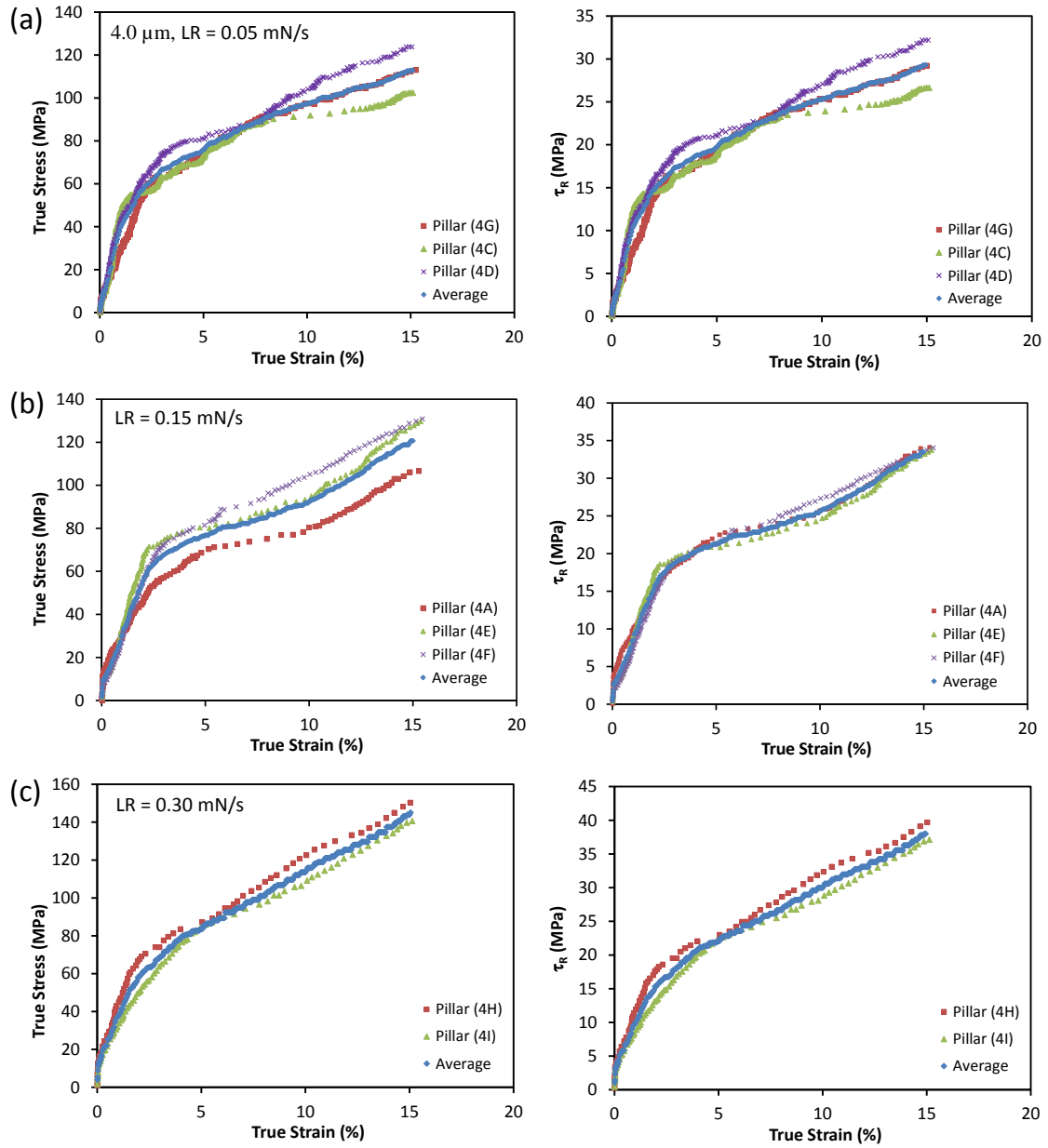
Figure 6.9: The true stress versus true strain responses and the corresponding τ_R versus true strain plots for 4.0 µm diameter Au micropillars compressed at three loading rates of (a) 0.05, (b) 0.15 and (c) 0.30 mN/s.
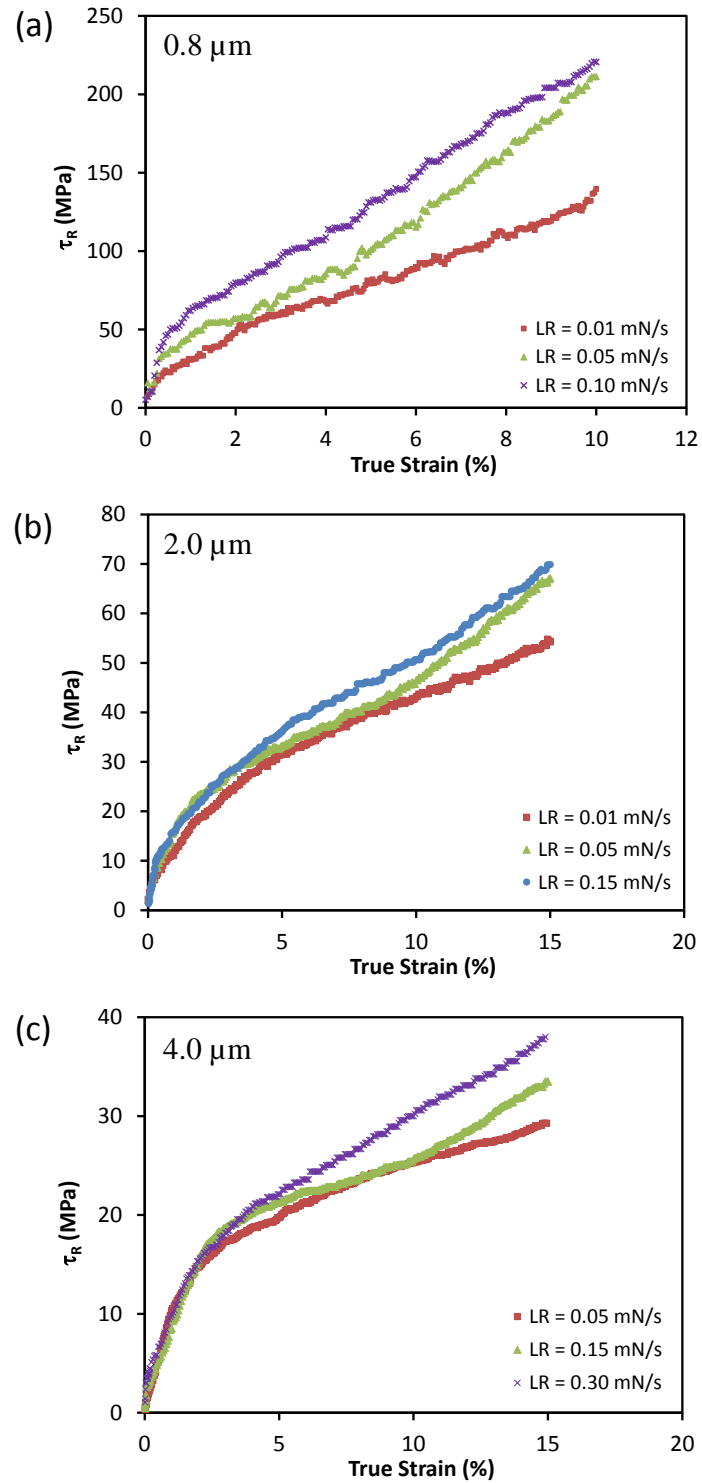
Figure 6.10: Critical resolved shear stress, τ_R versus true strain for (a) 0.8, (b) 2.0 and (c) 4.0 μm diameter Au micropillars, compressed at three loading rates ranging from 0.01 to 0.30 mN/s.

The surface area and volume of each Au microsphere was calculated prior to compression testing. The surface area to volume (SA/V) ratio was between 1 and 6, and increased with decreasing pillar diameter (Table 6.2).

Comparison of the results from the FIB-milled micropillars presented in this chapter with those from similar size annealed Au microspheres (Chapter 4) allows us to assess the effect of FIB-induced ion damage on the operative deformation mechanisms. Comparison of the *F-h* response of the micropillars and the microspheres (Figure 6.4 to Figure 6.6 and Figure 4.5) indicate that the number of discontinuities/load jumps is decreased in the micropillars compared to the similar size microspheres. These discontinuities are thought to result from dislocation nucleation at the free surface followed by rapid, uninhibited, motion of the dislocation through the defect-free sample. Since this appears to happen more frequently in the annealed Au microspheres we can conclude that the process of FIB milling invokes a certain amount of crystal defects in the micropillars and this tends to impede the dislocation motion. It should be noted that, since both the microspheres and the micropillars display similar increasing yield stress with decreasing sample size (Figure 4.8 and Figure 6.7 to Figure 6.9), the critical factor affecting the flow stress in the small size samples is the stress required to nucleate dislocations, most likely from the free surface of the sample, rather than the stress required to move the dislocations through the sample.

Further comparison between the Au micropillars and microspheres can be done by assessing their flow stress as a function of their SA/V ratio. For the microspheres the bottom surface of the sphere is attached to the sapphire substrate and it was found from the SEM images that 1/4 of the ideal sphere radius was reduced. Therefore, the reduced surface area and volume were calculated using partially-filled sphere standard formulae[4].

---

[4] For an ideal sphere, the surface area, $SA_I = 4\pi r^2$ and volume, $V_I = (4/3)\pi r^3$, where, r = sphere radius. If the sphere height is reduced by the amount of h_R, from the bottom/top of the sphere then, the sphere reduced surface area, $SA_R = 2\pi r h_R$ and reduced volume, $V_R = \pi h_R^2 (3r - h_R)/3$. The sphere actual surface area, $SA = SA_I - SA_R$ and actual volume, $V = V_I - V_R$ [35].

The calculated SA/V ratios for the Au microspheres of 6.0 to 0.8 µm diameter were found between 1 and 7.

Figure 6.11 depicts the compressive yield stress versus true strain and SA/V ratio for Au micropillars tested at a loading rate of 0.05 mN/s. In this plot, the data of 1.0 µm diameter pillars were obtained from Chapter 3. For a given level of strain, the yield stress increased significantly as the SA/V ratio increases (i.e. pillar diameter decreases). For example, the yield stress at 5% strain increased from 102 to 350 MPa as the SA/V ratio increased from 1 to 6. It is notable in Figure 6.11b that the yield stress increased significantly when SA/V ratio is above 5. This suggests that the basic operative mechanism of plastic deformation may be different in small test specimens when SA/V > 5.

Figure 6.12 shows the von Mises equivalent average centre-line stress − strain response for the Au microspheres reported in Chapter 4. For these microspheres the equivalent stress, corresponding to 5% equivalent strain, increased from 100 to 225 MPa with increasing SA/V ratio from 1 to 7. Like the micropillar data shown in Figure 6.11, a significant increase of the von Mises flow stress occurred when SA/V > 5.
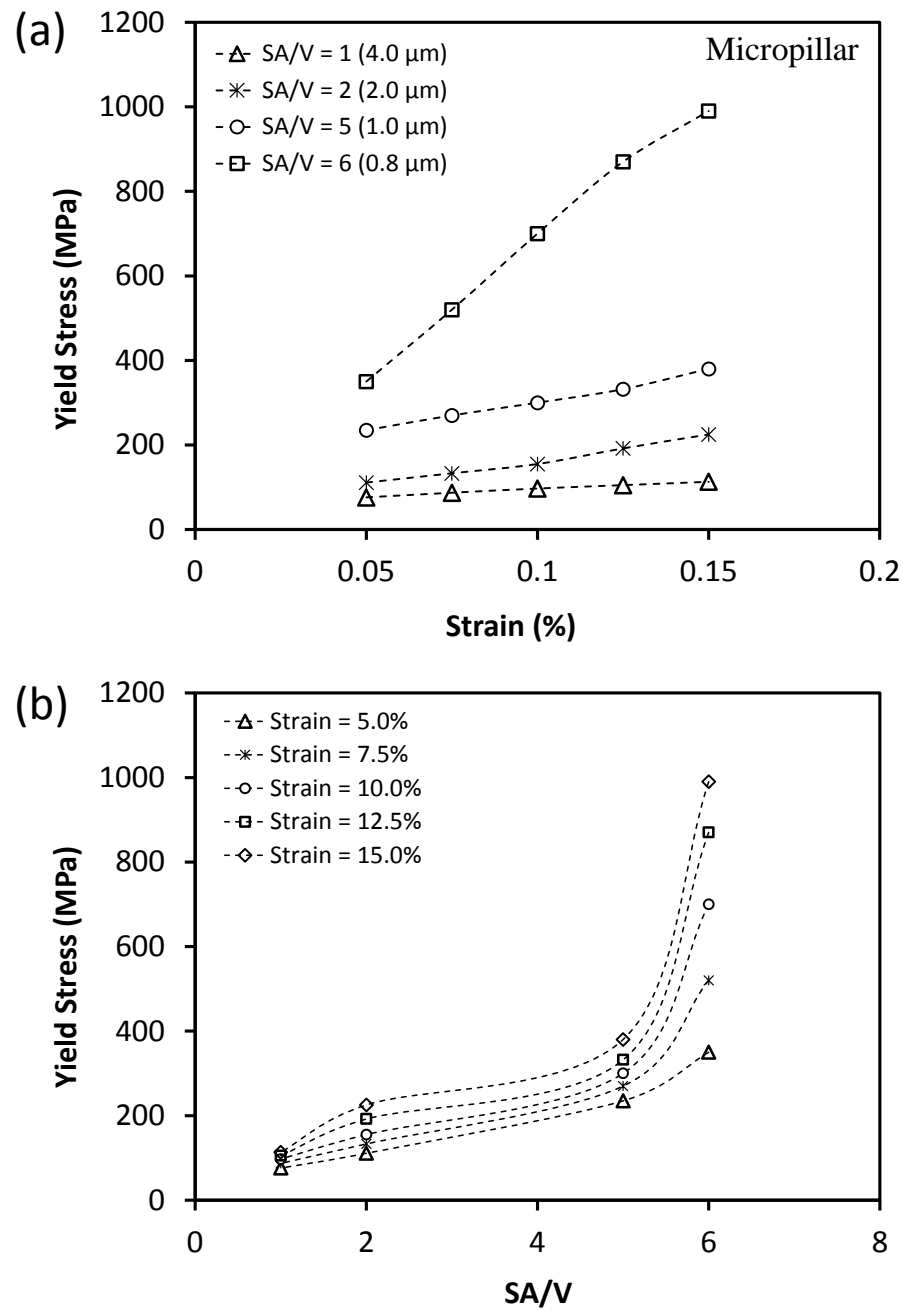
Figure 6.11: Effect of surface area to volume (SA/V) ratio on yield stress during Au micropillar deformation process. (a) Plot of the yield stress against strain for different SA/V ratios and (b) Shows the change of yield stress as a function of SA/V ratio at constant strain levels. The 1.0 µm diameter pillar data were obtained from Chapter 3.
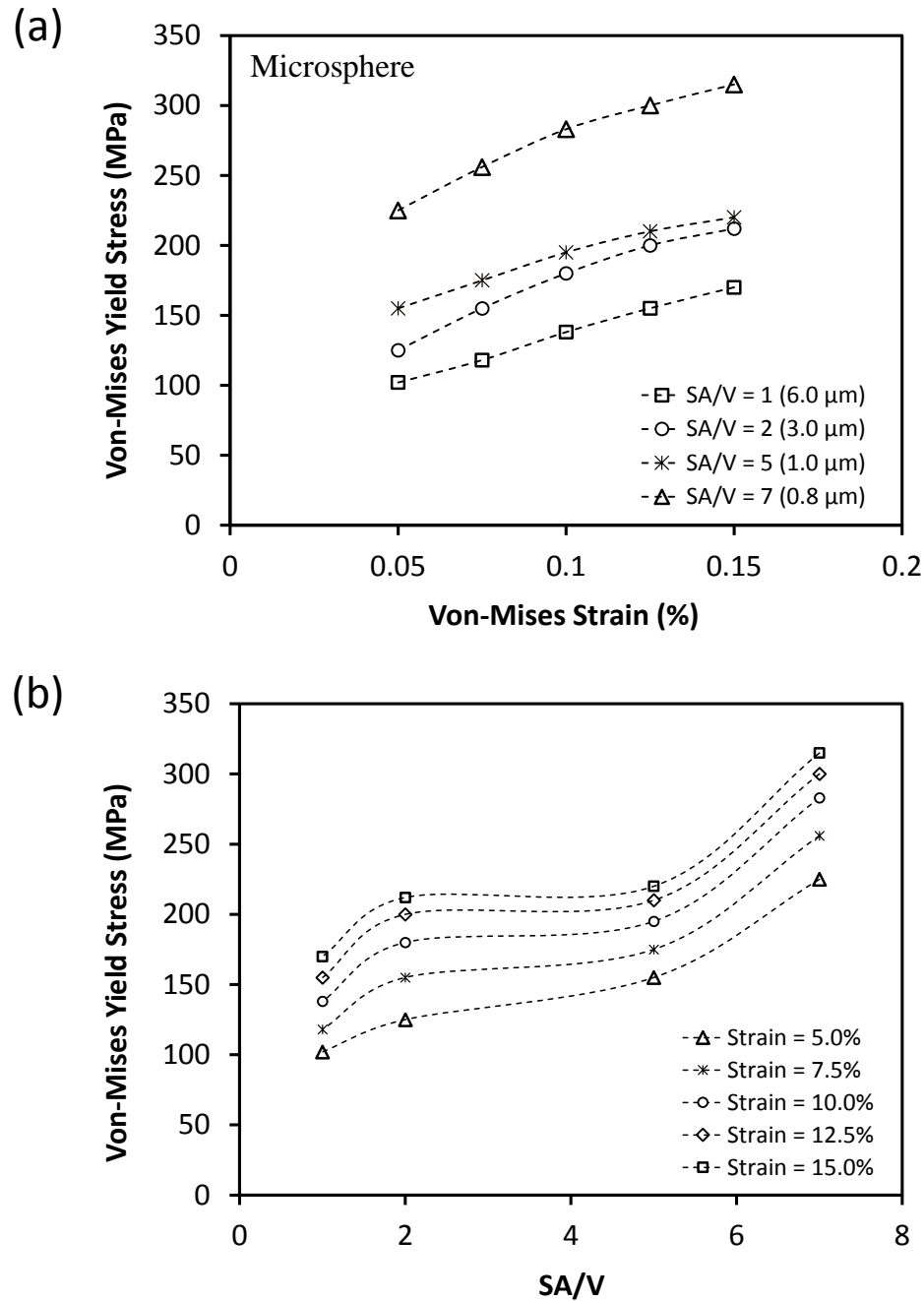
Figure 6.12: Effect of surface area to volume (SA/V) ratio on yield stress during Au microspheres deformation process. (a) Plot of the von Mises yield stress against strain for different SA/V ratios and (b) Shows the change of von Mises yield stress as a function of SA/V ratio at constant strain levels. The microspheres data were obtained from Chapter 4.

6.4 Analysis and Discussion

6.4.1 Prediction of Bulk Deformation

Besides enhanced strain rate sensitivity with decreasing micropillar size it is clear from Figure 6.7 to Figure 6.9 that small diameter pillars display a significantly higher flow stress than large diameter pillars and this is consistent with previously reported length scale-dependence of plasticity [2–4,6,10,13]. The strain, strain rate and temperature dependence of the flow stress σ of plastically deforming metals is often described in terms of an Arrhenius relationship of the following type [14];

$$\sigma = A\varepsilon^n \dot{\varepsilon}^m exp\left[-\frac{Q}{RT}\right]$$
(6.4)

where ε is strain, $\dot{\varepsilon}$ is strain rate, A is a material constant, n is the strain hardening exponent, m is the strain rate sensitivity exponent, Q is the thermal activation energy of the operative deformation mechanism, T is the absolute temperature and R is the universal gas constant. Figure 6.13 shows the logarithmic σ - $\dot{\varepsilon}$ response at $\varepsilon = 5\%$ for the 0.8, 2.0, and 4.0 µm diameter micropillars. The slope m of the data increases as the pillar diameter decreases.

Using the strain rate sensitivity values m, the apparent activation volume V^* characterizing the operative deformation rate limiting dislocation nucleation/glide mechanism can be calculated as [15–17];

$$V^* = \sqrt{3}kT/m\sigma$$
(6.5)

where k is the Boltzmann constant. With the above equation, the strain dependence of V^* was calculated for all the Au micropillars tested. In this calculation both the flow stress σ and resolved shear stress τ_R corresponding to $\varepsilon = 5\%$ were used in Eq. 6.5 to calculate V^*. As was mentioned earlier, τ_R was calculated from σ_T by using Eq. 6.1 and the maximum Schmid factor, calculated by EBSD assessment of the <hkl> orientation of the specific micropillar and the assumption that dislocation slip occurs on the <110>{111} slip system.

The calculated V^* values are listed in Table 6.3 and Table 6.4. The calculated V^* are normalized with respect to b^3, where the Burgers vector of Au was taken as $b = 0.289$ nm [18,19]. When the Au pillar diameter increased from 0.8 to 4.0 µm, V^* increased from $3b^3$ to about $57b^3$ when flow stress σ_T was used and from $10b^3$ to about $178b^3$ when the resolved shear stress τ_R was used in Eq. 6.5.
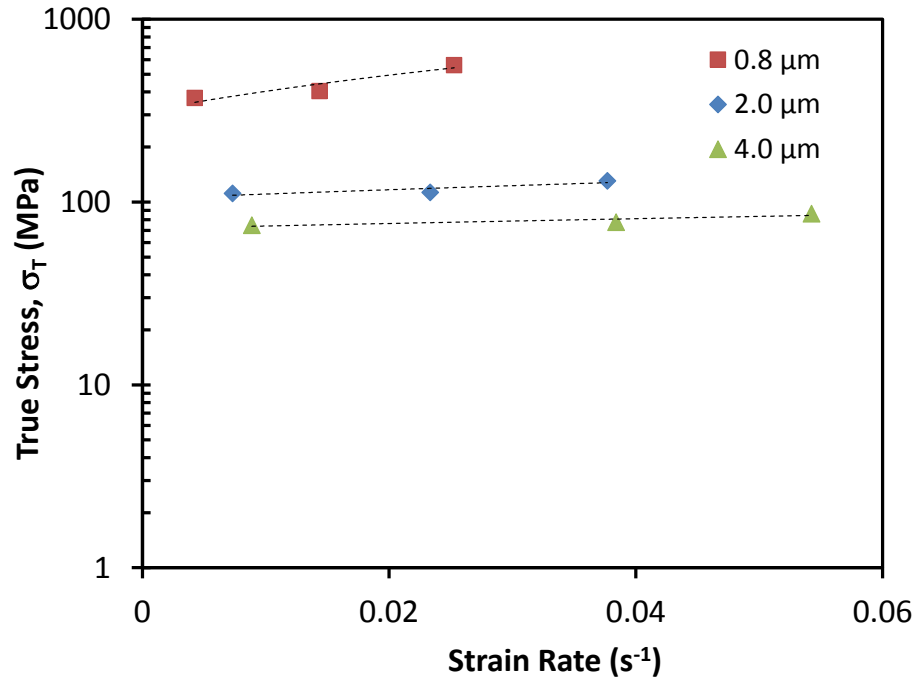
Figure 6.13: Logarithmic plot of flow stress σ_T, corresponding to $\varepsilon = 5\%$, versus strain rate. The calculated strain rate sensitivity exponent $m = 0.29$, 0.10 and 0.08 for the 0.8, 2.0 and 4.0 µm diameter Au pillars respectively.

The low V^* values, about $3b^3$, for the smaller diameter pillars is similar in magnitude to previously reported estimates for *FCC* metal nano-size samples that are deforming by a dislocation nucleation limited mechanism of plastic deformation [20]. The V^* magnitude $(31 - 57b^3)$ of the larger diameter pillars, is typical of the operation of a dislocation-obstacle interaction limited deformation mechanism which is common in bulk ductile metals [21].

The obtained V^* values were converted to parameters of apparent activation energy Q^*, necessary for a dislocation to overcome the obstacles that impede its movement through the sample using the relation [22]

$$Q^* = \tau V^* \hspace{4cm} (6.6)$$

In order to estimate the total athermal apparent activation energy, Q^*, of the deformation rate controlling obstacles, the estimated theoretical athermal stress of Au, $\tau_{0K} = 256$ MPa [23], was used along with values of V^* obtained in terms of the application of the normal stress σ_T and the resolved shear stress τ_R in Eq. 6.5. The calculated values of Q^* range between 0.12 to 2.20 eV when σ_T was considered and 0.38 to 6.85 eV when τ_R was considered but, in either case, Q^* increased with increasing micropillar diameter (Table 6.3 and Table 6.4).

In the case when Q^* is small, about 0.2 eV, the operative dislocation-obstacle interaction strength is weak and dislocation glide is essentially controlled by the lattice resistance [23]. The small values of Q^* observed for the small diameter Au micropillars suggest that this type of dislocation-obstacle interaction is occurring and is consistent with a very low number of dislocations being present within an otherwise perfect Au crystal. In the case of the larger diameter pillars Q^* is considerably larger, between 1 and 2 eV, suggesting that the rate of deformation is limited by the rate at which dislocations overcome stronger obstacles present in the microstructure of the pillar [23]. In the case of the larger diameter Au pillars, the internal obstacles to dislocation glide will be other dislocations present as dislocation clusters (or networks) created as a result of the plastic deformation process.

Table 6.3: The estimated apparent activation volume and energy during micropillar deformation, when the normal flow stress, σ_T was considered in Eq. 6.5.

Pillar Size	Deformation parameters at 5% of strain, considering σ_T in Eq. 6.5	
(µm)	Apparent activation volume, V^* (b^3)	Apparent activation energy, Q^* (eV)
0.8	3	0.12
2.0	31	1.19
4.0	57	2.20

Table 6.4: The estimated apparent activation volume and energy during micropillar deformation, when the resolved shear stress, τ_R was considered in Eq. 6.5.

Pillar Size	Deformation parameters at 5% of strain, considering τ_R in Eq. 6.5	
(µm)	Apparent activation volume, V^* (b^3)	Apparent activation energy, Q (eV)
0.8	10	0.38
2.0	87	3.35
4.0	178	6.85

6.4.2   Prediction of Incipient Deformation

During the early stage of plastic deformation noticeable jumps are displayed in the σ–ε response of sub-micrometer size metal samples. These "incipient" deformation events occur as a result of the nucleation of individual, or small groups of, dislocations followed by their rapid glide through otherwise perfect crystalline material culminating in their formation of a surface step when they reach the free surface of the sample. The magnitude of incipient deformation events decreases with increasing plastic strain or with increasing sample size since, in both cases, the crystal structure of the sample becomes more defected which complicates the operative mechanisms by which plastic deformation occurs.

In this section, the early stage of plastic deformation behavior of the Au micropillars, is studied to understand further the operative deformation mechanisms controlling the incipient plasticity events.

6.4.2.1 Estimation of the Initial Yield Stress

The variation of initial portion of the true stress-strain (σ_T-ε_T) curves obtained from the compression of Au micropillars is shown in Figure 6.14 to Figure 6.16. Included in the Figures are the linear elastic σ-ε trends calculated by applying the Hooke's law (E_{Au} = 79 GPa [24,25]).
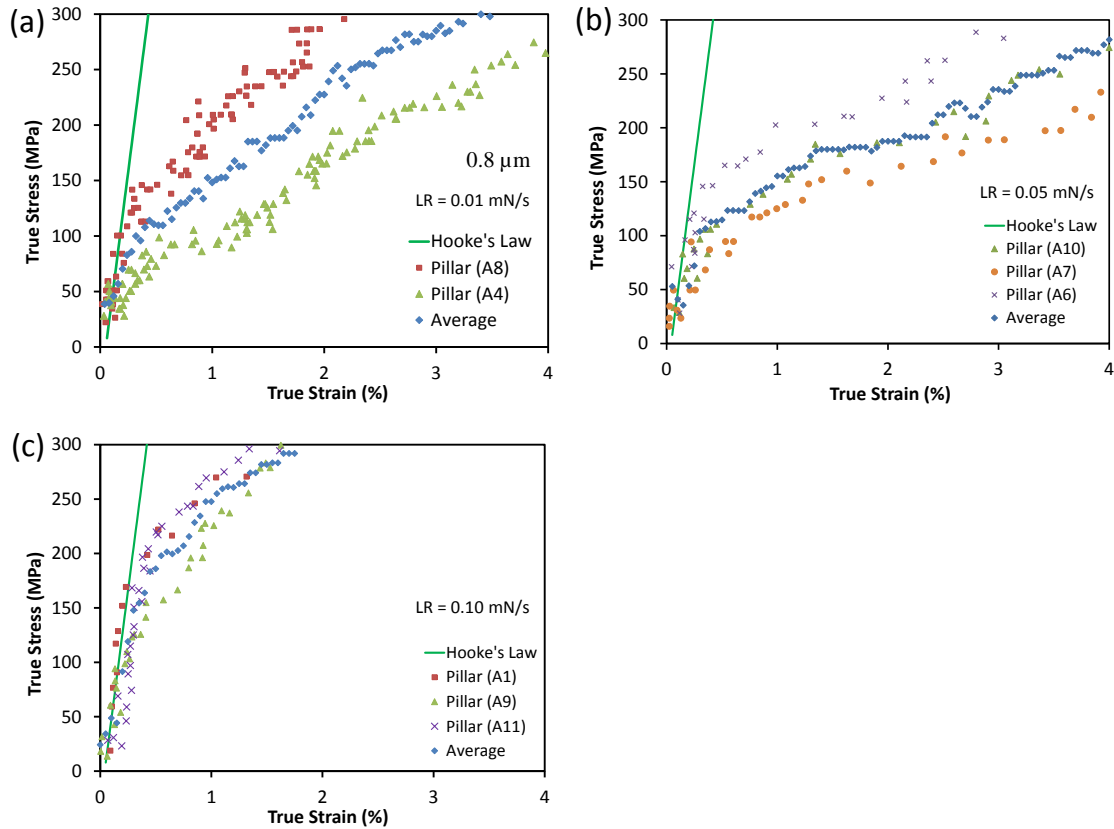
Figure 6.14: Initial portion of the individual true stress vs true strain curves of 0.8 µm diameter Au microspheres tested at loading rates of (a) 0.01, (b) 0.05 and (c) 0.10 mN/s, fitted with the elastic stress-strain response predicted by Hooke's law (solid green lines).

The σ-ε elastic response predicted by the Hooke's elastic equation are compared to the initial portion of the experimentally obtained σ_T-ε_T curves. The first deviation from the Hooke's elastic stress-strain profiles is considered as the initiation of incipient plasticity. These figures indicate that the incipient stress clearly displayed an increasing trend with increasing loading rates for each micropillar diameter. This indicates that the initial yield

strength, of these samples is strain rate sensitive. The incipient yield stress for all the Au micropillars tested is shown in Table 6.5.
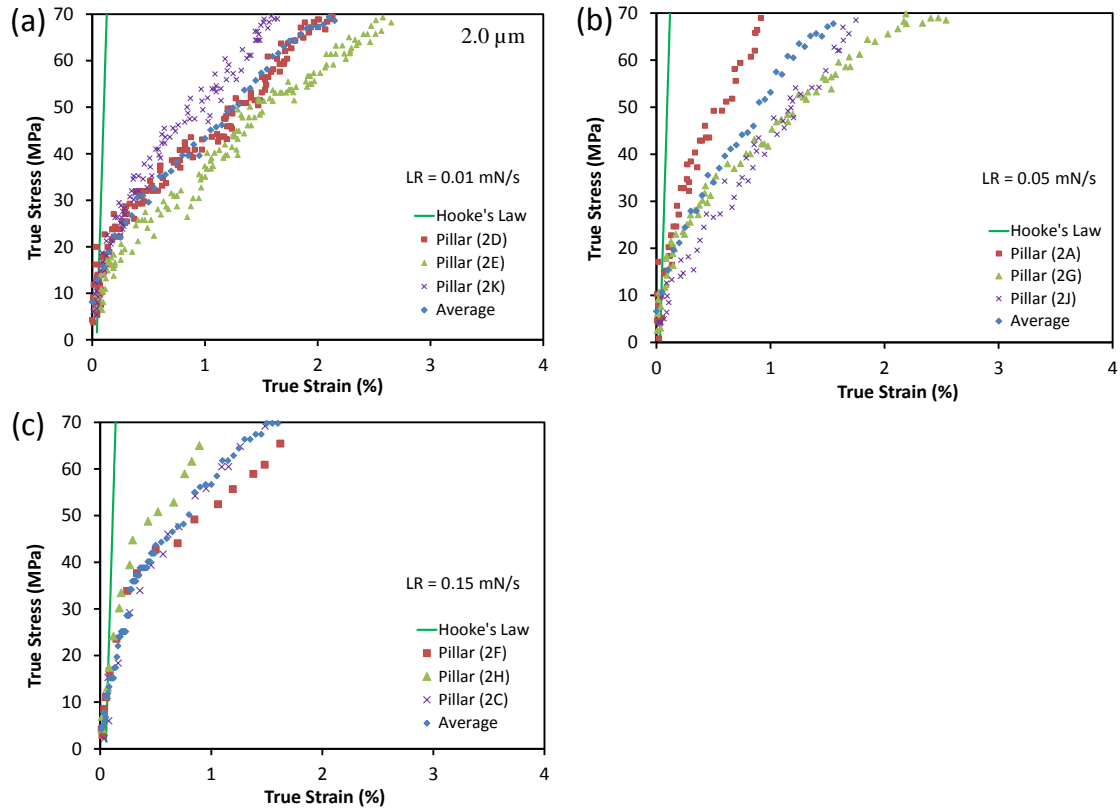
Figure 6.15: Initial portion of the individual true stress vs true strain curves of 2.0 µm diameter Au microspheres tested at loading rates of (a) 0.01, (b) 0.05 and (c) 0.15 mN/s, fitted with the elastic stress-strain response predicted by Hooke's law (solid green lines).
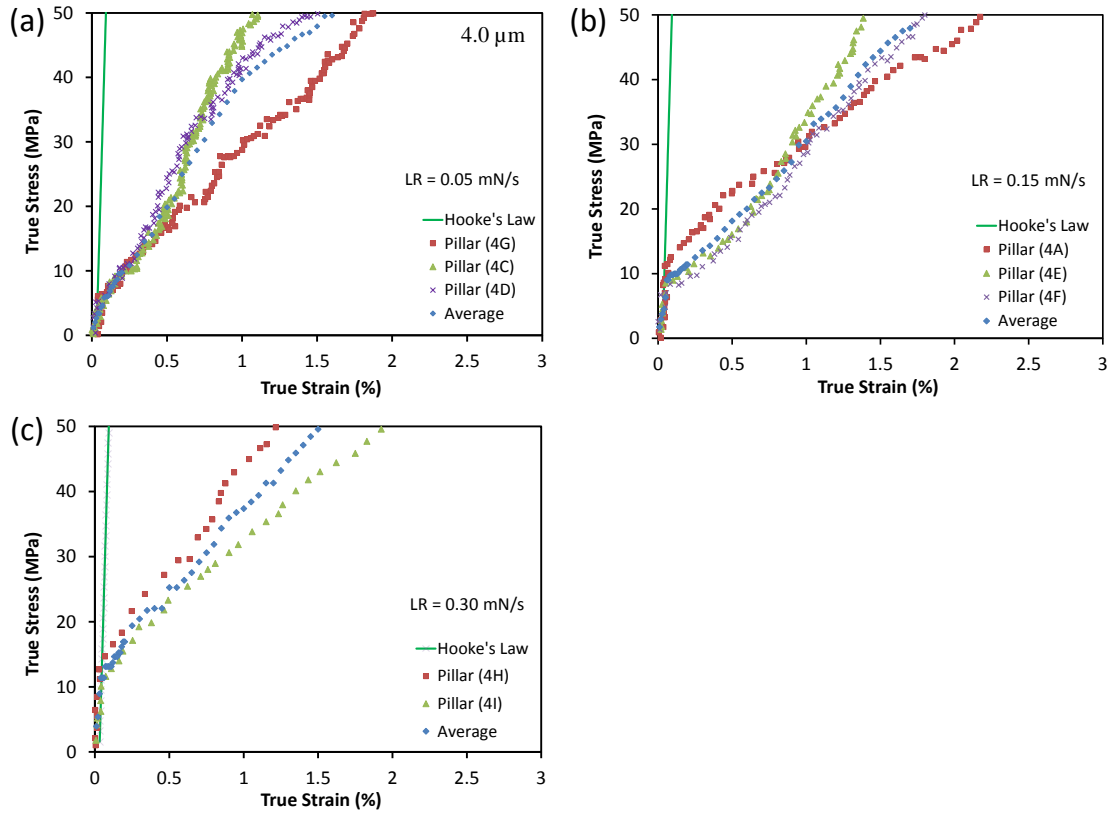
Figure 6.16: Initial portion of the individual true stress vs true strain curves of 4.0 µm diameter Au microspheres tested at loading rates of (a) 0.05, (b) 0.15 and (c) 0.30 mN/s, fitted with the elastic stress-strain response predicted by Hooke's law (solid green lines).

Table 6.5: Summary of loading rate and the corresponding initial yielding stress, incipient stress, of the tested Au micropillars

Au pillar diameter	Loading rate (mN/sec)	Strain rate (sec^{-1})	Incipient yield Stress (MPa)
	0.01	0.0032 ± 0.0033	89.2 ± 27.4
0.8 µm	0.05	0.0048 ± 0.0025	106.4 ± 33.4
	0.10	0.0062 ± 0.0043	158.4 ± 44.1
	0.01	0.0019 ± 0.0006	15.8 ± 2.0
2.0 µm	0.05	0.0033 ± 0.0015	19.3 ± 0.8
	0.15	0.0041 ± 0.0010	26.2 ± 2.5
	0.05	0.0014 ± 0.0010	7.4 ± 0.8
4.0 µm	0.15	0.0031 ± 0.0019	9.4 ± 1.5
	0.30	0.0053 ± 0.0005	13.7 ± 1.2

6.4.2.2   The Kinetics of Incipient Deformation of Au Micropillars

The analysis technique described in Chapter 5 (Section 5.3.4) is used here to estimate the apparent activation volume V^*, a characteristic signature of the deformation rate controlling obstacles in these deforming Au micropillars.

The normalized shear stress, corresponding to the first incipient plastic strain event, τ_{incip}/G, obtained from multiplying the incipient normal yield stress (Table 6.5) with the maximum Schmid factor (Eq. 6.1 and Table 6.1) of the micropillars compressed at different strain rates is shown in Figure 6.17. In this plot the elastic shear modulus of G_{Au} = 23.8 GPa was used [26]. The incipient shear stress increases with increasing strain rate for all the pillars. The incipient shear stress of the 4.0 µm diameter pillars is the lowest while the 0.8 µm diameter pillars is the highest. Also included on the graph is the theoretical shear strength, which is normally estimated between ~G/30 to G/10 for *FCC* metals such as Au [12,27,28].

The strain rate dependence of the incipient yield stress suggests that the deformation mechanism controlling these events involve a time-dependent diffusion-controlled

deformation process. In that sense, the size dependence of the incipient yield stress can be explained by increased available vacancy sites as the surface area of the micropillar increases. Salehinia et al. [29] demonstrated that the presence of vacancies underneath the indenter during a nano-indentation hardness test on single crystal Ni strongly affects the incipient loads. Increased population of vacancies underneath the larger contact area of the larger diameter micropillars. This study showed that the vacancy concentration beneath a nano-indenter will influence the subsequent dislocation nucleation stress and can thus influence the time-dependence of the deformation process. Thus, a similar type of mechanism may be at work during the deformation of the Au micropillars in this study.
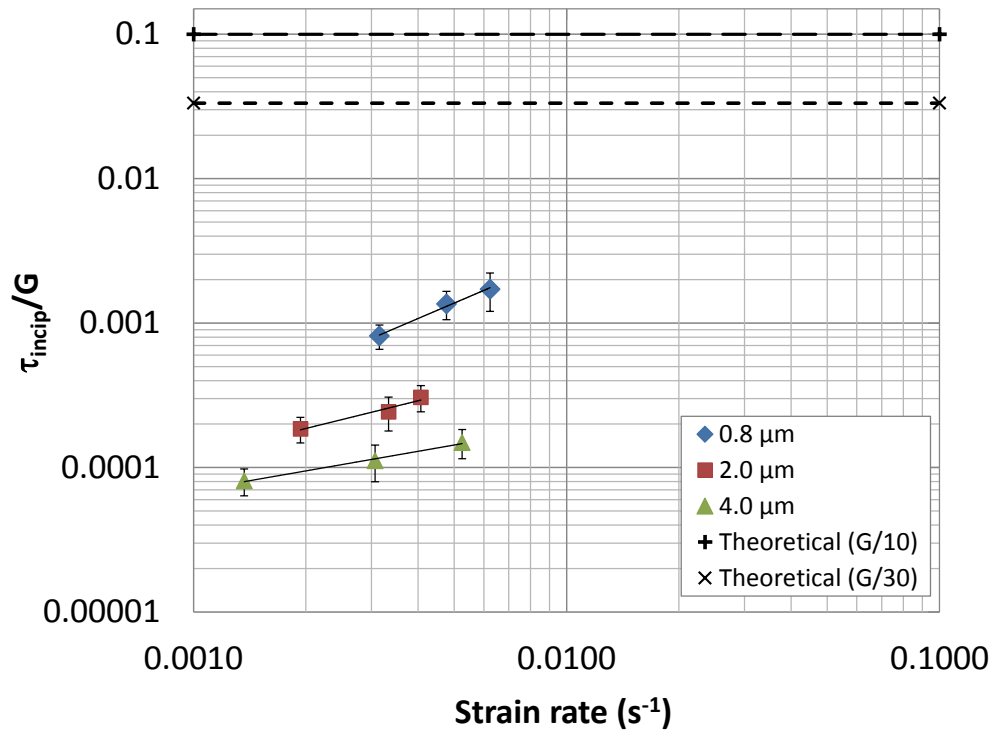
Figure 6.17: Normalized incipient shear stress versus strain rate of Au micropillars. Included in the plot are dashed lines indicating common estimates of the ideal theoretical shear strength ($\tau_{ideal} = G/30$ to $G/10$) of a metal.

The slope of strain rate dependence of τ in Figure 6.17 is kT/V^*, and thus provides information on the apparent activation Volume, V^*. The estimated values of V^* for the

micropillars, calculated by using this expression and the data from Figure 6.17 are listed in Table 6.6. The listed $V*$ are normalized with respect to b^3, where $b_{Au} = 0.289$ nm.

The estimated $V*$ during incipient plasticity of 0.8 µm diameter Au pillar is about $5.4b^3$. It is significant that the $V*$ values obtained here are lower than the $V*$ obtained during the bulk deformation ($\varepsilon = 5\%$). Similarly, the estimated average incipient $V*$ for the larger 2.0 and 4.0 µm diameter Au spheres are between 47 and $144b^3$ respectively.

Table 6.6: The estimated apparent activation volume and energy during incipient plasticity event of the tested Au micropillars when resolved shear stress was considered.

Deformation Parameters	0.8 µm Au	2.0 µm Au	4.0 µm Au
$V*$ (b^3)	5.4	47	144
$Q*$ (eV)	0.21	1.83	5.55

The lower activation volumes obtained here during initial yielding of Au micropillars is consistent with previously reported studies that have reported activation volumes of $1.5b^3$ for single crystalline Ni_3Al [30], $2 - 4b^3$ for Cu nanowire [31], $2.8b^3$ for Al nanoposts [20], $5.3b^3$ for Mo micropillar [32] and $9.6 - 62b^3$ for Cu nanopillars [33]. Molecular dynamic simulations performed by Zhu et al. have indicated that the process of dislocation nucleation from a metallic free surface has a characteristic activation volume between $1 - 10b^3$ [31]. In our study the low $V*$ is therefore attributed to heterogeneous dislocation nucleation events at pre-existing defects, such as individual vacancies or vacancy clusters located at, or near to, the free surface of the micropillars.

The estimated magnitudes of $V*$ ($5.4b^3$) and $Q*$ (~0.21eV) for 0.8 µm diameter Au pillars is of the order of surface self-diffusion based processes as reported by Liu et al. [34]. The estimated $Q*$ (~1.83 and ~5.55eV) for the 2.0 and 4.0 µm diameter Au micropillars suggests that deformation is controlled by a mechanism of obstacle-limited dislocation glide [23].

The above analysis of the sample size- and strain rate-dependence of the deformation of Au micropillars was performed by considering average pillar diameter and estimated Schmid factors determined from the EBSD analysis. The calculated values of V^* and Q^*, which are the fundamental findings of this study are highly dependent upon the magnitude of the pillar diameter and the calculated stress responsible for the plastic deformation process. In this chapter we calculated these parameters by considering the mean pillar diameter and either the average normal stress, σ or the resolved shear stress, τ acting on the close-packed crystal system displaying the highest Schmid factor. Table 6.7 shows values of V^* and Q^* calculated by three different approaches and a comparison plot between equivalent data from the Au micropillars and microspheres (Chapter 5) is shown in Figure 6.18.

In the case of the Au microspheres, the microsphere contact diameter with the flat-punch indenter used to determine the contact stress. This contact stress is therefore highly dependent upon the measured facet diameter and the assumption that, for the spheres since EBSD data were not available, the Schmid factor was 0.55. Therefore, to compare the microsphere results with the micropillar results, the additional analysis condition (c) in Table 6.7 was most appropriate, where the pillar top diameter and a Schmid factor of 0.55 was used. It is observed from Figure 6.18 that during the incipient plasticity event, the initial contact surface, play a very significant role. The initial contact surface, for the micropillars is the top diameter while for the microsphere it is the facet diameter which contacts the flat-punch indenter. The 0.8 µm diameter pillar and 3.0 to 6.0 µm diameter spheres have the same contact surface and the estimated V^* ($1.7 - 2.1b^3$) are also almost the same. However, for samples with larger contact surfaces, such as the 2.0 and the 4.0 µm diameter pillars, significantly higher V^* values were estimated ~17.9 to $49.5b^3$.

Table 6.7: Comparison of the estimated apparent activation volume (V^*) during incipient plasticity event of the tested Au micropillars, considering pillars average and top diameter for stress calculation, and also to compare the micropillar results with microsphere, same Schmid factor of microsphere (0.55) was used to calculate the shear stress

Au pillar size	Estimated incipient $V^*(b^3)$ of Au pillars in different condition, using Eq. 5.6				
	(a) Pillar average diameter		(b) Pillar top diameter		(c) Pillar top diameter and Schmid Factor = 0.55
	σ_T used	τ_R used	σ_T used	τ_R used	τ_R used
0.8 µm	1.8	5.4	1.3	3.9	2.3
2.0 µm	13.8	47.5	9.8	34.0	17.9
4.0 µm	38.1	144.0	27.2	102.8	49.5

Figure 6.18: A comparison of the normalized incipient shear stress versus strain rate of Au micropillars, from this chapter, and microspheres, from Chapter 5. In the plot, the V^* for micropillars are taken from Table 6.7 when condition (c) was considered.

6.5   Summary

In this study the sample size and strain rate dependence of the plastic deformation behavior of Au micropillars (0.8 to 4.0 µm diameter) subjected to uniaxial compression at ambient temperature was studied. It was observed that the dependence of the flow stress, after considerable plastic deformation corresponding to $\varepsilon = 5\%$, was dependent upon both strain rate and micropillar diameter. Analysis of the apparent activation volume, $V*$ and energy $Q*$ of the deformation process indicated that the operative deformation mechanism, for the small 0.8 µm diameter pillars was typical of a mechanism limited by the surface nucleation of dislocations, and for the larger 2.0 and 4.0 µm diameter pillars was controlled by the more common dislocation-obstacle interaction limited mechanism.

The deformation-rate dependence of the incipient plastic deformation behavior was also investigated for the micropillars. The incipient yield stress, for a particular sized micropillar, increased with increasing strain rate whereas, for a particular strain rate, it decreased with increasing micropillar diameter. The size dependence of incipient yield stress was attributed to the presence of vacancies whose amount increased, as a result of increased flat-punch/pillar contact area, in the larger diameter micropillars. The apparent activation volume, $V*$, and energy, $Q*$, values were found to be $5.4b^3$ and 0.21eV for 0.8 µm diameter pillars and increased to $144b^3$ and 5.55eV for 4.0 µm diameter pillars. These estimated values suggest that the incipient plasticity of the smallest diameter pillar is controlled by heterogeneous dislocation nucleation events occurring at, or near, the flat-punch/pillar top interface the rate of which is highly dependent upon the rate of surface self-diffusion based process.

The next chapter of this thesis will present the effect of a surface constraining layer on the mechanical yield strength and deformation mechanisms of Au microspheres.

References

1.   W. D. Callister, *Materials Science and Engineering: an Introduction*, 7th ed. New York, USA: John Wiley & Sons, Inc, 2007.

2.   J. Greer, 2006, "Bridging the gap between computational and experimental length scales: a review on nano-scale plasticity," *Rev. Adv. Mater. Sci*, Vol. 13, pp. 59–70.

3.   W. D. Nix, J. R. Greer, G. Feng, and E. T. Lilleodden, Feb. 2007, "Deformation at the nanometer and micrometer length scales: Effects of strain gradients and dislocation starvation," *Thin Solid Films*, Vol. 515, pp. 3152–3157.

4.   C. P. Frick, B. G. Clark, S. Orso, a. S. Schneider, and E. Arzt, Aug. 2008, "Size effect on strength and strain hardening of small-scale [111] nickel compression pillars," *Mater. Sci. Eng. A*, Vol. 489, pp. 319–329.

5.   D. Mordehai, S.-W. Lee, B. Backes, D. J. Srolovitz, W. D. Nix, and E. Rabkin, Aug. 2011, "Size effect in compression of single-crystal gold microparticles," *Acta Mater.*, Vol. 59, pp. 5202–5215.

6.   W. M. Mook, C. Niederberger, M. Bechelany, L. Philippe, and J. Michler, Feb. 2010, "Compression of freestanding gold nanostructures: from stochastic yield to predictable flow," *Nanotechnology*, Vol. 21, pp. 055701–9.

7.   A. S. Schneider, B. G. Clark, C. P. Frick, P. a. Gruber, and E. Arzt, May 2009, "Effect of orientation and loading rate on compression behavior of small-scale Mo pillars," *Mater. Sci. Eng. A*, Vol. 508, pp. 241–246.

8.   D. Mordehai, M. Kazakevich, D. J. Srolovitz, and E. Rabkin, Apr. 2011, "Nanoindentation size effect in single-crystal nanoparticles and thin films: A comparative experimental and simulation study," *Acta Mater.*, Vol. 59, pp. 2309–2321.

9.   S.-W. Lee, D. Mordehai, E. Rabkin, and W. D. Nix, Jul. 2011, "Effects of focused-ion-beam irradiation and prestraining on the mechanical properties of FCC Au microparticles on a sapphire substrate," *J. Mater. Res.*, Vol. 26, pp. 1653–1661.

10.   J. R. Greer, W. C. Oliver, and W. D. Nix, Apr. 2005, "Size dependence of mechanical properties of gold at the micron scale in the absence of strain gradients," *Acta Mater.*, Vol. 53, pp. 1821–1830.

11.   J. Greer and W. Nix, Jun. 2006, "Nanoscale gold pillars strengthened through dislocation starvation," *Phys. Rev. B*, Vol. 73, pp. 245410–6.

12.   H. Bei, S. Shim, G. M. Pharr, and E. P. George, Oct. 2008, "Effects of pre-strain on the compressive stress–strain response of Mo-alloy single-crystal micropillars," *Acta Mater.*, Vol. 56, pp. 4762–4770.

13. J. R. Greer, C. R. Weinberger, and W. Cai, Oct. 2008, "Comparing the strength of f.c.c. and b.c.c. sub-micrometer pillars: Compression experiments and dislocation dynamics simulations," *Mater. Sci. Eng. A*, Vol. 493, pp. 21–25.

14. R. W. Cahn, *Strengthening Methods in Crystals*, Vol. 17. Halstead Press Division, Wiley, 1972.

15. Y. Wang, a Hamza, and E. Ma, Jun. 2006, "Temperature-dependent strain rate sensitivity and activation volume of nanocrystalline Ni," *Acta Mater.*, Vol. 54, pp. 2715–2726.

16. H. Somekawa and C. A. Schuh, Dec. 2011, "Effect of solid solution elements on nanoindentation hardness, rate dependence, and incipient plasticity in fine grained magnesium alloys," *Acta Mater.*, Vol. 59, pp. 7554–7563.

17. T. Zhu, J. Li, S. Ogata, and S. Yip, Mar. 2009, "Mechanics of Ultra-Strength Materials," *MRS Bull.*, Vol. 34, pp. 167–172.

18. W. D. Nix and S. Lee, 2011, "Micro-pillar plasticity controlled by dislocation nucleation at surfaces," *Philos. Mag.*, Vol. 91, pp. 1084–1096.

19. V. Bhakhri and R. J. Klassen, Apr. 2009, "The strain-rate dependence of the nanoindentation stress of gold at 300 K: A deformation kinetics-based approach," *J. Mater. Res.*, Vol. 24, pp. 1456–1465.

20. W. M. Mook, M. S. Lund, C. Leighton, and W. W. Gerberich, Oct. 2008, "Flow stresses and activation volumes for highly deformed nanoposts," *Mater. Sci. Eng. A*, Vol. 493, pp. 12–20.

21. U. F. Kocks, a. S. Argon, and M. F. Ashby, Jan. 1975, "Thermodynamics and Kinetics of Slip," *Prog. Mater. Sci.*

22. J. M. Wheeler, C. Niederberger, C. Tessarek, S. Christiansen, and J. Michler, Jan. 2013, "Extraction of plasticity parameters of GaN with high temperature, in situ micro-compression," *Int. J. Plast.*, Vol. 40, pp. 140–151.

23. F. H. J. and M. F. Ashby, *Deformation-Mechanism Maps*, 1st ed. New York, USA: Pergamon Press, 1982.

24. C. A. Volkert and E. T. Lilleodden, Nov. 2006, "Size effects in the deformation of sub-micron Au columns," *Philos. Mag.*, Vol. 86, pp. 5567–5579.

25. C. A. Volkert, E. T. Lilleodden, D. Kramer, and J. Weissmüller, 2006, "Approaching the theoretical strength in nanoporous Au," *Appl. Phys. Lett.*, Vol. 89, p. 061920.

26. Y. Kamimura, K. Edagawa, and S. Takeuchi, 2013, "Experimental evaluation of the Peierls stresses in a variety of crystals and their relation to the crystal

structure," *Acta Mater.*, Vol. 61, pp. 294–309.

27. D. Hull and D. Bacon, *Introduction to dislocations*, 4th ed. Jordan Hill, Oxford: Butterworth-Heinemann, 2001.

28. S. S. Brenner, 1956, "Tensile strength of whiskers," *J. Appl. Phys.*, Vol. 27, pp. 1484–1491.

29. I. Salehinia, V. Perez, and D. F. Bahr, 2012, "Effect of vacancies on incipient plasticity during contact loading," *Philos. Mag.*, Vol. 92, pp. 550–570.

30. P. C. Wo, L. Zuo, and a. H. W. Ngan, 2005, "Time-dependent incipient plasticity in Ni3Al as observed in nanoindentation," *J. Mater. Res.*, Vol. 20, pp. 489–495.

31. T. Zhu, J. Li, A. Samanta, A. Leach, and K. Gall, 2008, "Temperature and strain-rate dependence of surface dislocation nucleation," *Phys. Rev. Lett.*, Vol. 100, p. 25502.

32. A. S. Schneider, B. G. Clark, C. P. Frick, and E. Arzt, Jan. 2009, "Correlation between Activation Volume and Pillar Diameter for Mo and Nb BCC Pillars," *MRS Proc.*, Vol. 1185, pp. 1185–II07–04.

33. A. T. Jennings and J. R. Greer, Mar. 2011, "Tensile deformation of electroplated copper nanopillars," *Philos. Mag.*, Vol. 91, pp. 1108–1120.

34. C. L. Liu, J. M. Cohen, J. B. Adams, and a F. Voter, 1991, "EAM study of surface self-diffusion," *Surf. Sci.*, Vol. 253, pp. 334–344.

35. A. D. Polyanin and A. V. Manzhirov, "Handbook of Mathematics for Engineers and Scientists," Chapman & Hall/CRC, Taylor & Francis Group, 2007, pp. 68–69.

Chapter 7

7 Effect of a Surface Constraining Layer on the Plastic Deformation of Au Microspheres

Single crystal Au microspheres of 3 μm diameter were coated with a sputter-deposited nano-crystalline Ni layer of 40 or 80 nm thickness to study the effect of extrinsic constraint on the mechanical yield strength and deformation mechanisms of micrometer-size ductile metal samples. Room temperature compression tests were performed at three loading rates. SEM images of the deformed microspheres displayed micro-cracking of the deposited Ni layer during plastic deformation. Force-displacement (*F-h*) curves of the coated Au microspheres were obtained and compared with *F-h* curves from similar diameter uncoated Au spheres. The initial portion of the *F-h* curves was fitted with a Hertzian contact model and the corresponding incipient force was measured.

The estimated apparent activation volume and energy corresponding to the initiation of incipient plasticity is nearly identical for the coated and the uncoated Au microspheres which suggests that the mechanism responsible for the initiation of first dislocation motion in the Au microspheres is essentially the same regardless of the presence of a constraining coating however the Ni coating does raise the stress required for dislocation nucleation slightly.

The apparent activation volume and energy of the rate-dependent deformation process after the Au microspheres have endured significant (about 5%) plastic strain is increased for the coated spheres compared to the uncoated spheres and increases with increasing Ni layer thickness. This reflects the effect of the Ni layer in constraining the motion of mobile dislocations and preventing them from reaching the free surface of the microspheres.

7.1   Introduction

It is well established that small metal samples, with length dimensions in the nanometer or micrometer range, display considerably enhanced mechanical strength compared to their bulk counterparts [1–7]. The data presented for such systems indicate quite conclusively that this increase in strength is due to a transition in the operative deformation mechanisms from one controlled by dislocation-obstacle interactions to one controlled by dislocation nucleation. In addition to this "intrinsic" deformation mechanism transition, the deformation of small samples is often affected by physical constraint imposed by rigid surrounding material. In such situations an increased density of "geometrically necessary" dislocations within the small sample is necessary to accommodate this constraint. Little experimental data exist on the effect of such extrinsic constraint on the activation energy of the dislocation nucleation and glide processes in these small ductile samples.

The majority of experiment-based studies of the effect of geometrical constraint on the deformation of micrometer-scale metal samples have been performed with coated- and noncoated- thin metal films [8–13]. The flow stress in the coated, also referred to as passivated, thin films is usually higher than the flow stress of the non-passivated films. Plastic deformation occurs by discrete dislocation glide through the thin metal film [14]. If the film is coated by a harder, adherent, layer the threading dislocation cannot leave the ductile material and the resulting dislocation pileup effectively hardens the metal film [15].

While polycrystalline metal thin films are employed widely in many applications, micro-spherical particles are also now being used in diverse applications such as, for example, pharmaceutical drug delivery systems or Li-storage media in Li-ion batteries. The increased application of surface-coated metal microspheres has motivated the study, described in this chapter, of the effect of passive Ni layer thickness on the strength and ductility of 3 µm diameter Au microspheres.

7.2   Materials and Methods

7.2.1   Sample Preparation and Passivation Layer

Gold microspheres were fabricated on a (0001)-oriented sapphire (α-Al_2O_3) surface. An A8 PMMA positive photoresist layer was spin-coated on an O_2 plasma cleaned sapphire wafer and e-beam lithography was used to project a grid of 8 µm diameter circles upon the photoresist. After the exposed photoresist was removed, a polycrystalline Au film of 400 nm thickness was deposited by e-beam evaporation. The remaining photoresist was then removed and the resulting Au cylinders, of 8 µm diameter and 0.4 µm height, were annealed in-vacuum at 1000°C. During annealing the Au de-wetted from the sapphire substrate and took the form of facetted single-crystal spheres of 3 µm diameter. The facets were {111} planes [16–18]. About 100 Au microspheres were fabricated. Sputter deposition technique was then used to deposit Ni layers of either 40 or 80 nm thickness on to these microspheres (Figure 7.1). An Edwards Auto500 sputter deposition tool, equipped with a thickness monitor, was used to perform the Ni layer deposition. A FIB-prepared cross sectional image of a 3 µm diameter Au microsphere containing a 40 nm thick Ni layer is shown in Figure 7.2. The e-beam deposited Ni layer has a grain size of less than 100 nm.
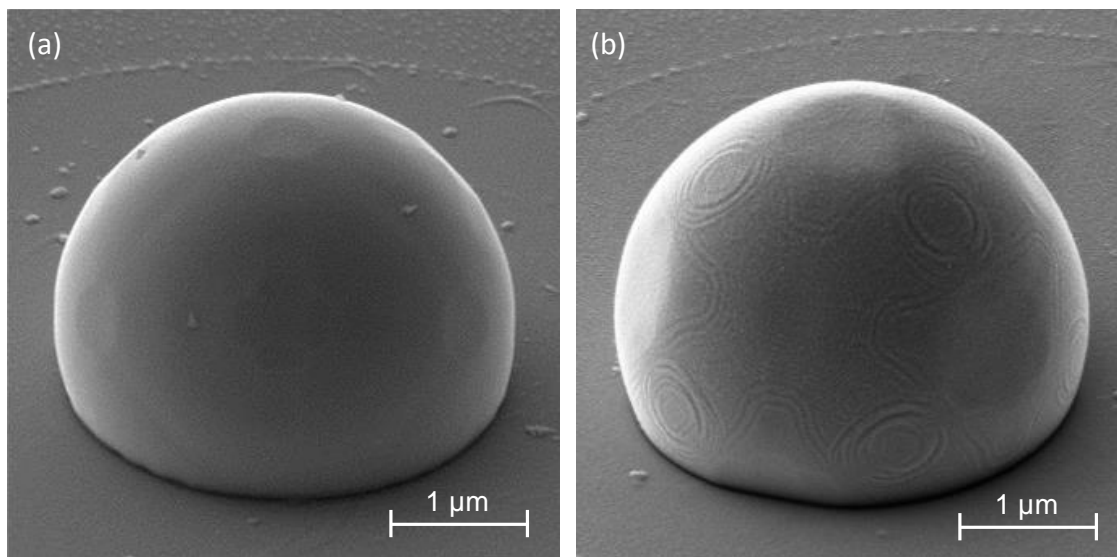
Figure 7.1: SEM images of 3 µm diameter Au microsphere coated with nanocrystalline Ni layer of (a) 40 and (b) 80 nm thickness.
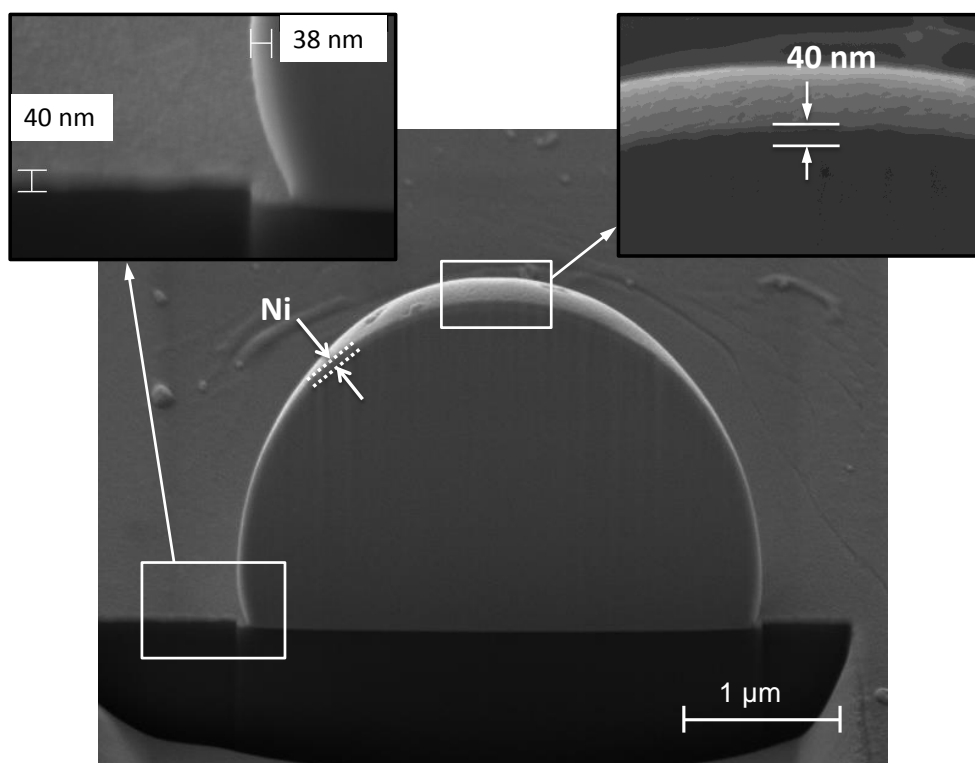
Figure 7.2: SEM images of a FIB milled cross-sectional view of a 40 nm Ni coated 3 µm diameter Au microsphere. The inset images display the deposited Ni layer around the Au periphery of the microsphere.

7.2.2   Microsphere Compression

The Ni-coated Au microspheres were compressed with an instrumented NanoTest platform made by Micro Materials Ltd (Wrexham, UK) fitted with a 9 µm diameter diamond flat punch indenter. About 40 compression tests were performed. The compression tests were carried out by loading the indenter at a constant loading rate to a maximum depth of about 20% of the initial sphere diameter. Three loading rates ranging from 0.05 to 0.50 mN/sec were used to study the effect of the Ni layer on the plastic deformation of the spheres.

7.2.3   Finite Element Simulation of the Microsphere Compression

FE simulations of the microsphere compression were implemented using the axisymmetric 2D mesh shown in Figure 7.3. The shape and dimensions of the 3 µm diameter Au microsphere were obtained from measurements made from SEM images as described in detail in Section 4.2.3. Isotropic elastic properties of the Au, $E = 79$ GPa [19], and $\nu = 0.42$ [20], were used for the microsphere. The plastic properties of Au were defined in the model by selecting the same multi-linear isotropic plastic flow curve of 3 µm diameter Au sphere, based on the plastic properties of Au at loading rates of 0.05, 0.15 and 0.50 mN/s (Section 4.2.3). For the Ni layer, isotropic elastic properties were again assumed, $E = 207$ GPa and $\nu = 0.31$ [6], and the plastic properties were defined by the plastic properties reported for nano-crystalline Ni of $53 - 137$ nm grain sizes from [21] at room temperature.
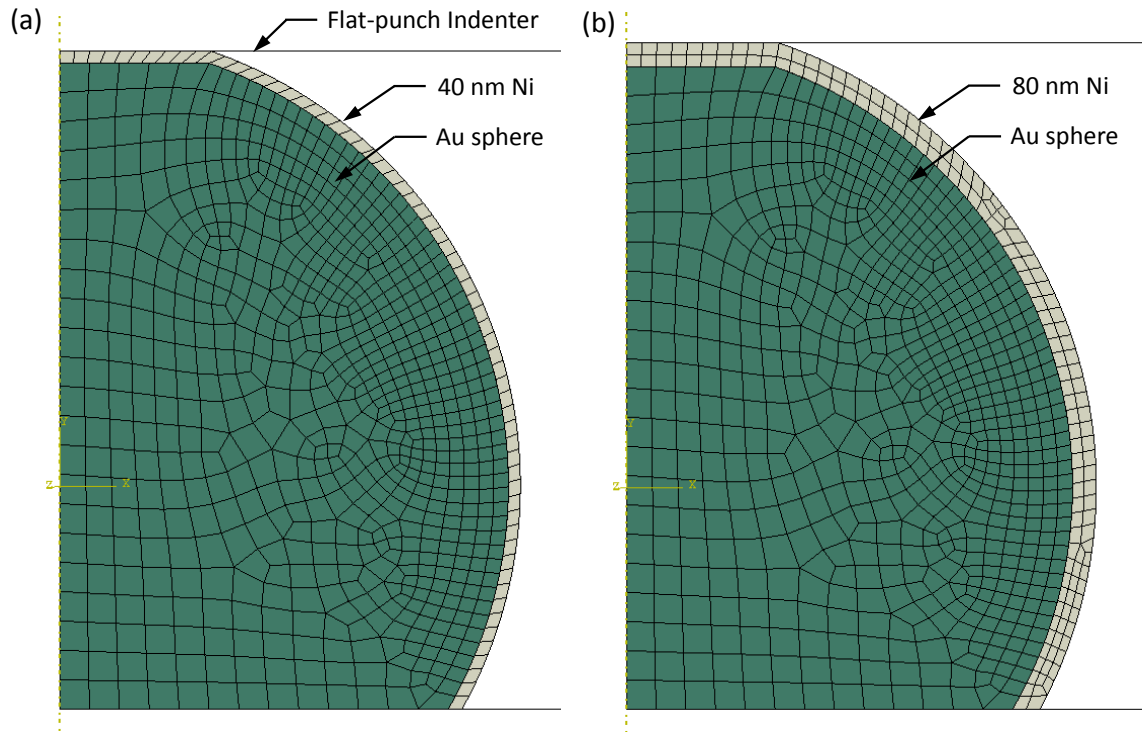
Figure 7.3: Finite Element model of a 3 µm Au sphere coated with a Ni layer of (a) 40 and (b) 80 nm thickness.

In the simulation, the flat-punch indenter and the substrate beneath the sphere were assumed to be rigid and frictionless. Both the Ni layer and microsphere were meshed with 4-node quadratic axisymmetric quadrilateral elements. The compression process was simulated by imposing downward displacement of the nodes at the flat punch/Ni coating interface. All simulations were done by defining multiple analysis steps. Two different types of interaction properties were defined between the Au sphere and coated Ni layer to understand the failure mechanism: (a) a surface based frictionless contact, that connect between two deformable bodies and (b) a surface based tie constraints, which ties two surfaces together for the duration of the simulation. The average experimental *F-h* curve obtained from the experiment and from these two different FE models of 3 µm Au spheres, containing Ni surface coatings of 40 or 80 nm thickness are shown in Figure 7.4. The *F-h* responses from both of the frictionless contact and tie constraint Ni layer model showed the same trend as the experimental *F-h* curve obtained at different loading rates. In comparison of the bonding between the Au sphere and Ni layer, the tie constraint

model required slightly more force to compress the sphere then the frictionless contact model for both of Ni layer thicknesses (Figure 7.4).
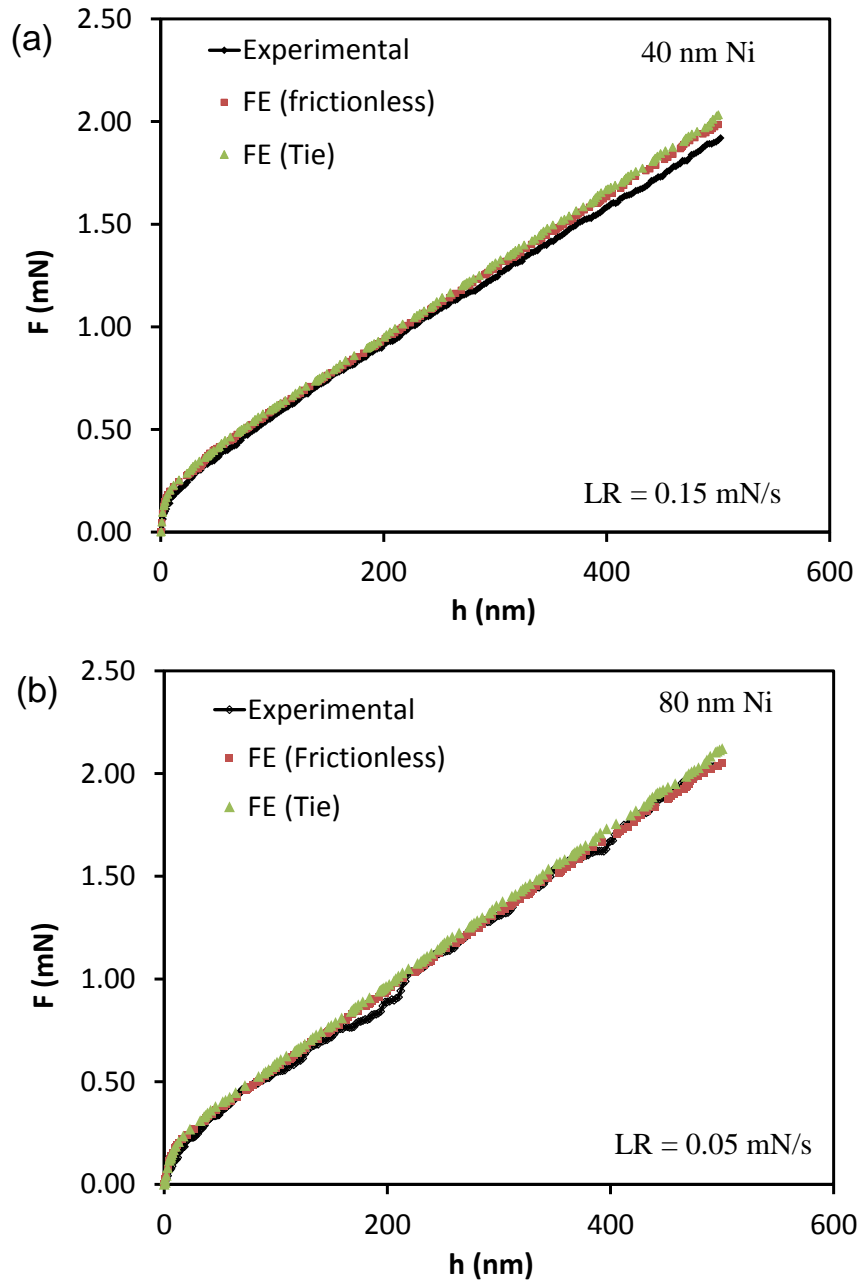
Figure 7.4: *F* vs. *h* responses obtained from the FE simulations and the experiments for the compression of 3 µm diameter Au spheres coated with a: (a) 40 and (b) 80 nm thickness Ni layer. Two criteria are used in the FE simulation to simulate the extreme cases of Ni/Au bonding: i) Frictionless sliding contact and ii) rigid "Tie" bonding.

7.3 Data Analysis

7.3.1   Experimental Micro-compression of Passivated Spheres

Figure 7.5 shows the experimental force-displacement (*F-h*) response, at the three loading rates, of the 40 and 80 nm thick Ni-coated Au microsphere. The deformation force, *F,* of the coated microspheres shows a dependence upon loading rate similar to what was observed for the uncoated microspheres (Figure 4.5c, Chapter 4).

Both the coated microspheres did not display noticeable load jumps during the initial deformation up to about 100 nm. This is in contrast to similar diameter uncoated Au microspheres which displayed distinct load jumps features in this initial deformation range. After about 100 nm deflection the 80 nm thick Ni-coated microspheres showed similar discrete load jump features as the uncoated 3 µm Au spheres. In contrast, the 40 nm thick Ni-coated spheres displayed much smoother *F-h* response over a much larger deflection up to about 500 nm (Figure 7.5). SEM images of the deformed Ni-coated Au microspheres are shown in Figure 7.6. Both thicknesses of coated spheres showed cracked Ni layers after deformation.
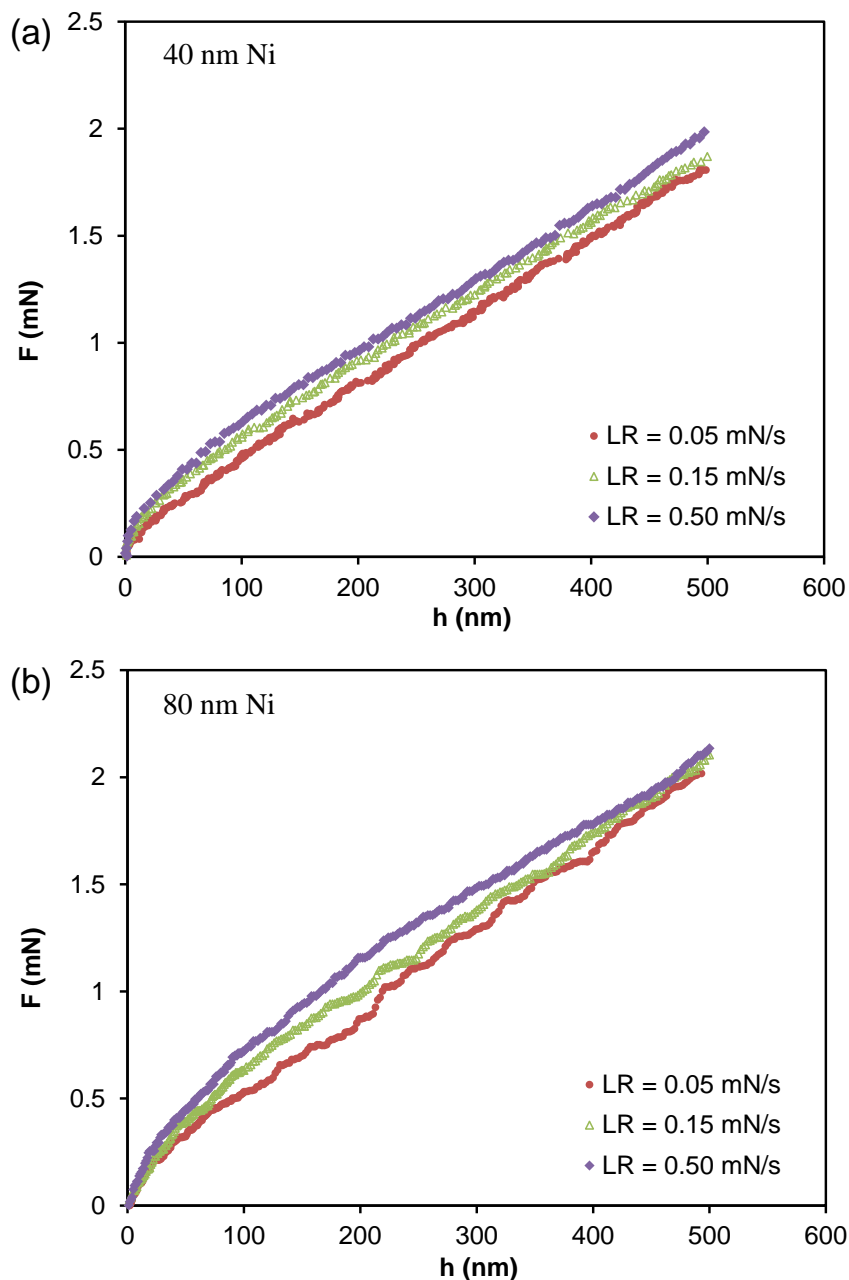
Figure 7.5: Experimentally obtained force, *F* versus displacement, *h* response for a 3 µm diameter Au microsphere coated with Ni layer of (a) 40 and (b) 80 nm thickness, tested at three different loading rates. The 40 nm coated sphere displays much smoother *F-h* responses with low magnitude load jumps like features, whereas the 80 nm coated sphere shows discrete load jumps like features with higher magnitude of load during the jumps. Both of the cases the load jumps rate decreases with increasing loading rates.
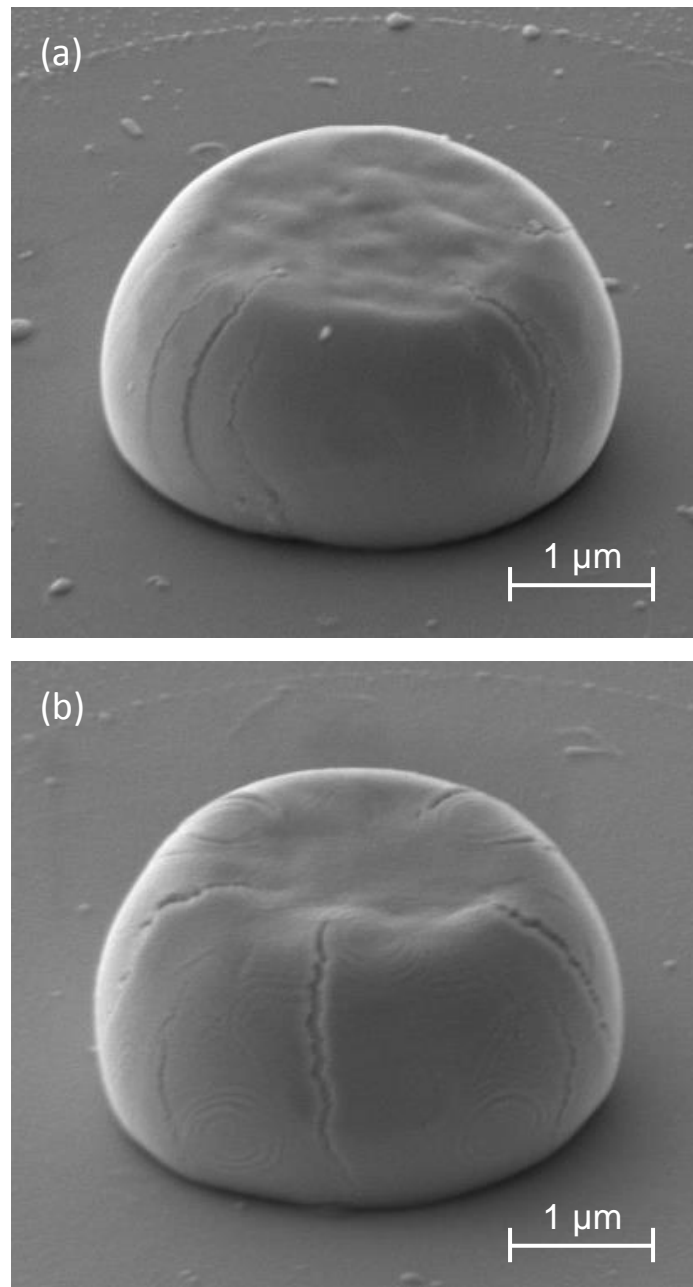
Figure 7.6: SEM images after compression of 3 µm diameter Au microspheres when coated with Ni layer of, (a) 40 and (b) 80 nm, in thickness. The compressed microspheres showing micro cracking and debonding of the Ni layer. It is visible that the crack opening of the coated Au microsphere of the 80 nm Ni coated layer is much bigger than the 40 nm Ni coated layer.

7.3.2 FE Simulation of the Compression of Coated Microspheres

The plastic deformation of the Ni-coated 3 µm diameter Au spheres was analyzed using FE simulation. Two FE models were considered: i) Ni-layer in frictionless contact with the Au sphere and ii) Ni-layer in rigid contact with the Au sphere.
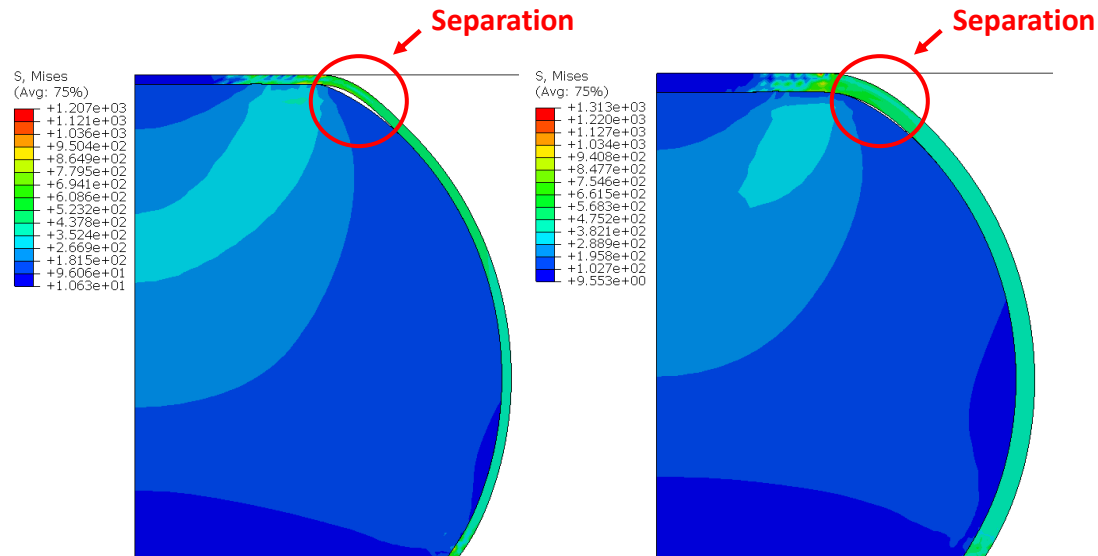
Figure 7.7: Contour plot of von Mises stress distribution from the FE simulation for 3 µm diameter Au microsphere when coated with (a) 40 and (b) 80 nm, layer of Ni by considering frictionless contact model between the Ni coating and Au sphere.

The distribution of the von Mises equivalent stress and strain during the plastic deformation at the lowest loading rate (0.05 mN/s) are showed in contour plot of Figure 7.7 and Figure 7.8. In both coating conditions, the Ni layer becomes separated, or debonded, from the Au sphere as deformation proceeds. The separation of the Ni layer started from the edge of the flat facet located at the top of the Au microsphere where the indenter contacts, and compresses, the sphere. This corresponds well with the location of the cracks observed on the SEM images of the deformed microspheres (Figure 7.6).

The contour plot of the von Mises equivalent plastic strain distribution in Figure 7.8 illustrates that plastic deformation within the Au microsphere is extensive and is maximum at the point where the flat-punch indenter begins contact with the sphere. This,

consequently, is also the point of maximum equivalent strain in the Ni layer and is where the Ni layer first debonds from the Au microsphere.
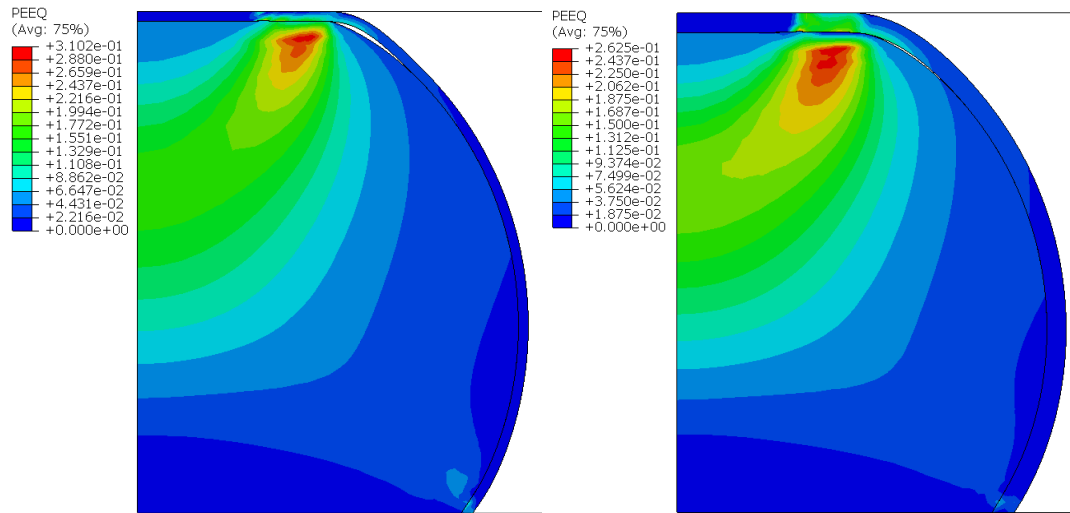
Figure 7.8: Contour plot of von Mises equivalent plastic strain distribution for 3 µm diameter Au microsphere when coated with (a) 40 and (b) 80 nm, layer of Ni by considering frictionless contact between the Ni coating and the Au sphere.

7.4   Results and Discussion

The *F-h* responses in Figure 7.9 indicate that, for slow loading rates of 0.05 and 0.15 mN/s, the force is required to deform the Au sphere increases as the coating thickness increases.

A comparison of the coated and uncoated 3 µm diameter Au microspheres at a selected loading rate, 0.05 mN/s, obtained from the FE simulation of the uniaxial compression (described in Section 7.2.3) are presented in Figure 7.10. The *F-h* curves obtained from the FE simulation show almost the same trend as observed experimentally (Figure 7.9a). The effect of the Ni layer on the initial, incipient, yielding will be analyzed further in the next section.
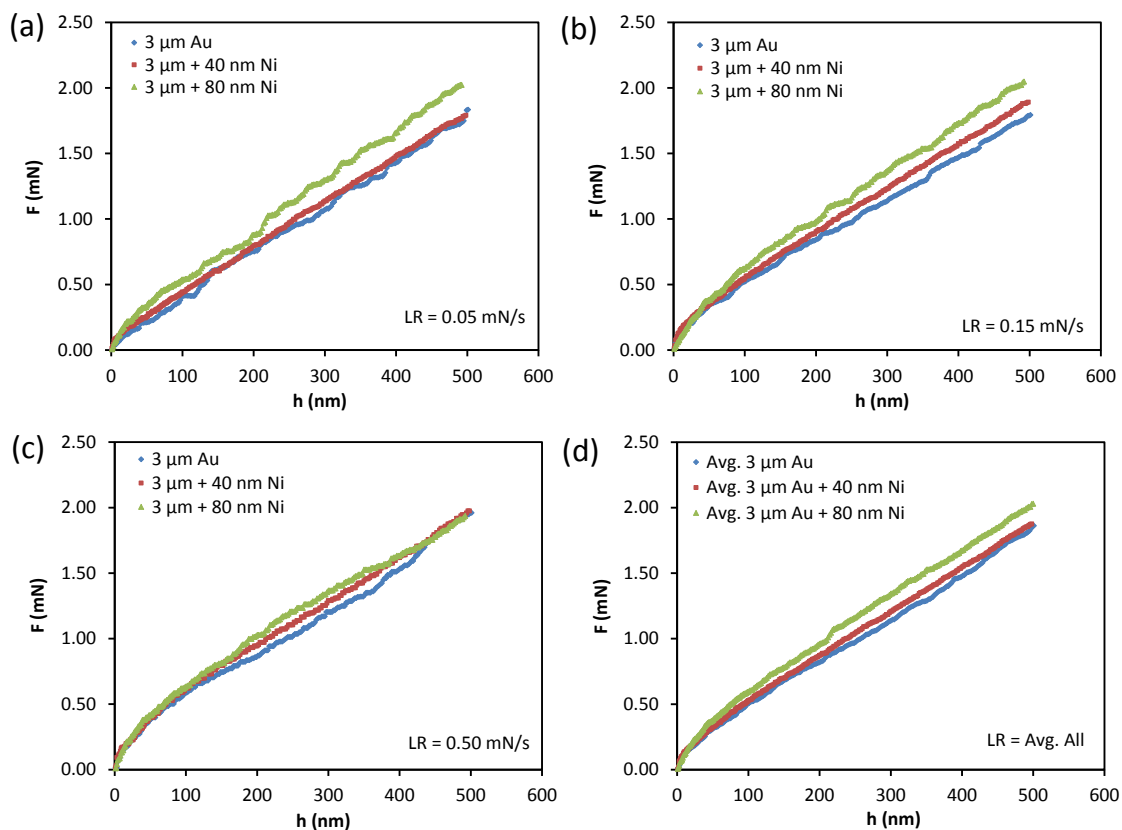
Figure 7.9: Experimentally measured *F-h* response of 3 µm diameter Au microsphere with and without 40 and 80 nm Ni coating deformed at three loading rates: (a) 0.05, (b) 0.15, (c) 0.50 mN/s, and (d) the average *F-h* responses of all loading rates are compared to observe the overall effect of the coating.
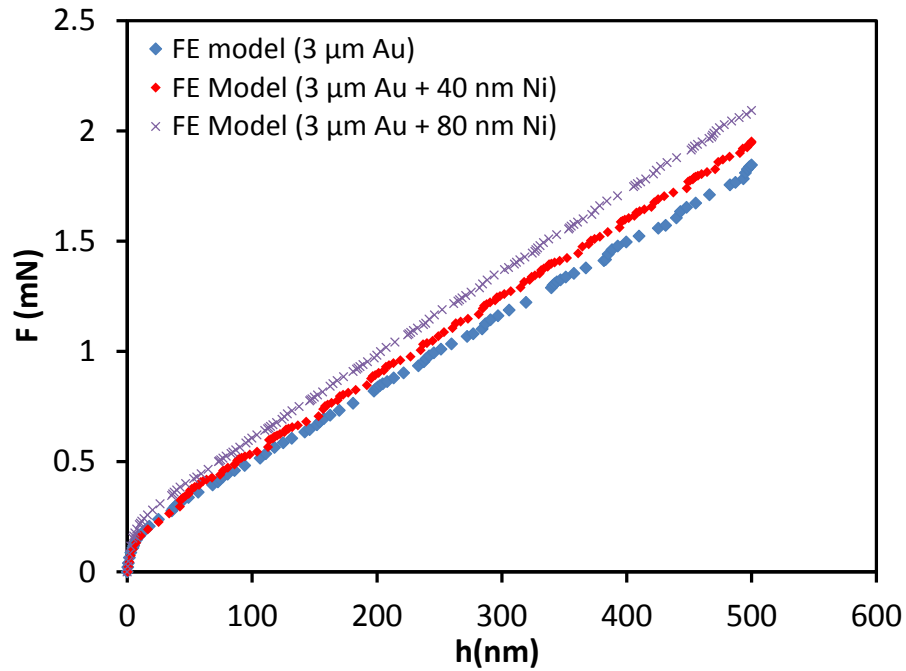
Figure 7.10: Comparison of the *F-h* response obtained from the FE models of the uncoated and coated 3 µm diameter Au microspheres when loaded at a rate of 0.05 mN/s.

The stress-strain distribution in the compressed coated Au microspheres was obtained from the FE simulations. The average von Mises stress-strain data, collected from the nodes along the axis of symmetry of the model, were recorded for each load-depth increment. Figure 7.11 shows the von Mises stress versus von Mises strain curves, averaged along the central axis of rotation on the model, for the 40 and 80 nm Ni coated 3 µm diameter Au spheres compressed at the three loading rates. The yield stress increases with increasing loading rates for both the Ni coatings thicknesses. A comparison plot of the von Mises stress-strain distribution between the coated and non-coated sphere is shown in Figure 7.12. It is obvious that the yield stress increases when the 3 µm diameter Au sphere was coated with a layer of Ni; however, increasing the layer thickness from 40 to 80 nm does not result in significantly further increase in stress.
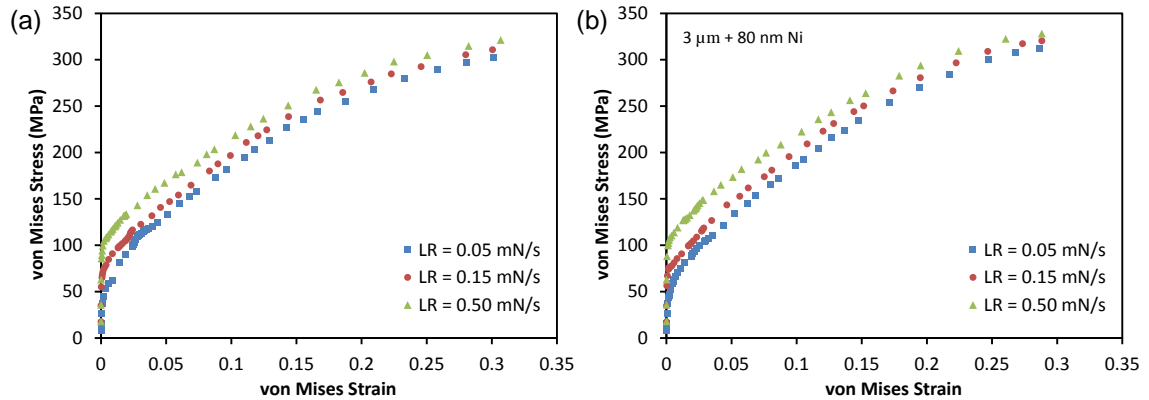
Figure 7.11: von Mises equivalent stress-strain response obtained from the FE models of 3 µm diameter Au sphere with (a) 40 and (b) 80 nm thick Ni coatings at three loading rates.
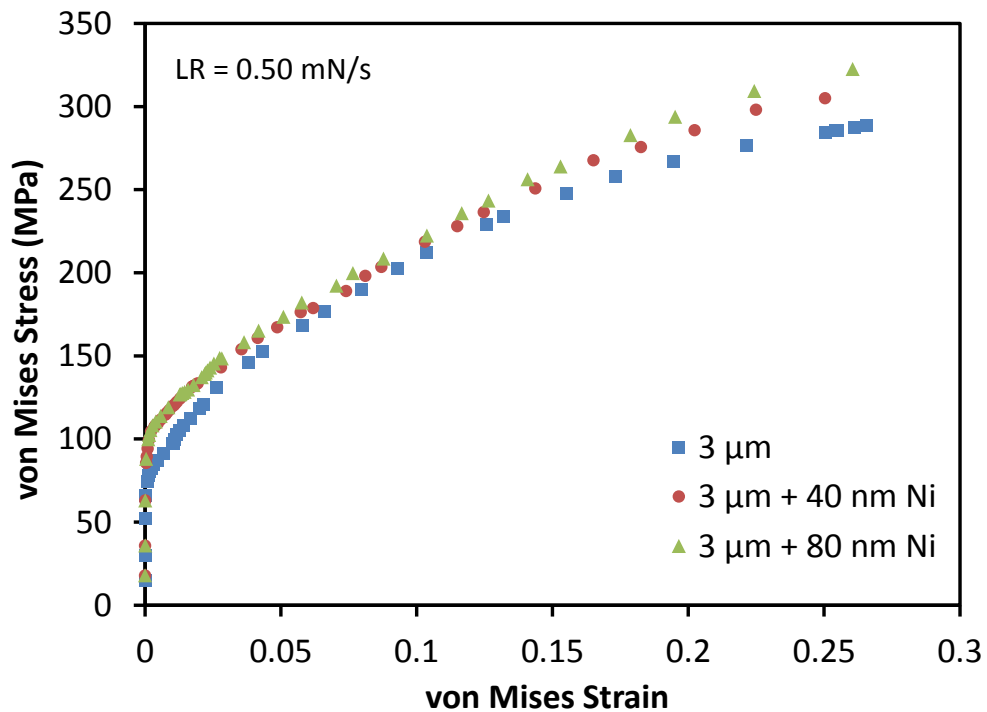
Figure 7.12: A comparison of the von Mises equivalent stress-strain response obtained from the FE models of the coated and uncoated 3 µm diameter Au sphere at 0.50 mN/s loading rate.

7.4.1 Estimation of Initial Yielding using Hertzian Elastic Contact

The variation in the experimentally measured *F-h* curves obtained from multiple specimens of 40 and 80 nm thick Ni-coated 3 µm diameter Au microspheres are shown in Figure 7.13 to Figure 7.15. Included in these graphs are the elastic loading trends calculated by applying the Hertzian equation for contact between an elastic sphere of radius $R_1 = \infty$ (i.e. a flat surface) compressing, to a depth *h*, another elastic sphere of radius $R_2 \approx 1.5$ µm. Because incipient yielding occurred in these microspheres when they were compressed to a very small depth and the yield strength of nano-crystalline Ni is much higher than Au, we are approximating the elastic *F-h* response by assuming that the two spheres in the Hertzian approximation have the elastic properties of Au.

In this Hertzian elastic contact model ($R_1 = \infty$, $R \approx R_2 \approx 1.5$ µm) the contact force, *F* is related to *h* as [22]

$$F = \frac{4}{3} E_r R^{1/2} h^{3/2}$$

(2.24)

where E_r is the reduced elastic modulus which is given as

$$\frac{1}{E_r} = \frac{1 - v_1^2}{E_1} + \frac{1 - v_2^2}{E_2}$$

(2.25)

where, E_1, E_2 are Elastic moduli and v_1, v_2 are Poisson's ratios associate with the Au sphere (R_2) and the diamond half-space (R_1). For this work, E_r was calculated by considering isotropic elastic properties of $E_1 = 1141$ GPa, $v_1 = 0.07$ for the diamond flat-punch indenter [23] and $E_2 = 79$ GPa [19], $v_2 = 0.42$ [20] for the Au sphere. *R* is the radius of the coated Au microsphere which is about 1.54 and 1.58 µm considering the 40 and 80 nm Ni coatings thickness. Additionally, considering the elastic properties of Ni, $E_2 = 207$ GPa, $v_2 = 0.31$ [6], The *F-h* profile obtained from Hertz contact model was also plotted in Figure 7.13 and Figure 7.14.
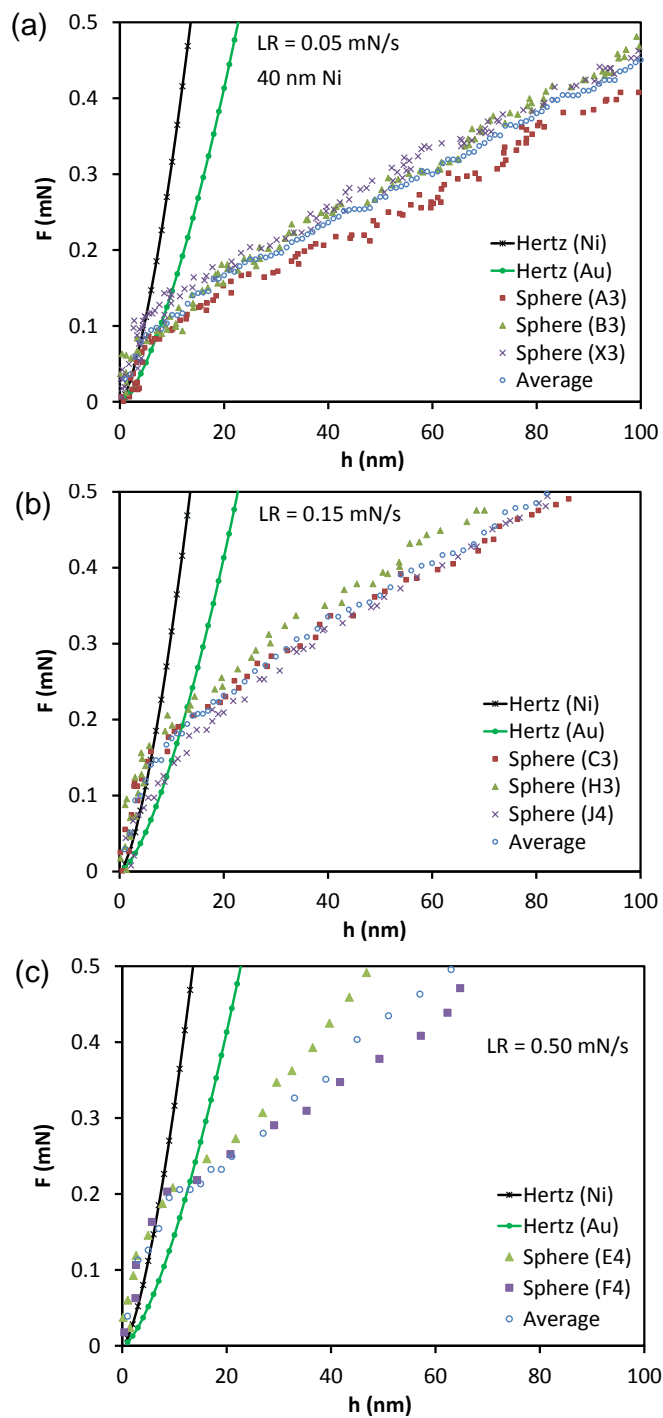
Figure 7.13: Individual *F-h* curves for 40 nm Ni coated 3 µm diameter Au microspheres tested at different loading rates. The solid lines show the elastic stress-strain response predicted by application of a Hertzian contact model. Deviation of the experimental data trend from the elastic model indicates the initiation of *incipient* plasticity.
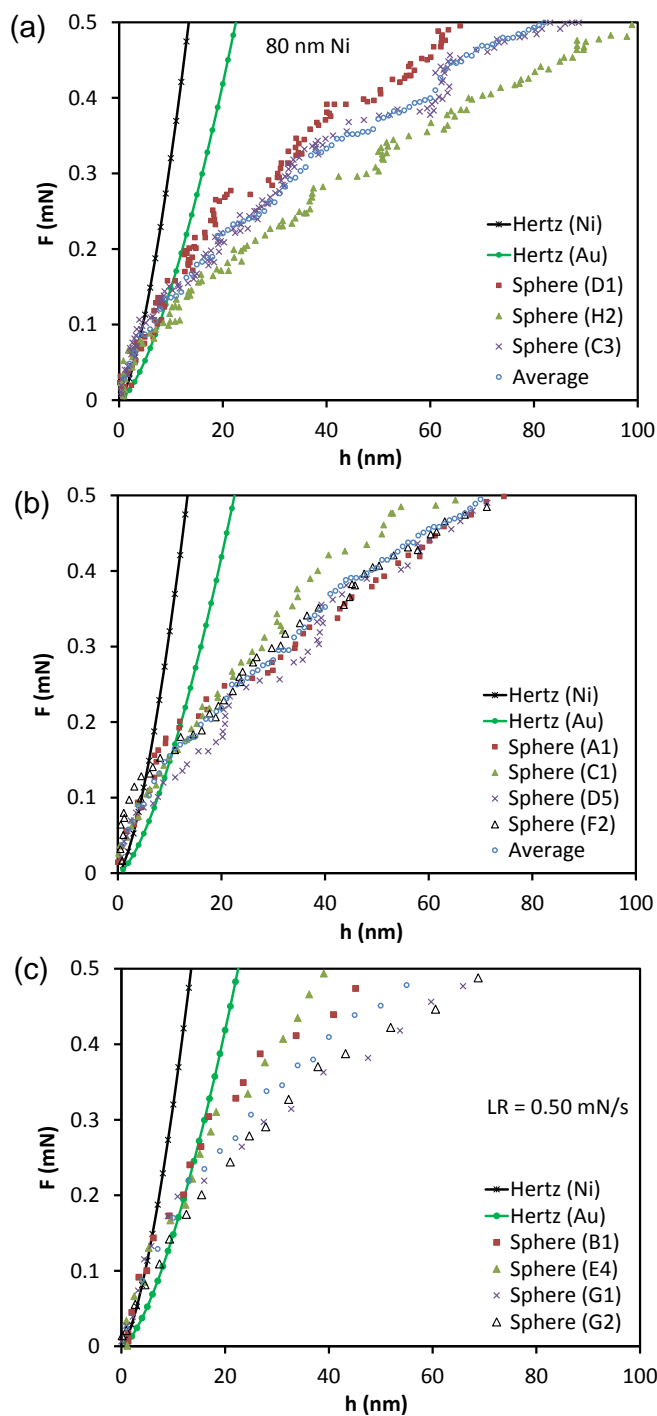
Figure 7.14: Individual *F-h* curves for 80 nm Ni coated 3 µm diameter Au microspheres tested at different loading rates. The solid lines show the elastic stress-strain response predicted by application of a Hertzian contact model. Deviation of the experimental data trend from the elastic model indicates the initiation of *incipient* plasticity.
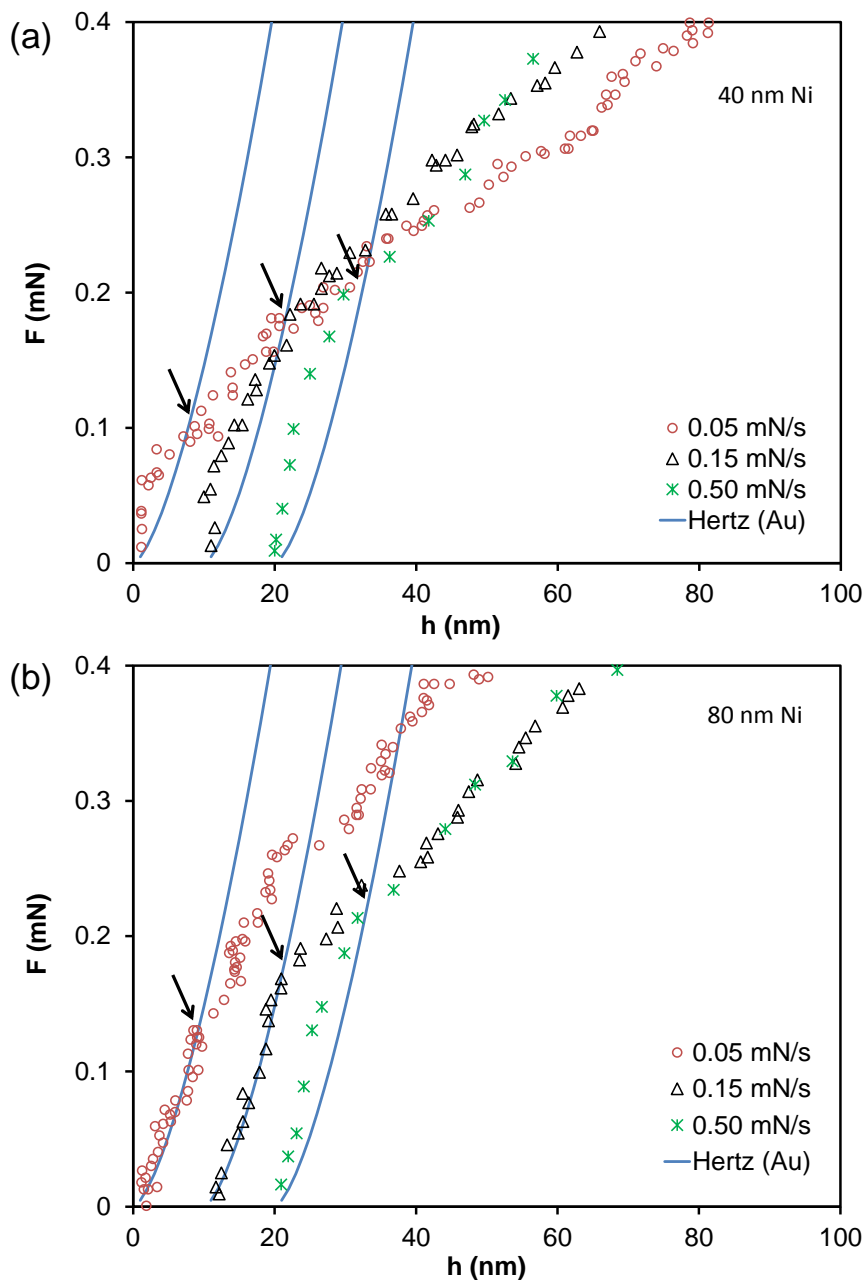
Figure 7.15: Comparison of the representative measured *F-h* curves of Au microspheres with (a) 40 and (b) 80 nm thick Ni coating at three loading rates. For each test the initial portion of the *F-h* curve is well matched by the *F-h* elastic response predicted by the Hertzian contact model (solid blue lines). The load corresponding to the first incipient plasticity event is marked by the black arrow. For the sake of clarity, the displacement data for three loading rates is offset by 10 nm in these figures.

The initial deviation of the experimental *F-h* data from the calculated Hertzian elastic loading profiles in Figure 7.15 is considered to be the point of initiation of incipient plasticity. The incipient load displays an increasing trend with increasing loading rate for the coated microspheres. This indicates that the yield strength, of these samples is strain rate sensitive. A comparison of the incipient loads for both the coated and uncoated spheres is shown in Table 7.1. It is notable that the incipient load for the uncoated spheres is less than the coated sphere for all loading rates. This suggest that the yield strength during the incipient event of the Au microsphere is increased with the Ni coated layer. Similar behavior was observed by Ng and Ngan [24] when Al micropillars of 1.2 to 6.0 µm diameter were coated with tungsten. The coated pillars exhibited a notably higher strain-hardening rate and much smoother stress–strain response. The authors proposed that the tungsten layer suppressed the nucleation and motion of dislocation avalanches during the compression of the micropillars. Their TEM analyses confirmed the trapping of the dislocations inside the deforming Al pillars.

Table 7.1: Summary of loading rate and the corresponding incipient load of the tested uncoated and Ni coated 3 µm diameter Au microspheres

3 µm diameter Au Sphere	Loading rate (mN/sec)	Incipient Load (mN)
	0.05	0.096 ± 0.019
Uncoated	0.15	0.173 ± 0.051
	0.50	0.203 ± 0.061
	0.05	0.115 ± 0.029
Coated with 40 nm of Ni	0.15	0.184 ± 0.025
	0.50	0.213 ± 0.010
	0.05	0.136 ± 0.026
Coated with 80 nm of Ni	0.15	0.178 ± 0.034
	0.50	0.228 ± 0.041

7.4.2   Plastic Deformation of the Coated Spheres

The analysis technique described in Chapter 5 (Section 5.3.4) is used here to estimate the incipient apparent activation volume V^*, a characteristic signature of the deformation rate controlling mechanism in these coated Au microspheres.

In Figure 7.15 and Table 7.1, the increased incipient load with increasing loading rate indicates that the incipient yield stress σ_y, of the tested Ni-coated Au microspheres increased with increasing strain rates. The incipient load data were converted to a *representative* incipient stress by dividing by the area of the {111} facet upon which the flat-punch indenter contacted the coated Au sphere. The contact facet area of the uncoated sphere was measured from SEM images of the microspheres and this contact facet diameter was used for both the coated and uncoated spheres. A *representative* average strain rate at the incipient load was determined as $\dot{\epsilon} = \frac{d}{dt}\left(\frac{\Delta h}{D}\right)$ from the data of the tests performed at each loading rate. In this expression Δh is the compression depth, D is the height of the sphere, and t is the time.

The slope (kT/V^*) of the strain rate dependence of τ, provides information on the apparent activation volume, V^{*5}, (Eq. 5.6, Chapter 5). The τ values were determined from the incipient yield stress σ_y using the relationship (Eq. 5.3) described in detail in Chapter 5 (Section 5.3.2). The dependence of V^* upon Ni layer thickness is shown in Table 7.2 where V^* for the Ni-coated 3 µm Au spheres is compared with that of the uncoated Au spheres. The estimated V^* of the coated microspheres is normalized with respect to b^3, where $b_{Au} = 0.289$ nm [25,26]. The estimated V^* during incipient plasticity of the 40 and 80 nm thick Ni coated Au spheres is about 1.53 and $1.65b^3$ respectively (Table 7.2). It is important to note here that the incipient V^* values obtained for the coated microspheres is the same, within the experimental scatter, as the $V^* = 1.76b^3$ obtained from the uncoated microspheres (Chapter 5).

---

[5] We refer to V^* as the apparent activation volume because in this analysis we treat the stress and strain within the Au spheres as being constant. This is a clear simplification since the FE model predicts a complex, and highly varying stress and strain state in the deformed Au sphere.

The estimated V^* values were converted to the apparent activation energy, Q^*, of the deforming rate controlling obstacles, using the relation [27], $Q^* = \tau_{0K} V^*$, where τ_{0K} is the athermal yield stress of Au, $\tau_{0K} = 256$ MPa [28]. The calculated Q^* for both of the 40 and 80 nm thickness Ni coated Au spheres is about ~0.8eV, which is identical to the uncoated sphere.

Table 7.2: Estimated apparent activation volume, V^*, and energy, Q^*, during the incipient plasticity event of the uncoated and Ni-coated 3 µm diameter Au microspheres

Incipient Deformation Parameters	3 µm Au	3 µm Au + 40 nm Ni	3 µm Au + 80 nm Ni
V^* (b^3)	1.76 ± 0.18	1.53 ± 0.42	1.65 ± 0.34
Q^* (eV)	0.07 ± 0.01	0.08 ± 0.02	0.08 ± 0.02

The V^* of the coated microspheres during the plastic deformation process at 5% of strain can be calculated by using the method described in Chapter 4 (Section 4.4). For 40 and 80 nm coated spheres, the calculated values of the strain rate sensitivity m, corresponding to 5% strain is 0.136 and 0.124 respectively. Using Eq. 4.2 (Chapter 4), the estimated V^* is, $14.3b^3$ for 40 nm and $15.6b^3$ for 80 nm, Ni coated 3 µm diameter Au sphere. V^* increases with the Ni coating and also with the increasing coating thickness. The Q^* increased from 0.45 to 0.60 eV from the uncoated to the coated Au sphere. A comparison of the experimental scatter included values of V^* and Q^* for the uncoated and coated Au microspheres is given in Table 7.3.

Table 7.3: Estimated apparent activation volume, V^*, and energy, Q^*, during plastic deformation at 5% of strain for the uncoated and coated 3 μm Au microspheres

Bulk Deformation Parameters	3 μm Au	3 μm Au + 40 nm Ni	3 μm Au + 80 nm Ni
V^* (b^3)	11.7 ± 1.9	14.3 ± 2.6	15.6 ± 3.2
Q^* (eV)	0.45 ± 0.07	0.55 ± 0.10	0.60 ± 0.12

When considering the estimated V^* and Q^* values corresponding to the incipient initiation of plastic deformation we see that the coated and uncoated spheres are almost identical however, the incipient yield stress increases with the coating thickness and loading rate. This suggests that the general rate-controlling mechanism of *initial* plastic deformation remains the same for the uncoated and the coated 3 μm Au spheres despite the fact that the stress required to initiate the first dislocation movement is increased in the coated microspheres. It is notable that from the FE simulation, the Ni layers start debonding from the corner of Au sphere (Figure 7.8), and the initation of the debonding is observed at about 1% average compressive strain. Thus, one can deduce that the Ni-layer is still intact when incipient plasticity occurs.

When the same microspheres are examined after enduring a significant amount of plastic strain, corresponding to an average compressive strain of about 5%, the estimated V^* and Q^*, increase with Ni coating (Table 7.3). In this situation the Ni layer has begun to crack but is not fully seperated from the Au sphere (Figure 7.6). Thus, the Ni layer appears to still be constraining the movement of mobile dislocations within Au sphere and impeding their reaching the free surface.

7.5   Summary

Single crystalline Au microspheres of 3 μm diameter were coated with a Ni layer of either 40 or 80 nm thickness and tested by compression at different loading rates to study the effect of extrinsic constraint on the mechanical properties and deformation mechanisms of these small-size spheres.

The Ni coating resulted in a slightly increased *F-h* response compared to similar diameter uncoated Au microspheres and, in all cases the *F-h* response was clearly dependent upon loading rate.

The estimated apparent activation volume V^* corresponding to the initiation of incipient plasticity is nearly identical for the coated and the uncoated Au microspheres, $V^*_{uncoated}$ is about $1.76b^3$ while V^*_{coated} is between 1.53 and $1.65b^3$. This suggest that the mechanism responsible for the initiation of first dislocation motion in the Au microspheres is essentially the same regardless of the presence of a constraining coating however the Ni coating does raise the stress required for dislocation nucleation slightly.

When one considers the apparent activation volume and energy of the rate-dependent deformation process after the Au microspheres have endured significant (about 5%) plastic strain we observe that V^* is increased to between 14.3 and $15.6b^3$ for the coated spheres compared to 11.7 b^3 for the uncoated spheres and V^* increases with increasing Ni layer thickness from 40 to 80 nm. This increase in apparent activation volume reflects the effect of the Ni layer constraining the motion of nucleated dislocations and preventing them from reaching the free surface of the microspheres.

References

1. J. R. Greer, W. C. Oliver, and W. D. Nix, Apr. 2005, "Size dependence of mechanical properties of gold at the micron scale in the absence of strain gradients," *Acta Mater.*, Vol. 53, pp. 1821–1830.

2. W. D. Nix, J. R. Greer, G. Feng, and E. T. Lilleodden, Feb. 2007, "Deformation at the nanometer and micrometer length scales: Effects of strain gradients and dislocation starvation," *Thin Solid Films*, Vol. 515, pp. 3152–3157.

3. J.-Y. Kim and J. R. Greer, Oct. 2009, "Tensile and compressive behavior of gold and molybdenum single crystals at the nano-scale," *Acta Mater.*, Vol. 57, pp. 5245–5253.

4. W. Mook, J. Nowak, C. Perrey, C. Carter, R. Mukherjee, S. Girshick, P. McMurry, and W. Gerberich, Jun. 2007, "Compressive stress effects on nanoparticle modulus and fracture," *Phys. Rev. B*, Vol. 75, pp. 214112–10.

5. Z.-J. Wang, Z.-W. Shan, J. Li, J. Sun, and E. Ma, Feb. 2012, "Pristine-to-pristine regime of plastic deformation in submicron-sized single crystal gold particles," *Acta Mater.*, Vol. 60, pp. 1368–1377.

6. C. P. Frick, B. G. Clark, S. Orso, a. S. Schneider, and E. Arzt, Aug. 2008, "Size effect on strength and strain hardening of small-scale [111] nickel compression pillars," *Mater. Sci. Eng. A*, Vol. 489, pp. 319–329.

7. M. D. Uchic, D. M. Dimiduk, J. N. Florando, and W. D. Nix, Aug. 2004, "Sample dimensions influence strength and crystal plasticity.," *Science*, Vol. 305, pp. 986–9.

8. W. Nix, 1989, "Mechanical properties of thin films," *Metall. Trans. A*, Vol. 20.

9. R. Venkatraman and J. C. Bravman, 1992, "Separation of film thickness and grain boundary strengthening effects in Al thin films on Si," *J. Mater. Res.*, Vol. 7, pp. 2040–2048.

10. R. P. Vinci and J. J. Vlassak, Aug. 1996, "Mechanical Behavior of Thin Films," *Annu. Rev. Mater. Sci.*, Vol. 26, pp. 431–462.

11. D. Son, J. H. Jeong, and D. Kwon, 2003, "Film-thickness considerations in microcantilever-beam test in measuring mechanical properties of metal thin film," *Thin Solid Films*, Vol. 437, pp. 182–187.

12. P. Fredriksson and P. Gudmundson, 2005, "Size-dependent yield strength of thin films," *Int. J. Plast.*, Vol. 21, pp. 1834–1854.

13. H. Fan, Z. Li, M. Huang, and X. Zhang, 2011, "Thickness effects in polycrystalline thin films: Surface constraint versus interior constraint," *Int. J.*

Solids Struct., Vol. 48, pp. 1754–1766.

14. M. J. Kobrinsky and C. V. Thompson, 2000, "Activation volume for inelastic deformation in polycrystalline Ag thin films," *Acta Mater.*, Vol. 48, pp. 625–633.

15. R.-M. Keller, S. P. Baker, and E. Arzt, 1998, "Quantitative analysis of strengthening mechanisms in thin Cu films: Effects of film thickness, grain size, and passivation," *J. Mater. Res.*, Vol. 13, pp. 1307–1317.

16. D. Mordehai, S.-W. Lee, B. Backes, D. J. Srolovitz, W. D. Nix, and E. Rabkin, Aug. 2011, "Size effect in compression of single-crystal gold microparticles," *Acta Mater.*, Vol. 59, pp. 5202–5215.

17. D. Mordehai, M. Kazakevich, D. J. Srolovitz, and E. Rabkin, Apr. 2011, "Nanoindentation size effect in single-crystal nanoparticles and thin films: A comparative experimental and simulation study," *Acta Mater.*, Vol. 59, pp. 2309–2321.

18. S.-W. Lee, D. Mordehai, E. Rabkin, and W. D. Nix, Jul. 2011, "Effects of focused-ion-beam irradiation and prestraining on the mechanical properties of FCC Au microparticles on a sapphire substrate," *J. Mater. Res.*, Vol. 26, pp. 1653–1661.

19. C. A. Volkert and E. T. Lilleodden, Nov. 2006, "Size effects in the deformation of sub-micron Au columns," *Philos. Mag.*, Vol. 86, pp. 5567–5579.

20. D. Maharaj and B. Bhushan, 2014, "Nanomanipulation, nanotribology and nanomechanics of Au nanorods in dry and liquid environments using an AFM and depth sensing nanoindenter," *Nanoscale*, Vol. 6, p. 5838.

21. F. Ebrahimi, G. . Bourne, M. . Kelly, and T. . Matthews, May 1999, "Mechanical properties of nanocrystalline nickel produced by electrodeposition," *Nanostructured Mater.*, Vol. 11, pp. 343–350.

22. L. Kogut and I. Etsion, 2002, "Elastic-Plastic Contact Analysis of a Sphere and a Rigid Flat," *J. Appl. Mech.*, Vol. 69, p. 657.

23. D. Catoor, Y. F. Gao, J. Geng, M. J. N. V Prasad, E. G. Herbert, K. S. Kumar, G. M. Pharr, and E. P. George, 2013, "Incipient plasticity and deformation mechanisms in single-crystal Mg during spherical nanoindentation," *Acta Mater.*, Vol. 61, pp. 2953–2965.

24. K. S. Ng and a. H. W. Ngan, 2009, "Effects of trapping dislocations within small crystals on their deformation behavior," *Acta Mater.*, Vol. 57, pp. 4902–4910.

25. W. D. Nix and S. Lee, 2011, "Micro-pillar plasticity controlled by dislocation nucleation at surfaces," *Philos. Mag.*, Vol. 91, pp. 1084–1096.

26. V. Bhakhri and R. J. Klassen, Apr. 2009, "The strain-rate dependence of the

nanoindentation stress of gold at 300 K: A deformation kinetics-based approach," *J. Mater. Res.*, Vol. 24, pp. 1456–1465.

27. J. M. Wheeler, C. Niederberger, C. Tessarek, S. Christiansen, and J. Michler, Jan. 2013, "Extraction of plasticity parameters of GaN with high temperature, in situ micro-compression," *Int. J. Plast.*, Vol. 40, pp. 140–151.

28. F. H. J. and M. F. Ashby, *Deformation-Mechanism Maps*, 1st ed. New York, USA: Pergamon Press, 1982.

Chapter 8

8   Conclusion and Scope of Future Research

The main objective of this research was to use micro-mechanical test techniques to understand the effect of microstructure on the underlying mechanisms of plastic deformation of micron and sub-micron size *FCC* metal samples. The following conclusions can be drawn the results obtained from the experimental and numerical studies in this research:

In the first study in this thesis (Chapter 3), the length scale dependence of the operative plastic deformation mechanisms was studied using compression tests performed on Au micropillars and microspheres of 1.0 to 5.0 µm diameter. The samples were tested at room temperature and displayed deformation that had a component of random strain jumps. In the case of the Au micropillars, the frequency of the strain jumps showed a bilinear dependence upon pillar diameter with the frequency being larger, and more sensitive to diameter, when the pillar diameter was small (and τ_R was high). This indicates a transition from deformation occurring by multiple-slip to deformation occurring predominantly by single-plane dislocation slip when the pillar diameter is less than 2.0 µm.

The strain jump frequency during the constant-load micropillar creep tests showed a linear dependence upon τ_R. Constant-load creep tests performed on the microspheres of 5.0 µm diameter displayed displacement jump frequency that was essentially independent of applied load while the jump frequency increased with increasing load for the smaller 2.5 µm diameter microspheres. The difference is related to the volume of the microsphere: when the volume is small, the component of the deformation that occurs by a stochastic dislocation glide process is increased and becomes strongly dependent upon the magnitude of the applied local shear stress.

In the following study (Chapter 4), the dependence of the plastic deformation of Au microspheres upon sphere diameter (0.8 – 6.0 µm) and strain rate at ambient temperature

is investigated using micro-compression testing. The flow stress displayed nominal dependence upon both strain and strain rate, and diameter of the Au microspheres. Analysis of the apparent activation volume, V^* and energy Q^* of the deformation process indicated that the operative deformation mechanism, for the smaller 0.8 − 1.0 µm diameter spheres was typical of a mechanism limited by the surface nucleation of dislocation, and for the larger 3.0 − 6.0 µm diameter spheres was controlled by the dislocation-obstacle interaction limited mechanism, which is typical for bulk *FCC* metals. These findings are particularly important in case of emerging nano/micro-technologies, making use of materials at ever decreasing scales.

Subsequently in Chapter 5, flat-punch micro-compression testing was employed to investigate the deformation-rate dependence of the incipient plastic deformation of Au microspheres of diameter ranging from 0.8 to 6.0 µm. The incipient yield load increased with increasing loading rate for a particular sized microsphere, whereas, it decreased with increasing microsphere size. The size dependence of incipient loads was attributed to the presence of vacancies whose amount increased, as a result of increased flat-punch/sphere contact area, in the larger diameter microspheres. A thermal activation based model was used to interpret the loading-rate dependence of the measured incipient loads. The apparent activation volume, V^*, and energy, Q^*, values were found to be $0.2b^3$ and 0.01eV for 0.8 µm sphere and increased to $2.1b^3$ and 0.08eV for 6.0 µm sphere. These estimated values indicate that the incipient plasticity is controlled by heterogeneous dislocation nucleation events occurring at, or near, the flat-punch/sphere interface the rate of which is highly dependent upon the rate of surface self-diffusion of the Au atoms. This study illustrates the importance of surfaces on the onset of plastic deformation in crystalline metal nano-structures such as microspheres, micropillars and microbeams.

The sample size and strain rate dependence of the plastic deformation behavior of Au micropillars (0.8 to 4.0 µm diameter) subjected to uniaxial compression at ambient temperature was studied in Chapter 6. It was observed that the dependence of the flow stress, after considerable plastic deformation corresponding to ε = 5%, was dependent upon both strain rate and micropillar diameter. Analysis of the apparent activation volume, V^* and energy Q^* of the deformation process indicated that the operative

deformation mechanism, for the small 0.8 µm diameter pillars was typical of a mechanism limited by the surface nucleation of dislocations, and for the larger 2.0 and 4.0 µm diameter pillars was controlled by the more common dislocation-obstacle interaction limited mechanism.

The deformation-rate dependence of the incipient plastic deformation behavior was also investigated for the micropillars. The incipient yield stress, for a particular sized micropillar, increased with increasing strain rate whereas, for a particular strain rate, it decreased with increasing micropillar diameter. The size dependence of incipient yield stress was attributed to the presence of vacancies whose amount increased, as a result of increased flat-punch/pillar contact area, in the larger diameter micropillars. The apparent activation volume, V^*, and energy, Q^*, values were found to be $5.4b^3$ and 0.21eV for 0.8 µm diameter pillars and increased to $144b^3$ and 5.55eV for 4.0 µm diameter pillars. These estimated values suggest that the incipient plasticity of the smallest diameter pillar is controlled by heterogeneous dislocation nucleation events occurring at, or near, the flat-punch/pillar top interface the rate of which is highly dependent upon the rate of surface self-diffusion based process.

The final study of this thesis was to understand the effect of extrinsic constraint on the mechanical properties and deformation mechanisms of these small-size Au spheres. In this investigation single crystalline Au microspheres of 3.0 µm diameter were coated with a Ni layer of either 40 or 80 nm thickness and tested by compression at different loading rates. The Ni coating resulted in a slightly increased F-h response compared to similar diameter uncoated Au microspheres and, in all cases the F-h response was clearly dependent upon loading rate.

The estimated apparent activation volume V^* corresponding to the initiation of incipient plasticity is nearly identical for the coated and the uncoated Au microspheres, $V^*_{uncoated}$ is about $1.76b^3$ while V^*_{coated} is between 1.53 and $1.65b^3$. This suggest that the mechanism responsible for the initiation of first dislocation motion in the Au microspheres is essentially the same regardless of the presence of a constraining coating however the Ni coating does raise the stress required for dislocation nucleation slightly.

When one considers the activation volume and activation energy of the rate-dependent deformation process after the Au microspheres have endured significant (about 5%) plastic strain we observe that V^* is increased to between 14.3 and 15.6b^3 for the coated spheres compared to 11.7 b^3 for the uncoated spheres and V^* increases with increasing Ni layer thickness from 40 to 80 nm. This increase in activation volume reflects the effect of the Ni layer constraining the motion of nucleated dislocations and preventing them from reaching the free surface of the microspheres.

8.1 Scope of Future Research

The findings of the studies reported in this thesis open many research areas for future consideration. Some of these are described below:

1. Molecular Dynamic Simulation

It was found from this research that surfaces play a very important role to the deformation mechanism of the small size samples. Atomistic molecular dynamic simulation of the microsphere and pillar compression process can be performed to understand the effect of surface and the activity of dislocation at the interface of the flat-punch indenter and the microsphere facets and pillar top diameter. This is currently a very active area of research and one that Prof. R. J. Klassen's group has also now become involved with.

2. Surface Passivation Layer of Micropillar and Microsphere

In this study, 40 and 80 nm layer of Ni are used to passivate 3.0 µm diameter Au sphere, several different thickness layer of Ni can be deposited on the 3.0 µm diameter Au sphere and further study can be performed to know the effect of Ni layer thickness to the Au sphere deformation. Smaller diameter Au spheres (0.8 and 3.0 µm) can be coated with different layer of Ni to study the effect of coating to the size of the sphere. Different materials can be chosen to passivate the microspheres such that interfacial debonding can be avoided. Similar study can be performed on micropillars and the estimated deformation parameters can be compared with microspheres.

3. High Temperature Micro-compression

The strain rate-dependence plastic deformation behavior of these Au microspheres can be performed at elevated temperature. Uniaxial compression test at three different loading rates can be done on these Au spheres and pillars at 300, 400 and 500°C to accurately measure the thermal activation energy of the deformation process.

4. Long-duration Creep Testing at High Temperature

The kinetics of the time-dependent plastic deformation behavior of these Au microspheres can be studied further at ambient and elevated temperatures. These test can be performed by selecting three different level of compression force below the yield force of the microspheres. The resulting depth-time data obtained from these creep test can be analyzed further using thermal activation based model to find out the fundamental deformation rate controlling parameter activation volume to understand the kinetics of the creep deformation.

Appendices

Appendix A: Study of the effect of element size on the FE results

The FE model of the 3.0 µm diameter Au microspheres presented in Chapter 4, is further analyzed with a coarse to fine mesh to see how a change in mesh density affect the results. Corse to fine mesh of the Au sphere is shown in Figure A.1.
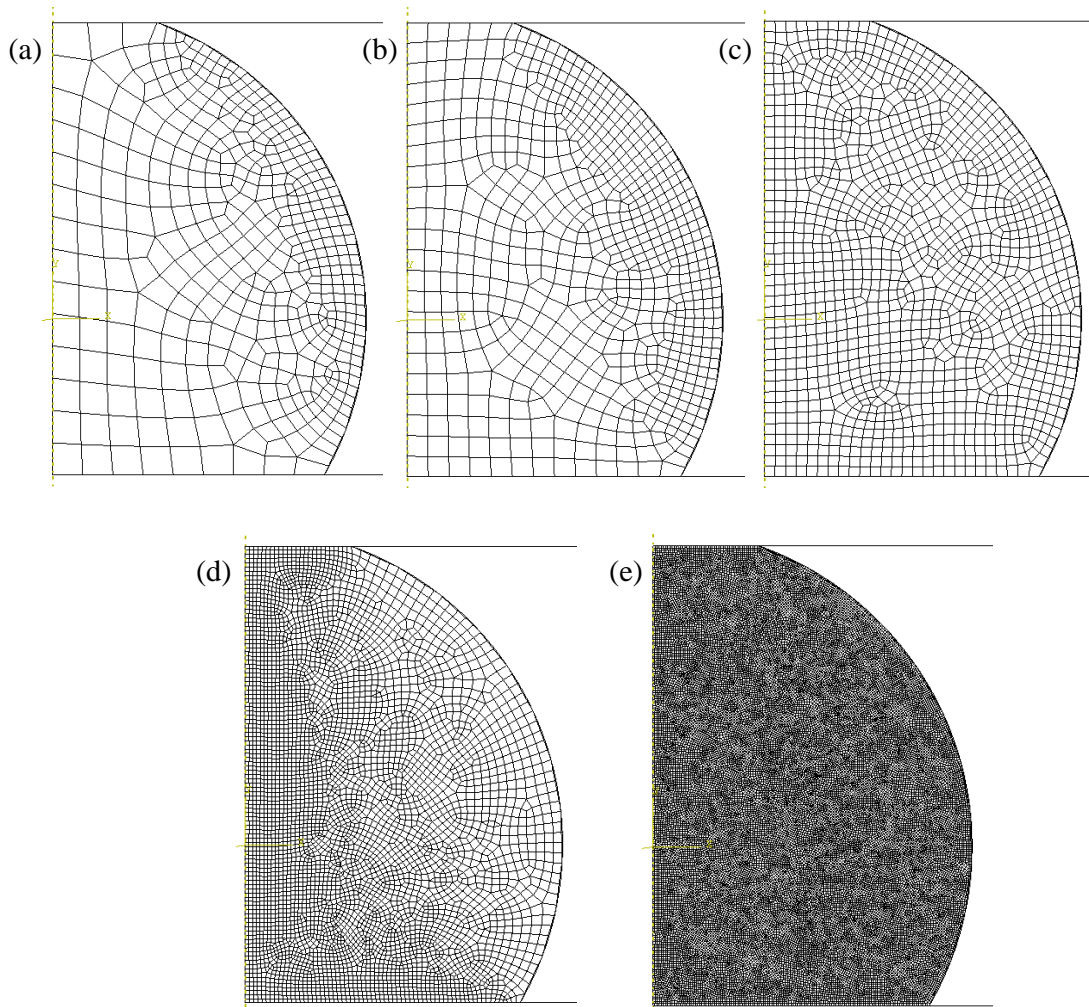

Figure A.1: Corse to fine mesh of the 3.0 µm diameter Au sphere FE model. The mesh is performed using approximate global element size control of (a) 0.15, total 448 elements (b) 0.10, total 664 elements, (c) 0.05, total 1257 elements, (d) 0.03, total 4867 elements and (d) 0.01, total 33701 elements.
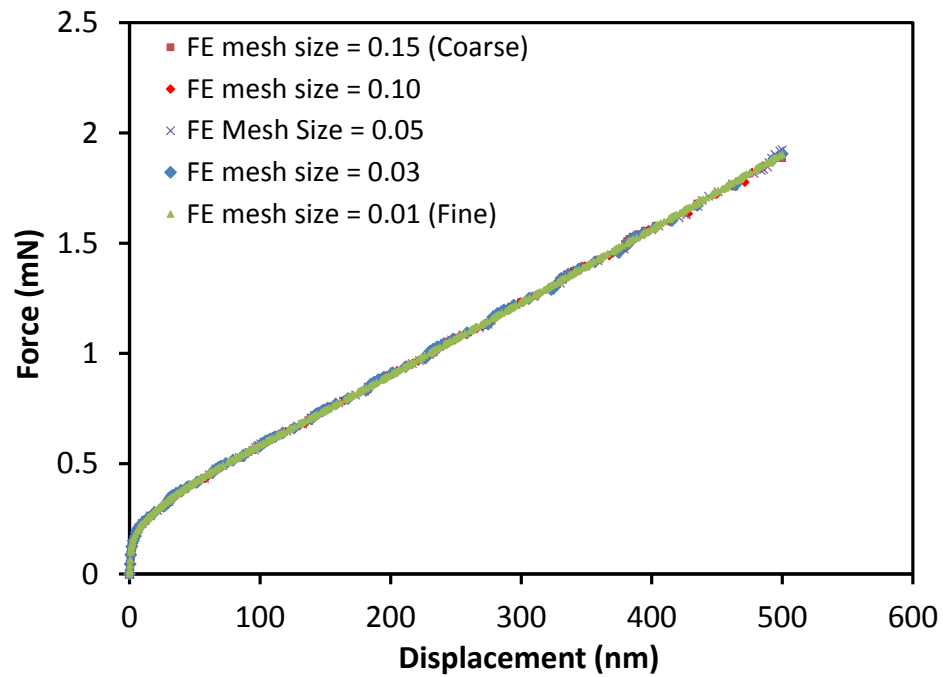
Figure A.2: The force-displacement (*F-h*) curve obtained from course to fine mesh of the 3.0 μm diameter Au microsphere uniaxial compression FE model. The *F-h* curves produced by different model does not noticeably affect the results.

Curriculum Vitae

Name: A Z M Ariful Islam

Post-secondary   Bangladesh University of Engineering and Technology
Education and   Dhaka, Bangladesh
Degrees: 1999 – 2004 B.Sc. (Mechanical Engineering)

                      The University of Western Ontario
                      London, Ontario, Canada
                      2008 – 2010 ME.Sc. (Mechanical and Materials Engineering)

                      The University of Western Ontario
                      London, Ontario, Canada
                      2010 – 2016 Ph.D. (Mechanical and Materials Engineering)

Honours and   Western Engineering Scholarship
Awards: 2008 – 2010, 2010 – 2015

                      Province of Ontario Graduate Scholarship (OGS)
                      2014 – 2015

Related Work   Research Assistant
Experience   The University of Western Ontario
                      2008 – 2010, 2010 – 2016

                      Teaching Assistant
                      The University of Western Ontario
                      2009 – 2010, 2010 – 2015

Publications and Conferences:

- AZM Islam and R. J. Klassen, Study of the Size Dependence of Time-dependent Plastic Deformation of Gold Micro-pillars and Micro-spheres, *MRS Proc.*, Vol. 1580, pp 1-6, May 2013 (http://dx.doi.org/10.1557/opl.2013.652).

- AZM Islam, V Bhakhri, R. J. Klassen, Plastic Deformation of Gold Microspheres, Proceedings of the 25th Canadian Congress of Applied Mechanics, London, Ontario, Canada, 2015

- AZM Islam and R. J. Klassen, Study of the plastic deformation of gold microsphere at ambient temperature, The 2014 MRS Spring Meeting, San Francisco, California, 2014.

- AZM Islam, R. J. Klassen, Time-dependent plastic deformation of Au micropillars and microspheres at room temperature, the 25th Canadian Materials Science Conference, McGill University, Montreal, 2013.

- AZM Islam, R. J. Klassen, Length-scale dependence of the constant-load creep of Au micropillars at room temperature", the 24th Canadian Materials Science Conference, London, 2012.

- AZM Islam, FE simulation and experimental validation of the plastic deformation and the residual stress at grain boundaries in an indented A600 Ni-based alloy, MESc Thesis, Western University, Ontario, Canada, 2010.

- AZM Islam, R. J. Klassen, FE analysis of residual stress at grain boundaries that undergo SCC in the A600 Ni-based alloy, the 22nd Canadian Materials Science Conference, Waterloo, 2010.

- AZM Islam, R. J. Klassen, A finite element simulation of the residual stress at grain boundaries near conical micro-indentations in an elastically anisotropic / plastically isotropic nickel-based alloy, the 21st Canadian Materials Science Conference, Kingston, 2009.